Structural Brain Network Degeneration and Functional Up-regulation In Huntington's disease

Thesis submitted for the degree of Doctor of Philosophy

Peter McColgan

Institute of Neurology

University College London

2018

For Nao, Daichiro and Kotaro

Declaration of authorship and originality

I, Peter McColgan, confirm that the work presented in this thesis is my own. Where information has been derived from other sources, I confirm that this has been indicated in the thesis.

Acknowledgements

Above all, I would like to thank the patients and their families. Without their involvement and dedication to Huntington's disease research none of this work would be possible. I hope that the work presented here will play a part in the search for curative treatments and that one day we may be able to prevent Huntington's disease completely.

I would like to thank my supervisors Sarah Tabrizi and Geraint Rees, who have provided me with exceptional support, mentorship and guidance. They have both helped and taught me more than I could possibly put into words here.

I would also like to thank Kiran Seunarine, Adeel Razi and Sarah Gregory. They have been a source of constant support and mentorship. I extend this thanks to the Imaging team at the Huntington's disease research centre – Rachael Scahill, Eli Johnson and Helen Crawford and the team at the Institute of Child health, particularly Chris Clark.

Finally I would like to thank my wife and sons, my parents and brother for their endless support and love.

Abstract

Huntington's disease (HD) is a neurodegenerative disorder caused by a CAG repeat expansion in the Huntingtin gene on chromosome 4. In recent years there have been significant advances in understanding both the cellular pathology and the macrostructural changes that occur in the striatum and cortical structures as the disease proceeds. However, it remains unclear how abnormalities at the cellular level lead to characteristic patterns of macrostructural change in the brains of HD patients. In this thesis I aim to link structural and functional brain network abnormalities with regional changes at the cellular level.

Using diffusion tractography and resting state functional MRI in well characterised HD cohorts I examine the relationship between structural and functional brain network organisation. I link these changes in structure and function to the neuropsychiatric symptoms prevalent in HD, occurring years before the manifestation of motor symptoms. By characterising changes in white matter brain networks I reveal how the brain network breaks down as HD progresses and show how this network deterioration leads to the emergence of clinical deficits. Using characteristics of the healthy white matter brain network I demonstrate how it is possible to predict the atrophy of specific brain connections in HD over time. In doing so I highlight a hierarchy of white matter connection vulnerability showing cortico-striatal connections are the first to be affected. In order to link these macrostructural white matter changes to cellular level abnormalities I utilise data from the Allen Institute transcription atlas and show how differences in regional gene expression in the healthy brain can account for the selective vulnerability of specific white matter connections in HD. The work presented in this thesis demonstrates how linking systems and cellular pathobiology in HD can inform us about disease mechanisms that drive brain atrophy and ultimately lead to clinical deficits.

Contents

Chapter 6. Topological length of white matter connections predicts their rate of atrophy in premanifest HD

Chapter 7. Brain regions showing white matter connectivity loss in premanifest HD are enriched for synaptic and metabolic genes

Chapter 8. General discussion

List of figures

List of tables

List of Abbreviations

AD	Alzheimer's disease
Ad	Axial diffusivity
ADC	Apparent diffusion coefficient
AIBS	Allen Institute of brain Science
ALS	Amyotrophic lateral sclerosis
ANOVA	Analysis of variance
A-P	Antero-posterior
ASO	Antisense oligonucleotide
BAIS	Baltimore Apathy and Irritability Scale
BCT	Brain connectivity toolbox
BDNF	Brain-derived neurotrophic factor
BDI	Beck Depression Inventory
BET	Brain extraction tool
BOLD	Blood oxygen level dependent
bvFTD	Behavioural variant fronto-temporal dementia
CAG	Cytosine-Adenine-Guanine
CBS	Cortical basal syndrome
CC	Corpus callosum
CJD	Creutzfeldt-Jakob disease
CSD	Constrained spherical deconvolution
CSF	Cerebrospinal fluid
CVA	Canonical variate analysis
DBS	Disease burden score
DFM	Default mode network
DLPFC	Dorsolateral prefrontal cortex

DTI	Diffusion tensor imaging
DWI	Diffusion weighted magnetic resonance imaging
EC	Eddy currents
EPI	Echo-planar imaging
ESM	Epidemic spreading model
FA	Fractional anisotropy
FDR	False discovery rate
FID	Free induction decay
fMRI	Functional magnetic resonance imaging
FOD	Fibre orientation distribution
FOV	Field of view
FWE	Family wise error
GM	Grey Matter
GP	Globus Pallidus
GO	Gene ontology
HADS	Hospital Anxiety and Depression Score
HEA	Head coil element anterior
HEP	Head coil element posterior
HD	Huntington's disease
HTT	Huntingtin
IPL	Inferior parietal lobule
LMER	Linear mixed effects regression
MAPT	Microtubule-Associated Protein Tau
MD	Mean Diffusivity
MDD	Major depressive disorder
MEG	Magnetic Encephalography
MRI	Magnetic resonance imaging

MSN	Medium spiny neuron
MYRF	Myelin regulatory factor
NBS	Network-based statistics
PCA	Principle components analysis
PCC	Posterior Cingulate Cortex
PD	Parkinson's disease
PET	Positron Emission Tomography
PGC1α	Peroxisome-proliferator-activated receptor gamma co-activator α
PGSE	Pulsed gradient spin echo
PLS	Partial least squares
PNFA	Progressive non-fluent aphasia
PreHD	Premanifest Huntington's disease
QC	Quality control
rTMS	Repetitive trans-cranial stimulation
rs-fMRI	Resting state functional magnetic resonance imaging
RD	Radial diffusivity
RF	Radiofrequency
ROI	Region of interest studies
ROS	Reactive oxygen species
RNA	Ribonucleic acid
SD	Semantic dementia
SDMT	Symbol digit modalities test
SENSE	Sensitivity Encoding
SFG	Superior frontal gyrus
SIFT	Spherical deconvolution informed filtering of tractograms
SMA	Supplementary motor area
SWR	Stroop word reading

TBSS	Tract based spatial statistics
TE	Echo time
TMS	Total motor score
TR	Repetition time
UHDRS	Unified HD rating scale
VCP	Voxel connectivity profile
WM	White Matter

Chapter 1. Introduction and background

1.1. Aims of this thesis

Huntington's disease is characterized by atrophy of the striatum early in the disease process with variable cortical atrophy in the latter stages, as evidenced by post mortem studies (Vonsattel, 1985). The advent of advanced neuroimaging techniques has confirmed these earlier findings and has also revealed that grey and white matter volume loss begins many years before symptom onset (Tabrizi et al., 2012). The absence of symptoms in the context of brain atrophy has lead to the suggestion of functional compensation. While functional MRI techniques has shown altered activation of brain regions in Huntington's disease gene carriers relative to controls the link between brain structure and function is unclear (Kloppel et al., 2015). In this thesis I aim to explore the relationship between the healthy white matter brain network and variation in functional brain network activation in premanifest Huntington's disease (preHD) in order to gain insights into potential mechanisms of neuronal compensation that may be exploited in order to delay symptom onset.

Psychiatric symptoms occur years before the onset of motor symptoms in preHD (Julien et al., 2007) and can have a profound impact on quality of life (Ho et al., 2009) however few studies have evaluated how these relate to brain structure and function. Understanding brain network correlates of psychiatric symptoms in HD will highlight which brain regions are involved in this process thus enabling the development of therapies that may modulate this network disturbance. In this thesis I will evaluate the structural and functional brain networks correlates of psychiatric symptoms in preHD.

White matter volume loss is seen many years from onset in preHD however the affect this has on specific white matter connections between brain regions is unclear (Tabrizi et al., 2012). I will therefore characterise global and regional changes in white matter brain networks in HD and identify how these system level changes relate to cognitive and motor disturbance prior to and following the diagnosis of manifest disease.

The earliest white matter changes in HD occur around the striatum, within the corpus callosum and in the posterior white matter tracts (Tabrizi et al., 2011). However it is not understood why these specific regions are

selectively vulnerable in HD. I will investigate how network properties in the healthy brain can enable the development of mechanistic theories, which explain this selective vulnerability. I will then test these hypotheses by identifying regional gene expression profiles of the healthy brain that relate to regional white matter connectivity loss in HD.

1.2. Introduction

Huntington's disease (HD) is a progressive, fatal, neurodegenerative disorder characterised by motor, cognitive and psychiatric disturbance. It is caused by a dominantly inherited CAG trinucleotide repeat expansion in the Huntington Gene on chromosome 4. This results in the production of a mutant huntingtin (*HTT*) protein with an abnormally long polyglutamine repeat (1993). HD has a prevalence of 10.6-13.7 individuals per 100,000 in Western populations (Bates et al., 2015b). Although HD is relatively rare when compared to other neurodegenerative diseases such as Alzheimer's and Parkinson's disease, patients develop symptoms in mid-life with death occurring 15-20 years later (Ross and Tabrizi, 2011). Furthermore the autosomal dominance and full penetrance of HD in mutation carriers with > 39 CAG repeats mean a diagnosis of HD is not only devastating for the patient but also for their entire extended family.

Conversely the full penetrance of HD makes it possible to predict with certainty those that will develop the disease. We can therefore study the preclinical phase with aim of identifying the optimal time for therapeutic intervention prior to irreversible neuronal damage. With the advent of huntingtin lowering therapies preclinical therapeutic intervention has become a real possibility (Wild, 2016). Thus the work in this thesis aims to link systems level and cellular abnormalities in HD thereby identifying the earliest disease related changes that may prompt therapeutic intervention.

1.3. Pathogenesis

Mutant *HTT* results in neuronal dysfunction and death through a number of mechanisms. These include direct effects from toxic N-terminal fragments, its propensity to form abnormal aggregates and its effects on cellular proteostasis, transcription, translation and mitochondrial function (see figure 1.1) (Ross and Tabrizi, 2011). Medium spiny neurons (MSNs) of the striatum are selectively vulnerable to the effects of mutant *HTT*. Striatal pathology follows a biphasic course with initial loss of MSNs of the indirect pathway leading to a hyperkinetic phenotype followed by loss of MSNs of the direct pathway resulting in a hypokinetic phenotype (Plotkin and Surmeier, 2015). The cause for the selective vulnerability of indirect pathway MSNs is unclear, however dopamine D2 receptors may be a factor as they are expressed by indirect but not direct MSNs and have been implicated in HD pathogenesis (Deyts et al., 2009), other hypotheses include the loss of brain derived neurotrophic factor or glutamate excitotoxicity from cortico-striatal projections (Andre et al., 2010; Zuccato et al., 2008).

At the macroscopic level post-mortem studies reveal diffuse atrophy of the caudate and putamen with degeneration occurring along a caudo-rostral, dorso-ventral and medio-lateral gradient. The globus pallidus and nucleus accumbens are also affected but to a lesser extent (Vonsattel and DiFiglia, 1998). A classification system for HD pathology has been developed which consists of 5 grades. Grade 0: clinical evidence for HD but no gross or microscopic abnormalities that could be related to HD. Grade 1: No macroscopic abnormalities in the caudate or putamen but moderate fibrillary astrocytosis at the microscopic level. Grade 2: Macroscopic changes in the caudate and putamen but no macroscopic changes in the Globus Pallidus. Grade 3: lateral segment of the globus pallidus showing fibrillary astrocytosis with the medial segment of the GP unchanged. Grade 4: Shrunken caudate yellow-brown in colour, widened anterior horn of lateral ventricle and smaller nucleus accumbens (Vonsattel, 1985). At grades 3 and 4, changes are also seen in other brain regions including the thalamus, sub-thalamic nucleus, white matter and cerebellum. Cerebral cortex atrophy is variable even in stages 3 and 4 (Vonsattel, 1985).

Advances in magnetic resonance imaging (MRI) have confirmed these early pathological findings in vivo, showing loss of caudate and putamen grey matter volume and loss of both striatal and cortical white matter, in

preHD (see figure 1.2) with more extensive changes seen in manifest HD (Tabrizi et al., 2011). However, it remains unclear how the effects of mutant huntingtin at the cellular level leads to a characteristic distributed pattern of macroscopic structural changes in the brain of HD patients. In this thesis I aim to bridge that gap by linking abnormalities in HD brain networks to regional differences in gene expression.

Figure 1.1. Schematic diagram of Huntington disease cellular pathogenesis. Yellow boxes highlight pathways with potential for biomarker development. In some cases, the molecule might be involved directly in pathogenesis, as with huntingtin itself, and might, therefore, also be a therapeutic target and serve as a pharmacodynamic marker, as well as a marker of disease status. Abbreviations: 3-HK, 3-hydroxykynurenine; Ac, acetyl group; BDNF, brain-derived neurotrophic factor; CSF, cerebrospinal fluid; KMO, kyurenine mono-oxidase; NMDA, *N*-methyl-d-aspartate; P, phosphate group; QUIN, quinolinic acid; ROS, reactive oxygen species; Su, SUMO post-translational modifications; TNF, tumour necrosis factor. Reproduced from Ross et al 2014 (Ross et al., 2014).

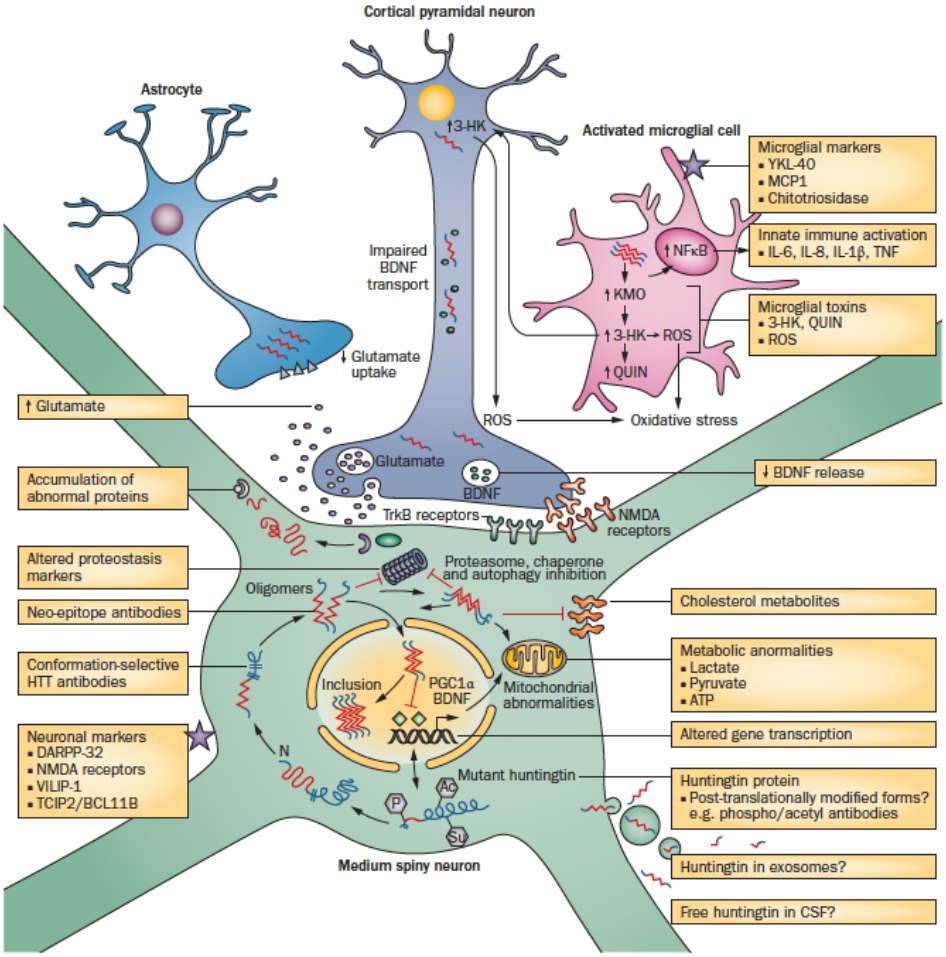

Figure 1.2. Atrophy in premanifest Huntington disease shown using 7T MRI. Bilateral atrophy of the caudate and putamen, and a concomitant increase in size of the fluid-filled lateral ventricle, is observed in the gene carrier compared with the control. This premanifest participant has only subtle signs and symptoms that are insufficient for diagnosing manifest Huntington disease. There are also subtle changes in the cortical grey matter and overall atrophy of subcortical white matter. Reproduced from Bates et al. 2015 (Bates et al., 2015a)

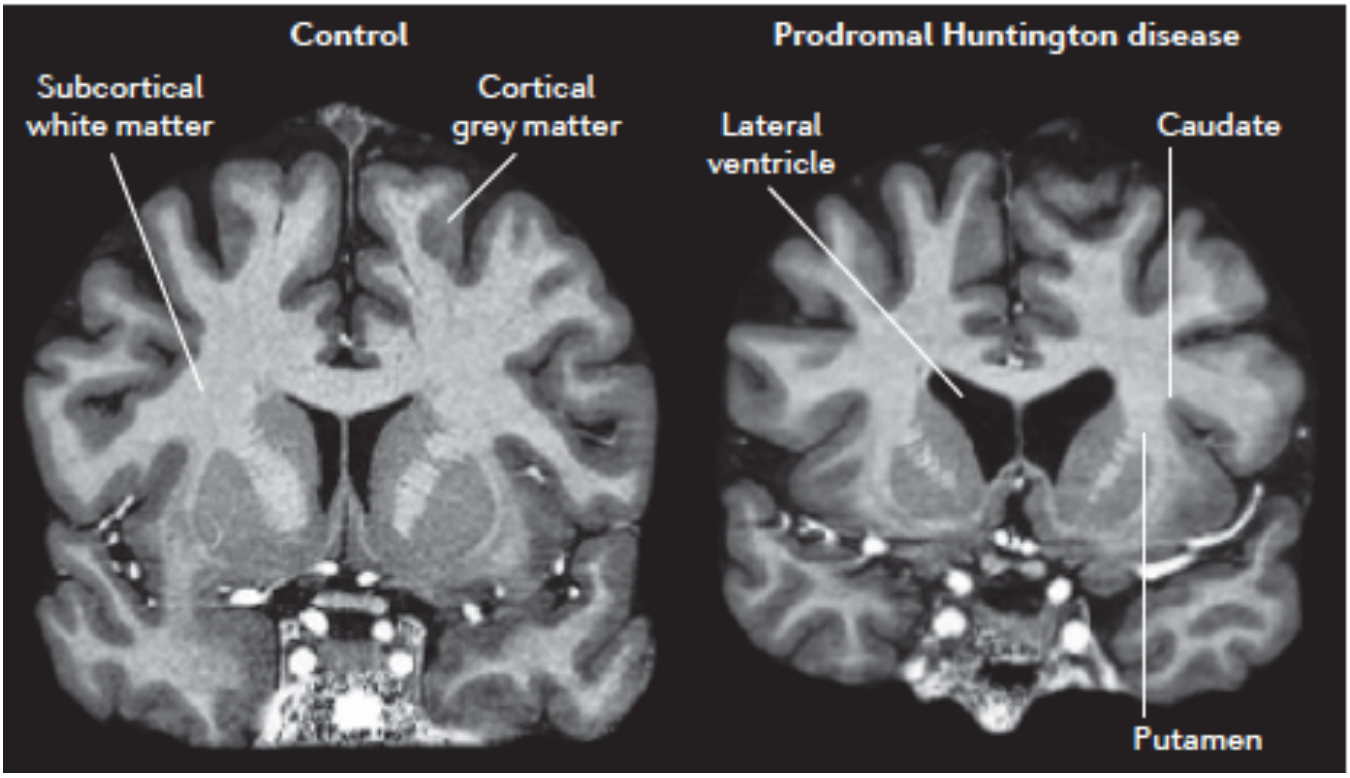

1.4. Clinical symptoms

1.4.1. Diagnosis

Diagnosis of HD is based on a confirmed family history or positive genetic test and the onset of motor disturbance as defined by the Unified HD rating scale (UHDRS) total motor score (TMS) diagnostic confidence score. This score ranges from 0 (no motor abnormalities suggestive of HD to 4 (≥99% motor abnormalities due to HD) with a score of 4 defining motor onset or 'manifest' HD. However subtle motor, cognitive and psychiatric deficits can be identified up to 10-15 years before the onset of manifest disease and this is referred to as the preHD (Ross et al., 2014), see figure 1.3. Experiments in this thesis have focused primarily on preHD as this represents the optimal time for therapeutic intervention.

Figure 1.3. Natural history of clinical HD. Reproduced from Ross et al 2014 (Ross et al., 2014).

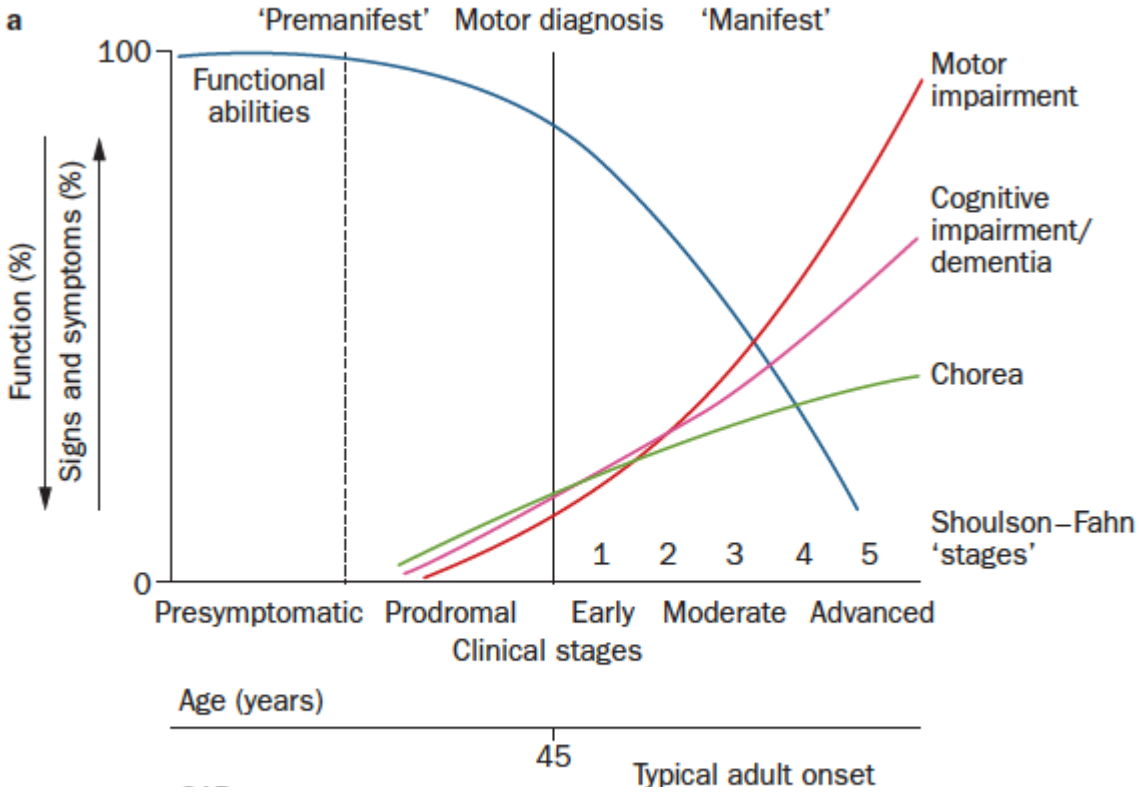

1.4.2. Motor disturbance

In keeping with the biphasic course of striatal pathology with initial loss of MSNs of the indirect pathway followed by loss of MSNs of the direct pathway (Plotkin and Surmeier, 2015), movement disturbance in HD can be split into a hyperkinetic phase with prominent chorea in the early stages of the disease, which then tends to plateau (Dorsey et al., 2013). The hypokinetic phase is characterised by bradykinesia, dystonia, balance and gait disturbance. The hypokinetic movement disorder shows association with disease duration and CAG length while chorea does not (Rosenblatt et al., 2006).

Assessment of motor disturbance is based on the UHDRS TMS, which assesses eye movements, speech, alternating hand movements, dystonia, chorea and gait. A number of longitudinal studies have demonstrated that the UHDRS TMS is sensitive to change over time (Dorsey et al., 2013; Tabrizi et al., 2012; Tabrizi et al., 2011) and predictive of disease onset (Paulsen et al., 2014), however it is also subject to inter-rater variability (Hogarth et al., 2005). More quantitative assessments such as the (quantitative) Q-motor battery, which includes tongue force variability, grip force, speeded and self paced tapping (Sampaio et al., 2014), have shown sensitivity to longitudinal change (Rowe et al., 2010; Tabrizi et al., 2011), particularly speeded tapping which shows longitudinal change even in those far from disease onset (Tabrizi et al., 2013). Given this sensitivity of the UHDRS TMS and speeded tapping in detecting change over time I have used these variables in my thesis in order to explore how changes in white matter brain networks at the global and regional level relate to the development of motor symptoms.

1.4.3. Cognitive disturbance

Cognitive disturbance can be seen many years before symptom onset and follows a sub-cortical pattern characterized by impaired emotion recognition, processing speed, visuospatial and executive function, smell identification and visual working memory (Henley et al., 2012; Paulsen et al., 2013; Say et al., 2011; Stout et al., 2012; Stout et al., 2011; Tabrizi et al., 2009; Tabrizi et al., 2013). Unlike cortical dementias such as Alzheimer's disease, semantic memory, language comprehension, spatial awareness and orientation remain relatively preserved (Papoutsi et al., 2014).

In early manifest disease, longitudinal changes can be demonstrated over 12 and 24 months by performance on the symbol digit modalities test (SDMT), which assesses psychomotor speed, Stroop word reading (SWR) which assesses executive function and indirect circle tracing, which is used to assess visuospatial performance and the emotion recognition test (Stout et al., 2012; Tabrizi et al., 2011). This extends to preHD at 36-months, with SWR demonstrating the highest sensitivity for those furthest from disease onset (Tabrizi et al., 2013). In this thesis I have investigated how performance in these cognitive measures relate to global and regional white matter brain network chractertistics.

1.4.4. Neuropsychiatric disturbance

A wide variety of neuropsychiatric symptoms occur in HD, including apathy, anxiety, irritability, depression, obsessive compulsive behaviours and psychosis. While high rates are seen in manifest HD(Craufurd et al., 2001; Paulsen et al., 2001), psychiatric disturbance is also common many years before symptom onset in the preHD (Julien et al., 2007; Tabrizi et al., 2009). The most recent study from the Registry cohort, which includes both preHD and manifest HD, shows that apathy is the most common neuropsychiatric symptom occurring in 28%, while depression, irritability and obsessive compulsive behavior occur in around 13%. Psychosis is relatively rare occurring in 1% (van Duijn et al., 2014).

While apathy, irritability and depression are all related to functional decline, apathy is the only neuropsychiatric symptom that has been shown consistently to progress with disease (Tabrizi et al., 2013). The link between depression, irritability and anxiety and disease progression is less clear however longitudinal change has been demonstrated over 10-years (Epping et al., 2015). This may be due to the lack of effective treatments for apathy in comparison to the use of anti-depressants and anti-psychotics for depression, anxiety and irritability. In this thesis I investigate how changes in structural and functional brain networks relate to depression, anxiety, irritability and apathy symptoms in preHD.

1.5. Neuroimaging in HD

1.5.1. Structural MRI

Structural MRI has been the most extensively studied imaging modality in HD to date. Track-HD evaluated changes in both grey and white matter volume at 3 time points one year apart and included 123 controls, 120 preHD and 123 HD at baseline (see figure 1.4). Track-On HD was an extension of this study, which also included diffusion and resting state fMRI data. Track-HD revealed grey matter volume loss in the striatum and loss of white matter volume around the striatum, within the corpus callosum and in the posterior white matter tracts in preHD extending to wide spread loss of white mater volume, and to a lesser extent grey matter, in manifest HD (Tabrizi et al., 2012; Tabrizi et al., 2011; Tabrizi et al., 2013). The limited decline in cognitive and motor function in the preHD coupled with this grey and white matter volume has lead to the suggestion that compensatory mechanisms such as neuroplasticity and network reconfiguration enable those with preHD to maintain normal function (Tabrizi et al., 2012).

Figure 1.4. Longitudinal data from TRACK-HD. Examples of the most robust changes in preHD and early HD identified by TRACK-HD over 36 months of longitudinal study.[16] a,b | Rates of atrophy. Changes in caudate and white matter volume, seen as statistical parametric maps and presented as atrophy rates by group. c | Tapping test to quantify motor function. d | Symbol Digit Modalities Test of visual attention and psychomotor speed. e,f | UHDRS scores. Asterisks refer to levels of significance (**P <0.01; ***P <0.001), and dashed lines indicate specific comparisons. Abbreviations: HD, Huntington disease; HD1, early HD; HD2, later-stage HD; PreHD-A, preHD far from onset; PreHD-B, preHD close to onset; TFC, Total Functional Capacity; TMS, Total Motor Score; UHDRS, Unified HD Rating Scale**.** Reproduced from Ross et al 2014 (Ross et al., 2014)

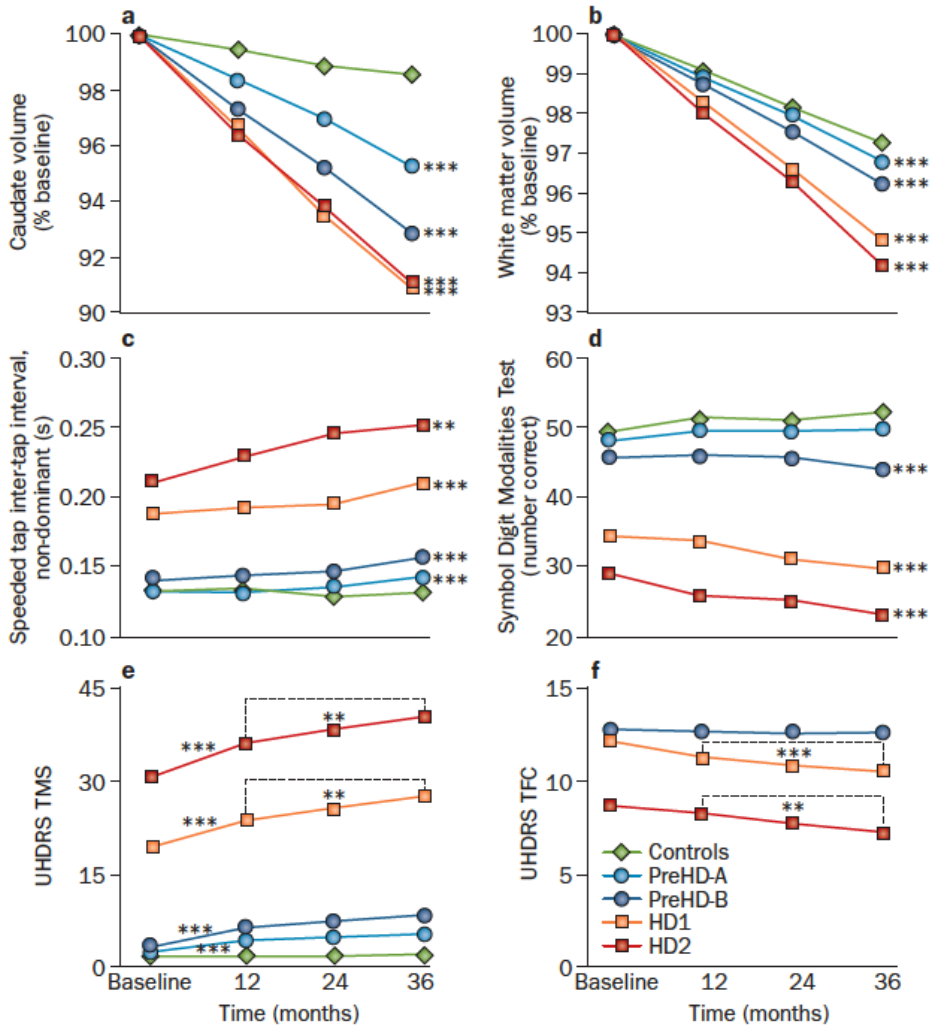

1.5.2 Diffusion weighted MRI

Diffusion weighted MRI (DWI) can be used to measure the diffusion of molecules in-vivo and is therefore capable of providing information about the microstructure of both grey and white matter in the brain (Dumas et al., 2012). The diffusion tensor, models the direction of displacement of molecules. This can then be analysed to generate diffusion metrics in order to provide information about tissue microstructure. These include mean diffusivity (MD), which characterizes the overall displacement of molecules, fractional anisotropy (FA) which indicates whether diffusion is restricted or unrestricted (ranging from 0 to 1). Axial and radial diffusivity (AD and RD) denote the principle direction of diffusion and direction perpendicular to the principle direction respectively (Le Bihan and Johansen-Berg, 2012).

Diffusion tensor imaging studies may focus on the diffusion properties of one or several brain regions, known as region of interest studies (ROI). Alternatively, voxel based approaches such as tract based spatial statistics (TBSS) may be used, where the focus is on the diffusion properties of major white matter tracts (Sritharan et al., 2010). While diffusion metrics are influenced by axonal density and myelination caution must be used when interpreting differences in these metrics in health and disease, as no one metric directly relates to specific biological properties or structures (Jones et al., 2013).

One major limitation of the diffusion tensor model occurs in regions of crossing fibres. The tensor model can only account for a single principle direction of diffusion. This has significant implications given that crossing fibres may occur in as much as 90% of the white matter in the human brain (Jeurissen et al., 2013). This problem has been addressed with the advent of diffusion tractography algorithms, such as constrained spherical deconvolution, that have the ability to resolve crossing fibres (Bohanna et al., 2008). Diffusion tractography can be used to delineate white matter tracts and investigate diffusion metrics within these tracts. More recently whole brain diffusion tractography has been used in the field of connectomics to generate white matter brain networks or structural connectomes (Jbabdi and Behrens, 2013). Connectomics will be discussed in more detail in subsequent sections.

A large number of diffusion MRI studies have been performed in HD, investigating microstructural alterations in both grey and white matter. The PADDINGTON study (Hobbs NZ, 2013) analysed cross-sectional differences in diffusion metrics in manifest HD compared to controls. This involved an ROI approach focusing on the grey matter of the caudate and putamen along with the white matter of the corpus callosum (CC) and whole brain. Effect sizes based on these regions for both diffusion and structural MRI analyses were compared. In keeping with a number of smaller studies increased FA and mean diffusivity was seen in the grey matter of both the caudate and putamen (Georgiou-Karistianis et al., 2013; Sanchez-Castaneda et al., 2012), while reduced FA and increased MD was seen in the CC (Di Paola et al., 2012; Rosas et al., 2010; Rosas et al., 2006). When compared to volumetric measurements effect sizes for diffusion metrics were smaller, possible due to lower signal to noise ratio in diffusion MRI acquisition (see figure 1.5).

Figure 1.5. Comparison of effect sizes for structural MRI and diffusion MRI metrics in different regions of interest. Reproduced from Hobbs et al 2013 (Hobbs NZ, 2013).

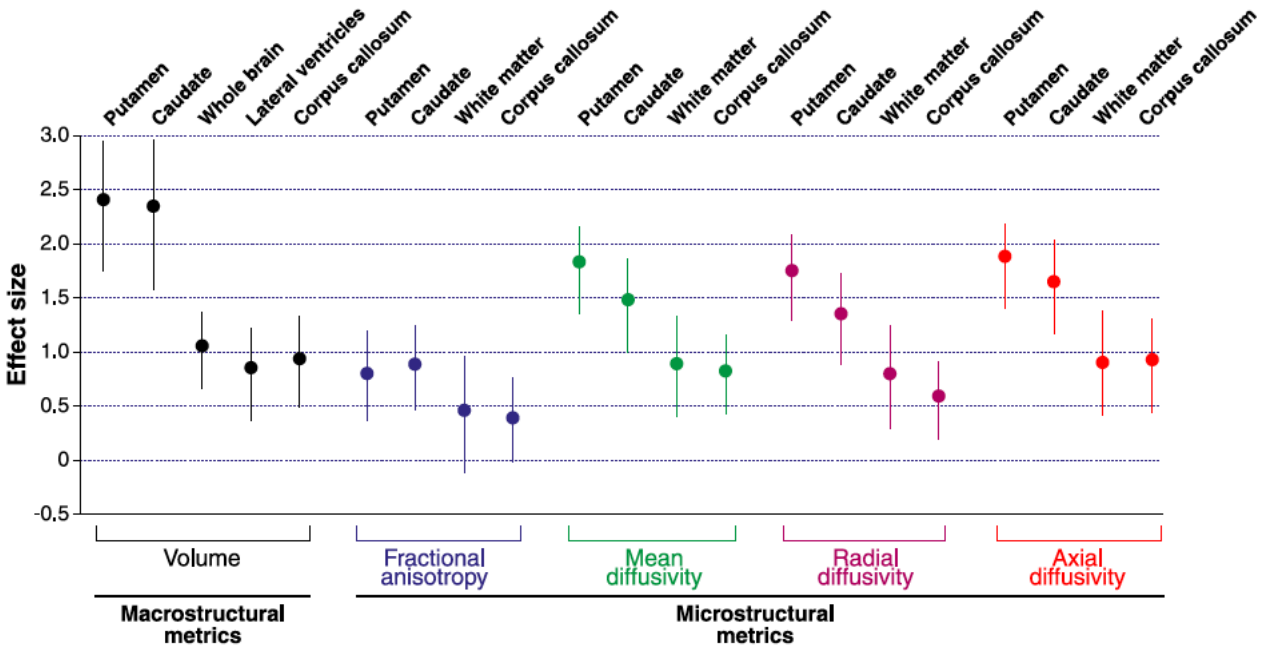

Similar differences have also been observed in preHD compared to controls (Di Paola et al., 2012; Georgiou-Karistianis et al., 2013; Rosas et al., 2010; Rosas et al., 2006; Sanchez-Castaneda et al., 2012). A recent meta-

analysis of diffusion MRI studies in HD confirmed these results (Liu et al., 2016). These changes in microstructure have pathological relevance as correlations are seen between cognitive and motor measures in HD and diffusion metrics of both cortical and subcortical areas, including the CC (Dumas et al., 2012; Rosas et al., 2010; Rosas et al., 2006), prefrontal cortex (Matsui et al., 2013) and striatum (Bohanna et al., 2011a; Sritharan et al., 2010). Other diffusion metrics such as apparent diffusion coefficient (ADC), a measure of diffusion magnitude (Dumas et al., 2012), radial diffusivity (RA) and axial diffusivity (AD) (Matsui et al., 2013; Rosas et al., 2010) are also abnormal in HD gene carriers but have been studied less extensively.

Analysis of diffusion metrics in major white matter tracts using TBSS has shown reductions in FA in the CC (Di Paola et al., 2012), internal capsule, longitudinal fasciculus, cingulate, thalamic radiations and cerebral peduncles (Stoffers et al., 2010) in preHD, while similar and in some cases more extensive FA changes may be seen in manifest subjects (Della Nave et al., 2010; Weaver et al., 2009). However, conflicting results have been reported (Bohanna et al., 2011b; Della Nave et al., 2010). MD increases are seen in similar areas (Bohanna et al., 2011b; Della Nave et al., 2010; Stoffers et al., 2010). Longitudinal change has also been demonstrated over 1 year in the FA of cortico-striatal and fronto-thalamic tracts in manifest HD relative to controls (Weaver et al., 2009). Changes in diffusion metrics, particularly in the corpus callosum, correlates with cognitive and motor variables (Bohanna et al., 2011b; Della Nave et al., 2010). One study investigating the relationship between neuropsychiatric measures and microstructural white matter revealed correlation between depression scores and FA in the splenium of the corpus callosum (Gregory et al., 2015b).

A number of studies have investigated diffusion metrics in white matter tracts delineated using diffusion tractography. The largest longitudinal study using this approach has shown changes in diffusion metrics over time in the superior fronto-occipital fasciculus white matter tract, with diffusion abnormalities in multiple tracts seen at baseline, in preHD relative to controls (Harrington et al., 2016). A longitudinal analysis focusing specifically on cortico-striatal tracts connecting caudate and putamen to motor, premotor and somato-sensory regions of the cortex has also been performed. This revealed change over time in diffusion metrics of the white tracts connecting the putamen and premotor regions in preHD compared to controls. Widespread changes across all tracts were seen at baseline (Shaffer et al., 2017).

Only a few studies have used diffusion tractography to assess the differences in strength of white matter connections, also known as structural connectivity, between brain regions in HD relative to controls. The first study to do this focused on white matter connections between the frontal cortex and striatum. Tractography was used to delineate white matter connections between the caudate and putamen (divided into anterior and posterior sub-regions) and Brodmann areas (Brodmann, 1909) of the frontal cortex. This revealed reduced structural connectivity between the posterior caudate and frontal cortex in preHD relative to controls. Group differences remained significant when splitting the preHD group into near and far from disease onset. Structural connectivity between the caudate and frontal cortex correlated with delays in generating saccadic eye movements (Kloppel et al., 2008). While the participant numbers in this study were relatively small (25 preHD and 20 controls) the selectively vulnerable of fronto-striatal connectivity to the posterior caudate is in keeping with the dorso-ventral gradient of pathology seen in post-mortem studies (Vonsattel, 1985).

The first study to investigate structural connectivity between the striatum and the whole cortex in HD revealed prominent loss of connectivity between the striatum (caudate and putamen) and frontal lobe in manifest HD relative to controls. Loss of connectivity was also seen between the striatum and parietal lobes and putamen and temporal lobes. No connectivity loss was seen between the cingulate cortex and the striatum. Connectivity between the striatum and occipital lobes could not be assessed, as connectivity to the occipital lobe was not seen even in the control population. The relationship between changes in connectivity and clinical measures was not investigated (Marrakchi-Kacem et al., 2013). While differences in fronto-striatal connectivity in this study were consistent with (Kloppel et al., 2008), lack of group differences in connectivity to the cingulate was not consistent with the grey matter volume loss of the cingulate that has been demonstrated in HD (Hobbs et al., 2011). Furthermore absence of connectivity between the striatum and occipital lobe even in controls is not consistent with diffusion tractography findings in the healthy population (Tziortzi et al., 2014). There may be a number of reasons for these discrepancies. The cohort in this study was small including only 15 manifest HD and 15 controls. Connections to cortical regions was based on streamlines reaching the cortical surface as opposed to those intersecting the grey matter white matter boundary, which is the criteria used widely in the literature (Smith et al., 2012).

Multivariate approaches have also been used to investigate connectivity between the striatum and cortex in HD. Using voxel connectivity profiles (Draganski et al., 2008), where a voxel in the striatum is allowed to connect with multiple regions in the cortex, canonical variate analysis revealed significant differences in cortico-striatal connectivity between HD and controls. No significant differences were seen between preHD and controls. Associations were seen between connectivity and motor and cognitive variables. Participant numbers in this study were small, including only 14 manifest HD, 17 preHD and 18 controls. Furthermore the use of multivariate analysis has limited interpretation in identifying specific regions in the cortex that are particularly vulnerable to structural connectivity loss in HD (Novak et al., 2015).

The studies outlined are informative about structural connectivity changes between HD gene carriers and controls, however low participant numbers, few clinical correlates and a lack of studies using whole brain approaches limit the insights into the relationship between white matter pathology and clinical phenotype. While associations have been reported between structural connectivity and cognitive and motor measures, the relationship between structural connectivity and psychiatric symptoms in HD is less clear.

In this thesis I will utilise data diffusion MRI data from the Track-HD and Track-On HD studies thus overcoming the limitations of low participant numbers affecting previous studies. I will perform whole brain diffusion tractography in order to construct white matter networks and investigate global and regional change in these networks over time relative to healthy controls. The extensive deep phenotyping of the Track-HD and Track-On HD cohorts will also allow me to investigate how HD related changes in brain networks relate to motor, cognitive and psychiatric deficits.

1.5.3. Functional MRI

Blood oxygen level dependent (BOLD) response in the brain, can be used as an indirect measure of neuronal activation, during a task or at rest, in functional MRI (fMRI). Statistical parametric maps can then be created to assess significant differences of brain activation between groups or correlations of brain activation with clinical measures (Vandenberghe et al., 2009). In this thesis I will use resting state fMRI data in order to construct functional brain networks enabling me to link structure and function at the systems level.

A number of cognitive tasks have been used to assess neuronal activation in manifest HD. These show reduced neuronal activation in striatal regions (Clark et al., 2002; Voermans et al., 2004) and throughout the cortex (Clark et al., 2002; Kim et al., 2004; Reading et al., 2004) and increased areas of activation predominantly in motor and prefrontal regions (Dierks et al., 1999; Georgiou-Karistianis et al., 2007; Voermans et al., 2004). Similarly in preHD, while areas of reduced activation can be seen during normal task performance in the anterior cingulate and striatum (Enzi et al., 2012; Paulsen et al., 2004; Reading et al., 2004; Saft et al., 2008; Zimbelman et al., 2007), increased areas of activation can also be seen in motor and prefrontal regions (Paulsen et al., 2004; Saft et al., 2008; Zimbelman et al., 2007). In near to onset preHD (Wolf et al., 2007) deactivation of the dorsolateral prefrontal cortex (DLPFC) and increased activation of the inferior parietal lobule (IPL) and superior frontal gyrus (SFG) occurs with increasing working memory load (Wolf et al., 2007). Increased activation is also seen during simple and complex finger tapping tasks in the caudal supplementary motor area (SMA) and superior parietal lobule (SPL) in preHD relative to controls, with greater pre-SMA and reduced SPL activation seen during a more complex task (Kloppel et al., 2009).

These findings suggest the presence of flexible compensatory mechanisms in preHD. Indeed this has been investigated using a compensation model, where increased performance related activation is seen in the right parietal cortex in preHD participants, as atrophy increased, in keeping with a compensatory process (Kloppel et al., 2015). By investigating the relationship between structural and functional brain networks in preHD I aim to gain insights into potential compensatory processes at the network level.

The relationship between neuronal activation during task fMRI and neuropsychiatric symptoms has also been investigated. Correlation is seen between depression and activation of the dorsolateral prefrontal cortex during a shifting response set task (Gray et al., 2013). In a separate study correlation was seen between depression and activation of the dorsomedial prefrontal cortex during a Stroop interference task (Unschuld et al., 2012). While these findings suggest a role for the prefrontal cortex in HD depression they are limited to predefined regions of interest. Therefore there is a gap in our knowledge regarding the role of other brain regions in HD depression. In this thesis I was investigate brain network correlates of depression enabling me to assess all brain regions.

1.5.4. Resting state fMRI

Measurement of BOLD fluctuations at rest when a subject is asked to either fixate on a target or lie with their eyes closed is referred to as resting state fMRI (rs-fMRI). In healthy subjects correlations are present between temporal fluctuations of different brain regions. These brain regions make up resting state networks (Buckner et al., 2013). Perhaps the most well known of these is the default mode network (DFM). These brain regions are thought to be activated at rest during periods of introspection (Buckner et al., 2008).

Abnormalities in the DFM network have been demonstrated in both manifest (Quarantelli et al., 2013; Werner et al., 2014) and preHD (Wolf et al., 2012) and are associated with cognitive performance. In preHD reduced functional connectivity is also seen in sensorimotor, dorsal attention and visual networks (Dumas et al., 2013; Poudel et al., 2014a). Evidence of compensation has also been shown using rs-fMRI in preHD, where increased coupling of the right dorsolateral prefrontal cortex and a left hemisphere network was predictive of cognitive performance as atrophy increased (Kloppel et al., 2015). To date longitudinal rs-fMRI studies have not demonstrated differences in functional connectivity between HD gene carriers and healthy controls (Odish et al., 2014; Seibert et al., 2012).

1.6. Connectomics and graph theory

While abnormalities are seen in both functional activation and structural white matter in HD the relationship between HD related changes in structure and function is unclear. Connectomics, through the construction of functional and structural white matter networks, provides a framework in which to investigate this structure-function relationship. I will use this framework to investigate how changes in functional brain networks in preHD relate to the organisation of structural white matter networks. I will then investigate how these network changes relate to psychiatric symptoms and cognitive and motor performance.

Functional and structural brain networks can be constructed using resting state fMRI and diffusion tractography respectively. The brain can be divided into a number of distinct regions using a brain atlas (Bullmore and Sporns, 2009). These atlases are constructed based on prior anatomical or structural information (Desikan et al., 2006) or derived from fMRI studies of healthy controls (Yeo et al., 2011), representing a functional atlas. More recently atlases incorporating both structural and functional information, termed multimodal, have also become available (Fan et al., 2016; Glasser et al., 2016). Each brain region in an atlas represents a node and each node may be connected to another node in the brain network. In a structural brain network these connections represent anatomical white matter connections, whereas in a functional brain network these connections represent temporal correlations from fMRI time series (see figure 1.6) (Fornito and Bullmore, 2015).

Figure 1.6. Constructing structural and functional brain networks. Reproduced from Bullmore et al. 2009 (Bullmore and Sporns, 2009).

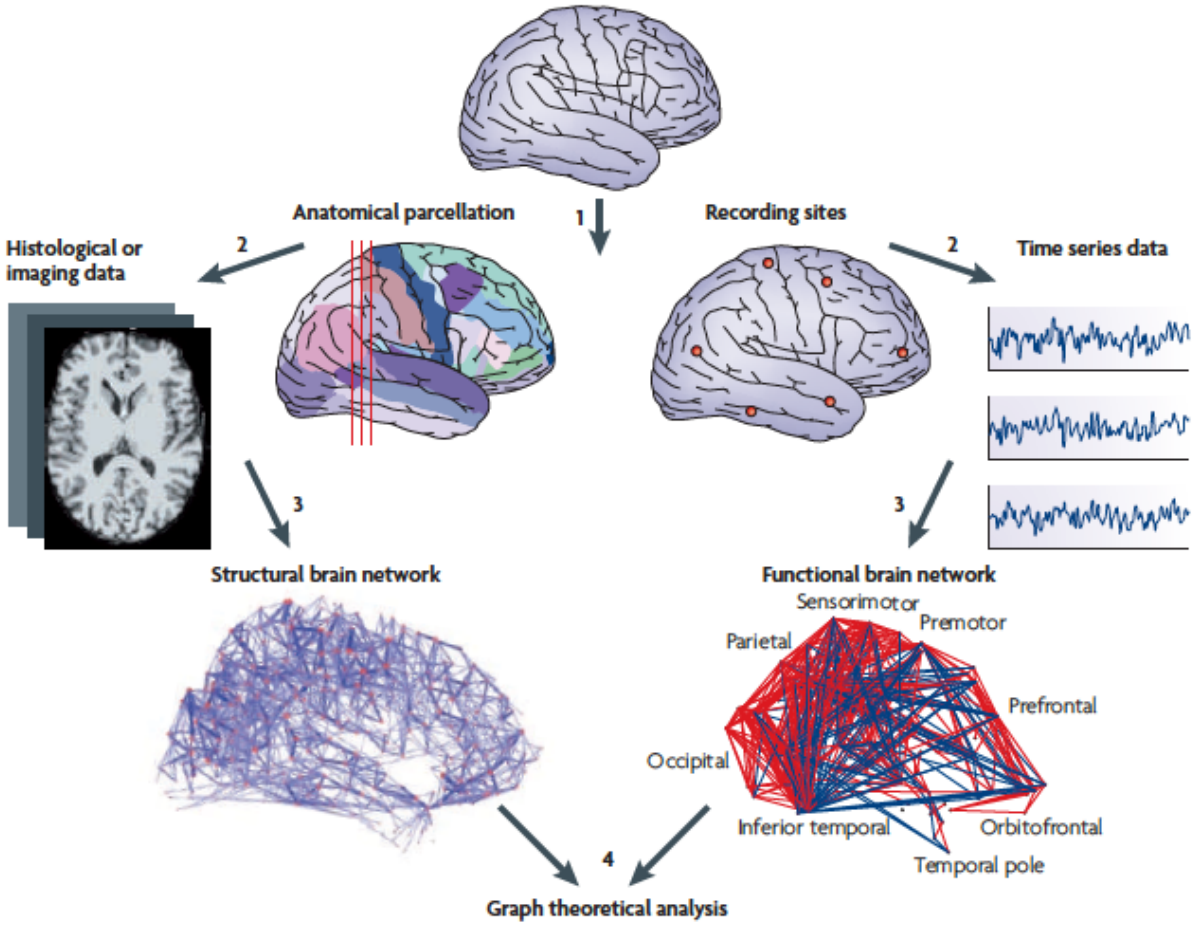

The topological characteristics of these brain networks can be described using a mathematical approach known as graph theory (Rubinov and Sporns, 2010). Graph theory can be used to explain the properties of any network type, including transport networks, social networks (Barrat et al., 2004) and biological networks (Miller et al., 2010). Networks can described as either regular, with high levels of local clustering, or random, with low levels of local clustering but more connections between distant nodes in the network. Regular and random networks represent two ends of the spectrum with respect to organisation. Through the study of different network systems Watts and colleagues recognised that many networks types lie somewhere in the middle of this spectrum, such that a network has a high level of local clustering but has also contains connections between distant nodes enabling global communication throughout the entire network (Watts and Strogatz, 1998) (see

figure 1.7). This is termed small world organisation and has been demonstrated in the brain network organization across a diverse range of species, beginning with the C. Elegans worm at the microstructural level through to the mouse, cat, macaque monkey and human brain at the macrostructural level (van den Heuvel et al., 2016).

Figure 1.7. The Watts–Strogatz model and the generation of small-world networks. The model begins with a regular lattice network in which each node is placed along the circumference of a circle, and is connected to its k nearest neighbors on that circle. Then, with probability p, edges are rewired uniformly at random such that (1) at p = 0, the network is a lattice and (2) at p =1, the network is random. Interestingly, at intermediate values of p, the network has so-called "small-world" characteristics with significant local clustering (from the lattice model) and short average path length facilitated by the topological short-cuts created during the random rewiring procedure. Reproduced from Bassett et al. 2016 (Bassett and Bullmore, 2016)

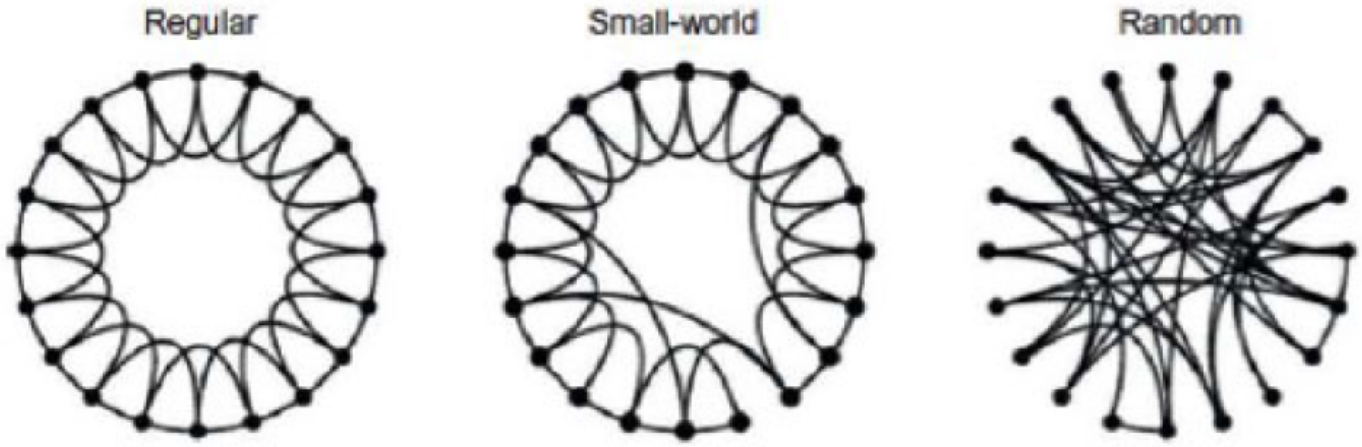

From a mathematical perspective small worldness may be defined as the optimal balance between local clustering (clustering coefficient) and shortest path length. Clustering coefficient represents the fraction of a node's neighbours that are connected to each other. At the global level the mean clustering coefficient of a network represents the extent of clustered connectivity around individual nodes and is a measure of network segregation. The shortest pathlength is the minimum number of connections that must be traversed to go from one node to another. Thus networks with connections between distant nodes will have a shorter average pathlength. The inverse of shortest average path length is termed global efficiency, such that networks with shorter average path lengths will have greater efficiency of global communication throughout the network. Both

average shortest path length and global efficiency are measures of network integration. When making statistical inferences regarding network characteristics measures such as mean clustering coefficient and average shortest path length are commonly normalised relative to a random network and thus reported as normalised mean clustering coefficient and normalised average path length (Bullmore and Sporns, 2009; Rubinov and Sporns, 2010).

Local clustering of nodes in brain networks results in the existence of specialized functional modules. Communication between these specialized functional modules is facilitated by the backbone of the brain network, which is composed of nodes that are both highly connected to each other and to the rest of the network (van den Heuvel et al., 2012). These are nodes are termed rich club regions and they permit an integrated system of communication throughout the brain network (van den Heuvel and Sporns, 2011, 2013).

Computationally the brain may be sub-divided into modules using graph theory modularity algorithms (Sporns and Betzel, 2015), as with clustering coefficient, network modularity provides a measure of brain network segregation. Modularity algorithms also provide information as to the size and composition of these specialized functional modules. They sub-divide the network such that a module is defined as regions that are highly connected to each other with minimally connections outside the module (Rubinov and Sporns, 2010). While a number of algorithms are available the Louvain algorithm performs well for large networks and is typically used in connectomic studies (Blondel et al., 2008).

Graph theory metrics can also be used to define the importance of brain regions in the network, which is known as nodal centrality. Degree is the most basic measure of centrality and represents the number of binary connections a brain region has. Strength is a weighted version of degree and represents the sum of connection weights for a given brain region. More complex measures of centrality take into account the relationship of the node to shortest paths in the network. One example is betweenness centrality which is defined as the fraction of all shortest paths in the network that pass through a given node (Rubinov and Sporns, 2010). Eigen vector centrality takes into account both the connectivity of a node and the connectivity of its neighbours, such that

nodes are assigned increasing importance if both they and their neighbours are highly connected to hub regions (Fagerholm et al., 2015). See figure 1.8 for illustration of different graph theory metrics.

Figure 1.8. Measures of network topology. An illustration of key complex network measures (in italics). These measures are typically based on basic properties of network connectivity (in bold type). Thus, measures of integration are based on shortest path lengths (green), while measures of segregation are often based on triangle counts (blue) but also include more sophisticated decomposition into modules (ovals). Measures of centrality may be based on node degree (red) or on the length and number of shortest paths between nodes. Hub nodes (black) often lie on a high number of shortest paths and consequently often have high betweenness centrality. Patterns of local connectivity are **quantified by network motifs (yellow).** Reproduced from Rubinov et al. 2010 (Rubinov and Sporns, 2010).

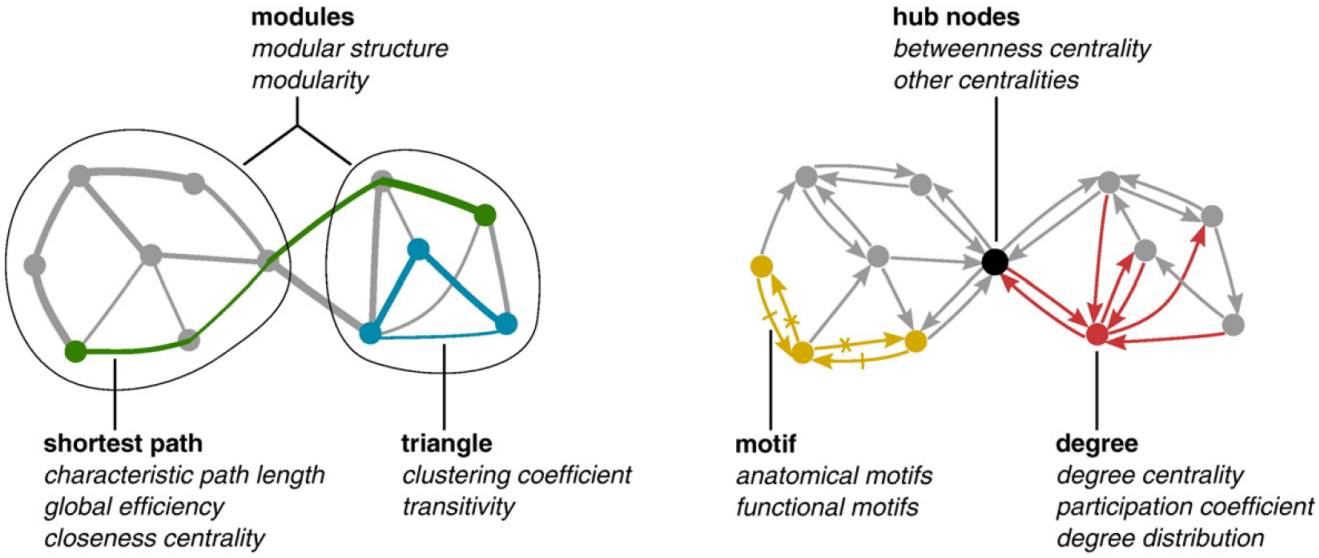

1.6.1. Mathematical derivations of graph theory metrics

In this section I present an overview of the derivation of graph theory metrics used in this thesis. Please refer to (Rubinov and Sporns, 2010) for further details. The degree of a node i is calculated as follows (Eq. 1):

$$k_i = \sum_{j \varepsilon N} a_{ij}$$

where N is the set of all nodes in the network and a_{ij} is the connection between nodes i and j. Nodal strength is calculated using the weighted connection (Eq. 2):

$$s_i = \sum_{j \varepsilon N} w_{ij}$$

The (weighted) clustering coefficient for a node or brain regions calculated by the following equation (Eq. 3):

$$C_i = \frac{1}{n} \sum_{i \varepsilon N} \frac{2t_i}{w_i(w_i - 1)}$$

where t_i is the number of triangles around a node (Eq. 4):

$$t_i = \frac{1}{2} \sum_{j,h \varepsilon N} w_{ij}\, w_{ih} w_{jh}$$

The (weighted) clustering coefficient of a network is calculated as follows (Eq. 5):

$$C = \frac{1}{n} \sum_{i \varepsilon N} C_i$$

The characteristic path length of a node is defined as follows, where d_{ij} is the (weighted) shortest path length between two nodes (Eq. 6):

$$L_i = \frac{1}{n} \sum_{i \varepsilon N} \frac{\sum_{j \varepsilon N, j \neq i} d_{ij}}{n - 1}$$

The characteristic path length for the network is calculated by taking the average across all nodes (Eq. 7):

$$L = \frac{1}{n} \sum_{i \varepsilon N} L_i$$

The small-worldness is the ratio of network clustering coefficient relative to network characteristic path length. These values are normalised using path length (L_{rand}) and clustering coefficients (C_{rand}) of random networks (Eq. 8):

$$S_m = \frac{C/C_{rand}}{L/L_{rand}}$$

Modularity of a network is calculated as follows, where e_{uv} is the portion of connections that link nodes in module u with nodes in module v (Eq. 9):

$$Q = \sum_{u \varepsilon M} \left| e_{uu} - \left(\sum_{u \varepsilon M} e_{uv} \right)^2 \right|$$

Betweenness centrality is the number of shortest paths between pairs of node in the network that pass through a given node i divided by the total number of shortest paths in the network, this is given by (Eq. 10):

$$b_i = \frac{1}{(n-1)(n-2)} \sum_{\substack{h,j \varepsilon N \\ h \neq j, h \neq i, j \neq i}} \frac{\rho_{hj}(i)}{\rho_{hj}}$$

Eigenvector centrality is a centrality measure that takes into account the centrality of nodes connected to the node of interest, such that the centrality of node i, denoted by x_i is proportional to the average centralities of it's neighbours:

$$x_i = \frac{1}{\lambda} \sum_{j=1} A_{ij} x_j$$

This can re-written as:

$$\lambda x = A \cdot x$$

Such that x is an eigenvector of connectivity matrix with eigenvalue λ, therefore eigenvalue centrality is the eigenvector associated with the largest eigenvalue of a given node in a connectivity matrix.

1.6.2. Network based statistics

While graph theory allows characterisation of brain network topology emerging techniques such as network-based statistics (NBS) allow investigation of brain networks at the level of connections between nodes (Zalesky et al., 2010). Using an NBS framework, a test statistic is calculated for each connection independently. A primary threshold ($p < 0.05$, uncorrected) is then applied to form a set of supratheshold connections. Permutation testing is then used to ascribe a p-value controlled for family wise error (FWE) to each set of suprathreshold connections. For each permutation the test statistic is recalculated, after which the same threshold is applied to define a set of suprathreshold connections. The maximal component size for each permutation is determined giving a null distribution of maximal component size. Finally the FWE corrected p-value of the observed component size k is estimated by finding the proportion of permutations for which the maximal component is greater than k. The FWE adjusted p- value is set at 0.05. Both graph theory and NBS approaches are being increasingly used to understand brain network dysfunction both in neurological and psychiatric disease (Fornito et al., 2015).

1.6.3 Connectomics in HD

To date relatively few studies have investigated the connectome in HD. A structural connectome analysis revealed reduced connectivity in the a fronto-parietal-striatal network in preHD, with more extensive changes occurring in manifest HD relative to controls. These changes correlated with motor and cognitive deficits (Poudel et al., 2014b). A functional connectome analysis has shown weakened fronto-striatal connections and strengthened anterior-posterior connections in preHD compared to controls. Anterior-posterior connections showed greatest connectivity in subjects closest to onset suggesting that this may represent a compensatory mechanism in the context of increasing disease load. In contrast to structural connectomics these changes did not correlate with clinical measures (Harrington et al., 2015).

The findings of a recent longitudinal structural connectome study in HD were not consistent with the previous cross-sectional study. No group differences were seen at baseline and longitudinal changes were only seen in the left orbitofrontal cortex and left paracentral lobule with no regional changes seen in the striatum. This is likely

due to the small sample size and the division of preHD into new and far from onset sub-groups (Odish et al., 2015). Similarly a longitudinal functional connecotme study failed to show change in functional connectivity over time (Gargouri et al., 2016). However both cross-sectional and longitudinal functional connectome studies did show loss of network hubs and more random network topology in HD compared to controls (Gargouri et al., 2016; Harrington et al., 2015). In this thesis I will perform the largest structural connectome analysis to date in preHD and manifest HD. I will also investigate how the structural connectome relates to changes in the preHD functional connectome relative to controls.

1.7. Relationship between brain structure and function

1.7.1. The healthy brain

Numerous studies have attempted to understand the relationship between structural and functional connectivity in both health and disease. Correlations between structural and functional connectivity in the literature, measured as a correlation coefficient, vary widely between 0.25-0.62 (Hagmann et al., 2008; van den Heuvel et al., 2013; Zhang et al., 2011). Various approaches have been used to model functional connectivity based on structural connectivity. These include graph theoretical approaches (Goni et al., 2014) and network diffusion models (Abdelnour et al., 2014). The wide variation in the structure-function relationship can be partly explained by the presence of strong functional connections between regions that do not have a direct anatomically connection, the tendency for brain regions in close proximity to have greater functional connectivity and variability of resting state fMRI across scanning sessions (Honey et al., 2009). The majority of the variance in functional connectivity can be explained by non-stationary nature of temporal correlations (Messe et al., 2014). There is a consistent message in the literature however, that functional connectivity is constrained by the underlying structural connectivity, which acts as a backbone or substrate (Goni et al., 2014; Honey et al., 2009; Messe et al., 2014; Misic et al., 2016; van den Heuvel and Sporns, 2013).

1.7.2. The aging brain and disease

The relationship between structural and functional connectivity also varies in healthy aging and disease. A stronger relationship is seen between structural and functional connectivity as the brain matures between infancy and late adolescence (Hagmann et al., 2010). In a study ranging from childhood to late adulthood reduced structural connectivity is seen, while connections between resting state networks increase and connectivity within resting state networks decrease in later years. The relationship between structural and functional connectivity also increases with age (Betzel et al., 2014). Interestingly this increased structural-functional correlation is also seen in Schizophrenia (van den Heuvel et al., 2013). This is interpreted as pathological relating to less dynamic functional connectivity, which is more constrained to the underlying structural network. Reduced coupling between structural and functional connectivity has been shown in idiopathic generalized epilepsy and correlates with disease duration suggesting this may represent accumulation of pathology

throughout the disease course (Zhang et al., 2011). In amyotrophic lateral sclerosis (ALS) increased functional connectivity is seen in areas of reduced structural connectivity in patients compared to controls, particularly in those with faster rates of disease progression. This led the authors to interpret this as progressive loss of inhibitory cortical influence relating to underlying structural damage (Douaud et al., 2011). However another study in ALS showed overlap between reductions in functional and structural connections in patients relative to controls (Schmidt et al., 2014). Decoupling between structural and functional connectivity has also been demonstrated in older adults with white matter hyperintensities and is associated with poorer cognitive function (Reijmer et al., 2015).

1.7.3. Gene expression and connectomics in the healthy brain

Connectomics can provide a wealth of information linking brain structure and function at the macrostructural level, however there is a large gap exists between our understanding at a systems level and how this relates to structure and function at a cellular level. A major advance in this regard is the creation of the Allen Institute of brain Science (AIBS) human brain atlas (Hawrylycz et al., 2015; Hawrylycz et al., 2012). This is an atlas based on gene expression microarray data from 6 post-mortem human brains with no known neuropsychiatric or neuropathological history. RNA is extracted from 900 anatomically defined regions thus providing the most comprehensive regional transcription atlas of the human brain. As part of the AIBS atlas protocol participants' brains also undergo MRI imaging therefore allowing one to map regional transcription in MRI space. This has lead to several studies linking connectomics at the structural level to gene expression at the cellular level.

Richiardi and colleagues where the first to demonstrate the relationship between co-expression of genes across brain regions and rs-fMRI brain networks, showing regions within the same rs-fMRI network had correlated gene expression profiles. Furthermore the strength of rs-fMRI networks was highly correlated with genes involved in synaptic function (Richiardi et al., 2015). Subsequent studies confirmed this link between rs-fMRI and regional gene expression (Krienen et al., 2016). Brain regions with long-range connections are enriched with genes involved in oxidative metabolism and mitochondrial function (Vertes et al., 2016) in keeping with previous observations that hub brain regions are more metabolically active (Liang et al., 2013). Myelination in

adolescence has also been linked to brain regions enriched for genes involved in synaptic function (Whitaker et al., 2016).

Regional gene expression data from the AIBS transcriptome atlas has also been used to explain vulnerability of brain regions in disease. In a cohort of participants with Parkinson's disease regional expression of the MAPT tau gene is associated with loss of functional connectivity (Rittman et al., 2016). Similarly regional expression of genes associated with schizophrenia are linked to regional loss of structural connectivity in schizophrenia patients relative to healthy controls (Romme et al., 2016).

In this thesis I have utilized data from the AIBS transcriptome atlas in order to investigate how the relationship between regional gene expression in the healthy brain and regional white matter loss in preHD. By using gene ontology I further identify the biological processes associated with these specific gene expression profiles thus providing a link between systems level white matter loss and pathobioloigy at the cellular level.

1.8. Modeling neurodegeneration in the healthy brain

1.8.1 Network spread of neurodegeneration

The organisation of the healthy brain can be used to predict regional patterns of disease in brain (Iturria-Medina and Evans, 2015). In one of the first studies to demonstrate this, Seeley and colleagues revealed intrinsic resting state fMRI networks in young healthy controls mirrored atrophy patterns in a range of neurodegenerative diseases including Alzheimer's disease (AD), behavioural variant fronto-temporal dementia (bvFTD), semantic dementia (SD), progressive non-fluent aphasia (PNFA) and cortical basal syndrome (CBS) (Seeley et al., 2009). In order to do this brain regions with the greatest degree of atrophy relative to controls, in each disease, were used as 'seeds'. Brain regions showing temporal correlations in their fMRI time-series with a seed region were said to be functional connected, such that each seed region formed a functional network. Functional networks of each seed region were then compared with patterns of atrophy in disease. Remarkably there was consistent overlap with functional networks in the healthy brain and atrophy patterns in neurodegeneration (see figure 1.9). This work was the first to suggest that disease specific patterns of neurodegeneration are not random but linked to the organisation of the healthy brain.

Figure 1.9. Convergent Syndromic Atrophy, Healthy ICN, and Healthy Structural Covariance Patterns. (A) Five distinct clinical syndromes showed dissociable atrophy patterns, whose cortical maxima (circled) provided seed ROIs for intrinsic connectivity networks (ICN) and structural covariance analyses. (B) ICN mapping experiments identified five distinct networks anchored by the five syndromic atrophy seeds. (C) Healthy subjects further showed gray matter volume covariance patterns that recapitulated results shown in (A) and (B). For visualization purposes, results are shown at $p < 0.00001$ uncorrected (A andC) and $p < 0.001$ corrected height and extent thresholds (B). In (A)–(C), results are displayed on representative sections of the Montreal Neurological Institute (MNI) template brain. Color bars indicate t-scores. In coronal and axial images, the left side of the image corresponds to the left side of the brain. ANG, angular gyrus; FI, frontoinsula; IFGoper, inferior frontal gyrus, pars opercularis; PMC, premotor cortex; TPole, temporal pole. Reproduced from (Seeley et al., 2009).

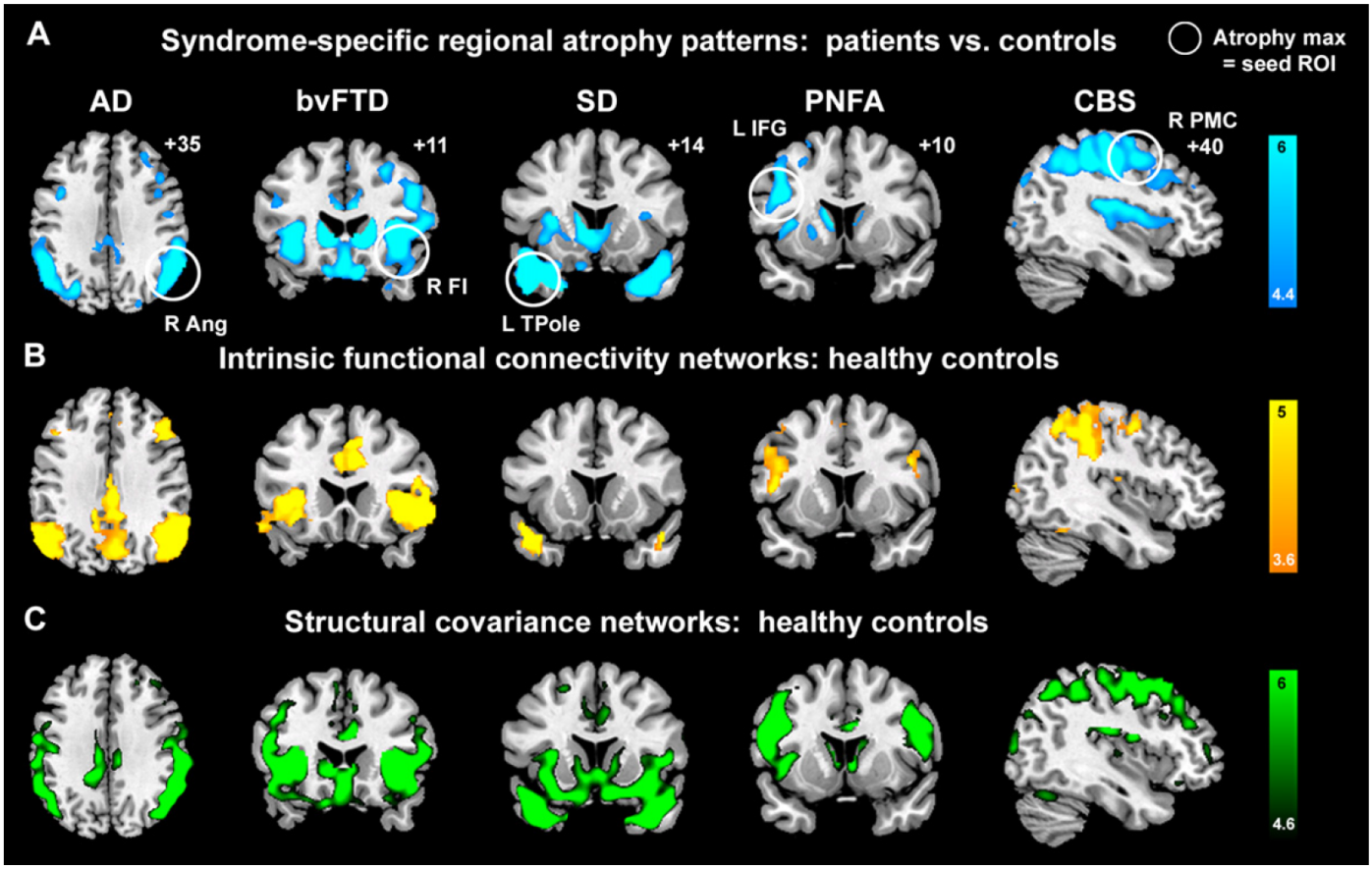

This group subsequently applied a graph theoretical analysis to the same data testing the hypothesis that regions with high network flow (defined by number of connections to a brain region), low clustering of neighbouring brain regions and close proximity to disease specific epicentres would show the greatest degree of atrophy (Zhou et al., 2012). This hypothesis was based on the concept of prion-like spread were the spread of pathogenic proteins throughout the brain from cell-to-cell resembles the spread of infectious prion proteins in Creutzfeldt-Jakob disease (CJD) (Guo and Lee, 2014). By demonstrating that brain regions with high flow, low clustering of neigbours and in close to proximity to disease epicenter were most vulnerable to

neurodegeneration (Zhou et al., 2012) suggested this was evidence for the prion-like spread of neurodegeneration at the systems level.

These findings were further supported by (Raj et al., 2012), who used a network diffusion model to simulate the prion-like spread of pathogenic protein throughout the white matter brain network. Using this the white matter brain network of young healthy controls was decomposed into a series of different modes that matched atrophy patterns of AD and bvFTD. Furthermore reported prevalence rates of these conditions could be predicted based on the contribution of the disease related modes to the healthy brain network. In a follow-up study this model was used to predict atrophy and metabolism changes in a longitudinal cohort of AD patients (Raj et al., 2015). An epidemic spreading model (ESM) has also been used to represent the prion-like spread of neurodegeneration in brain networks. In an AD cohort the ESM model was able to reproduce regional patterns of Amyloid-β deposition, measured using (Positron Emission Tomography) PET (Iturria-Medina et al., 2014).

Both the structural and functional connectivity of the healthy brain have been used in combination to predict regional brain atrophy in neurodegeneration. In PD topological distance from the substania nigra, the presumed disease epicentre, as measured by the shortest path length in healthy functional and structural brain networks showed significant correlation with PD-related atrophy (Zeighami et al., 2015). In PNFA longitudinal change in both grey and white matter was predicted using the healthy brain, where the functional connectivity network created from the disease epicentre, the inferior frontal gyrus, predicted grey matter atrophy over time. Furthermore the connectivity of the white matter tracts connecting regions in the healthy brain network was predictive of white matter change over time (Mandelli et al., 2016). More complex models of disease spread have also emerged combining a number of imaging modalities including functional MRI, diffusion MRI, PET and arterial spin labeling. Using this approach one can estimate the individual contributions that vascular, neuronal, metabolic and structural systems have on disease (Iturria-Medina et al., 2017; Iturria-Medina et al., 2016).

1.8.2. Hub region vulnerability

In the context of the prion-like spread hypothesis brain regions with high connectivity, low clustering of neigbouring brain regions and short topological distance form disease epicentres would be expected to have greatest exposure to pathogenic proteins and thus show greatest brain atrophy. While Zhou and others did indeed demonstrate this (Zeighami et al., 2015; Zhou et al., 2012), there is an alternative explanation that can account for the selective vulnerability of brain regions exhibiting these properties. Rich club brain regions are brain regions that are highly connected both to each and to the rest of the brain network (van den Heuvel and Sporns, 2011). These regions act as the backbone of the brain network facilitating communication across diverse specialized systems of the brain (van den Heuvel et al., 2012). Rich club regions have high connectivity strength, low clustering of neighbouring brain regions and given they are highly connected within the network they have short topological distances to other regions in the brain network (van den Heuvel and Sporns, 2011). Thus the findings by (Zhou et al., 2012) can be explained as a selective vulnerability of rich club regions as opposed a vulnerability of regions with greatest exposure to pathogenic protein.

The vulnerability of hub regions is generalizable across all brain diseases. This was shown in a large meta-analysis, were grey matter lesion maps were created based on a meta-analysis of over 2000 subjects in 26 disorders (Crossley et al., 2014). The location of these lesions was then compared to the location of hub brain regions as defined by diffusion MRI data from healthy controls, were a hub was defined as a region with dense white matter connections. This revealed that hubs were more likely to be abnormal than non-hubs across many brain disorders (see figure 2.0). The authors suggested this may be related to the high metabolic demands of hub brain regions and that lesions of hub may result in greater symptomatology and thus clinical diagnosis as opposed to lesions of peripheral brain regions. In the context of neurodegenerative disease however, it is possible that selective vulnerability of brain regions may result as combination of both hub vulnerability and the prion-like spread of pathogenic proteins.

In keeping with the studies detailed here in this thesis I investigate how properties of the healthy white matter brain network such as connection strength and topological length can explain the selective vulnerability of specific white matter connections demonstrated in preHD.

Figure 2.0. MRI lesions identified meta-analytically from the primary literature on 26 clinical brain disorders impact preferentially on the hubs of the normal connectome. (A) A meta-analytic map of multiple cortical and subcortical grey matter MRI lesions that were significantly abnormal 'on average' over 26 specific disorders. (B) Nodes of the normative DTI connectome, represented in anatomical space, and (C) in a spiral, where nodes of similar degree are arranged in the same circle, and the different circumferences arranged so that the tip of the spiral has the highest degree hub nodes, while the base the most peripheral nodes. Nodes are sized in proportion to their degree, and coloured according to the proportion of voxels, which are generically lesioned, i.e. the percentage of lesion voxels each node comprises. The strongest 0.1% of edges between nodes, which highlight pairs of nodes with consistently high number of streamlines interconnecting them, are shown for illustrative purposes. (D) Plot of the probability of lesion voxels (y-axis) versus the degree of DTI connectome nodes (x-axis). The red line is a fitted logistic regression model. (E) Plot of the probability of lesion voxels (y-axis) versus the degree of the functional co-activation network nodes (x-axis). The red line is a fitted logistic regression model. Reproduced from Crossley et al. (Crossley et al., 2014).

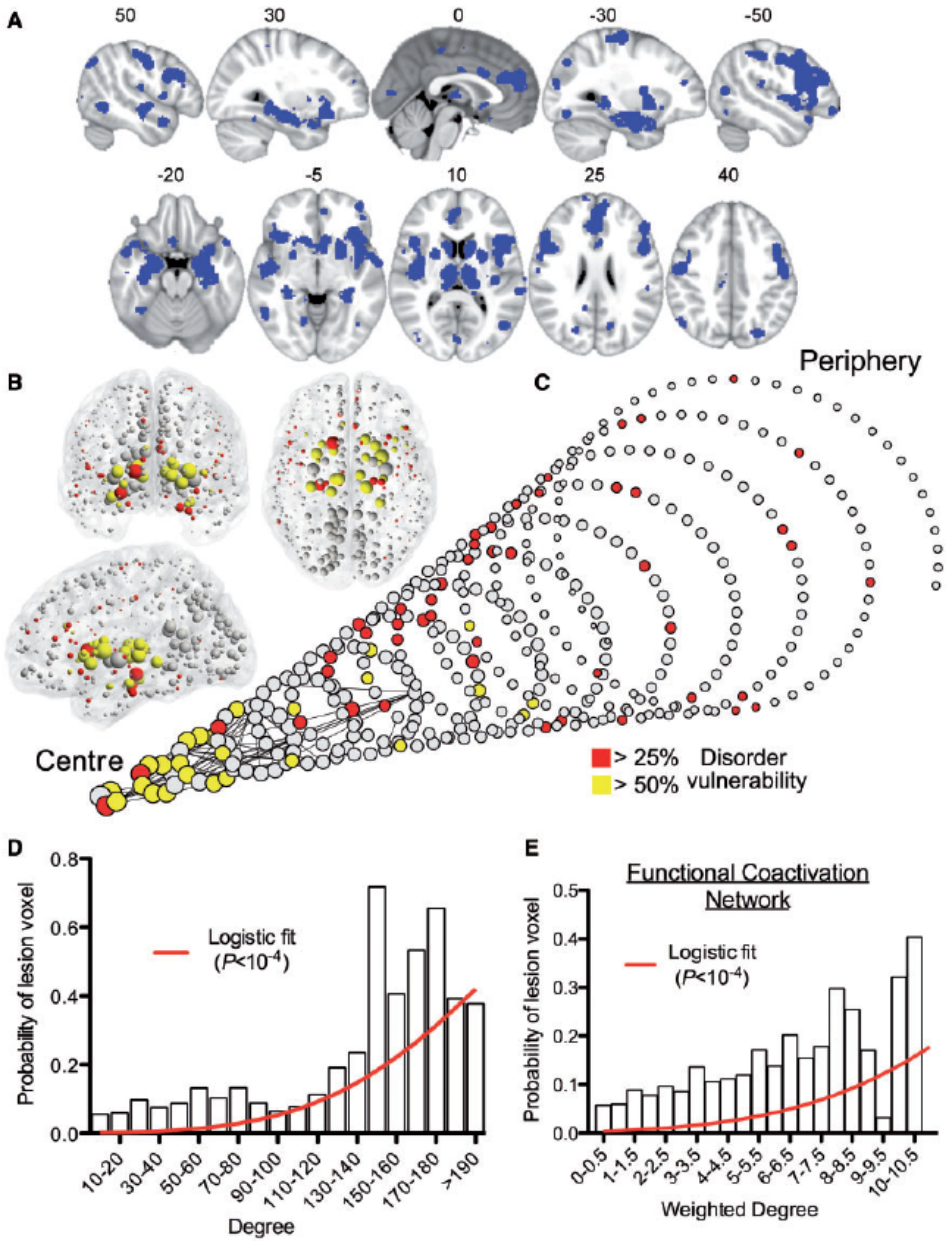

1.9. Conclusions

It is unclear how abnormalities caused by mutant huntingtin at the cellular level result in the characteristic HD related atrophy of grey and white matter at the macrostructural level. Using connectomics in this thesis I will investigate how the white matter structural brain network relates to functional brain network changes in preHD. I will evaluate how changes in structural and functional networks relate to the psychiatric symptoms experienced by HD gene carriers years before motor manifestation of the disease. Using graph theoretical analysis I will characterise HD related changes of the white matter brain network at both the global and regional level and assess how these system level abnormalities result in cognitive and motor deficits associated with HD. By analysing the healthy white matter brain network I will investigate how network properties can predict the atrophy of specific white matter connections over time, thereby providing systems level explanations for the selective vulnerability of specific brain regions in HD. In utilising data from the AIBS transcriptome atlas I will then link these system level properties to pathobiological processes at the cellular level. Linking systems and cellular pathobiology in HD will inform us about disease mechanisms that drive brain atrophy and ultimately lead to clinical deficits.

Chapter 2. General methods

2.1. Introduction

This chapter outlines the methods general to all experiments in this thesis. I begin by covering the basic principles MRI with an emphasis on diffusion MRI and functional MRI. I then detail the MRI acquisitions used in experiments. Following this I describe preprocessing and processing strategies for the T1, DWI and rs-fMRI images including quality control, image segmentation and parcellation and construction of structural and functional connectomes. Finally I detail the cohort studies, Track-HD and Track-On HD, which have been used in this thesis. Graph theory and statistical methods differ between each experiment and are therefore described in the individual methods sections of the experimental chapters.

2.2. Basic principles of MRI

2.2.1. MRI Physics

Hydrogen ions contain a single positively charged proton that is constantly spinning and this creates a magnetic field. When an external field, termed B0, is applied the magnetic field of each proton either aligns parallel or anti-parallel to the external field, with the majority aligning parallel as this requires the least energy. The overall effect is a change in the rotational axis of the protons, which is called precession. Frequency of precession, also known as Larmor frequency (ω_0) is defined by a constant (γ), known as the gyromagnetic ratio, and the strength of the external field (B_0). This is known as the Larmor equation:

$$\omega_0 = \gamma B_0$$

By applying a radiofrequency (RF) pulse in the same frequency as the Larmor frequency protons move to a higher energy state and align anti-parallel to B_0, they also begin spinning in phase. Once the RF pulse is turned off the protons begin to dephase and return to the lower energy state, this is known as relaxation. As different human tissue types have different rates of relaxation this produces different contrasts on an MRI scan. T1 longitudinal relaxation occurs due to protons moving from the higher to lower energy state, while T2 transverse relaxation occurs due to the dephasing of protons. These processes occur both simultaneously and independently resulting in decay of signal over time, which is termed free induction decay (FID). The signal used

to generate MRI images is not that created from FID but echo signals. These may take the form of spin or gradient echo. Spin echo is generated when a 180 pulse is applied following the initial 90° pulse causing protons to precess in the opposite direction. In the case of gradient echo magnetic field gradients are applied following the 90° RF pulse.

2.2.2. T1 and T2 weighting

In order to generate T1 and T2 weighted images additional parameters are manipulated during MRI acquisition such as echo time (TE) and repetition time (TR). TE is the time between application of the RF pulse and induction of the signal in the MRI coil. TR refers to the time between two RF pulses. Short TR allows differences caused by T1 relaxation to develop before the next RF pulse, while short TE limits T2 effects, thus these are used when generating T1-weighted images. Long TR and TE parameters generate T2-weighted images. T2 relaxation is affected by local tissue inhomogeneity such as the presence of iron or blood. While the use of spin-echo helps to remove these effects acquisitions such as gradient echo are sensitive to these local differences. T2 relaxation, which includes these local effects, is known as T2*. This is particularly important in the case of fMRI where the detection of deoxyhaemoglobin forms the basis of the BOLD signal. This will be covered in detail in subsequent sections.

2.2.3. Image generation

In order to generate an MRI image signals must be localised in space. This is achieved using 3 separate magnetic field gradients: slice selection gradient, phase encoding gradient and frequency encoding gradient. In order to acquire sufficient information the pulse sequence is repeated many times. At each repetition the phase encoding gradient is increased in increments and generates an echo. This echo is stored in a data matrix known as k-space, such that each echo generates one line of data in k-space. Following adequate population of k-space a mathematical transform, known as a Fourier transform, is applied in order to generate an MRI image (Currie et al., 2013).

2.2.4. Echo Planar Imaging

Echo-planar imaging (EPI) enables the acquisition of multiple lines of data in k-space in one TR. Using this approach acquisition times can be shortened and susceptibility to motion related artifacts reduced dramatically. As with spin echo, EPI sequences begin with a 90º and 180º RF pulse. Following this the frequency encoding gradient oscillates rapidly, where each oscillation corresponds to one line of imaging data in k-space. In this thesis EPI sequences have been used to acquire both diffusion and functional MRI data (Poustchi-Amin et al., 2001).

2.3. Principles of diffusion MRI

2.3.1. Diffusion weighted imaging

The unrestricted diffusion of a substance follows a Gaussian distribution, where the mean squared displacement is characterised by the diffusion coefficient and the time interval over which diffusion takes place. Hahn first noted in the 1950s that diffusion of water molecules in a magnetic field resulted in a decrease in signal intensity (Hahn, 1950). Stejskal and Tanner subsequently used a pulsed gradient spin echo (PGSE) sequence to measure diffusion (Stejskal and Tanner, 1965). This PGSE sequence included the addition of two gradient pulses to the standard spin echo sequence to induce a phase shift. Because the strength of the gradient varies with position molecules undergoing diffusion would be subject to a phase shift proportional to their displacement. Therefore greater diffusion would result in greater phase shift translating to low signal in high areas of diffusion. The diffusion weighting or b-value is the proportional to the product time interval and square of the gradient strength. A single DWI image is created by a single pulse in a single direction and represents one point in q-space, which is analogous to k-space in standard MRI imaging. Therefore repeated pulses with multiple directions creates more points in q-space and a more detailed diffusion image (Hagmann et al., 2006).

2.3.2. Diffusion tensor imaging and crossing fibres

In the diffusion tensor model, diffusion is assumed to have an anisotropic Gaussian distribution, which can represented as an ellipsoid, where the principle direction of diffusion runs parallel to the axon. This type of distribution requires 6 degrees of freedom denoting diffusion in 6-planes and thus can be generated from 6 points in q-space. Mathematically it can be represented by a 3x3 matrix. Eigenvalue decomposition of this results in three eigenvectors (λ_1, λ_2 and λ_3) (see figure 2.1). The diffusion tensor can then provide information regarding local white matter structure in the form of diffusion metrics such as FA (Le Bihan et al., 2001). However one major limitation of the model is the assumption of anisotropic diffusion. This assumption no longer holds true in regions of the brain that contain crossing white matter fibres. Given that this may occur in as much as 90% of the brain's white matter (Jeurissen et al., 2012) there is a move beyond DTI with the use of more advanced approaches that can account for crossing fibres (Tournier et al., 2011). One such approach is CSD, which I have used in the work presented in this thesis. Details regarding CSD will be covered in detail in subsequent sections.

Figure 2.1. The diffusion tensor represented as an ellipsoid with eigenvectors λ_1, λ_2 and λ_3 in the principle axes of diffusion

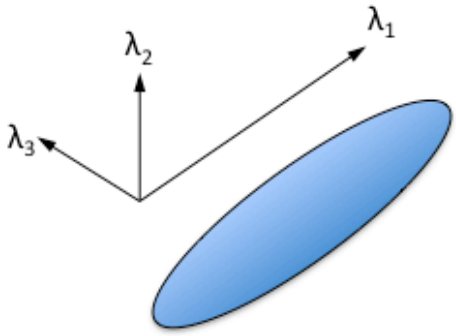

2.4. Principles of functional MRI

2.4.1. BOLD contrast

As mentioned previously T2* relaxation is affected by local tissue inhomogeneity. As deoxyhaemoglobin is paramagnetic, meaning it induces a magnetic field in the direction of the external field b0, this results in loss of signal in regions with high deoxyhaemoglobin. Oxyhaemoglobin is weakly diamagnetic and thus has minimal effect to on the overall signal. Ogawa and colleagues were the first to show that regional changes in cerebral blood flow cause a Blood Oxygen-Level Dependent (BOLD) contrast in the context of altered metabolic demands, such as in hypoglycaemic or anaesthetised states (Ogawa et al., 1990). Subsequently the relationship between neuronal activity and BOLD response was demonstrated by showing local field potentials, reflecting intra-cortical processing, were correlated with BOLD response, following stimulation of the visual cortex in ananesthetised Monkeys (Logothetis et al., 2001).

2.4.2. Haemodynamic response function

Following functional stimuli the BOLD fMRI response consists of three phases: a small initial decrease in signal due to oxygen consumption; a large increase in oxygenated blood and a decrease back to baseline once the oxygenated blood has diminished. This is known as the haemodynamic response function BOLD can be affected by blood flow, blood volume and blood oxygenation (Heeger and Ress, 2002).

2.4.3. Basis of the haemodynamic response

There are number of theories as to the physiological basis of the haemodynamic response. The haemodynamic response may occur in order to replenish oxygen deficit caused by neuronal activity. This view is supported by the fact that oxygen consumption increases with neuronal activity; neurons utilize high levels of oxygen and rely on oxidative metabolism of lactate. Arguments against this theory cite the large mismatch between the large amount of oxygen delivered by blood and the small amount of oxygen used by neurons. Another theory suggests that the blood response acts to deliver glucose due to increased metabolic demand, such that the increase in blood flow is proportional to the increase in glucose consumption but not oxygen (Heeger and Ress, 2002). However the observation that the BOLD response can be elicited in in animals maintained in hyperoxic

and hyperglycaemic states (Lindauer et al., 2010; Wolf et al., 1997), suggest oxygen or glucose deficit may not be a key factor. Other theories suggest a role for vasodilators, for example, increase in glutamate following neuronal activity may be detected by astrocytes leading to generation of prostaglandins, which in turn cause vasodilation. Similarly pericytes may cause capillary vasoconstriction following electrical stimulation. Given that no one mechanism has been clearly established it is likely that the BOLD response occurs due to a combination of mechanisms (Hillman, 2014).

2.4.4. Resting state fMRI

Biswal and colleagues first identified temporal correlations between motor regions in fMRI time series when participants were instructed to remain at rest (Biswal et al., 1995). Since this initial observation, the presence of a number of resting state networks have been established. These include the default mode, visual, attention and fronto-parietal networks (van den Heuvel and Hulshoff Pol, 2010). The use of rs-fMRI is particularly attractive in clinical populations as no task is required however motion can have a significant impact and many strategies exist to account for this (Power et al., 2014). In chapters 3 and 4 of this thesis I analyse rs-fMRI data preHD and healthy controls. Methods for preprocessing and analysing rs-fMRI data are detailed later in this chapter.

2.5 Image processing and connectome construction

2.5.1. Structural T1-wighted images

2.5.1.1. Quality control

Two T1 scans were collected during study visits for both Track-HD and Track-On HD. Following collection of imaging data all scans were transferred to IXICO (http://www.ixico.com) for quality control (QC). Scans were checked to ensure correct acquisition and absence of artefacts. Common artefacts include those related to the participant, such as motion, which is particularly common in those with manifest HD. Acquisition based artifacts may also occur, such as aliasing where the field of view is smaller than the size of the object being imaged (Heiland, 2008). Image analysts in the UCL Huntington's Disease Centre also carried out visual quality control. The two T1 images were compared and the optimal image selected for further analysis.

Following QC, bias field correction was applied. Bias field or illumination artefact occurs due to inhomogeneity of radio-frequency (RF) excitation across the MRI image. This may be caused by a number of factors including lack of uniform sensitivity of RF emitting and receiving coils and magnetic susceptibility of tissues. This can be corrected by using an iterative algorithm consisting of the following steps: tissue types are classified and a bias free image is created, a residual image is then generated by removing the bias free image from the original image and this is used to estimate the bias field (Gispert et al., 2004). For the Track-HD and Track-On HD data the N3 bias field correction algorithm was applied to each T1 image (Sled et al., 1998).

2.5.2.2. T1 Segmentation

When dealing with large imaging data sets manual segmentation becomes unfeasible therefore there is a need to perform this in an automated fashion while maintaining accuracy and reproducibility. Freesurfer was one of the first software packages to address this problem. This is done using a probabilistic model, which takes into account spatial probabilities within the brain. By using a surface based co-ordinate system of the human brain probabilities of specific anatomical structures occurring in a specified region can be calculated (Fischl et al., 1999). Probabilities of neigbouring structures can also be accounted for as well as the probability that a structure will contain certain MRI imaging properties, such as intensities. By using a combination of these features in the model one can include known anatomical information, while also accounting for anatomical variability between subjects (Fischl et al., 2002; Fischl et al., 2004).

The probabilities used by Freesurfer are based on a training set atlas where brain regions are manually classified. For the purpose of analyses in this thesis we used the Desikan atlas (see figure 2.2). This included 40 subjects across a range of ages encompassing 4 groups; young adults, middle aged adults, elderly adults and patients with Alzheimer's disease. By including subjects with age and neurodegenerative related atrophy this better accounts for inter-subject variability (Desikan et al., 2006), particularly in the case of our cohort, which contains adults across a range of ages and those with HD. The Desikan atlas includes 84 regions: 70 cortical regions, 12 subcortical regions (caudate, putamen and thalamus, globus pallidus, nucleus accumbens and amygdala bilaterally) and the left and right cerebellum. For analyses in this thesis the globus pallidus, nucleus accumbens and amygdala were not included as automatic segmentation of these regions is not sufficiently reliable. This is evidenced by low inter-site reproducibility across a range of segmentation tools (Hibar et al., 2015). The

cerebellum was not included as associated diffusion data was incomplete. This resulted in 76 ROIs (70 cortical regions and 6 subcortical regions).

In practical terms the Freesurfer pipeline performs the following steps:

1) Skull stripping is performed where non-brain material is removed from the image in order to improve subsequent registration steps.
2) The T1 is registered to the Talairach space. This is performed using an affine registration, which preserves global features of the image, such as straight lines and planes. Talairach space refers to registration to the Talairach atlas, which provides a 3-dimensional co-ordinate system and is based on a post mortem human brain (Talairach and Tournoux, 1988).
3) An initial labeling of cortical and sub-cortical structures is performed and bias field correction applied.
4) A non-linear registration of the T1 to the Talairach atlas is preformed. The non-linear registration allows local features of the image to be taken into account providing a more accurate registration.
5) Re-labeling then performed following the non-linear registration

With respect to longitudinal analysis additional considerations must be taken account when segmenting brain structures. Bias may be introduced when different scanners, different scanner software or different acquisitions are used at different time points. Properties of brain tissues may also change over time, especially in the case of neurodegenerative disease where changes in iron composition of the basal ganglia may affect certain acquisitions. Bias may also occur with respect to the pre-processing of data. Traditionally scans have been registered to their baseline image, such that both are in the same MRI space, however asymmetry in the registration step such that A to B is not the same as B to A introduce biases. Additionally by processing follow up scans in a different manner to the baseline scan biases are also introduced (Reuter and Fischl, 2011). In order to address these issues the Freesurfer developers have developed a longitudinal pipeline where all images at all time points are processed together in order to generate an unbiased template. For the longitudinal analysis in chapter 6 the Freesurfer longitudinal pipeline has been used (Reuter et al., 2012).

Figure 2.2. An example of a Freesurfer segmentation. Blue – caudate, red –putamen, dark green - thalamus

2.5.3 Diffusion MRI

2.5.3.1. Quality control

DWI data can be susceptible to artifacts due to the nature of the acquisition. Eddy currents (EC), for example, can be caused when strong gradient pulses are switched rapidly. This can produce geometric distortions of the image including contraction, dilatation and shearing. DWI sequences are also very sensitive to motion artifacts which results in a phenomenon known as ghosting (Le Bihan et al., 2006). Other artefacts may occur due to signal dropout where slices may have very low signal or sinus artifact due to hyperintensities in areas near the sinuses, particularly regions in the frontal and temporal lobes (see figure 2.3).

Figure 2.3. Examples of DWI artefacts

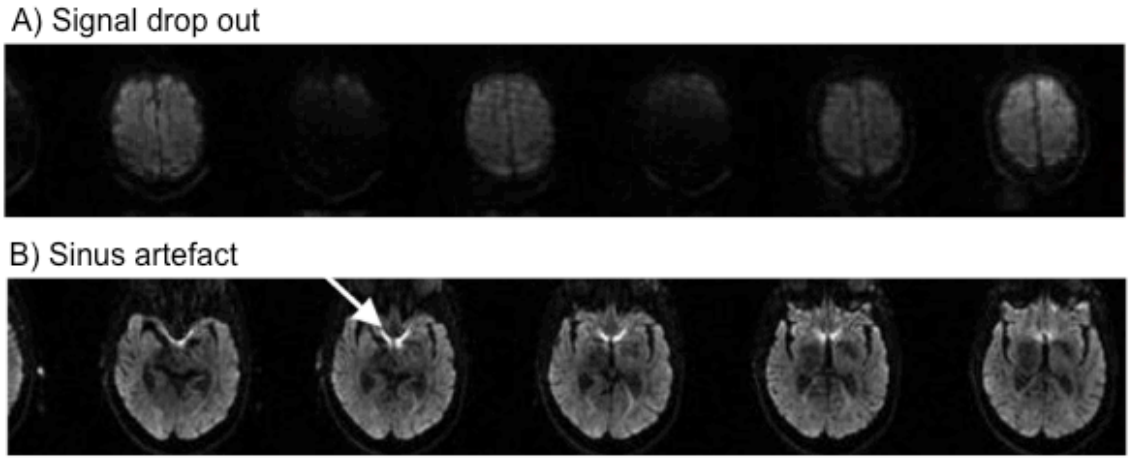

Following acquisition of DWI data visual quality control was performed in order to detect artifacts. Eddy current and motion correction was also applied using FSL eddy_correct. Using this approach each diffusion volume is registered to the b=0 image, which has no diffusion gradient, thereby allowing for simultaneous correction of EC and motion. Gradient directions were then updated to reflect the changes to the image orientations. FSL eddy_correct has been superseded by FSL eddy, which registers a diffusion volume to a model free prediction of how it should look in undistorted space (Andersson and Sotiropoulos, 2016). While this has been shown to produce improved correction (Graham et al., 2016) it was released in 2015 after the processing of much of the Track-HD and Track-On HD data therefore FSL eddy_correct was used in order to maintain consistency.

Following EC and motion correction of DWI data the b=0 image was used to generate a brain mask using FSL's brain extraction tool (BET). This removes non-brain mater, such as eyes, muscle and other structures in the head and neck in order to improve subsequent registration steps. BET creates a brain/non-brain intensity threshold and then works out from the centre of the brain until this threshold is reached. All mater beyond this threshold is then removed from the image (Smith, 2002). Visual inspection of images following BET revealed sub-optimal performance therefore eroding by one voxel was additionally performed in order to provide a more stringent mask.

2.5.3.2. Fitting the diffusion tensor model

The b=0 mask and DWI image are the used to fit the tensor model using the following operations in MRtrix3 software (Tournier et al., 2012). The diffusion tensor was fitted using the dwi2tensor command. This takes the natural log of the diffusion signal and fits the diffusion tensor using a weighted linear least squares approach, where weights take into account variance in the diffusion signal (Veraart et al., 2013). The tensor is then used to calculate the FA image using the tensor2metric command (see figure 2.4) (Basser et al., 1994). Mathematically the diffusion tensor is represented by a 3x3 matrix. An eigenvalue decomposition of this results in three eigenvectors λ_1, λ_2 and λ_3, which denote the diffusion along the major axes of the tensor and are used to calculate FA.

Figure 2.4. Diffusion weighted image, diffusion tensor image and FA image.

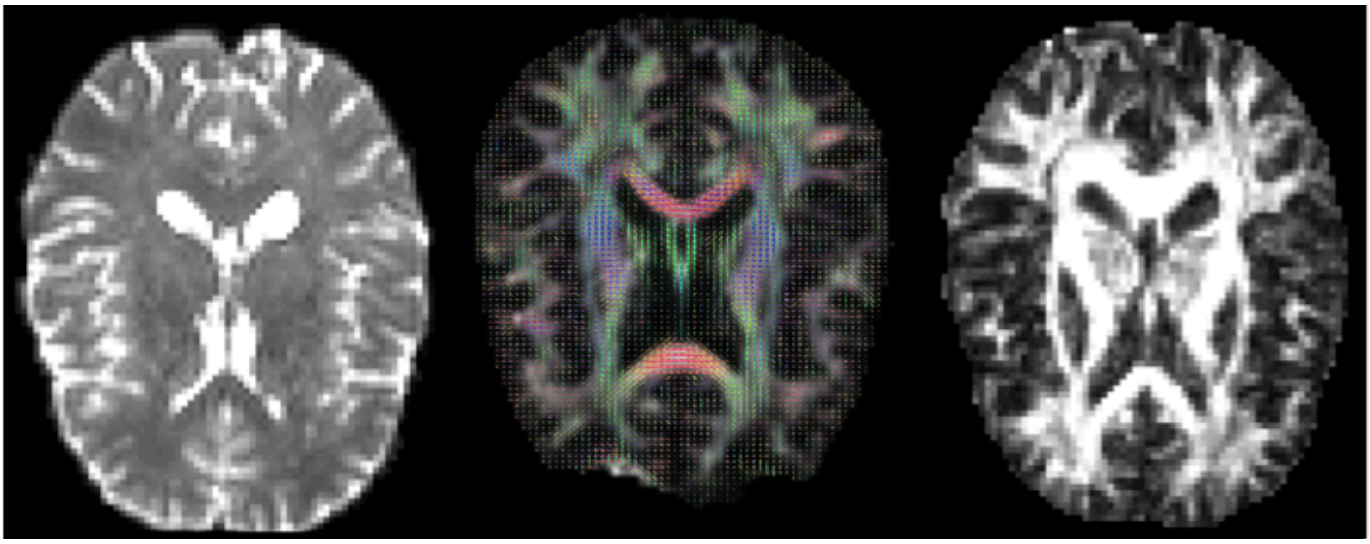

2.5.3.3. Constrained spherical deconvolution

The diffusion tensor model is incapable of resolving crossing fibres. In recent years a number of algorithms have been developed in order to address this problem these include constrained spherical deconvolution (CSD), diffusion spectrum imaging and q-ball imaging among others (Tournier et al., 2011). CSD provides better angular resolution than many other multiple-fibre reconstruction algorithms, while maintaining a modest computation time (Seunarine and Alexander, 2013; Tournier et al., 2007). It also performs better than other crossing fibre algorithms in diffusion data acquired in patient populations, where b-values are typically lower (Ramirez-Manzanares et al., 2011; Wilkins et al., 2015). This in particularly important for manifest HD populations were longer scanning times required to attain higher b-values are likely to result in greater motion artifact.

Using a CSD approach DWI signal can be modeled as the sum of signals from individual fibre populations, where the signal attenuation from individual fibre populations along the z-axes is denoted as the response function. The response function is computed using the dwi2reponse command in MRtrix. Spherical deconvolution of the response function is then used to calculate the fibre orientation distribution (FOD) using the command dwi2fod. This gives the fraction of fibres within a given fibre population that are aligned along a particularly direction. As it is impossible to have negative FOD values a non-negative constraint is applied (Tournier et al., 2007). The CSD reconstruction used a maximum spherical harmonic order of 6 for both the response and the fibre orientation distribution functions, as this is most appropriate for DWI acquisitions of b value = 1000 s/mm^2 (Tournier et al., 2013), as was case for DWI data used in this thesis.

2.5.3.4. Registration of T1 images to diffusion space

Freesufer ROIs generated from T1 segmentation were registered to diffusion space by finding the mapping between the T1-weighted image and fractional anisotropy (FA) map using the NiftyReg toolkit (Modat et al., 2010) and applying the resulting warp to each of the ROIs. This involved an initial affine registration followed by a non-linear registration of the Freesurfer T1 image to the FA image, using the commands reg_aladin and reg_f3d, respectively. An affine registration maps the image in terms of global properties, while the non-linear registration takes into account local properties in the image. The Freesurfer ROIs were then registered to the FA images using the reg_resample command. Freesurfer segmentations were also used to generate the grey and white matter masks for tractography by adding images together using fsl_maths (Smith et al., 2004).

2.5.3.5. Diffusion tractography

Tractography can be performed using either deterministic or probabilistic algorithms. Deterministic tractography assumes a single fibre orientation from each voxel using principal direction of diffusion or the peak of the FOD. Probabilistic algorithms take into account all the information in the FOD providing probabilities of the fibres travelling along different routes (Descoteaux et al., 2009). Validation of these algorithms cannot be performed using the human brain therefore simulated ground truths are used containing geometry similar to the human brain. Using this approach shows that probabilistic tractography derived connectomes have large numbers of false positives; whereas deterministic tractography derived connectomes have large numbers of false negatives (Maier-Hein et al., 2017). In the case of probabilistic tractography streamline filtering and graph theory thresholding can be applied to reduce the likelihood of false positives (Drakesmith et al., 2015; Smith et al., 2013). This will covered in detail in subsequent sections. Probabilistic approaches have been shown to have greater test-retest reliability for graph theory metrics and is therefore the approach I used in the work presented in this thesis (Owen et al., 2013).

Whole brain probabilistic tractography was performed using the iFOD2 algorithm (Tournier et al., 2010), with the command tckgen, in MRtrix (Tournier et al., 2012). Using this algorithm five million streamlines were seeded throughout the white matter, in all foreground voxels where fractional anisotropy was >0.2. The probability of a white matter connection, termed a streamline, travelling along any number of paths is calculated

using the FOD. Probabilities are represented by the product of FOD amplitudes at regular intervals along the tangent of the path. Streamlines were terminated when they either reached the cortical or subcortical grey-matter mask or exited the foreground mask. In order to avoid spurious peaks in the FOD streamlines were also terminated if they did not reach a FOD with an amplitude greater than 0.05.

2.5.3.6. Streamline filtering

Inherent biases exist in tractography algorithms such longer white matter pathways are present in greater volume and thus over represented, streamlines tend to follow the straightest path and streamlines do not have an associated volume. In order to address these biases the spherical deconvolution informed filtering of tractograms (SIFT) algorithm (Smith et al., 2013) uses the results of the spherical deconvolution of the diffusion signal to determine which streamlines to remove from the dataset. This results in reconstructed connections, which are proportional to the fiber density as estimated by the diffusion model. For studies in chapters 3-5 the SIFT algorithm was used (tcksift) while for the studies in chapters 6 and 7 an updated version of the SIFT algorithm named SIFT2 was used (tcksift2) (Smith et al., 2015b).

2.5.3.7. Connectome construction

Following streamline filtering the Freesurfer ROIs are used to construct a structural connectome whereby streamlines are assigned to pairs of ROIs thereby creating a 76x76 undirected weighted symmetrical connectivity matrix (see figure 2.6). Subsequent steps including normalisation, thresholding and generation of graph theory metrics differ between chapters and will therefore be covered in the methods section for each experiment.

Figure 2.6. Structural white matter connectome. Colours represent diffusion along the y-axes: green, x-axes: red and z-axes: purple.

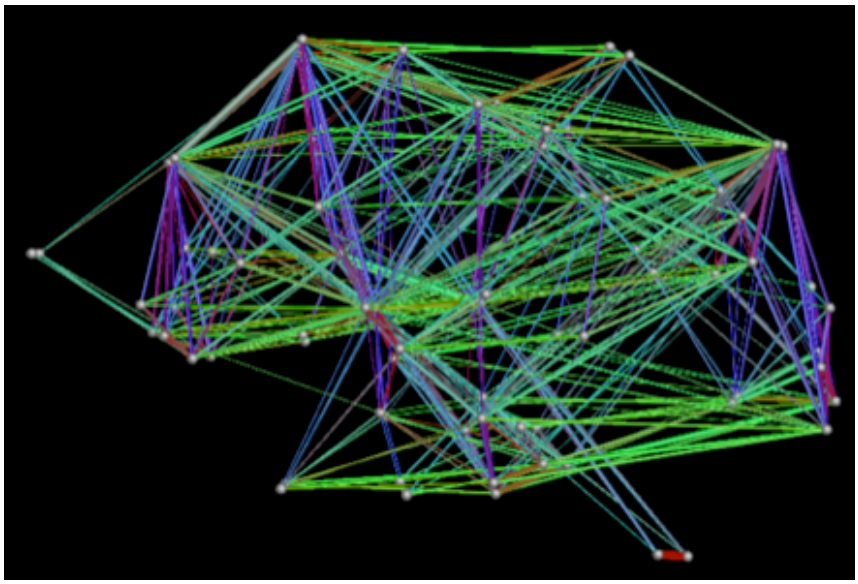

2.5.3.8. Considerations generating structural connectivity matrices

Connectivity matrices can be influenced by factors such as the choice of the brain parcellation scale, tractography algorithm, weighting scheme, thresholding approach and streamline filtering (Bullmore and Sporns, 2009; Qi et al., 2015; Smith et al., 2013).

When choosing parcellation scheme a trade off exists in that fine parcellations (i.e. those with large numbers of brain regions) may contain more detailed information, whereas coarse parcellations contain less detail but are more reproducible (Cammoun et al., 2012). Thus the decision regarding atlas must be based on the hypothesis in question. In the case of the work presented as I carried out both cross-sectional and longitudinal connectome analyses reproducibility of connectome construction was paramount such that I used the freesurfer Desikan atlas (Desikan et al., 2006), which has a relatively coarse parcellation.

Connectomes may be either binary or weighted. In the context if binary connectomes connections represent the absence or presence of a connection, alternatively connectomes may be weighted by streamline count of diffusion metrics such as FA. There is currently no consensus in the literature as to the optimal approach with some studies using a combination of methods (van den Heuvel and Sporns, 2011). In the work presented here I used the SIFT and SIFT2 algorithms, these approaches aim to derive connectomes based on the underlying diffusion signal. The authors of these approaches advised against binarisation as this is likely to be a poor representation of the underlying white matter biology. Furthermore FA weighting is discouraged due to concerns regarding the interpretation of this measure in crossing fibre regions (Smith et al., 2012, 2013, 2014, 2015b).

Probabilistic tractography results in dense connectomes with many false positives (Zalesky et al., 2016). Graph thresholding is an effective and widely used strategy to remove the false positives created by the probabilistic approach (Achard and Bullmore, 2007; Rubinov and Sporns, 2010). As the name suggests, graph thresholding entails applying a quantitative threshold below which the connections are removed (by setting them to zero in the adjacency matrix) from further consideration. This procedure is useful on two accounts: firstly it helps to remove the spurious connections (the false positives discussed above) and secondly by inducing the sparsity that helps minimize the multiple comparison problem. This is potentially important because the metrics calculated from the ensuing sparse graphs are sensitive to the amount and the method of thresholding (Simpson et al., 2013; Zalesky et al., 2016). There are multiple thresholding approaches described in the literature - for example absolute, proportional, consensus and consistency thresholding. However currently there is no agreement in the literature regarding the best practice for threshold implementation (Qi et al., 2015). An absolute threshold defines a value, below which connections are removed (Daianu et al., 2015; Drakesmith et al., 2015; Li et al., 2016). A relative threshold retains a defined proportion of the strongest connections in the network (Mueller et al., 2015; Yao et al., 2010). Consensus thresholding retains only the connections present in a defined percentage of the group (McColgan et al., 2015; van den Heuvel and Sporns, 2011; van den Heuvel et al., 2013). More recently, consistency thresholding has been proposed, whereby the most consistent connections across a group, as defined by coefficient of variation, are retained. Graph metrics may also be computed over a range of threshold values (Bai et al., 2012; Bassett et al., 2008). While thresholding methods are widely used in the field of structural connectomics one major limitation is the arbitrary nature of threshold constraints and their lack of relevance to the underlying white matter biology and inherent biases prevalent in tractography algorithms. In keeping with the seminal rich club paper (van den Heuvel and Sporns, 2011). I used a consensus threshold

approach for the rich club analysis in chapter 5. I elected to not perform connectome thresholding in subsequent chapters chossing to use the SIFT2 algorithm as an alternative to control for false positives.

2.5.4 Resting state fMRI

2.5.4.1. Analysis approaches

A wide-range of methods are available from rs-fMRI analysis. One of the first and perhaps most common methods is the seed based approach. Here a seed region is defined, such as the posterior cingulate, and correlations performed between the time series of voxels in the seed region and all other grey matter voxels in the brain, thereby identifying regions that are temporally correlated with the seed region. This can be used to identify resting state networks, such as the DFM (Biswal et al., 1995; Fox et al., 2005; Raichle et al., 2001). More recently data driven approaches, such as independent component analysis (Erhardt et al., 2011) and principal component analysis (Leonardi et al., 2013), have been developed that avoid the need for aprioi defined seed regions. Using these approaches fMRI time series for grey matter voxels in the brain can decomposed into components consisting of time series and associated spatial maps.

The methods described above are preformed at the voxel level. This requires normalisation to a standard template, such as the Montreal Neurological Institute (MNI) template. Smoothing may also be applied, which involves blurring of images to improve alignment between subjects. However careful considerations need to be taken into account when including these steps in an analysis. The process of normalisation assumes that anatomy across subjects and between groups is similar (Brett et al., 2002). This may not be the case when investigation group differences between healthy controls and a patient population with significant brain atrophy. Caudate atrophy for example, which is seen HD, may result in comparisons between rs-fMRI time series from caudate grey matter in controls with time series from CSF voxels in patients. This would likely result in spurious group differences showing reduced regional connectivity (Seibert and Brewer, 2011).

Due to the methodological concerns highlighted above for rs-fMRI analysis presented in chapters 3 and 4 I performed a ROI-ROI analysis. Using this approach ROIs are defined from an atlas. The time-series for each voxel in each ROI is averaged and correlations are performed between each pair of regions (Whitfield-Gabrieli and Nieto-Castanon, 2012). A large number of atlases are available for rs-fMRI analyses however there is no consensus as to the optimal approach (Arslan et al., 2017). Choice of atlas is therefore based on the research question, thus in in order to compare structural functional brain networks the freesurfer Desikan atlas (Desikan

et al., 2006) was also used for the rs-fMRI analysis. This enabled analysis in native space without the need for normalization or smoothing and allowed direction comparisons between structural and functional brain networks.

2.5.4.2. Quality control

Visual quality control was performed on all rs-fMRI scans in order to assess for motion artefacts and signal drop out. Following this artefact detection was carried out using ArtRepair software movie function. This assesses for rapid motions, which cause artefact during volume reconstruction and large slow movements, which cause motion residuals after realignment. Abrupt changes in signal intensity were also then investigated using tsdiffana software, which assesses signal intensity between slices. I elected not to perform scrubbing, which removes outliers in rs-fMRI images, as this is subjective and based on arbitrary cut-offs. Visual QC was also performed at all subsequent stages in the pipeline to ensure artefacts were not introduced.

2.5.4.3. Preprocessing

Segmentation of the anatomical native space T1 image was performed using the VBM8 toolbox (http://dbm.neuro.uni-jena.de/vbm) in SPM8 (http://www.fil.ion.ucl.ac.uk/spm/software/spm8) run in MATLABv8.3. Using this approach the T1 image is segmented into WM, GM and CSF based on signal intensities of different tissue types. The first four rs-fMRI images were discarded to allow for steady state equilibrium and images were realigned. During the realignment of images 6 motion parameters encompassing translations and rotations in the major planes are generated and regressed out during the noise correction procedures documented below. Following realignment co-registration was performed between the T1 GM segmentation and rs-fMRI images to ensure all images were in a common space.

2.5.4.4. Physiological noise correction

Options for physiological noise correction include band pass filtering and regression of white matter, CSF and global signal. More recently concerns regarding global signal regression (Carbonell et al. 2014) have led to more conservative approaches were only the principal components of white matter and CSF signals are regressed. This is referred to the anatomical CompCor method (Behzadi et al. 2007). Wavelet decomposition has also been

used in order to remove signal attributable to physiological noise. Using this approach the signal is broken down into its underlying constituent frequencies.

For the analyses presented in chapters 3 and 4 processing steps were implemented using the CONN functional connectivity toolbox version 14 (https://www.nitrc.org/projects/conn/) using SPM 8 and MATLABv8.3 (Whitfield-Gabrieli and Nieto-Castanon, 2012). Regression of noise ROIs (without global signal regression), band-pass filtering and the calculation of bivariate correlations were performed as this processing strategy has been shown to produce the most reliable graph theory measures (Andellini et al., 2015; Aurich et al., 2015; Liang et al., 2012).

2.5.4.5. Functional connectome construction

Following correction for physiological noise an average BOLD time series was calculated from the voxels contained in each Freesurfer ROI. Bivariate-correlation coefficients were calculated by extracting the average BOLD time series for each Freesrufer ROI pair across the 76 brain regions (resulting in 2,850 possible functional connections). A Fisher transform was then applied in order to normalise the data. This resulted in a 76x76 symmetrical undirected functional connectivity matrix for each participant. The use of bivariate correlations has disadvantages in that one is unable to tell if a connection between two nodes is direct or due to influence of another node. This can be overcome by using partial correlations that take into account the influence of other nodes. However the calculation of partial correlations in rs-fMRI data is non-trivial and requires additional statistical processing. Furthermore partial correlations based networks tend to have lower test retest reliability (Liang et al., 2012). Subsequent steps including thresholding and generation of graph theory metrics differ between chapters and will therefore be covered in the methods section for each experiment. See figure 2.7 for an overview of structural and functional connectome pipelines.

Figure 2.7. Resting state fMRI and diffusion tractography processing pipelines. BET = brain extraction tool; CONN = functional connectivity toolbox; CSD = constrained spherical deconvolution; DTI = diffusion tensor imaging; FA = fractional anisotropy; fODF = fibre orientation distribution function; GM = grey matter; QC = quality control, WM = white matter; SPM = statistical parametric mapping.

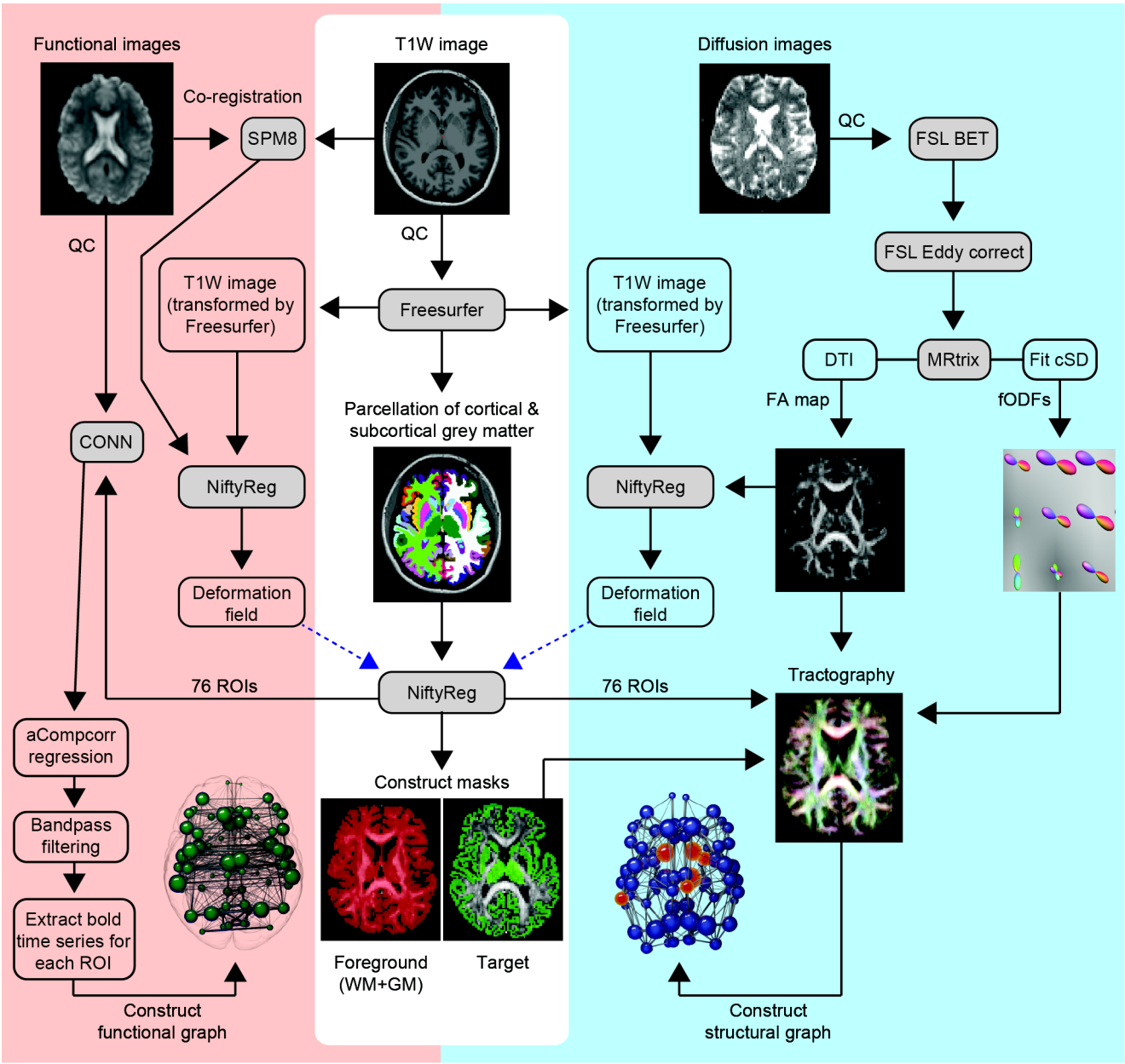

2.6. Cohorts

Structural, diffusion and rs-fMRI and clinical data from the Track-HD and Track-On HD studies were used in the studies detailed in this thesis. For Track-HD only data from the Track-HD 36-month time-point was used, while data from all three visits of Track-On HD were analysed. For all studies included in this thesis left-handed or ambidextrous participants were excluded from the analyses to avoid confounding effects caused by differences in structural connectivity in those who are right hemisphere dominant.

2.6.1. Track-HD

The Track-HD study is a multi-centre longitudinal observational study designed to identify biomarkers for clinical trials (Tabrizi et al., 2009). Data was collected over 4 annual visits between 2008 and 2011 in 4 sites: London (UK), Leiden (Netherlands), Paris (France) and Vancouver (Canada). This included structural MRI data, and extensive clinical data on cognitive, motor and psychiatric assessments. Diffusion MRI data was only collected at sites: London, Leiden and Paris for the 24-month and 36-month time points. At baseline the cohort consisted of 366 participants, including 123 controls, 123 HD and 120 preHD. At 36-month follow-up 97 controls, 94 preHD and 108 early HD completed the study (Tabrizi et al., 2013). Written and informed consent was obtained from all subjects who meet inclusion criteria. The study was approved by local ethics committees. Inclusion and exclusion criteria were defined as follows:

All subjects

- Aged between 18 and 65 years
- Ability to tolerate MRI and biosample collection
- Absence of major psychiatric disorder or history of significant head injury at the time of enrollment
- Subjects were not excluded based on medication usage, unless actively part of an experimental therapeutic trial
- Comorbid medical conditions were noted, but unless they prevented subject assessment were not considered exclusions

Controls

- Age and gender matched to individuals in preHD/HD group and were selected from the partners or spouses of individuals with preHD/HD or were gene negative siblings, to ensure consistency of environments with carriers of the *HTT* expansion

PreHD/Early HD

- Undergone voluntary genetic testing with a CAG repeat length ≥ 40 (confirmed by post-recruitment blood sample)
- PreHD: Disease burden of pathology (calculated by (CAG-35.5) X age (Penney et al., 1997)) > 250. In order to increase the yield of disease related changes. This approximates to ~15 years to estimated disease onset
- PreHD: UHDRS TMS ≤ 5
- Early HD: Motor features consistent with HD and a diagnostic confidence score of 4 on the UHDRS
- Early HD: Shoulson and Fahn stage 1 or 2 assessed according to the UHDRS Total functional capacity (Shoulson and Fahn, 1979) (i.e. TFC ≥ 7)

2.6.2. Track-On HD

Track-On HD was designed to investigate compensatory mechanisms that allow *HTT* expansion gene carriers to maintain normal cognitive and motor performance in the context of grey and white matter brain atrophy as noted in the Track-HD study (Tabrizi et al., 2013). Data was collected over 3 annual time-points between 2012-2014 in 4 sites: London (UK), Leiden (Netherlands), Paris (France) and Vancouver (Canada). This included structural MRI, diffusion MRI, task and rs-fMRI data. Extensive clinical data on cognitive, motor and psychiatric assessments was also collected. The baseline cohort included 243 participants, including 112 controls, 110 preHD and 21 early HD. Most preHD and control participants were recruited from the Track-HD study. Newly recruited preHD participants were required to have a CAG repeat length ≥ 40 and a disease burden score greater than 250 at recruitment. Inclusion and exclusion criteria were the same as those defined in Track-HD (Tabrizi et al., 2009). See (Kloppel et al., 2015) for further details.

2.7 MRI acquisition

2.7.1 MRI Acquisition Track-HD

3T MRI data were acquired were acquired on Siemens (London and Paris) and Philips (Leiden) 3T MRI scanners. Scanning time was approximately 10 minutes for T1-weighted and 9 minutes for diffusion weighted acquisitions.

Head coil information: Siemens Tim Trio 3T (London/Paris) - 12 channel head matrix with HEA (head coil element anterior)/HEP (head coil element posterior) coils selected; Philips Achieva 3T (Leiden) - 8 channel SENSE (SENSitivity Encoding) head coil.

Structural T1: T1-weighted image volumes were acquired using a 3D MPRAGE acquisition sequence on 3.0 T Siemens (London and Paris) and Phillips (Leiden) whole body imager with the following imaging parameters: TR = 2200ms (Siemens); 7.7ms (Philips); TE=2.2ms (Seimens); 3.5ms (Philips); flip angle =10◦ (Seimens); 8◦ (Philips); FOV= 28cm (Seimens); 24cm (Philips); matrix size 256x256 (Seimens); 224x224 (Philips), 208 (Seimens); 164 (Philips) sagittal slices to cover the entire brain with a slice thickness of 1.0 mm with no gap.

Diffusion: Diffusion-weighted images with 42 unique gradient directions (b=1000 sec/mm^2) were collected with either seven images (Siemens) with no diffusion weighting or one image with no diffusion weighting (Phillips). For scans collected in London, dimensions were 128 pixels × 96 pixels × 65 slices per volume, with TE=84ms and TR=7600ms; for Paris, dimensions were 128 pixels × 128 pixels × 75 slices per volume, with TE=88ms and TR=13100ms and for Leiden, dimensions were 112 pixels × 112 pixels × 55 slices per volume, with TE=56ms and TR=8078ms. Voxel size for Siemens scans was 2x2x2mm^3 and for Phillips 1.96 x 1.96 x 2mm^3.

2.7.2 MRI Acquisition Track-On HD

3T MRI data were acquired on two different scanner systems (Philips Achieva at Leiden and Vancouver and Siemens TIM Trio at London and Paris). Scanning time was approximately 12 minutes for T1-weighted, 10 minutes for diffusion-weighted acquisitions and 15 mins for rs-fMRI.

Head coil information: 3T MRI data were acquired on two different scanner systems (Philips Achieva at Leiden and Vancouver and Siemens TIM Trio at London and Paris), both using a 12-channel head coil.

Structural T1: T1-weighted image volumes were acquired using a 3D MPRAGE acquisition sequence with the following imaging parameters: TR = 2200ms (Siemens)/ 7.7ms (Philips), TE=2.2ms (S)/3.5ms (P), FA=10◦ (S)/8◦(P), FOV= 28cm (S)/ 24cm (P), matrix size 256x256 (S)/224x224 (P), 208 (S)/164 (P) sagittal slices to cover the entire brain with a slice thickness of 1.0 mm with no gap. In this protocol, a volumetric T2-weighted image (SPACE sequence in Siemens, VISTA in Philips) was acquired with the identical field of view, acquisition matrix, and slice thickness as the T1-weighted images, to provide complementary multispectral information for some methods of analysis.

Diffusion: Diffusion-weighted images were acquired with 42 unique gradient directions (b = 1000 sec/mm^2). Eight images with no diffusion weighting (b = 0 sec/mm^2) and one image with no diffusion weighting (b = 0 sec/mm^2) were acquired from the Siemens and Philips scanners respectively. For the Siemens scanners, TE = 88ms and TR = 13s; for the Phillips scanners, TE = 56ms and TR = 11s. Voxel size for the Siemens scanners was 2 x 2 x 2 mm and for the Phillips scanners 1.96 x 1.96 x 2. 75 slices were collected for each diffusion-weighted and non-diffusion weighted volume.

Resting state: For rs-fMRI, 165 whole-brain volumes were acquired at a repetition time of 3s using a T2*-weighted echo planar imaging (EPI) sequence with the following parameters: TE 30ms, FOV 212mm, flip angle

80°, 48 slices in ascending order (slice thickness: 2.8mm, gap: 1.5mm, in plane resolution 3.3 x 3. mm) and bandwidth of 1906 Hz/Px. Field maps were acquired with TR 1020 ms, TE1 10.0 ms, TE2 12.46 ms, FOV 212 mm and 2 mm slice thickness. All data were visually inspected by IXICO. Standardization of data acquisition across sites were performed based on previous suggestions (Glover et al., 2012).

Chapter 3. White matter predicts functional up-regulation in premanifest HD

3.1. Introduction

In chapter 1 of this thesis I reviewed the work by Seeley and colleagues (Seeley et al., 2009; Zhou et al., 2012) who showed that regional grey matter atrophy in neurodegenerative disease does not occur randomly but in a stereotyped fashion. These disease-specific patterns of structural change arise from the functional connectivity of the healthy human brain. Specifically, brain regions with stronger connections to distant regions and fewer connections to neighbouring regions in a healthy brain show greater grey matter loss in patients with Alzheimer's disease, frontotemporal dementia and corticobasal syndrome (Zhou et al., 2012). Subsequent studies have demonstrated a similar relationship between structural connectivity of the healthy brain and atrophy patterns in Alzheimer's (Raj et al., 2012) and Parkinson's disease (Zeighami et al., 2015). This suggests that organisation principles of healthy brain networks govern the stereotyped patterns of atrophy seen in neurodegenerative disease.

HD is a fully penetrant monogenic neurodegenerative disorder. As the timing of clinical onset can be predicted with certainty it provides a unique opportunity to study the earliest structural and functional changes in the brain occurring years before clinical onset in preHD (Ross et al., 2014). The first study examining changes in white matter (structural) brain networks in HD revealed loss of structural connectivity in a fronto-parietal-striatal network in preHD relative to controls, with more extensive connectivity loss occurring in manifest HD. These changes correlated with cognitive and motor deficits (Poudel et al., 2014b). Alterations of functional brain networks have also been demonstrated in preHD. As disease burden increases reduced connectivity is seen in fronto-striatal connections, while increased connectivity is seen frontal-posterior connections. This has lead to the suggestion that increased connectivity may be a compensatory mechanism that prevents the emergence of symptoms in the preHD stage, even in the context of brain atrophy (Harrington et al., 2015). Indeed a subsequent study in preHD, using a compensation model, showed that increased coupling of the right

dorsolateral prefrontal cortex and a left hemisphere network was predictive of cognitive performance as atrophy increased (Kloppel et al., 2015).

In this chapter of my thesis I aim to investigate how these structural and functional brain network changes in preHD relate to the organisation of the healthy white matter brain network. Understanding such a relationship is critical to understanding the link between brain structure and function in neurodegeneration. It is changes in white matter connectivity and functional coupling between brain areas that underlies behavioural change. A model of neurodegeneration in HD where reduction in white matter connections between brain areas is always associated with loss of functional connections and consequent behavioural change may be too simple. Some brain regions may show increased functional coupling as a compensation for regional grey and white matter loss in order to maintain sensory, cognitive or motor function (Harrington et al., 2015; Kloppel et al., 2015). Therefore it is important to determine whether there are organisation principles of the healthy white matter brain network underlying changes in structural and functional connectivity between brain areas in preHD.

In order to test the hypothesis that changes in white matter connectivity and functional coupling in preHD relate to the organisation of the healthy white matter brain network I studied a large and well characterized cohort of preHD patients from the Track-On HD study (Kloppel et al., 2015). Using graph theoretical measures I characterised the organisation of healthy white matter. Brain regions with strong connections to distant regions were defined by high levels of centrality, using the graph theory metrics degree, betweenness centrality and eigenvector centrality. Conversely brain regions with strong connections to their neighbours were defined by high clustering coefficients. Based on the observations by (Zhou et al., 2012) I tested the hypothesis that regions with stronger connections to distant regions in the healthy brain would show white matter connectivity loss, while those with stronger connections with their neigbours would show increases in functional connectivity, in preHD relative to controls. As brain regions with stronger connections to distant regions are more susceptible to atrophy (Seeley et al., 2009) I modelled functional connectivity in terms of up-regulation and down-regulation. Up-regulation was defined when functional connectivity increased in highly connected regions and down-regulation was defined when connectivity decreased in highly connected regions, in preHD relative to controls.

I found evidence in support of my hypothesis. Furthermore I found up-regulation of functional connectivity in anterior brain regions. While in more posterior regions down-regulation of functional connectivity was seen. These findings were confirmed by demonstration of a gradient of functional regulation along the antero-posterior axis. This striking antero-posterior dissociation of functional coupling in individuals with preHD provides new evidence concerning the potential for compensation in pre-clinical neurodegeneration.

3.2. Materials and Methods

3.2.1. Cohort

The cohort included participants from the first visit of the Track-On HD study from all sites (London, England; Leiden, Netherlands; Paris, France; and Vancouver, Canada) (Kloppel et al., 2015). Of the participants included, 31 preHD and 29 controls had participated previously in Track-HD. From a total Track-On HD cohort of 243, participants were excluded (see chapter 2 for detailed inclusion/exclusion criteria) due to; manifest disease (21), left handed or ambidextrous (24), poor quality fMRI data (11) and poor quality diffusion weighted imaging (DWI) data (36). To age-match the remaining cohort 21 participants <30 and > 60 years of age were excluded. This left a cohort of 64 preHD individuals and 66 healthy controls described in Table 3.1.

Table 3.1. Functional up-regulation study: Patient demographics. N – participant number, SD – standard deviation, M – male, F – female, ISCED = International standard classification of education, CAG – CAG repeat length, DBS – disease burden score, CPO – cumulative probability of onset.

	PreHD	Control	Statistical test	P-value
N	64	66	-	-
Age (SD)	43.5 (8)	45.5 (7.5)	2 tail t-test	0.15
Gender (M/F)	35/29	26/40	Chi-square	0.081
ISCED (2/3/4/5/6)	3/13/22/24/1	5/11/21/27/2	Chi-square	0.851
Study Site (N) (Leiden/London/Paris/Vancouver)	11/24/16/13	15/24/17/10	Chi-square	0.8
CAG (SD)	42.67 (2.03)	-	-	-
DBS (SD)	300.3 (53.6)	-	-	-
CPO (SD)	0.24 (0.15)	-	-	-

3.2.2. Construction of structural and functional connectivity matrices

Diffusion tractography and resting state fMRI was performed as detailed in chapter 2. For structural connectivity matrices ROIs were defined as connected if a fibre originated in ROI 1 and terminated in ROI 2. For functional matrices ROIs were defined as functionally connected if there was a correlation between the time series of ROI 1 and ROI 2. Structural connections were weighted by streamline count, while functional connections were weighted by magnitude of correlation. Connections were then combined into 76x76, undirected and weighted matrices. Thresholding was applied in order to remove weak spurious connections (Rubinov and Sporns, 2010). For both structural and functional connectivity matrices only those connections present in 75% of control participants with retained, consistent with thresholding strategies used in the literature (van den Heuvel and Sporns, 2011; van den Heuvel et al., 2013).

3.2.3. Structural hub regions

Structural hub regions were defined to enable interpretation of the role of hub regions in the subsequent functional regulation analysis. Hubs were defined as the top 12 brain regions with highest degree for the group averaged control brain-network in keeping with previous studies (van den Heuvel and Sporns, 2011; van den Heuvel et al., 2013).

3.2.4. Calculation of graph theory metrics

All graph theory metrics were calculated using the brain connectivity toolbox (Rubinov and Sporns, 2010).. Graph theory metrics have been discussed in detail in chapter 1. Degree, defined as the as the number of binary connections to a brain region, was calculated for the control averaged structural connectivity matrix to define structural hub regions. Graph theory strength, defined as the sum of weighted connections for each brain region, was calculated for the analyses using healthy white matter to predict functional and structural connectivity changes, in preHD relative to controls, and for the antero-posterior (A-P) analysis.

3.2.5. Characteristics of healthy white matter organisation

To define healthy white matter organization degree, clustering coefficient, betweenness centrality and eigenvector centrality were calculated for each brain region. Clustering coefficient is the fraction of brain regions neighbours that are also neighbours of each other. Betweenness centrality is defined as the fraction of shortest paths in the network that pass through a given brain region. Eigenvector centrality is a self-referential measure that assigns a high level of importance to brain regions if they are connected to other highly connected brain regions (see figure 3.1. for a schematic representation of graph theory measures). Please refer to chapter 1 for further discussion of graph theory metrics. These metrics were calculated for the un-weighted average control white matter brain-network. Streamline weighting was not included to allow direct comparison with structural and functional modalities.

Figure 3.1. Schematic description of graph theory metrics. (a) Degree is the number of connections a brain region has. (b) Clustering coefficient indicates how highly connected a region is to its neighbours and (c) Betweeness centrality represents brain region network traffic. (d) Eigenvector centrality represents network traffic along the brains 'busiest' pathways. Black circles represent regions with high degree, clustering coefficient, betweeness centrality or eigenvector centrality. These graph theory metrics correspond to the graph metrics on the y-axis of figures 2, 3 and 4.

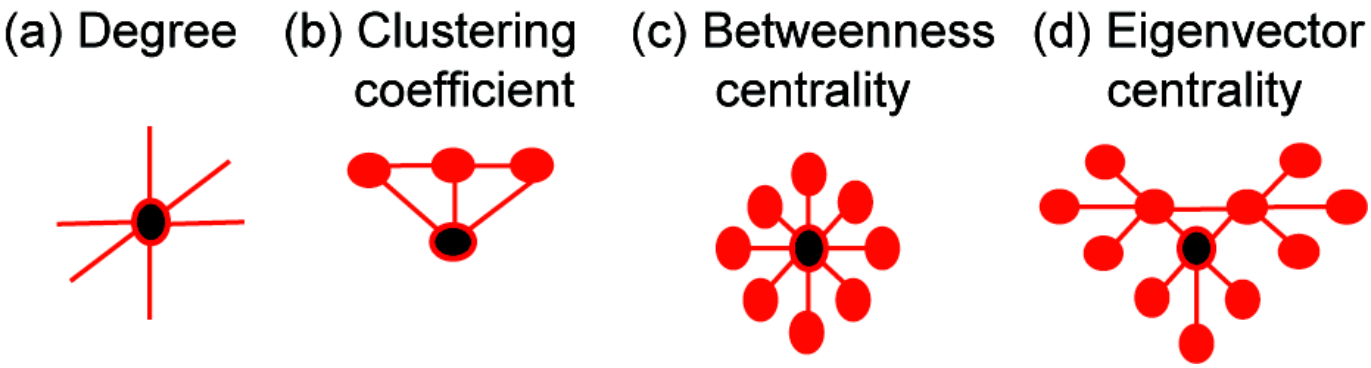

3.2.6. Prediction of structural and functional change using healthy white matter organization

Correlations were performed against both functional regulation coefficients (calculation of functional regulation coefficients is detailed below) and functional strength for each brain region and their corresponding graph theory metrics in the average control white matter brain network; degree, clustering coefficient, betweenness centrality and eigenvector centrality. A Bonferroni correction ($p<0.0125$) was applied for multiple comparisons. To allow comparison between structural and functional changes correlations were also performed between structural strength for each brain region and their corresponding graph theory metrics in the average control white matter brain-network as outlined above. Similarly a Bonferroni correction ($p<0.0125$) was applied for multiple comparisons.

3.2.7. Split-site and 'off medication' analyses

To establish whether my findings were influenced by study site a split-site analysis was carried out. Sites were paired based on type of MRI scanner; London-Paris (Siemens) (40 preHD individuals and 41 healthy controls) and Leiden-Vancouver (Philips) (24 preHD individuals and 25 healthy controls). As psychoactive medications influence brain activation in fMRI studies (Viviani et al., 2014) I also performed a control analysis in only those off psychoactive medications for more than 6 months. Patients excluded from the 'off medication' cohort included 2 taking anti-psychotics, 16 taking selective serotonin reuptake inhibitors, 1 taking a serotonin-noradrenaline reuptake inhibitor, 1 taking bupropion, 5 taking benzodiazepines, 2 taking tri-cyclic anti-depressants and 1 taking melatonin. This resulted in a cohort of 43 preHD individuals and 59 controls.

3.2.8. Functional regulation analysis

I introduce the 'functional regulation coefficient' as a summary measure of the relative change in functional connectivity of a pair of brain regions comparing preHD with healthy controls. This was calculated as follows; an averaged control and an averaged preHD functional connectivity matrix were created. Subtracting the averaged preHD matrix from the averaged control matrix then created a difference matrix. For each brain region, the magnitude of a connection in the average control matrix was correlated against the magnitude of that connection in the difference matrix. Up-regulation was defined as a positive correlation (stronger control connections show greater increases in preHD), whereas down-regulation was defined as a negative correlation (stronger control connections show greater decreases in preHD). For example if region 3 was connected to regions 5, 26 and 74, magnitude of connections for region pairs 3-5, 3-27 and 3-74 for averaged controls were plotted against the differences in those connections (average preHD– average controls). This provides a measure of how much the functional connectivity with a brain region is modified in preHD as a function of the pre-existing functional connectivity in healthy control brains. A Bonferroni correction ($p < 0.0007$) was then applied to account for the 76 brain regions tested.

3.2.9. Antero-Posterior (A-P) analysis

I investigated the spatial distribution of relative changes in functional connectivity across the brain by calculating the correlation between A-P axis coordinates of each brain region and its corresponding functional regulation coefficient. To investigate whether any relationship was common to changes in both structural and functional connectivity, correlations were also performed against A-P axis co-ordinate and functional and structural (graph theory) strength. A Bonferroni correction ($p < 0.017$) was applied to account for multiple testing.

3.3. Results

3.3.1. Healthy white matter organization and structural connectivity loss in preHD vs. controls

There were significant correlations ($df = 74$) between decreases in structural strength and degree (Rho = 0.45, $p = 3.94 \times 10^{-5}$); clustering coefficient (Rho = -0.35, p = 0.0023); betweenness centrality (Rho = 0.31, p = 0.0074) and eigenvector centrality (Rho = 0.43, $p = 1.1 \times 10^{-4}$). All correlations survived Bonferroni-correction ($p < 0.0125$) for number of graph theoretic measures (see figure 3.2.). This indicates that specific features of healthy white matter organization can predict decreases in corresponding structural connectivity in preHD relative to healthy controls.

Figure 3.2. Prediction of structural strength decrease based on healthy white matter organization. Regions with (a) high degree, (b) low clustering and (c,d) low network traffic (betweenness and eigenvector centrality) show greatest decrease in structural connectivity strength in preHD. Each data point represents a brain region in the Freesurfer Desikan atlas. The graph theory metric value of a brain region in the average control WM brain network, on the y-axis, is plotted against the difference in structural graph theory strength (controls – preHD) for that corresponding brain region, on the x-axis. The red line represents a least squares linear regression line. Rho = correlation coefficient, P = p-value, DF = degrees of freedom.

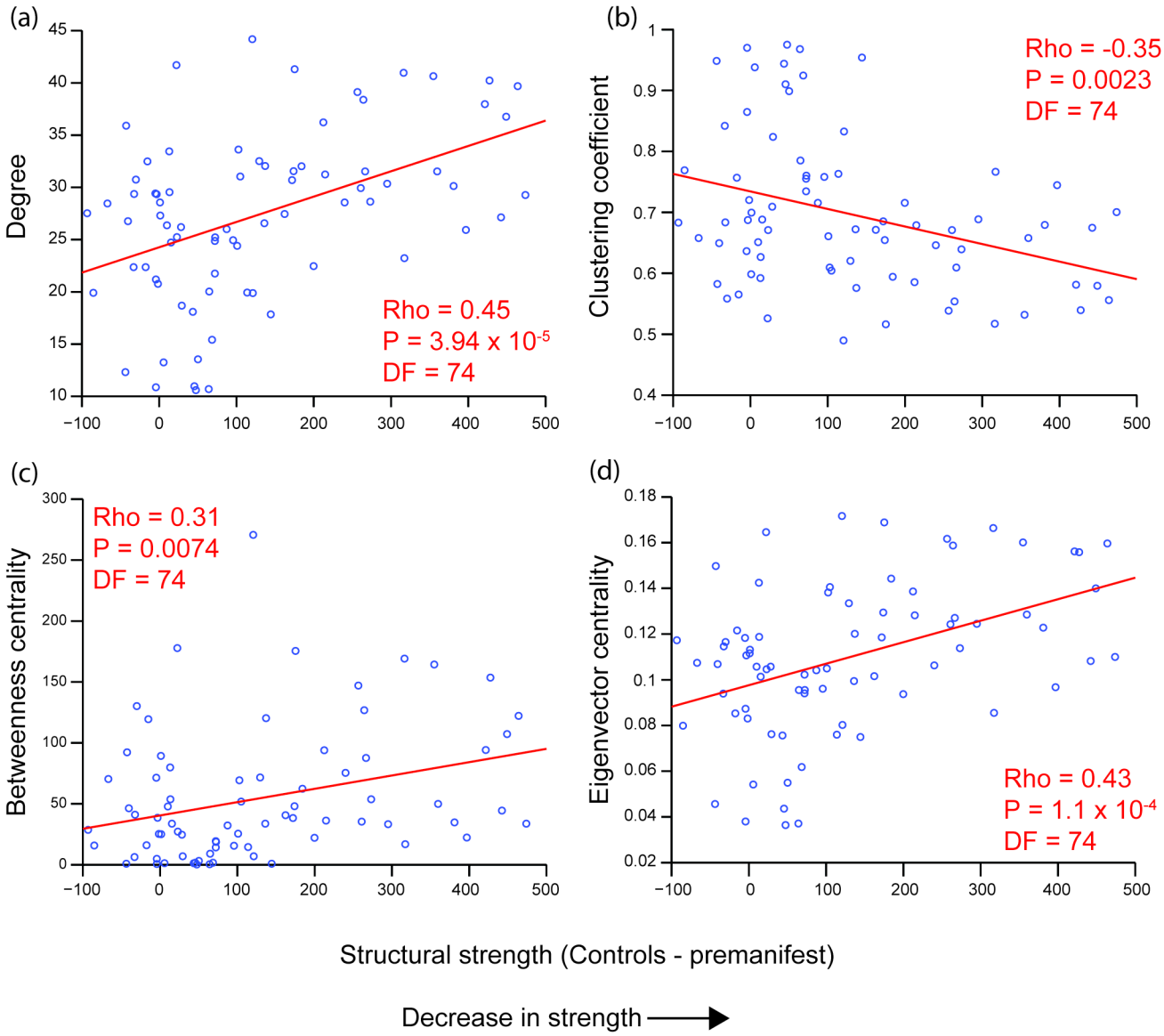

3.3.2. Healthy white matter organization and functional connectivity increase in preHD vs. controls

There were significant correlations (*df* = 74) between the regulation coefficient and degree (Rho = -0.45, p = $3.66x10^{-5}$); clustering coefficient (Rho = 0.5, p = $3.9x10^{-6}$); betweenness centrality (Rho = -0.29, p = 0.01) and eigenvector centrality (Rho = -0.48, p = $1.21x10^{-5}$). See figure 3.3. Similar patterns were seen for correlations between functional strength (df = 74) and degree (Rho = -0.36, p = 0.0016); clustering coefficient (Rho = 0.36, p = 0.0014) and eigenvector centrality (Rho = -0.38, p = $6x10^{-4}$). There was no significant correlation between functional strength and betweenness centrality (Rho = -0.19, p = 0.0948). All significant correlations survived Bonferroni-correction ($p < 0.0125$) for number of graph theoretic measures. See figure 3.4. This indicates that as with structural neurodegeneration, specific features of healthy white organisation can predict corresponding inter-regional increases in functional connectivity in preHD relative to healthy controls.

Figure 3.3. Prediction of functional up-regulation based on healthy white matter organization. Regions with (a) low degree, (b) high clustering and (c,d) low network traffic (betweenness and eigenvector centrality) show greatest functional up-regulation in preHD. Each data point represents a brain region in the Freesurfer Desikan atlas. The graph theory metric value of a brain region in the average control WM brain network, on the y-axis, is plotted against the functional regulation coefficient for that corresponding brain region, on the x-axis. The red line represents a least squares linear regression line. Rho = correlation coefficient, P = p-value, DF = degrees of freedom.

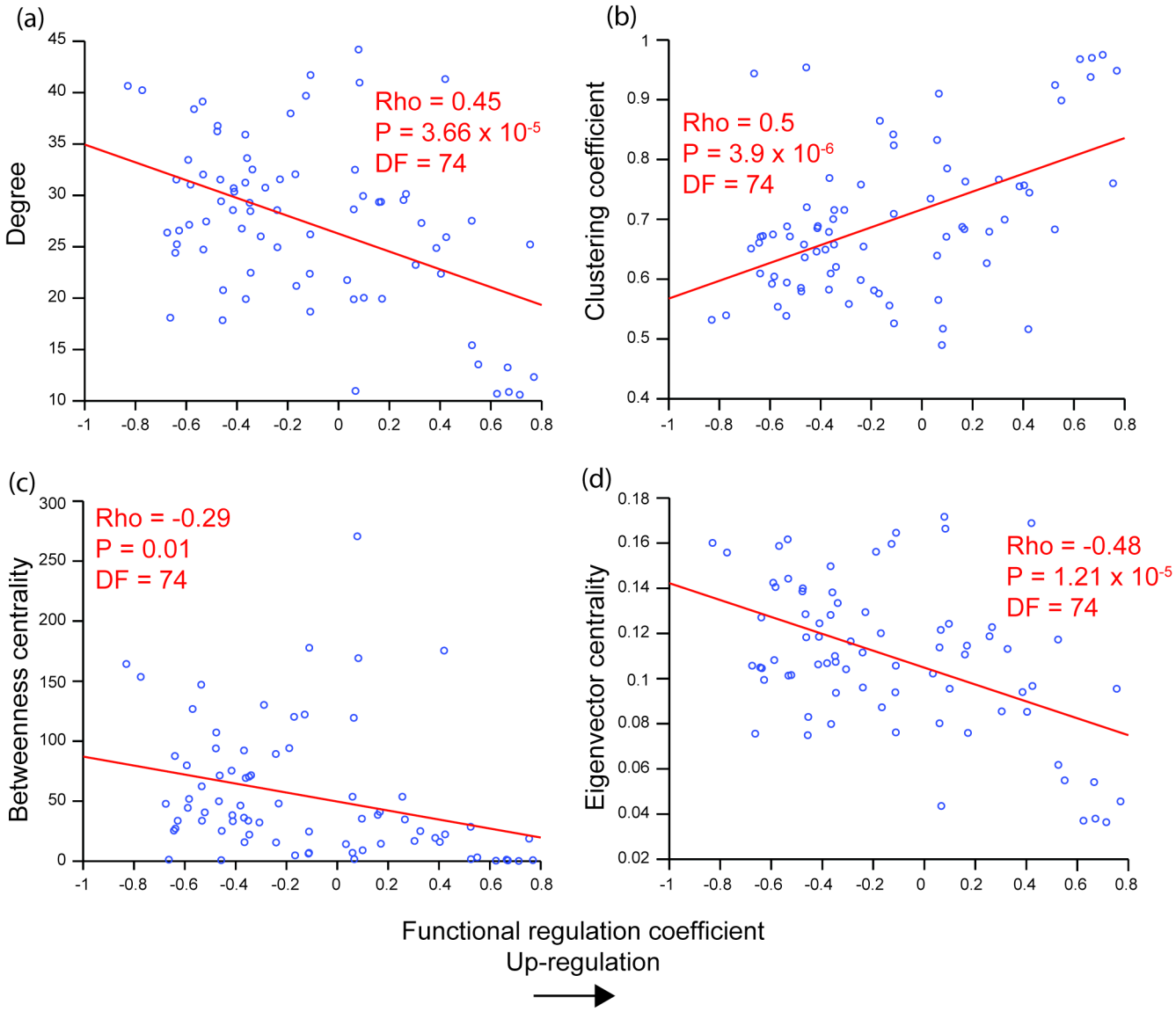

Figure 3.4. Prediction of functional strength increase based on healthy white matter organisation. Regions with (a) low degree, (b) high clustering and (c,d) low network traffic (eigenvector centrality) show greatest increase in functional connectivity strength in preHD. Each data point represents a brain region in the Freesurfer Desikan atlas. The graph theory metric value of a brain region in the average control WM brain network, on the y-axis, is plotted against the difference in functional graph theory strength (preHD - controls) for that corresponding brain region, on the x-axis. The red line represents a least squares linear regression line. Rho = correlation coefficient, P = p-value, DF = degrees of freedom. Red text = significant results, black text = non-significant results.

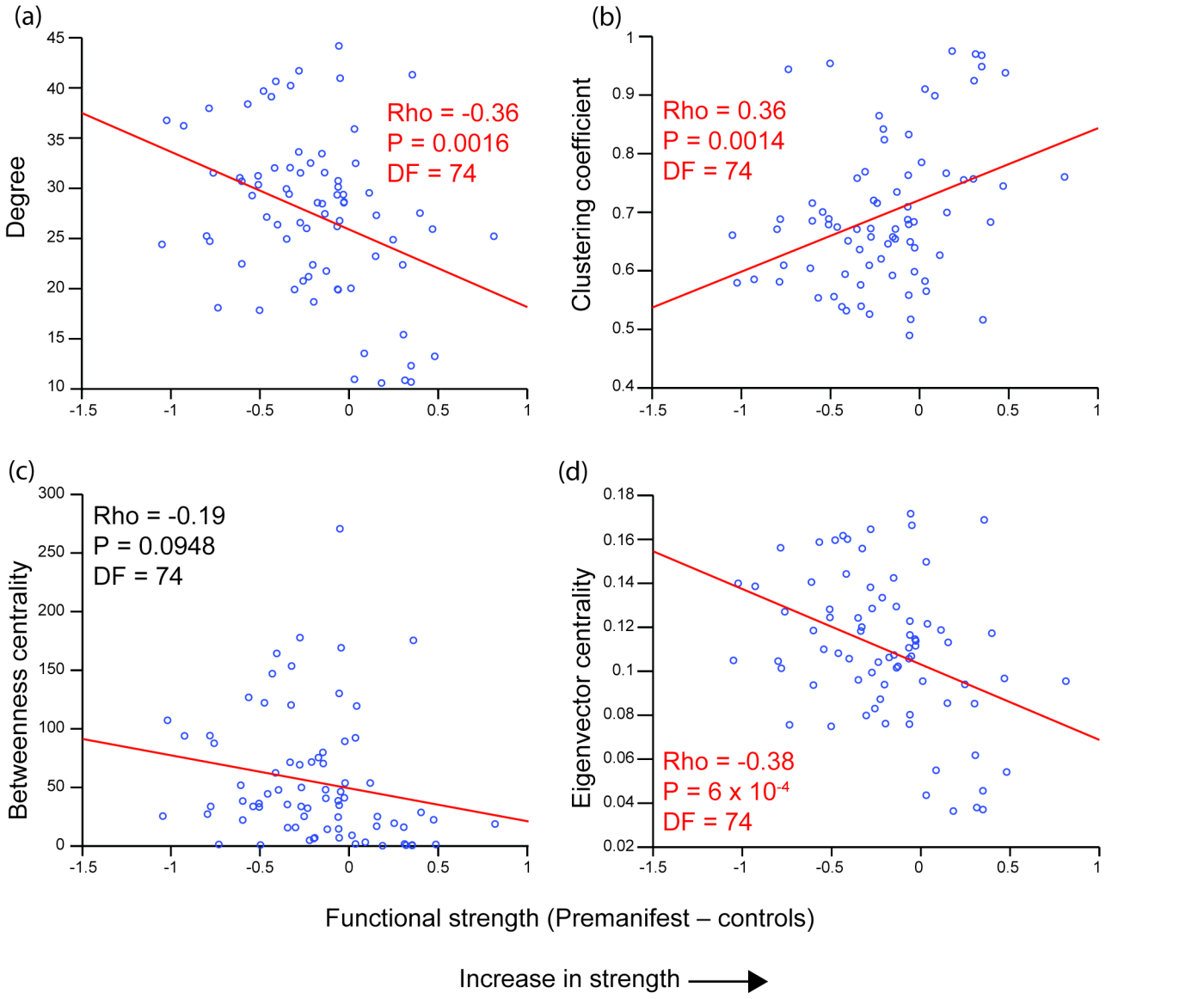

3.3.3. Split-site and 'off medication' analyses

Correlations between graph metrics and structural strength, functional strength and functional regulation for split-site and 'off medication' cohorts revealed qualitatively similar findings with the exception of betweenness centrality (see table 3.2.). Thus neither site nor medication status affected the results reported here.

Table 3.2. Split-site analyses and Off medication analyses. (a) Structural strength (b) Functional (c) Functional strength. Rho = correlation coefficient

(a) Structural strength	**Degree (Rho)**	**Clustering coefficient (Rho)**	**Betweeness centrality (Rho)**	**Eigenvector centrality (Rho)**
Off medication	0.45	-0.33	0.36	0.41
Leiden-vancouver	0.22	-0.23	0.12	0.21
London-paris	0.43	-0.26	0.27	0.43

(b) Functional regulation				
Off medication	-0.47	0.49	-0.26	-0.48
Leiden-vancouver	-0.32	0.3	-0.11	-0.39
London-paris	-0.33	0.38	-0.3	-0.3

(c) Functional strength				
Off medication	-0.32	0.31	-0.16	-0.33
Leiden-vancouver	-0.17	0.19	-0.02	-0.21
London-paris	-0.33	0.34	-0.27	-0.33

3.3.4. Functional regulation in preHD relative to controls

While the functional regulation of all brain regions were tested, structural hub regions were investigated specifically in order to investigate whether these regions showed 'up-regulation' (positive functional correlation coefficient) or 'down-regulation' (negative functional correlation coefficient). Hub regions included the caudate, thalamus, superior frontal, precentral, precuneus and insula bilaterally (see figure 3.5.). Only anterior non-hub regions, with the exception of the left superior frontal, showed functional up-regulation (an increase in functional connectivity in preHD relative to controls) while predominantly posterior regions, including the caudate, precuneus and insula hubs (bilaterally) showed functional down-regulation. The functional regulation of all significant hub and non-hub regions is shown in figure 3.6. along with example scatter plots for the top regions showing up-regulation and down-regulation. See table 3.3 for a list of all significant functional regulation coefficients.

Figure 3.5. Structural hub regions (red –hub, blue – non-hub), defined in order to highlight the role of structural hubs in the functional regulation analysis. Hub region classification based on brain regions with the highest degree in the healthy white matter brain network.

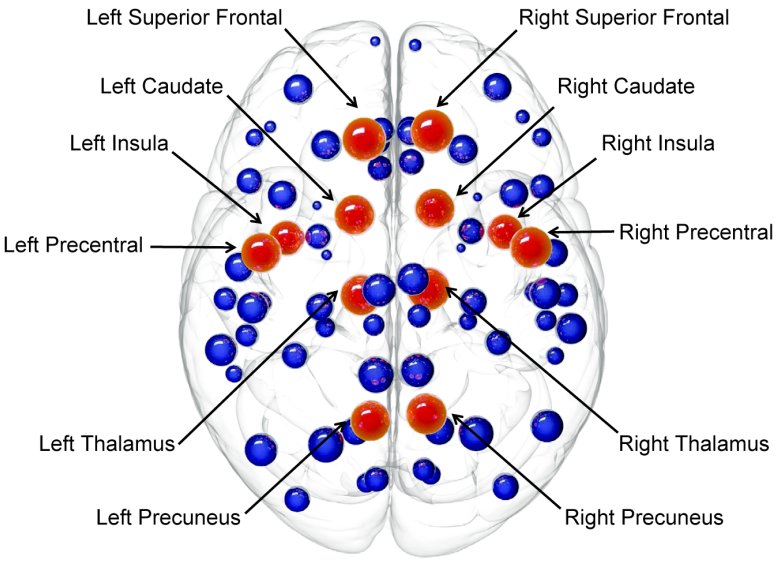

Figure 3.6. Functional regulation analysis. For each brain region in the average control network, correlations were performed against the strength of functional connection to all other 75 regions in the network (where a functional connection was present) and average group differences (preHD minus controls) in these functional connections. Up-regulation is defined as a positive correlation (stronger control connections show greater increases in preHD), whereas down-regulation is defined as a negative correlation (stronger control connections show greater decreases in preHD). Brain regions that show significant positive (green) and negative (purple) correlations are highlighted. The size of the sphere represents the number of structural connections (thus largest spheres indicate hub brain regions). Correlation plots showing the brain regions with the most significant positive (green) and negative (purple) correlations are also displayed below. For each plot each data point represents a connection to the brain region specified. The strength of that connection for the avaerage control network, on the y-axis, is plotted against the difference (preHD minus controls) of that connection's strength on the x-axis. The red line represents a least squares linear regression line. Rho = correlation coefficient, P = p-value, DF = degrees of freedom.

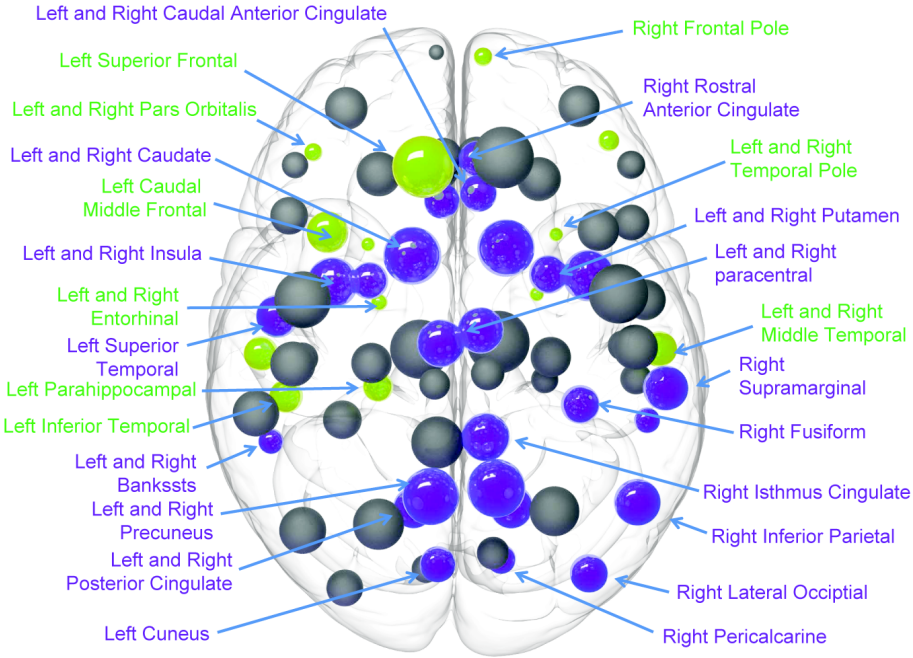

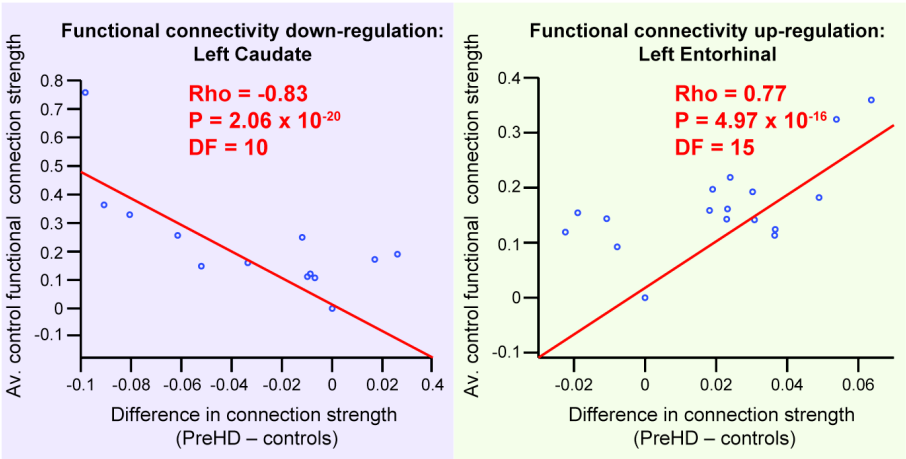

Table 3.3. Functional regulation analysis: Regional correlations. Related to figure 6. Rho = correlation coefficient, P = p-value. Brain regions derived from the Freesurfer Desikan-Killiany atlas (37).

Up-regulation			**Down-regulation**		
Region	**Rho**	**P**	**Region**	**Rho**	**P**
L.entorhinal	0.77	4.97×10^{-16}	L.caudate	-0.83	2.06×10^{-20}
L.middletemporal	0.75	3.52×10^{-15}	R.caudate	-0.77	2.79×10^{-16}
R.temporalpole	0.71	4.64×10^{-13}	R.rostralanteriorcingulate	-0.67	2.35×10^{-11}
R.entorhinal	0.67	3.21×10^{-11}	R.bankssts	-0.66	6.96×10^{-11}
L.parsorbitalis	0.67	5.10×10^{-11}	L.caudalanteriorcingulate	-0.64	3.99×10^{-10}
L.temporalpole	0.62	1.75×10^{-09}	R.lingual	-0.64	5.43×10^{-10}
R.frontalpole	0.55	2.51×10^{-07}	R.caudalanteriorcingulate	-0.64	6.45×10^{-10}
R.parsorbitalis	0.53	1.07×10^{-06}	L.putamen	-0.63	1.29×10^{-09}
L.caudalmiddlefrontal	0.53	1.11×10^{-06}	R.isthmuscingulate	-0.59	1.78×10^{-08}
R.middletemporal	0.42	1.32×10^{-04}	R.lateraloccipital	-0.59	2.34×10^{-08}
L.superiorfrontal	0.42	1.56×10^{-04}	R.posteriorcingulate	-0.58	3.10×10^{-08}
L.parahippocampal	0.40	3.06×10^{-04}	L.precuneus	-0.57	8.25×10^{-08}
L.inferiortemporal	0.39	5.79×10^{-04}	R.precuneus	-0.54	6.39×10^{-07}
			L.posteriorcingulate	-0.53	6.84×10^{-07}
			L.cuneus	-0.53	7.22×10^{-07}
			R.putamen	-0.52	1.35×10^{-06}
			L.insula	-0.48	1.26×10^{-05}
			R.insula	-0.48	1.36×10^{-05}
			R.inferiorparietal	-0.47	2.23×10^{-05}
			L.lingual	-0.46	2.54×10^{-05}
			L.bankssts	-0.46	3.31×10^{-05}
			R.pericalcarine	-0.46	3.63×10^{-05}
			R.fusiform	-0.42	1.88×10^{-04}
			L.superiortemporal	-0.41	2.06×10^{-04}
			R.supramarginal	-0.41	2.25×10^{-04}

3.3.5. Antero-Posterior (A-P) analysis

Correlations (*df* =74) were also performed between the functional regulation coefficient and the corresponding A-P axis co-ordinate for each brain region. This analysis revealed a significant positive correlation between functional regulation and the co-ordinate of each brain region along the A-P axis (Rho = 0.35, p = 0.0018). Finally, I investigated the A-P effect for both structural and functional (connectivity) by calculating the correlations between functional and structural strength and the corresponding A-P axis co-ordinate for each brain region. Significant Bonferroni-corrected correlations were found for functional (Rho = 0.28, p = 0.0148), but not structural strength (Rho = -0.12, p = 0.31) (see figure 7).

Figure 3.7. A-P correlation analysis for functional regulation, functional and structural strength. More anterior regions show greater increases in (a) regulation coefficient and (b) functional but not (c) structural strength in preHD. Each data point represents a brain region in the Freesurfer Desikan atlas.. The co-ordinate of that brain region along the anterior-posterior axis, on the y-axis, is plotted against regulation coefficient or strength on the x-axis.The red line represents a least squares linear regression line. Rho = correlation coefficient, P = p-value, DF = degrees of freedom.

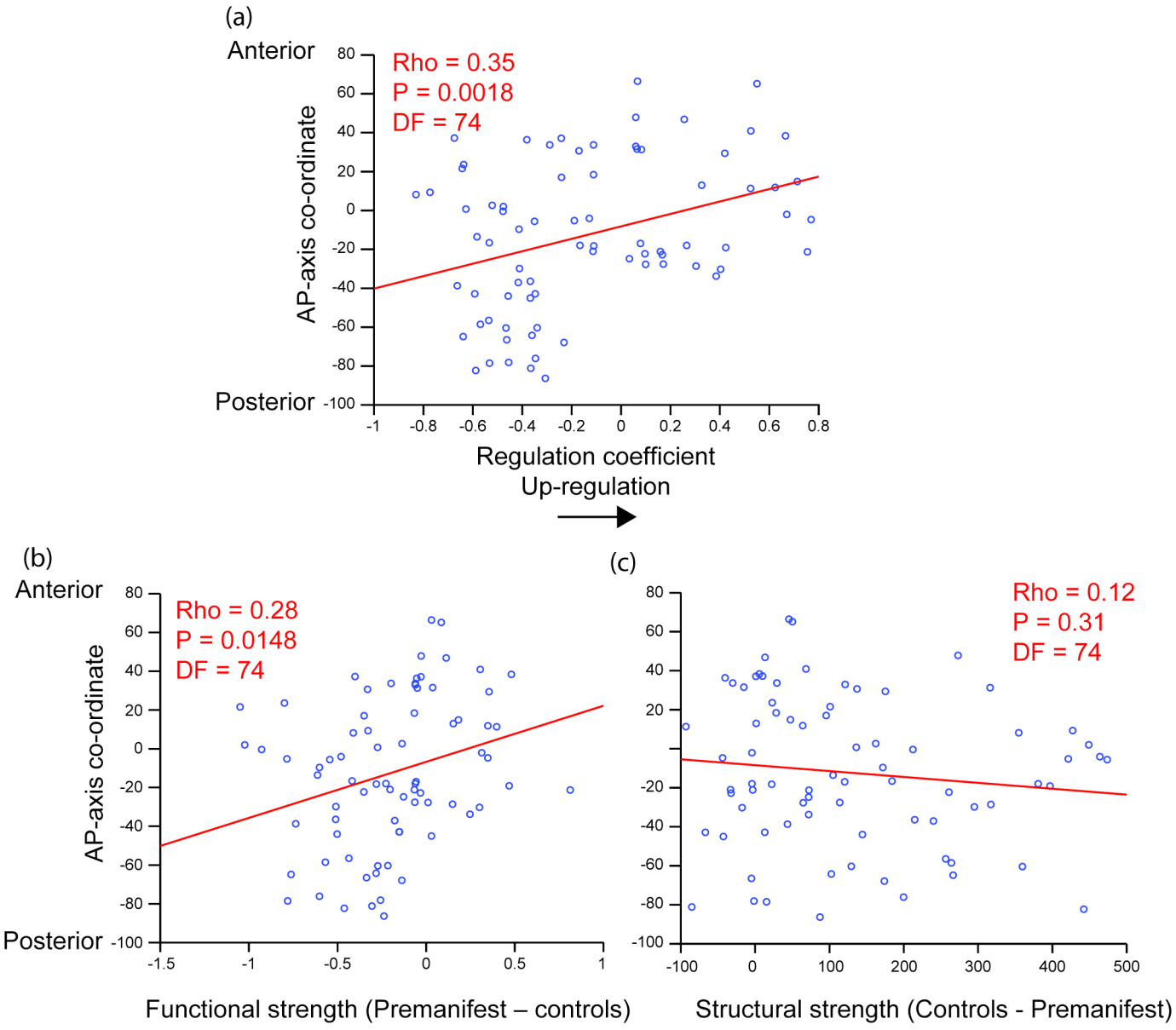

3.4. Discussion

In this chapter I have shown how the organisational properties of healthy white matter can predict decreases in structural connectivity and increases in functional connectivity in preHD relative to controls. Through novel modelling of functional regulation I reveal an antero-posterior dissociation of changes in functional connectivity in preHD. Compared to healthy controls, preHD participants showed both functional up-regulation, where strong connections in anterior non-hub regions were stronger; and down-regulation where strong connections in posterior hub regions were weaker.

3.4.1. Linking structure and function in Huntington's disease

Changes in structural and functional connectivity have been observed in preHD (Dumas et al., 2013; Harrington et al., 2015; Kloppel et al., 2015; Poudel et al., 2014a; Poudel et al., 2014b). However, until now how such changes related to underlying white matter organisation of the healthy brain was unknown. To date only one study has investigated the relationship between structural and functional connectivity in HD (Muller et al., 2016). This was performed in a manifest HD cohort. While structural and functional connectivity differences relative to controls were observed independently no correlation was found between structure and functional connectivity in manifest HD participants. Using functional connectivity analyses combined with structural characterisation of white matter connectivity, my work thus goes significantly beyond those earlier observations by demonstrating that features of healthy white matter organisation can predict regional decreases in structural connectivity and increases in functional connectivity in preHD relative to controls. In keeping with these findings, brain regions with strong connections to their neighbours in the healthy brain showed greatest increases in functional connectivity in preHD.

3.4.2. Functional compensation

While my study was not designed to detect whether these increases in functional connectivity are compensatory or pathological, the fact these increases are seen in regions with low white matter connectivity loss suggest they may either represent the earliest signs of the disease process prior to structural connectivity loss or may indeed represent regions with intact structural connectivity up-regulating as a compensatory mechanism (Kloppel et al.,

2015). If the latter is correct then this has important implications for therapies aimed to enhance compensatory mechanisms. Two such therapies, repetitive trans-cranial stimulation (rTMS) (Fregni and Pascual-Leone, 2007) and neurofeedback (Subramanian et al., 2011) are efficacious in other neurodegenerative diseases. If the functional increases I observed are compensatory this suggests targeting these therapies specifically to anterior brain regions may provide the most optimal approach, as these are the regions with greatest capacity for functional up-regulation based on the observations in this study.

3.4.3. Anterior-posterior dissociation

My functional regulation analysis revealed a striking A-P dissociation where anterior regions in the brain showed functional up-regulation of connectivity while posterior regions in the brain showed down-regulation. A similar anterior-posterior shift in brain activation (rather than connectivity) is seen in healthy ageing using task-based fMRI (Davis et al., 2008), which the authors interpret as a compensatory mechanism used to maintain cognitive performance as the brain ages. Although the physiology of aging and pathology of Huntington's disease are clearly very different processes, this anterior-posterior shift may possibly represent a shared mechanism of compensation common to both healthy aging and preclinical neurodegeneration. However it is difficult to make direct comparisons as Davis and colleagues measured brain activation during the performance of a cognitive task while we investigated brain activation at rest.

I provide additional evidence for A-P dissociation by showing a positive correlation between the location of a brain region along the A-P axis and the increase in functional regulation and functional strength observed in preHD. As no such spatial correlation was seen with structural connectivity strength this suggests the A-P effect is not mediated by underlying structural connectivity but may reflect a solely functional process. Thus if this is a compensatory mechanism it suggests this may be driven by a functional neurochemical process as opposed to structural alterations. Indeed the concentration of dopamininegric D2 receptors show a rostro-caudal gradient, present in highest concentrations in prefrontal cortex and lowest concentrations in the occipital cortex (Lidow et al., 1989), furthermore D2 receptors are implicated in HD pathogenesis (Charvin et al., 2008; Charvin et al., 2005; Deyts et al., 2009). It is therefore possible that changes in dopamine levels in preHD may facilitate compensation and thus explain this A-P dissociation.

3.4.4. Previous evidence of anterior-posterior dissociation

Grading of striatal neuropathology in HD reveals that degeneration occurs along a caudo-rostral gradient (Vonsattel, 1985). In keeping with this previous studies in manifest HD have shown greater loss of white matter volume (Tabrizi et al., 2011) and cortical thickness (Rosas et al., 2002; Tabrizi et al., 2009) in posterior compared to anterior areas of the brain. Therefore I postulate that the functional antero-posterior dissociation I demonstrate in preHD may be a precursor to the structural changes in grey and white matter seen in manifest disease. With clinical trials currently underway for potential disease modifying therapies (Wild and Tabrizi, 2014), the presence of this functional dissociation may represent the optimum time for therapeutic intervention prior to irreversible structural damage. Future multimodal imaging studies in young adults far from disease onset will allow us to confirm if this functional A-P dissociation is indeed one of the earliest brain changes in HD prior to disease onset.

3.4.5. Conclusion

The findings in this chapter reveal the organizational principles of healthy white matter that determine structural and functional connectivity changes in preHD. Specifically, brain regions with strong connections to distant regions show decreases in structural connectivity, while those with strong connections to their neighours show increases in functional connectivity in pre-clinical neurodegeneration relative to healthy controls. In addition I demonstrate a functional A-P dissociation in pre-clinical neurodegeneration where anterior regions in the brain show up-regulation, while posterior regions show down-regulation. These increases in functional connectivity may represent either compensatory change or the earliest brain changes of pre-clinical neurodegeneration prior to structural connectivity loss. If increases in functional connectivity are pathological as opposed to compensatory it is likely that they may correlate with HD related symptoms occurring in the preHD stage. Therefore in the next chapter I will examine how these structural and functional brain network changes relate to psychiatric symptoms in preHD that occur years before symptom onset.

3.5. Publications relating to this chapter

The work presented in this chapter was published as:

White matter predicts functional connectivity in premanifest Huntington's disease. **McColgan P**, Gregory S, Razi A, Seunarine KK, Gargouri F, Durr A, Roos RAC, Leavitt BR, Scahill RI, Clark CA, Tabrizi SJ, Rees G and the Track On-HD Investigators. **Ann Clin Transl Neurol.** 2017 Jan 16;4(2):106-118.

Chapter 4. Structural and functional brain networks correlates of depressive symptoms in preHD HD

4.1. Introduction

In chapter 3 I demonstrated how organizational principles of the healthy white matter brain network can be used to identify which brain regions show changes in structural and functional connectivity in preHD relative to controls. Brain regions with strong connections to their neigbours but weak connections to more distant regions showed the greatest capacity for functional up-regulation. A number of studies in preHD have suggested that increases in functional connectivity may be compensatory (Harrington et al., 2015; Kloppel et al., 2015) allowing those in the preHD stage to maintain normal motor and cognitive function in the context of brain atrophy. However it is also possible that increases in functional connectivity in the preHD stage may represent the earliest signs of pathological change. Indeed increased functional connectivity, relative to healthy controls, is well recognized in other disease states such as Parkinson's disease, multiple sclerosis and traumatic brain injury (Hillary and Grafman, 2017). In major depressive disorder (MDD) functional connectivity increases are seen in the default mode network (Gong and He, 2015).

Given the functional connectivity changes demonstrated in MDD and the potential overlap with HD depression my aim in this chapter was to investigate how depressive symptoms relate to changes in structural and functional connectivity in preHD. Depression can precede the onset of motor symptoms in HD by many years (Tabrizi et al., 2009). It has a significant impact on morbidity (Beglinger et al., 2010) with a lifetime prevalence of 20% in preHD (Julien et al., 2007). Given the potential overlap with other neuropsychiatric symptoms I also investigated how apathy and anxiety relate to changes in structural and functional connectivity. Characteristics of depression and apathy in HD may overlap (Epping et al., 2013). However others report the presence of a distinct apathy syndrome in HD separate from depression (Levy et al., 1998; Naarding et al., 2009), which begins in the preHD (Martinez-Horta et al., 2016) and progresses over time (Thompson et al., 2012). Anxiety has a

lifetime prevalence of 17% in preHD (Julien et al., 2007) and may occur concurrently with depression (Dale and van Duijn, 2015).

A number of neuroimaging studies have identified specific brain variations associated with depression in HD including gray matter volume loss and white matter microstructural abnormalities in the rostral anterior cingulate, (Hobbs et al., 2011; Sprengelmeyer et al., 2014), and abnormal task-based activations in prefrontal cortex (Gray et al., 2013; Unschuld et al., 2012). Abnormalities in white matter microstructure of the splenium of the corpus callosum also correlate with depressions scores in HD (Gregory et al., 2015b). While variations in these regions occur generally in HD (Tabrizi et al., 2009) these studies suggest they are particularly affected in HD patients with depression. Few studies have investigated neural correlates of other psychiatric symptoms in HD. Delmaire and colleagues showed correlation between apathy score on the problem behaviours assessment and white matter microstructure of the gyrus rectus of the frontal lobe (Delmaire et al., 2012). However a subsequent study also using diffusion MRI failed to show correlates with apathy (Gregory et al., 2015b). Irritability in preHD has been linked to abnormal connectivity between the amygdala and orbitofrontal cortex using task fMRI (Kloppel et al., 2010).

In this chapter I test the hypothesis that increases in functional connectivity and reductions in structural connectivity relate to depressive symptoms in preHD. In order to test if variations in these network analyses are related to pathological change I also perform between group analyses of preHD and healthy controls. Brain network correlates with apathy and anxiety were also investigated. I employ a data reduction approach by initially identifying a depression sub-network. This is done by decomposing the brain into modules and assessing the correlation between depression scores and within module connectivity. This allows me to identify a depression specific sub-network and further explore how specific connections in this network that relate to depression.

4.2. Methods

4.2.1 Cohorts

Track-On HD (2012) (Kloppel et al., 2015) and Track-HD (2011) (Tabrizi et al., 2009) cohorts were included in this study. The structure-function analysis was performed in the Track-On HD cohort and the structural replication analysis was performed in the Track-HD cohort. The Track-On HD fMRI cohort included 186 participants (92 preHD and 94 controls) (see table 4.1.1). Baltimore self-reported apathy data was missing from 3 preHD subjects from the fMRI cohort. The diffusion MRI cohort included 151 (70 preHD and 81 controls) (see table 4.1.2). The replication analysis included 96 participants with diffusion MRI data only (50 preHD and 46 controls) (see table 4.1.3). Of the participants in Track-On HD, 31 preHD and 29 controls had previously participated in Track-HD. Although not significant, depression scores differed between preHD and controls (see tables 4.1.1-4.1.3). See chapter 2 for detailed inclusion/exclusion criteria.

Evaluation for psychiatric symptoms was performed on the day of MRI scanning by a neurologist or psychiatrist using the Hospital Anxiety and Depression Score (HADS), the Baltimore Apathy and Irritability Scale (BAIS) and the Beck Depression Inventory-2 (BDI-II). See tables 4.1.4 and 4.1.5 for clinical breakdowns of the BDI-II and HADS depression (HADS-D) and anxiety scores (HADS-A). The self reported Baltimore apathy scale was chosen as the apathy measure of interest due to incomplete data for the companion reported Baltimore apathy scale. While I acknowledge the possibility of bias or cognitive deficit in self-reports, comparison of companion reported and self-reported apathy scores in Huntington's disease shows high correlation suggesting validity of self reported apathy in Huntington's disease (Mason and Barker, 2015). Given the potential for overlap between depression, apathy, anxiety and irritability scores Pearson correlations between scales were calculated for the Track-On HD fMRI and diffusion MRI cohorts (see table 4.1.6).

Table 4.1.1. Track-On HD fMRI cohort. SD = standard deviation, M = male, F = female, N = number. ISCED = International standard classification of education. CAG = CAG repeat expansion length, DBS = disease burden scale (Penney et al., 1997)

	PreHD	**Control**	**Statistical test**	**P-value**
N	92	94	-	-
Age (SD)	41.8 (9.5)	47.7 (10.6)	2 tail t-test	0.0001
Gender (M/F)	49/43	38/56	Chi-square	0.079
ISCED (2/3/4/5/6)	7/22/27/35/1	9/16/32/35/2	Chi-square	0.748
Study Site (N) (Leiden/London/Paris/Vancouver)	17/26/24/25	24/25/24/21	Chi-square	0.673
CAG (SD)	43.1 (2.3)	-	-	-
DBS (SD)	301.4 (52)	-	-	-
BDI (SD)	6.8 (8.2)	4.8 (6.1)	2 tail t-test	0.071
HADS-D (SD)	3 (4)	2.1 (2.6)	2 tail t-test	0.068
HADS-A (SD)	5 (3.8)	4.2 (3.3)	2 tail t-test	0.126
BAIS self reported apathy (SD)	11.4 (7)	8.8 (4.8)	2 tail t-test	0.004

Table 4.1.2. Track-On HD Diffusion fMRI cohort. SD = standard deviation, M = male, F = female, N = number. ISCED = International standard classification of education. CAG = CAG repeat expansion length, DBS = disease burden scale (Penney et al., 1997)

	PreHD	Control	Statistical test	P-value
N	70	81	-	-
Age (SD)	42.6 (9.3)	48.3 (9.8)	2 tail t-test	0.0004
Gender (M/F)	38/32	31/50	Chi-square	0.049
ISCED (2/3/4/5/6)	5/14/23/27/1	7/14/28/30/2	Chi-square	0.972
Study Site (N) (Leiden/London/Paris/Vanc	12/25/18/15	18/25/22/16	Chi-square	0.841

ouver)				
CAG (SD)	43 (2.3)	-	-	-
DBS (SD)	301 (51.9)	-	-	-
BDI (SD)	6.9 (8.8)	4.7 (6.1)	2 tail t-test	0.0674
HADS-D (SD)	3 (4.3)	1.9 (2.6)	2 tail t-test	0.043
HADS-A (SD)	5 (3.8)	4.1 (3.4)	2 tail t-test	0.1
BAIS self reported apathy (SD)	11.3 (7.3)	8.3 (4.1)	2 tail t-test	0.0017

Table 4.1.3 Track-HD Diffusion MRI cohort. SD = standard deviation, M = male, F = female, N = number. ISCED = International standard classification of education. CAG = CAG repeat expansion length, DBS = disease burden scale (Penney et al., 1997)

	PreHD	Control	Statistical test	P-value
N	50	46	-	-
Age (SD)	42.2 (8.9)	47.7 (9)	2 tail t-test	0.004
Gender (M/F)	26/24	15/31	Chi-square	0.055
ISCED (2/3/4/5/6)	2/7/19/22/0	7/9/12/ 17/1	Chi-square	0.192
Study Site (N) (London/Leiden/Paris)	13/21/16	11/20/15	Chi-square	0.972
CAG (SD)	43 (2.1)	-	-	-
DBS (SD)	301.3 (52.5)	-	-	-
BDI (SD)	6.1 (7.5)	5.8 (6.7)	2 tail t-test	0.8307
HADS-D (SD)	2.8 (3.5)	2.5 (2.7)	2 tail t-test	0.6405
HADS-A (SD)	4.8 (3.4)	4.7 (3.6)	2 tail t-test	0.909
BAIS self reported apathy (SD)	10.9 (6.3)	9.4 (3.5)	2 tail t-test	0.156

Table 4.1.4. Beck's Depression Inventory (BDI)-II scores for each cohort

Track-On HD fMRI	BDI-II		
		PreHD	Controls
0-13	Minimal	79	86
14-19	Mild	6	3
20-28	Moderate	6	4
29-63	Severe	1	1
Track-On HD Diffusion	**BDI-II**		
		PreHD	**Controls**
0-13	Minimal	60	76
14-19	Mild	3	3
20-28	Moderate	6	2
29-63	Severe	1	1
Track-HD Diffusion	**BDI-II**		
		PreHD	**Controls**
0-13	Minimal	42	40
14-19	Mild	3	5
20-28	Moderate	4	0
29-63	Severe	1	1

Table 4.1.5. Hamilton Anxiety and Depression score (HADS)-D and HADS-A scores for each cohort

Track-On HD fMRI	HADS-D			Track-On HD fMRI	HADS-A		
		PreHD	Controls			PreHD	Controls
0-7	Normal	82	88	0-7	Normal	71	77
8 --10	Borderline	3	5	8 --10	Borderline	11	11
11 --21	Abnormal	7	1	11 --21	Abnormal	10	6
Track-On HD Diffusion	**HADS-D**			**Track-On HD Diffusion**	**HADS-A**		
		PreHD	**Controls**			**PreHD**	**Controls**
0-7	Normal	61	76	0-7	Normal	55	67
8 --10	Borderline	3	4	8 --10	Borderline	7	9
11 --21	Abnormal	6	1	11 --21	Abnormal	8	5
Track-HD Diffusion	**HADS-D**			**Track-HD Diffusion**	**HADS-A**		
		PreHD	**Controls**			**PreHD**	**Controls**
0-7	Normal	47	43	0-7	Normal	38	36
8 --10	Borderline	2	2	8 --10	Borderline	9	6
11 --21	Abnormal	1	1	11 --21	Abnormal	3	4

Table 4.1.6. Pearson correlations between HADS-A, BDI-II, HADS-D and BAIS rating scales.

Track-On HD fMRI	HADS-A	BDI-II	HADS-D	BAIS - Apathy	BAIS - Irritability
HADS-A	1	0.704536049	0.637834475	0.384766281	0.708949936
BDI-II	0.704536049	1	0.8329522	0.643847703	0.683147895
HADS-D	0.637834475	0.8329522	1	0.72575884	0.628810573
BAIS - Apathy	0.384766281	0.643847703	0.72575884	1	0.433598255
BAIS - Irritability	0.708949936	0.683147895	0.628810573	0.433598255	1
Track-On HD Diffusion MRI	**HADS-A**	**BDI-II**	**HADS-D**	**BAIS - Apathy**	**BAIS - Irritability**
HADS-A	1	0.707288444	0.620022271	0.354160956	0.570366989
BDI-II	0.707288444	1	0.847052939	0.645947106	0.537502447
HADS-D	0.620022271	0.847052939	1	0.739202222	0.546214596
BAIS - Apathy	0.354160956	0.645947106	0.739202222	1	0.451392782
BAIS - Irritability	0.570366989	0.537502447	0.546214596	0.451392782	1

4.2.2. Construction of structural and functional connectivity matrices

Diffusion MRI and rs-fMRI pipelines are detailed in chapter 2. For structural connectivity matrices ROIs were defined as connected if a fibre originated in ROI 1 and terminated in ROI 2. For functional matrices ROIs were defined as functionally connected if there was a correlation between the time series of ROI 1 and ROI 2. Structural connections were weighted by streamline count, while functional connections were weighted by magnitude of correlation. Connections were then combined into 76x76, undirected and weighted matrices. Thresholding was applied in order to remove weak spurious connections (Rubinov and Sporns, 2010). For both structural and functional connectivity matrices only those connections present in 75% of controls subjects were retained, consistent with thresholding strategies used in the literature (van den Heuvel and Sporns, 2011; van den Heuvel et al., 2013). Binary matrices were created by converting the weights in matrices to 0 or 1 to denote the absence or presence of a connection. A significant correlation between connectivity and a clinical variable in the context of binary matrices suggests that there is a relationship between the magnitude of the clinical correlation and the likelihood that the connection is present.

4.2.3. Cortical modules and depression

A cortical module associated with depression was first identified. This was done by calculating an average functional connectivity matrix across participants, for cortical regions only. This was then decomposed in a data-driven manner using the Louvain method for community detection (Blondel et al., 2008) as implemented in the Brain connectivity toolbox (BCT) (Rubinov and Sporns, 2010). The Louvain method for community detection calculates brain modules by splitting the brain into non over-lapping groups of regions, which maximizes the number of within-group connections, and minimizes the number of between-group connections. A resolution parameter is chosen in order to detect either small modules (<1) or large modules (>1). In this study a value of 0.5 was chosen in order to identify large modules and thus avoid excluding brain regions that may be implicated in depression. This resulted in decomposition of the brain into 2 modules.

Pearson and Spearman rank partial correlations were then performed between depression scores HADS-D and BDI-II and the total number of functional connections within each module. Age, gender, site and CAG repeat length were included as covariates. The brain regions in the module showing correlations with depression were then combined with the caudate and thalami as these regions are implicated in depression (Gong and He, 2015). This network was then used an input in the network based statistic (NBS) correlation analysis in order to identify which specific connections within the module are associated with HADS-D and HADS-A, BDI-II and the self-reported Baltimore apathy scale.

4.2.4. Network based statistics

Using NBS, a test statistic is calculated for each connection independently. A primary threshold ($p < 0.05$, uncorrected) is then applied to form a set of suprathreshold connections. Permutation testing is then used to ascribe a p-value controlled for FWE to each set of suprathreshold connections. For each permutation the test statistic is recalculated, after which the same threshold is applied to define a set of suprathreshold connections. The maximal component size for each permutation is determined giving a null distribution of maximal component size. Finally the FWE corrected p-value of the observed component size k is estimated by finding the proportion of permutations for which the maximal component is greater than k. The FWE adjusted p- value is set at 0.05 (Zalesky et al., 2010).

Results reaching FWE corrected $p < 0.05$ are reported as significant, with p-values relating to the significance of all the connections within a sub-network as a whole as opposed to individual connections. Both binary and weighted networks were investigated as both have been reported in the depression literature (Gong and He, 2015). Age, gender, site were included as covariates for the between group analysis and control correlation analysis. For the preHD correlation analysis, CAG repeat length was included as an additional covariate. Group analyses between depressed and non-depressed preHD participants were not performed due to a limited number of preHD participants reaching moderate or severe depression. This was also the case for control groups. Thus I focused on correlations across the spectrum of depressive symptoms as opposed to clinically significant depression.

Based on observations from the literature that depression shows positive correlation with functional connectivity and negative correlation with structural connectivity in the DMN and basal ganglia (Gong and He, 2015), positive correlations were tested in the resting state fMRI analysis, while negative correlations were tested in the diffusion MRI analysis (thus a one-tailed correlation for each analysis).

4.2.5. Replication analysis

The structural connectivity analysis was replicated in the separate Track-HD 2011 cohort.

4.2.6. Off medication analyses

In order to account for the effect of antidepressant medication NBS analyses for depression were repeated with inclusion of a binary covariate, where 1 denoted those taking antidepressant medication within 30 days of the MRI scan and 0 denoting those not on antidepressant medication during this time period. While I acknowledge pharmacological heterogeneity the inclusion of a binary covariate allows us to account for common sources of variance in the data associated with medication. While a binary covariate may not fully capture the subtleties of every type of pharmacological heterogeneity, such heterogeneity is likely to be uncorrelated with apathy and so

serve as noise in the analysis, reducing my power to detect effects but not calling into question any of the effects I have actually identified.

4.3. Results

4.3.1. Within modular functional connectivity and depression

The average functional cortical matrix was split into 2 modules, defined in a data driven manner using the Louvain method (Blondel et al., 2008) for community detection. Module 1 contained 48 regions, while module 2 contained 22 regions (see table 4.2). For Pearson partial correlations the total number of connections within module 2 showed significant correlation with both HADS-D (df = 89, Rho = 0.29, p = 0.0054) and approached significance after Bonferroni correction for BDI-II (df = 89. Rho = 0.25, p = 0.02) See figure 4.2. Similarly for Spearman rank correlations the total number of connections within module 2 showed significant correlation with both HADS depression (df = 89, Rho = 0.29, p = 0.0059) and approached significance after Bonferroni correction for BDI-II (df = 89. Rho = 0.22, p = 0.051). I observed that all connections in module 2 have been reported previously as belonging to the default mode network (Buckner et al., 2008). No correlations were seen with module 1. Results reported relate to the binarised matrix as no significant correlations were found with the weighted functional matrix.

Table 4.2. Cortical modules generated using Louvain algorithm

Module 1	Module 2

L.bankssts	R.caudalmiddlefrontal	L.entorhinal
L.caudalanteriorcingulate	R.cuneus	L.inferiorparietal
L.caudalmiddlefrontal	R.fusiform	L.isthmuscingulate
L.cuneus	R.inferiortemporal	L.medialorbitofrontal
L.fusiform	R.lateraloccipital	L.middletemporal
L.inferiortemporal	R.lateralorbitofrontal	L.parahippocampal
L.lateraloccipital	R.lingual	L.precuneus
L.lateralorbitofrontal	R.paracentral	L.rostralanteriorcingulate
L.lingual	R.parsopercularis	L.frontalpole
L.paracentral	R.parsorbitalis	L.temporalpole
L.parsopercularis	R.parstriangularis	L.hippocampus
L.parsorbitalis	R.pericalcarine	R.hippocampus
L.parstriangularis	R.postcentral	R.entorhinal
L.pericalcarine	R.posteriorcingulate	R.inferiorparietal
L.postcentral	R.precentral	R.isthmuscingulate
L.posteriorcingulate	R.rostralmiddlefrontal	R.medialorbitofrontal
L.precentral	R.superiorfrontal	R.middletemporal
L.rostralmiddlefrontal	R.superiorparietal	R.parahippocampal
L.superiorfrontal	R.superiortemporal	R.precuneus
L.superiorparietal	R.supramarginal	R.rostralanteriorcingulate
L.superiortemporal	R.transversetemporal	R.frontalpole
L.supramarginal	R.insula	R.temporalpole
L.transversetemporal	R.bankssts	
L.insula	R.caudalanteriorcingulate	

Figure 4.1. Cortical modules and total within module (2) connectivity correlation with depression scores. Spheres represent brain regions. Red - module 1 and purple – module 2. Significant Pearson partial correlations between total within module functional connectivity and HADS-D and BDI-II scores were only seen with module 2. Rho = correlation coefficient, P = p-value, DF = degrees of freedom.

Step 1: fMRI healthy connectome split into 2 modules using Louvain algorithm

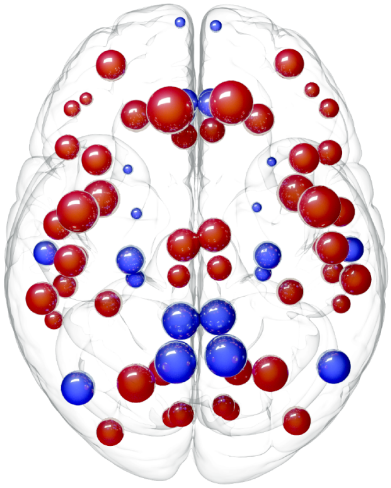

Module 1

Module 2

Step 2: Correlations with depression, Module 2 results only show significance

Covariates: age, gender, site, CAG

Within module connectivity and HADS-D

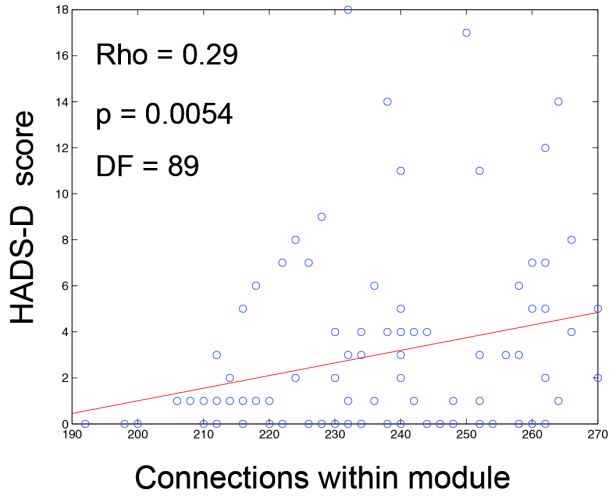

Within module connectivity and BDI-II

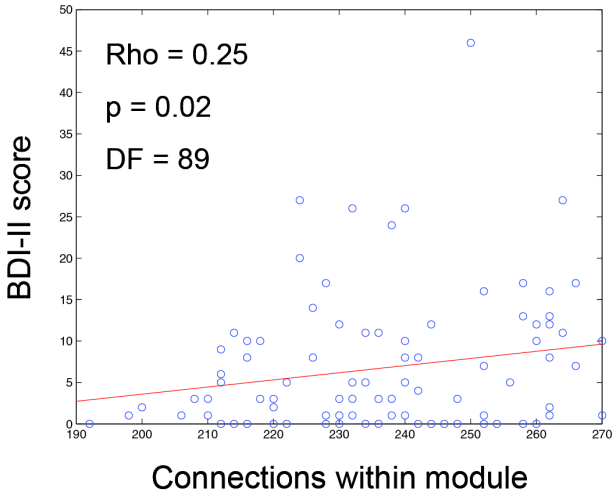

4.3.2. Depression correlates with increased functional connectivity in preHD

Positive correlations were seen between depression score and functional connectivity (binary matrices only) for both HADS-D (df = 89, p^{FWE} = 0.008) and BDI-II (df = 89, p^{FWE} = 0.026), notably in the connections between the rostral anterior cingulate, medial orbitofrontal, precuneus and parahippocampal regions. No significant correlations were seen with depression score and functional connectivity for the controls or for weighted networks. See figure 4.2 and table 4.3. Additionally no significant reciprocal (negative correlations) were observed.

Figure 4.2. Track-On HD fMRI cohort: NBS analysis displaying connections that show positive correlation with depression scores for resting state fMRI in preHD. Blue lines indicate significant correlations between functional connections and HADS-D (*df* = 89, p = 0.008) and BDI-II (*df* = 89, p = 0.026) depression scores.

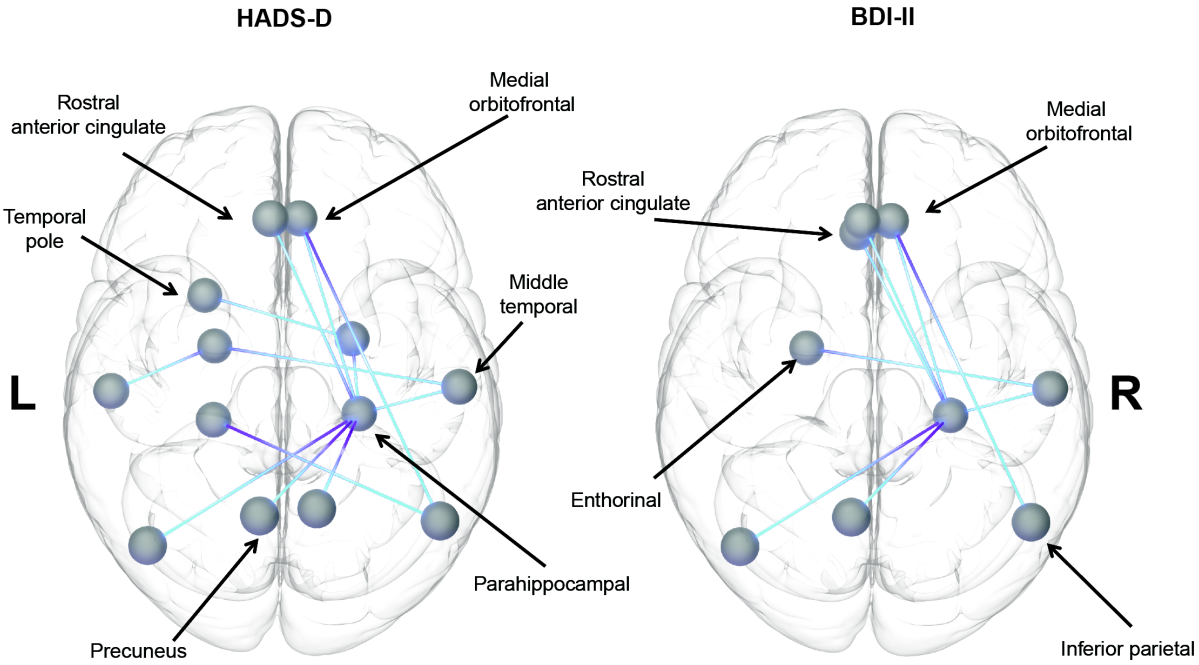

Table 4.3. Resting state fMRI Track-On HD and depression: Association between increase in functional connections and HADS (p = 0.008) and BDI (p = 0.026) scores in preHD. ROI – regions of interest, T-stat – t-statistics.

Resting state fMRI Track-On HD			
HADS-D	**ROI 1**	**ROI 2**	**T-stat**
	L.entorhinal	L.middletemporal	2.11
	L.temporalpole	R.entorhinal	1.9
	L.parahippocampal	R.inferiorparietal	1.71
	R.inferiorparietal	R.medialorbitofrontal	1.97
	L.entorhinal	R.middletemporal	1.71
	L.inferiorparietal	R.parahippocampal	2.28
	L.precuneus	R.parahippocampal	2.57
	L.rostralanteriorcingulate	R.parahippocampal	2.56
	R.entorhinal	R.parahippocampal	1.82
	R.medialorbitofrontal	R.parahippocampal	1.91
	R.middletemporal	R.parahippocampal	2.74
	R.parahippocampal	R.precuneus	1.83
BDI-II	**ROI 1**	**ROI 2**	**T-stat**
	R.inferiorparietal	R.medialorbitofrontal	1.77
	L.entorhinal	R.middletemporal	1.81
	L.inferiorparietal	R.parahippocampal	2.66
	L.medialorbitofrontal	R.parahippocampal	1.89
	L.precuneus	R.parahippocampal	1.99
	L.rostralanteriorcingulate	R.parahippocampal	2.33
	R.medialorbitofrontal	R.parahippocampal	2.16
	R.middletemporal	R.parahippocampal	2.59

4.3.3. Depression correlates with reduced structural connectivity in preHD

Negative correlations were seen between depression score and structural connectivity (binary matrices only) for both HADS-D (df = 67, p^{FWE} = 0.036) and BDI-II (df = 67, p^{FWE} = 0.019), notably in the connections between the rostral anterior cingulate, medial orbitofrontal, precuneus and caudate and thalamus regions. No significant correlations were seen with depression score and structural connectivity for the controls. See figure 4.3 and table 4.4. Additionally no significant positive correlations were observed.

Figure 4.3. Track-On HD diffusion MRI cohort: NBS analysis displaying connections that show negative correlation with depression scores for diffusion MRI in preHD. Red lines indicate significant positive correlations between structural connections and HADS-D (*df* = 67, p = 0.036) and BDI-II (*df* = 67, p = 0.019) depression scores.

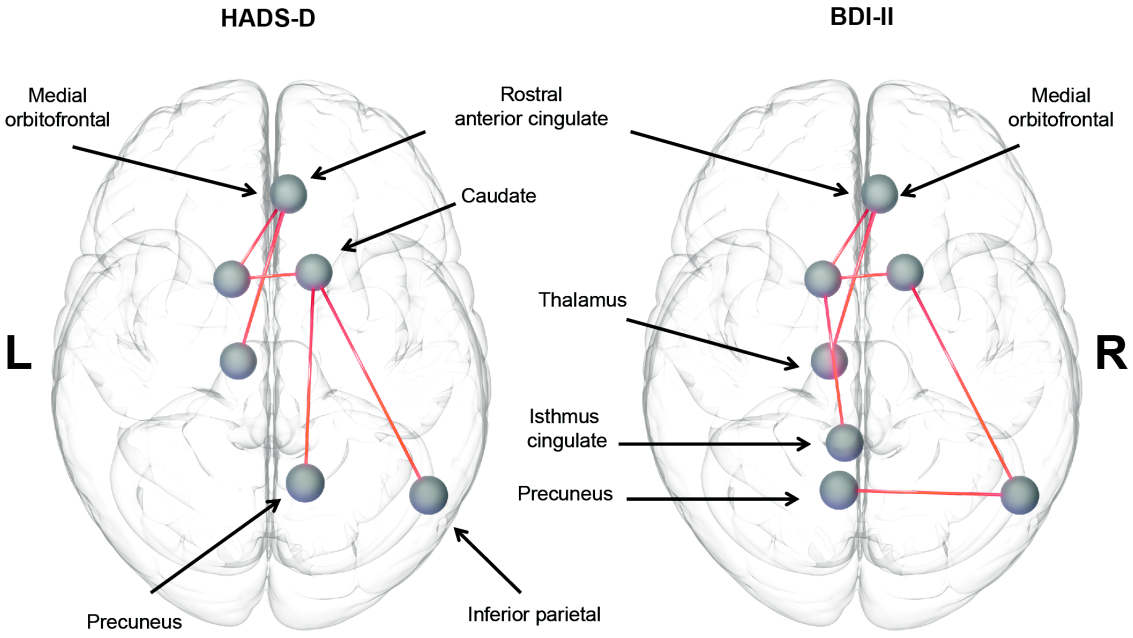

Table 4.4. Diffusion MRI Track-On HD and depression: Association between decrease in structural connections and HADS (p = 0.036) and BDI (p = 0.019) scores in preHD. ROI – regions of interest, T-stat – t-statistics.

Diffusion MRI Track-On HD			
HADS-D	**ROI 1**	**ROI 2**	**T-stat**
	L.caudate	R.caudate	2.22
	R.caudate	R.inferiorparietal	2.48
	L.thalamus	R.medialorbitofrontal	2.4
	L.caudate	R.medialorbitofrontal	3.43
	R.caudate	R.precuneus	1.73
	L.thalamus	R.rostralanteriorcingulate	2.01
BDI-II	**ROI 1**	**ROI 2**	**T-stat**
	L.isthmuscingulate	L.caudate	1.78
	L.caudate	R.caudate	1.73
	L.precuneus	R.inferiorparietal	2.03
	R.caudate	R.inferiorparietal	2.7
	L.thalamus	R.medialorbitofrontal	2.92
	L.caudate	R.medialorbitofrontal	3.27
	L.thalamus	R.rostralanteriorcingulate	1.83

4.3.4. Apathy correlates with increased functional but not structural connectivity in preHD

Positive correlations were seen between self-reported apathy and both binary ($df = 86$, $p^{FWE} = 0.005$) and weighted functional matrices ($df = 86$, $p^{FWE} = 0.034$), however no correlation with apathy and structural (binary or weighted) matrices was observed. See figure 4.4 and tables 4.5 and 4.6. HADS-A showed no correlation with functional or structural (binary or weighted) connectivity matrices. This suggests that the correlations I demonstrate between depression scores and connectivity are specific for depressive symptoms and not anxiety.

Figure 4.4. Track-On HD fMRI cohort: NBS analysis displaying connections that show positive correlation with Baltimore self-reported apathy score for resting state fMRI in preHD. Blue lines indicate significant negative correlations between binary ($df = 86$, $p = 0.036$) and weighted ($df = 86$, $p = 0.005$) functional connections and Baltimore self-reported apathy score.

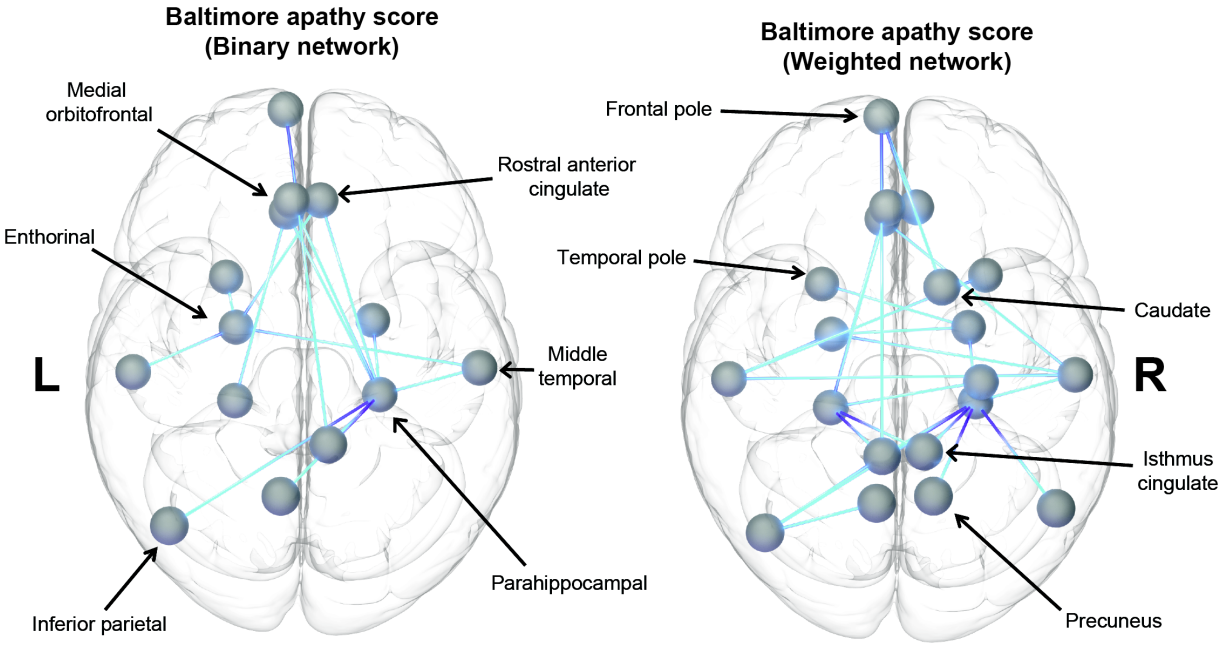

Table 4.5. Resting state fMRI TrackOn-HD (binary network) and apathy: Association between increase in functional connections and Baltimore self-reported apathy in preHD for binary (p = 0.005) and weighted (p = 0.034) networks. ROI – regions of interest, T-stat – t-statistics.

Resting state fMRI Track-On HD			
Apathy (binary network)	**ROI 1**	**ROI 2**	**T-stat**
	L.entorhinal	L.middletemporal	2.91
	L.medialorbitofrontal	L.parahippocampal	1.8
	L.entorhinal	L.temporalpole	1.76
	L.frontalpole	R.isthmuscingulate	1.9
	L.entorhinal	R.medialorbitofrontal	2.58
	L.entorhinal	R.middletemporal	2.62
	L.inferiorparietal	R.parahippocampal	2.28
	L.medialorbitofrontal	R.parahippocampal	2.75
	L.precuneus	R.parahippocampal	2.22
	L.rostralanteriorcingulate	R.parahippocampal	1.88
	R.entorhinal	R.parahippocampal	1.95
	R.isthmuscingulate	R.parahippocampal	1.93
	R.medialorbitofrontal	R.parahippocampal	1.94
	R.middletemporal	R.parahippocampal	2.59

Table 4.6. Resting state fMRI TrackOn-HD (weighted network) and apathy: Association between increase in functional connections and Baltimore self-reported apathy in preHD for binary (p = 0.005) and weighted (p = 0.034) networks. ROI – regions of interest, T-stat – t-statistics.

Apathy (weighted network)	ROI 1	ROI 2	T-stat
	L.inferiorparietal	L.isthmuscingulate	1.94
	L.entorhinal	L.middletemporal	2.37
	L.isthmuscingulate	L.parahippocampal	2.57
	L.medialorbitofrontal	L.parahippocampal	2.45
	L.inferiorparietal	L.precuneus	2.38
	L.parahippocampal	L.rostralanteriorcingulate	1.82
	L.isthmuscingulate	L.frontalpole	1.97
	L.medialorbitofrontal	L.frontalpole	2.02
	L.frontalpole	R.caudate	2
	L.parahippocampal	R.hippocampus	1.79
	L.entorhinal	R.entorhinal	1.78
	L.temporalpole	R.entorhinal	2.3
	L.parahippocampal	R.isthmuscingulate	2.57
	L.frontalpole	R.medialorbitofrontal	2.14
	L.entorhinal	R.middletemporal	2.15
	L.medialorbitofrontal	R.middletemporal	2.2
	L.middletemporal	R.middletemporal	1.85
	L.inferiorparietal	R.parahippocampal	2.43
	L.isthmuscingulate	R.parahippocampal	1.85
	R.entorhinal	R.parahippocampal	2.44
	R.inferiorparietal	R.parahippocampal	1.95
	R.isthmuscingulate	R.parahippocampal	1.78
	R.middletemporal	R.parahippocampal	1.86
	R.parahippocampal	R.precuneus	1.72
	L.middletemporal	R.temporalpole	1.73

4.3.5. Structural connectivity replication analysis

For weighted connectivity matrices negative correlations were seen between depression score and structural connectivity for both HADS-D ($df = 47$, $p^{FWE} = 0.014$) and BDI-II ($df = 47$, $p^{FWE} = 0.045$), notably in the connections between the rostral anterior cingulate, medial orbitofrontal, precuneus and caudate and thalamus regions. See figure 4.5. No significant correlations were seen between depression score and structural connectivity for the controls. No significant correlations were seen between binary matrices and depression scores for either group. See table 4.7 and 4.8. Additionally no significant reciprocal (positive) correlations were observed.

Figure 4.5. Track-HD diffusion MRI replication cohort. NBS analysis displaying connections that show negative correlation with depression scores for diffusion MRI in preHD. Red lines indicate significant positive correlations between structural connections and HADS-D ($df = 67$, $p = 0.036$) and BDI-II ($df = 67$, $p = 0.019$) depression scores.

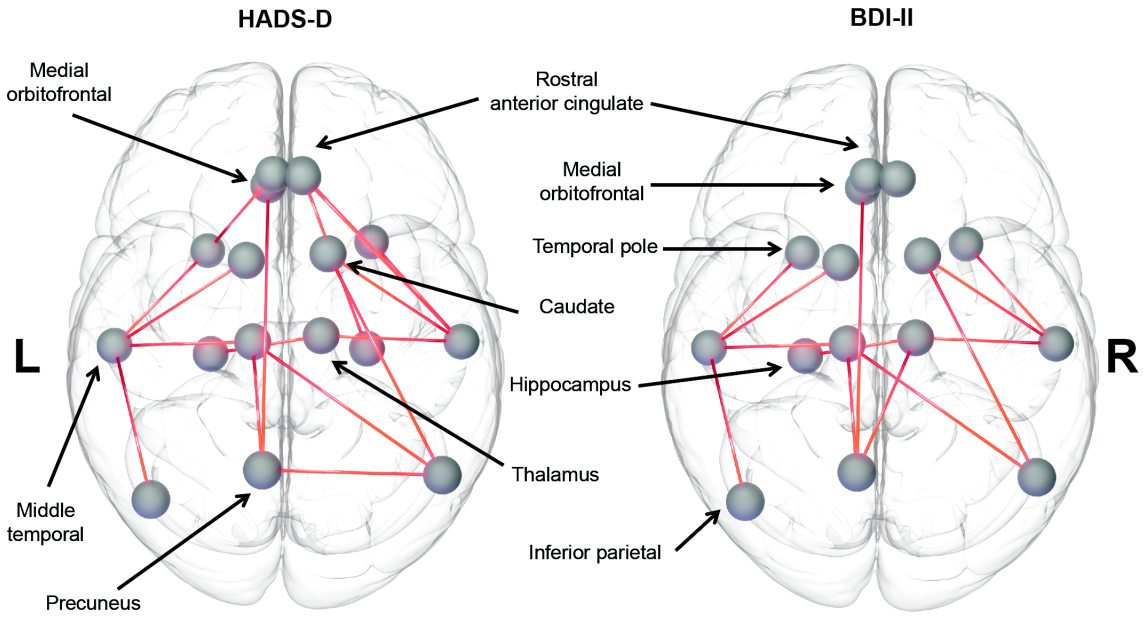

Table 4.7. Diffusion MRI Track-HD and depression replication analysis HADS-D: Association between decrease in structural connections and HADS (p = 0.014) and BDI (p = 0.045) scores in preHD. ROI – regions of interest, T-stat – t-statistics.

Diffusion MRI Track-HD			
HADS-D	**ROI 1**	**ROI 2**	**T-stat**
	L.inferiorparietal	L.middletemporal	1.74
	L.medialorbitofrontal	L.precuneus	2.4
	L.middletemporal	L.temporalpole	1.85
	L.rostralanteriorcingulate	L.temporalpole	2.22
	L.middletemporal	L.thalamus	1.74
	L.precuneus	L.thalamus	2.67
	L.middletemporal	L.caudate	1.76
	L.hippocampus	R.thalamus	2.17
	L.precuneus	R.inferiorparietal	2.06
	L.thalamus	R.inferiorparietal	2.56
	R.caudate	R.inferiorparietal	1.97
	R.hippocampus	R.medialorbitofrontal	1.86
	R.thalamus	R.middletemporal	3.17
	R.caudate	R.middletemporal	3.05
	R.medialorbitofrontal	R.middletemporal	1.83
	L.medialorbitofrontal	R.rostralanteriorcingulate	1.93
	L.rostralanteriorcingulate	R.rostralanteriorcingulate	2.05
	R.hippocampus	R.rostralanteriorcingulate	2.29
	R.middletemporal	R.rostralanteriorcingulate	1.82
	R.middletemporal	R.temporalpole	2

Table 4.8. Diffusion MRI Track-HD and depression replication analysis BDI-II: Association between decrease in structural connections and HADS (p = 0.014) and BDI (p = 0.045) scores in preHD HD. ROI – regions of interest, T-stat – t-statistics.

BDI-II	ROI 1	ROI 2	T-stat
	L.inferiorparietal	L.middletemporal	1.87
	L.medialorbitofrontal	L.precuneus	2.38
	L.middletemporal	L.temporalpole	1.94
	L.middletemporal	L.thalamus	2.21
	L.precuneus	L.thalamus	2.75
	L.middletemporal	L.caudate	2
	L.precuneus	R.thalamus	1.92
	L.hippocampus	R.thalamus	2.44
	L.thalamus	R.inferiorparietal	2.99
	R.caudate	R.inferiorparietal	2.17
	R.thalamus	R.middletemporal	2.27
	R.caudate	R.middletemporal	3.35
	L.medialorbitofrontal	R.rostralanteriorcingulate	1.87
	L.rostralanteriorcingulate	R.rostralanteriorcingulate	2.34
	R.middletemporal	R.temporalpole	1.74

4.3.6. Group differences between preHD and controls

For cohorts with no significant group differences in depression scores (Track-On HD fMRI and Track-HD diffusion) preHD participants showed greater functional connectivity (binary matrices only) between precuneus, isthmus cingulate and inferior parietal regions bilaterally compared to controls ($p^{FWE} = 0.036$) and reduced structural connectivity between basal ganglia hubs and cortical regions including the precuneus, isthmus cingulate, inferior parietal and medial orbitofrontal compared to controls ($p^{FWE} = 0.018$), (weighted matrices only). See figure 4.6. Similarly for the Track-On HD diffusion cohort reduced structural connectivity was seen between basal ganglia hubs and cortical regions ($p^{FWE} = 0.035$) (weighted matrices only), however in this cohort there were significant group differences in depression scores raising the possibility that depression may be driving this result.

Figure 4.6. NBS analysis displaying connections that show group differences in preHD vs controls for resting state fMRI (Track-On HD) and diffusion MRI (Track-HD) cohorts. Blues lines indicate significance for preHD > controls (p = 0.036), while red lines indicate significant connections for controls > preHD (p = 0.0144).

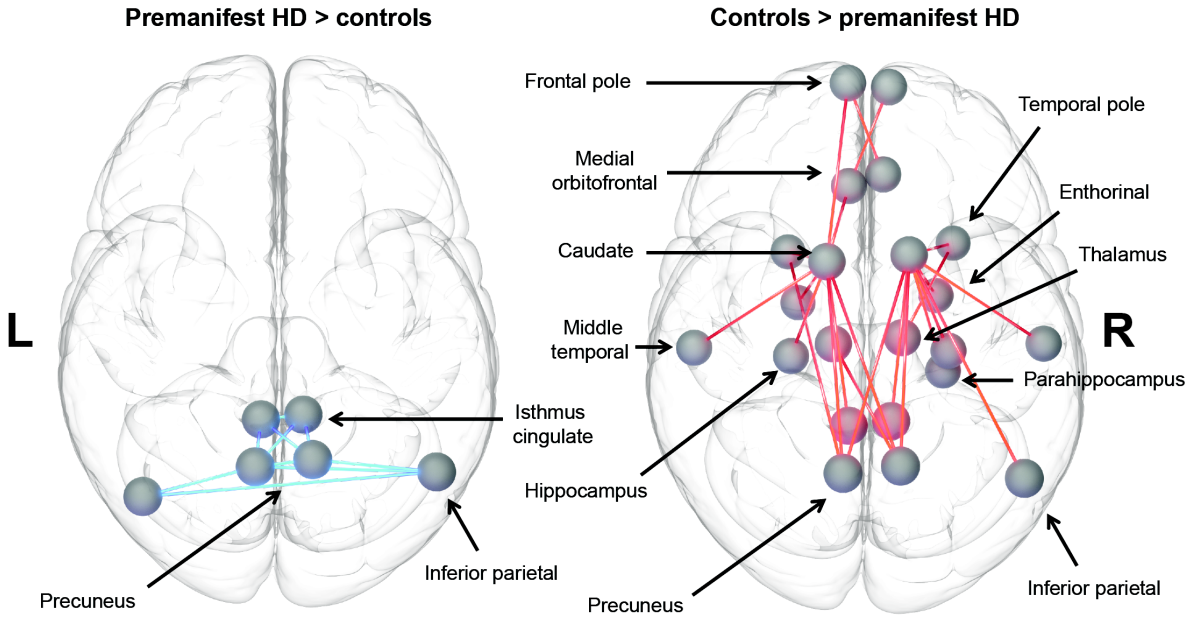

4.3.7. Off medication analyses

All analyses in the study were repeated with the use of anti-depressant medications included as a covariate and revealed similar results. A binary covariate was used with 1 denoting use of antidepressants within 30 days prior to MRI scanning and 0 denoting no antidepressant use within this time period. The Track-On HD fMRI cohort had 33 preHD and 11 controls on anti-depressants, the diffusion tractography cohort had 25 preHD and 10 controls on anti-depressants and the Track-HD replication cohort had 8 preHD and 3 controls on anti-depressants. See summary table 4.9.

Table 4.9. Summary table for Track-On HD fMRI and Track-On HD and Track-HD diffusion structural cohorts showing depression and group NBS analyses. Red – significant, Blue – approaching significance.

HADS-D	fMRI Track-On HD	Diffusion MRI Track-On HD	Diffusion MRI Track-HD
PreHD(Binary)	0.008	0.036	0.917
PreHD (Weighted)	0.118	0.363	0.0114
Controls (Binary)	0.935	0.931	0.925
Controls (Weighted)	0.933	1	0.795
PreHD (Binary, drugs covaried)	0.024	0.0589	0.918
PreHD (Weighted, drugs covaried)	0.075	0.223	0.075
Controls (Binary, drugs covaried)	0.95	0.44	0.485
Controls (Weighted, drugs covaried)	0.744	0.64	0.784
BDI-II			
PreHD (Binary)	0.026	0.019	0.255
PreHD (Weighted)	0.157	0.592	0.045
Controls (Binary)	0.875	0.938	0.884
Controls (Weighted)	0.358	0.918	0.784
PreHD (Binary, drugs covaried)	0.047	0.222	0.537
PreHD (Weighted, drugs covaried)	0.14	0.221	0.012
Controls (Binary, drugs covaried)	1	0.931	0.887
Controls (Weighted, drugs covaried)	0.35	0.589	0.411
Group differences			
PreHD vs Controls (Binary)	0.036	0.0841	0.093
PreHD vs Controls (Weighted)	0.657	0.035	0.0184
PreHD vs Controls (Binary, drugs covaried)	0.133	0.0965	0.102
PreHD vs Controls (Weighted, drugs covaried)	0.516	0.0304	0.0144

4.4. Discussion

In this chapter brain network connections that correlated with depressive symptoms and apathy scores in preHD were identified. Positive correlations between depressive symptoms and apathy scores were seen with functional connections, predominantly between the default mode regions, while negative correlations in structural connections were seen between the cortex and basal ganglia (for depressive symptoms but not apathy). Furthermore these connectivity variations associated with depressive symptoms were also seen in similar regions when comparing preHD and control groups, when depression scores were not significantly different between groups.

4.4.1. Pathology versus compensation

These findings reveal that the increases in functional connectivity in preHD relative to controls demonstrated in chapter 3 correlate with neuropsychiatric symptoms in preHD. Therefore increased functional connectivity may relate to early pathological changes as opposed to compensatory mechanisms. It may be the case however that attempts to compensate may fail resulting in aberrant increases in functional connectivity. The concepts of successful and attempted compensation were previously proposed in order to understand potential compensatory mechanisms in normal aging and have since been applied to neurodegeneration. Attempted compensation requires 2 criteria: (1) an inverted U-shape curve with respect to neural activity and structural brain decline and (2) an inverted U-shape curve with respect to neural activity and task demands (Scheller et al., 2014). While my focus in this chapter is not specifically on compensation, given the findings of increased functional connectivity in chapter 3 and correlates with neuropsychiatric symptoms demonstrated here coupled with evidence of brain network compensation in the literature (Kloppel et al., 2015) it seems likely that attempted compensation may lead to aberrant increases in functional connectivity causing network disturbance and resulting in neuropsychiatric symptoms

4.4.1. Previous neuroimaging studies in Huntington's disease depression

Previous neuroimaging studies have identified brain regions associated with depression in HD. In preHD and manifest HD there is a negative correlation between grey matter volume loss of the rostral anterior cingulate and

BDI score (Hobbs et al., 2011). White matter microstructural abnormalities have also been identified in early HD and preHD patients with depressive symptoms using diffusion tensor imaging (DTI). Variations in fractional anisotropy are seen in anterior cingulate, ventromedial frontal cortex, superior frontal cortex, insula and cerebellum (Sprengelmeyer et al., 2014). Similarly task based fMRI reveal an association between depression and activation of the ventromedial prefrontal cortex in preHD (Unschuld et al., 2012) and activation of dorsolateral prefrontal cortex in manifest HD (Gray et al., 2013). Similar findings were observed in the present study with respect to both structural and functional connectivity of the rostral anterior cingulate and medial orbitofrontal regions. Loss of structural connectivity between medial orbitofrontal and thalamus, hippocampus and frontal pole are also seen between preHD and controls.

4.4.2. Relationship to brain network abnormalities in major depressive disorder

While only a small number of participants have depression scores consistent with a diagnosis of clinical depression, with most having sub-clinical depressive symptoms, my results show marked similarities to connectivity variations in major depressive disorder without HD. I demonstrate in preHD that depression symptoms are positively correlated with the functional connectivity of a brain module which includes the precuneus, isthmus cingulate, inferior parietal, hippocampus, parahippocampal gyrus, entorhinal, temporal pole, rostral anterior cingulate and medial orbitofrontal. These regions are found in the default mode brain network (Buckner et al., 2008), which shows increases in functional connectivity in those with MDD (Greicius et al., 2007). The DMN can be further sub-divided into anterior and posterior components. The anterior DMN consists of the medial prefrontal, posterior cingulate and parietal regions, while the posterior DMN includes the posterior cingulate and parietal regions (Damoiseaux et al., 2008; Li et al., 2013). Using independent components analysis of resting state fMRI data (Li et al., 2013) demonstrated increased functional connectivity in anterior and posterior default mode sub-networks in MDD. In keeping with this, using a brain network approach, I demonstrate similar findings in preHD participants, showing a correlation between depressive symptoms and increased functional connectivity between anterior and posterior regions of the DMN.

With respect to the structural networks, a recent study in MDD revealed reduced structural connections between 2 sub-networks, one including the precuneus, isthmus cingulate and rostral anterior cingulate and the

other including the thalamus, caudate and medial orbitofrontal regions (Korgaonkar et al., 2014). In keeping with this I found loss of structural connectivity between medial orbitofrontal, thalamus, caudate, rostral anterior cingulate, precuneus and inferior parietal.

4.4.3. Apathy and brain networks

Apathy scores showed positive correlations with functional connections; however no significant correlations were identified between apathy scores and structural connections. The lack of significant correlation with apathy and structural connections suggests apathy may be driven by a functional process, such as neurochemical disturbance, as opposed to underlying structural variation. Indeed dopamine modulation is thought to play a role in apathy related to Parkinson's disease thus a similar mechanism may account for apathy in HD (Sinha et al., 2013). As discussed in chapter 3, dopamine D2 receptors show a rostro-caudal gradient present in highest concentration in the prefrontal cortex and lowest concentrations in the occipital cortex, thus the A-P gradient of functional connectivity change shown in chapter 3 may result in apathy (Lidow et al., 1989). Functional connections correlating with apathy, including medial orbitofrontal and cingulate connections to the parahippocampal gyrus, were consistent with the brain regions implicated in apathy in other neurodegenerative disorders (Benoit et al., 2002; Thobois et al., 2010).

4.4.4. Huntington's disease vs. healthy controls

Group differences were found in connections associated with depression comparing preHD and controls, such as functional connections between precuneus, inferior parietal and isthmus cingulate and structural connections between the precuneus, isthmus cingulate, caudate, thalamus and medial orbitofrontal regions. This analysis was performed in cohorts were depression scores did not differ significantly between preHD and controls suggesting that the group differences identified may relate to HD pathology rather the depression.

A small proportion of both my preHD and control participants were taking regular antidepressants. I control for the effect of this by repeating all analyses and including the use of anti-depressants as a covariate, which provided similar findings to those demonstrated in the main analysis.

4.4.5. Limitations

A number of factors must be taken into account when applying and interpreting psychiatric rating scales. A good scale should measure a psychopathological construct and be composed of items that cover symptoms associated with that construct. Internal consistency assesses the correlation between individual scale items, to see if items are measuring related symptoms. The BDI-II has a high internal consistency ranging from 0.83-0.96 (Wang and Gorenstein, 2013). Similarly internal consistencies for the both the HADS-D and HADS-A are high ranging from 0.82-0.9 and 0.78-0.93 respectively (Mykletun et al., 2001). A rating scale must also demonstrate test re-test reliability, such that testing of the same patient after a short interval should reveal similar results. Test re-test reliability is high for both BDI-II, ranging between 0.73-0.96 (Wang and Gorenstein, 2013) and for the HADS at 0.83 (Marrie et al., 2017). Internal consistency and test re-test reliability metrics are not available for the BAIS as this is a relatively new scale, which has been developed specifically for HD (Chatterjee et al., 2005).

Rating scales may also be sensitive to s syndrome subtypes. This can be investigated using factor analysis. An example of this can be seen with the BDI-II, in which scale items can be attributed to cognitive-affective depression and somatic-vegetative depression (Wang and Gorenstein, 2013). This is particularly important when applying the scale to a clinical population, for example scale items related to cognitive-affective depression may erroneously reflect cognitive dysfunction as depression. In this context it is also important scale items do not measure symptoms outside of the psychopathological construct. For example depression scales measuring anxiety or apathy. However this is difficult to avoid given the co-occurrence of psychiatric symptoms. Indeed cross-correlations are seen with depression, apathy and irritability scales used in this chapter and have also been reported in the literature (Mykletun et al., 2001; Wang and Gorenstein, 2013).

Only a small number participants included in this study had clinically significant psychiatric symptoms, with few scoring moderate or severe on the BDI-II. For this reason I focused on psychiatric symptoms as opposed to comparing preHD participants with psychiatric diagnoses against those without. This is based on the assumption that mild sub-clinical psychiatric symptoms and more severe psychiatric symptoms that fulfill diagnostic criteria exist on a continuous spectrum. Therefore the brain changes seen at the severe end of the spectrum are likely to be similar, with respect to the connections affected, but more pronounced than those changes seen at the mild end of the spectrum. It is possible however that additional or even different brain connections may become involved once patients fulfill diagnostic criteria. Thus the approach presented here may miss brain connection changes associated with more severe symptoms.

While it is difficult to perform large imaging studies in preHD looking specifically at depression and apathy, by conducting a correlation analysis over a range of clinical scores this enabled us to perform the largest imaging study to date looking specifically at depressive symptoms and apathy in HD. One limitation of this approach is the inability to identify whether these network variations are specific for preHD related depression rather than major depressive disorder or depression associated with other neurodegenerative diseases, such as Alzheimer's disease. I try and account for this by showing an absence of correlation between depressive symptoms in controls and functional and structural connectivity, particularly in a control cohort with no significant differences in depression scores relative to preHD. While a group analysis between depressed preHD participants and non-depressed preHD participants may have been preferable, low numbers of those with moderate or severe depression made this unfeasible thus a correlation analysis was performed to examine connectivity relationships over a wide range of depressive symptoms.

The structural and functional Track-On HD analyses only showed significant results with binary matrices while the replication structural analysis only showed significant results with weighted matrices. Binary matrices indicate the absence or presence of a connection while weighted matrices indicate the strength of a connection. Thus this discrepancy between cohorts may be due to the fact that the higher depression scores seen in Track-On HD relate to connection loss, while lower depression scores seen in Track-HD relate to reductions in connection in strength.

Both the nucleus accumbens and globus pallidus have been implicated in the pathophysiology of apathy (Sinha et al., 2013). However I was unable to include these structures in my analysis as automatic segmentation of these regions are not sufficiently reliable (Hibar et al., 2015).

4.4.6. Conclusion

Increased functional connections between the default mode network are associated with depressive and apathy symptoms in preHD, while reduced structural connections between the basal ganglia and the default mode network are associated with depressive symptoms but not apathy. Furthermore these connectivity variations associated with depressive symptoms were also present between preHD and control groups, regardless of depression or apathy. These findings suggest that the increases in functional connectivity demonstrated in chapter 3 may represent early pathological change that manifests clinically as neuropsychiatric disturbance. This may be due to attempted compensation resulting in aberrant increases in functional connectivity. While the first two experimental chapters of this thesis have focused on the relationship between structural and functional connectivity it is unclear how brain networks change as the disease progresses from preHD to manifest HD. In chapter 5 I will examine changes in white matter networks in preHD and HD at the global, regional and connection level in order to define topological changes across the disease course and how these relate to the cognitive and motor symptoms in HD.

4.5. Publications relating to this chapter

The work presented in this chapter was published as:

Structural and functional brain network correlates of depressive symptoms in preHD Huntington's disease. **McColgan P**, Razi A, Gregory S, Seunarine KK, Durr A, A C Roos R, Leavitt BR, Scahill RI, Clark CA, Langbehn DR, Rees G, Tabrizi SJ; Track On-HD Investigators. **Hum Brain Mapp**. 2017 Jun;38(6):2819-2829.

Chapter 5. Selective vulnerability of rich club brain regions in HD

5.1. Introduction

Loss of caudate volume and surrounding white matter (WM) occur early in preHD, while more extensive grey and WM loss, extending to cortical regions is seen in manifest HD (Tabrizi et al., 2011). Consistent with this grey and WM loss, recent investigations using diffusion tractography reveal loss of structural connectivity between the basal ganglia and cortex (Bohanna et al., 2011a; Kloppel et al., 2008; Marrakchi-Kacem et al., 2013; Novak et al., 2015) and across a fronto-parietal-striatal network (Poudel et al., 2014b).

While these studies have focused on specific white matter tracts or sub-networks apriori, analysis of the whole brain functional network has been performed in preHD using rs-fMRI. This revealed increases in global efficiency in participants closer to the onset of manifest disease. Clustering coefficient at the whole brain level was unchanged suggesting no changes in network segregation in preHD relative to controls. The increase in global efficiency was interpreted as functional brain networks in preHD exhibiting a more random topology compared to healthy controls (Harrington et al., 2015). Similar findings were seen in a subsequent study investigating the functional brain network in HD (Gargouri et al., 2016). These studies have focused on functional brain networks, therefore how the white matter brain network changes across disease stages in HD is unknown. My first aim in this chapter was to examine how the white matter brain network changes at the global and regional level in preHD and HD and how these topological properties relate to cognitive and motor deficits. Correlates with psychiatric symptoms were not investigated, as this was the focus of chapter 4.

In chapter 3 of this thesis I demonstrated how properties of the healthy white matter brain network could predict regional loss of structural connectivity in preHD relative to controls, such that regions with strong connections to distant regions and few connections to their neighbours were vulnerable to structural connectivity loss. Brain regions exhibiting these properties have been defined as rich club brain regions (van den Heuvel and Sporns, 2011). These rich club brain regions are more highly connected to each other, than the rest of the network, forming a high-cost high capacity backbone of the brain network (van den Heuvel et al., 2012; van den Heuvel and Sporns, 2013). Such topological centrality of the rich club network supports integrative processing and adaptive behaviours (Senden et al., 2014). Consistent with this, the degree of structural rich club connectivity predicts general cognitive performance in healthy older adults (Baggio et al., 2015). Cortical rich

club regions include the superior frontal, superior parietal, precuenus and insula and are reproducible across studies (van den Heuvel and Sporns, 2011; van den Heuvel et al., 2013).

Rich club organization has been investigated in preHD using rs-fMRI. This revealed that the density of connections between rich club regions decreases with proximity to disease onset (Harrington et al., 2015). Vulnerability of rich club brain regions occurs in a wide range of brain disorders (Crossley et al., 2014). Although the reason for this is unclear, in the case of HD the prion-like spread of pathogenic huntingtin protein would be expected to target regions with greatest network centrality. Indeed prion-like spread has been proposed as a mechanism of brain network dysfunction in other neurodegenerative diseases (Zhou et al., 2012). Alternatively brain regions with high centrality in the network have the largest metabolic demands (Liang et al., 2013) therefore downstream metabolic dysfunction caused by mutant huntingtin may also result in rich club dysfunction and connectivity loss. It may be the case that rich club vulnerability is a consequence of both metabolic dysfunction and prion-like spread. My second aim in this chapter was to investigate selective loss of rich club structural connectivity in HD.

Using diffusion tractography and graph theoretical analysis in preHD and manifest HD and healthy individuals I set out to test the following hypotheses; (1) HD leads to selective structural connectivity loss of rich club regions causing breakdown of the whole brain network. (2) Such regional rich club and whole brain network changes are associated with cognitive and motor deficits seen in HD. (3) Highly connected brain regions with high network traffic and low clustering of neighboring regions are more susceptible to structural connectivity loss.

5.2. Materials and Methods

5.2.1. Cohort

I studied a cohort including HD (n = 38), preHD (n = 50) and control participants (n = 47) from the London, Paris and Leiden sites of the Track-HD study (see table 5.1). Premanifest gene carriers required a DBS > 250, on the basis of their medical records at the time of assessment, and a UHDRS TMS of five or less, indicating no substantial motor signs. Controls were selected from the spouses or partners of individuals with preHD or early HD or were gene-negative siblings, to ensure consistency of environments. Additional inclusion and exclusion criteria are detailed elsewhere (Tabrizi et al., 2009). Statistical analysis was carried out using SAS version 9.4. The study was approved by the local ethics committees, and written informed consent was obtained from each participant. Left-handed participants were excluded from the analyses to avoid confounding effects caused by differences in structural connectivity in those who are right hemisphere dominant.

.

5.2.2. Construction of Structural Brain Network

The diffusion MRI processing pipeline is detailed in chapter 2. ROIs were defined as connected if a fibre originated in ROI 1 and terminated in ROI 2. These connections were weighted by streamline count and combined into a 76x76, undirected and weighted, structural connectivity matrix. In addition I also created volume normalised matrices for our analyses. This was done by dividing the number of streamlines connecting two ROIs by the sum of their volumes. Both un-normalised and normalised matrices were used in the analysis as it is unclear from the current literature whether normalisation is required or not.

The threshold masks for generating sparse connectivity matrices for the subsequent graph theoretic analyses were created for connections present in 25%, 50%, 75% and 100% of control participants. These masks were then used to threshold individual connectivity matrices across all groups, consistent with thresholding strategies in the seminal rich club paper (van den Heuvel and Sporns, 2011). By using the control group to generate threshold masks I aimed to exclude connections due to noise as opposed to pathology. A value of 75% was used in keeping with the chosen threshold in the seminal human rich club paper (van den Heuvel and Sporns, 2011).

Figure 5.1: Summary of processing pipeline. BET = Brain Extraction Tool; CSD = constrained spherical deconvolution; DTI = diffusion tensor imaging; FA = fractional anisotropy; fODF = fibre orientation distribution function; GM = grey matter; QC = quality control; WM = white matter.

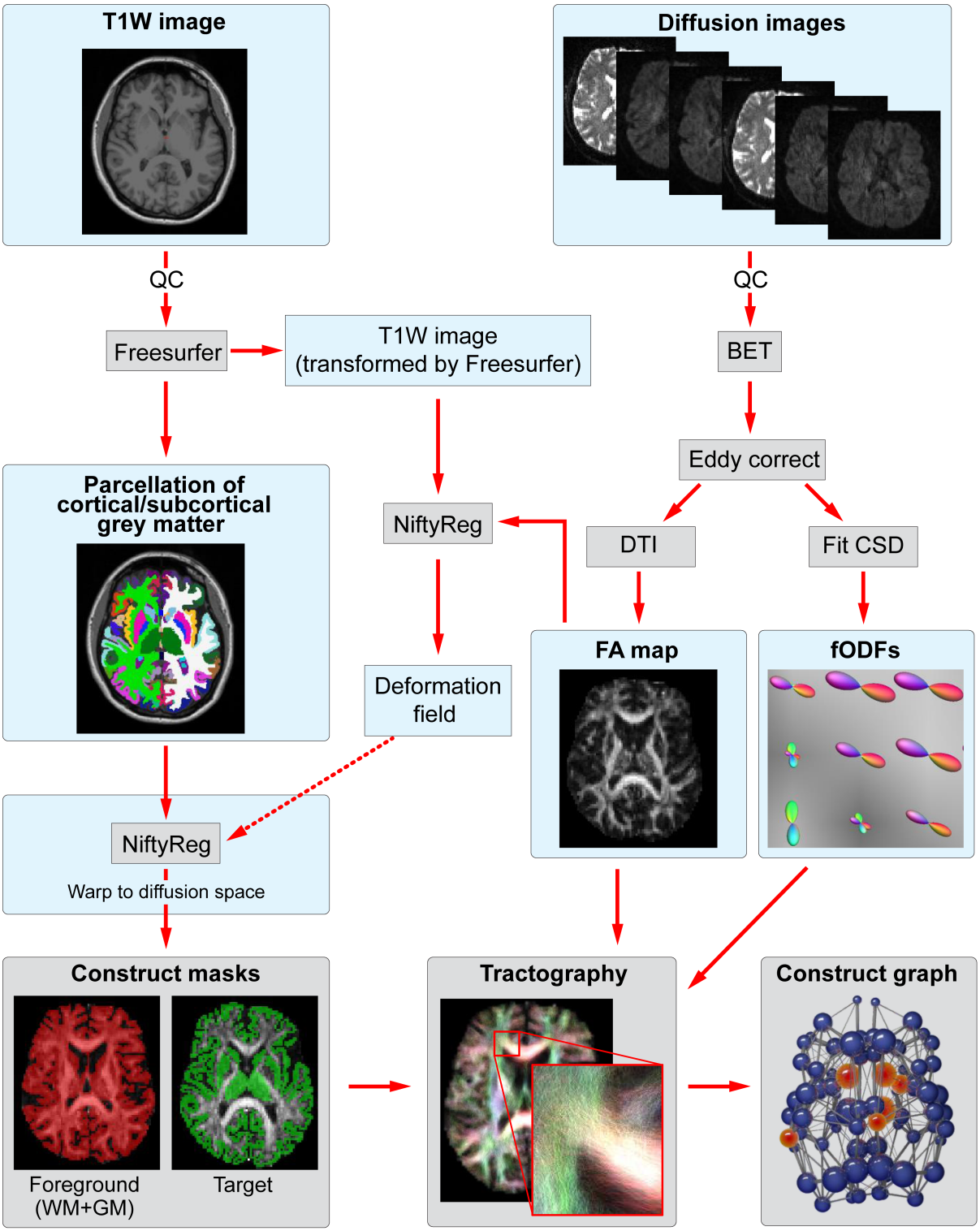

5.2.3. Graph theoretical analysis

Various graph metrics were calculated using the brain connectivity toolbox (Rubinov and Sporns, 2010) and have been discussed in detail elsewhere (Bullmore and Sporns, 2009). I analysed the structural networks using both global and local nodal summary statistics. Global graph metrics characterise the brain network properties as a whole whereas using node-level local metrics I can probe more region-based differences. Detailed descriptions of graph theory metrics are included in chapter 1 of this thesis. Global brain network segregation was assessed using normalised clustering coefficient and modularity. Brain network integration was assessed using normalised average path length and global efficiency. Small worldness was also investigated. Path lengths and clustering coefficients were normalised relative to a set of 1000 random networks. Altered topology in individual brain regions was assessed using degree, strength, betweenness centrality and clustering coefficients. For ease of understanding betweenness centrality is referred to as "network traffic" throughout this chapter. Similarly, strength is referred to as (graph theory) strength to avoid confusion with streamline density.

Statistically significant group differences in graph metrics were analysed using permutation testing (10,000 permutations) with two-tailed t-tests in order to investigate both increases and decreases in structural connectivity. Age, sex, education and study site were included as covariates. For individual brain region metrics, a FDR correction was applied across the 76 brain regions, and a Bonferroni correction was applied for the multiple graph theory measures tested in both the regional and whole brain analyses.

5.2.4. Rich Club Analysis

A rich club analysis (van den Heuvel and Sporns, 2011) was performed to identify rich club organisation and regions in each group. Rich club organisation is a tendency for highly connected brain regions to be more densely connected among themselves than brain regions with fewer connections. The weighted rich club coefficients were calculated for each participant and normalised relative to a set of 1000 comparable random networks. The presence of rich club organisation was identified by performing two-tailed t-test permutation testing (10,000 permutations) of the area under the curve (normalised weighted rich club coefficient against degree) for each group vs. random network. FDR correction was then applied to correct for multiple

comparisons across a range of degrees, in line with a similar analysis in the literature (van den Heuvel et al., 2013). Rich club regions were defined as the top 12 brain regions with the highest degree.

5.2.5. Clinical Correlations

I investigated how differences in brain networks relate to performance in cognitive and motor tests. Participants were assessed using SDMT (Smith, 1968), SWR (Stroop, 1935), Indirect Circle Tracing (log of the indirect circle annulus) (Say et al., 2011; Tabrizi et al., 2011), Negative Emotion Recognition (Ekman and Friesen, 1976), Speeded Tapping (mean inter-tap interval non-dominant hand) (Reilmann, 2005) and TMS (Huntington Study Group, 1996). These variables were chosen because of their demonstrated sensitivity in Huntington's disease (Stout et al., 2012; Tabrizi et al., 2013). I used partial Pearson correlations controlling for age, sex, study site, education and CAG length to assess how graph metrics related to clinical variables for HD gene. Regional correlations were FDR corrected across 76 brain regions and Bonferroni corrected for four local metrics and six clinical measures ($p < 0.05/24$). Whole brain correlations were Bonferroni corrected for five global metrics.

5.2.6. Network Based Statistics

To further probe which specific structural connections showed group differences in preHD vs. controls I used the NBS method (Zalesky et al., 2010). This is covered in detail in the methods section of chapter 4. A general linear model was used to model group differences with age, sex, education and study site included as covariates. Permutation testing, using unpaired t-tests, was performed with 5000 permutations. A test statistic was then computed for each connection and a threshold applied ($t = 3.1$) to produce a set of suprathreshold connections, thereby identifying anatomical networks, which show significant differences in structural connectivity between groups. A family-wise error correction was also applied ($p < 0.05$).

5.2.7. Selective vulnerability: streamline density, network traffic, regional clustering and distance from the striatum

In order to build on the findings in chapter 3, properties of the healthy white matter brain network were correlated with group differences (HD vs. controls, HD vs. preHD, preHD vs. controls) both at the connection level and at the brain region level. Correlations were performed between the average control group streamline density for each brain connection against group differences in streamline density for that brain connection, both for all brain connections in the network and for cortico-basal ganglia connections only. For cortico-basal ganglia connections only, separate analyses were performed using streamline data generated from the graph theory pipeline (volume un-normalised and normalised) and from the cortico-basal ganglia connectivity pipeline (volume normalised only).

At the brain region level average control brain region network traffic was correlated with group differences in (graph theory) strength and degree for each brain region, were high brain region traffic indicates strong connections to distant regions. I also performed correlations between regional clustering coefficient and group differences between degree and (graph theory) strength for each brain region, were clustering coefficient is a measure strength of connections to neighbours.

Proximity to the basal ganglia as an indicator of connectivity vulnerability was also investigated as this represents the disease epicentre in HD. Partial Pearson correlations, controlling for Euclidean distance, were performed for average control path length to the basal ganglia and group differences in connection density for each cortico-basal ganglia connection, separate analyses were performed using streamline data generated from the graph theory pipeline (volume un-normalised and normalised) and from the cortico-basal ganglia connectivity pipeline (volume normalised only). For this analysis, a Bonferroni correction was applied for (twenty-seven) multiple comparisons.

5.2.8. Group-Averaged Voxel Connectivity Profiles (VCPs)

For the VCPs, 5000 streamlines were seeded for each voxel within the sub-cortical ROIs and terminated when they reached the cortical mask or exited the hemisphere mask. The probability of connectivity between every seed voxel and every target region was established for each subject and the data were stored as individual subject connectivity probability maps. The connectivity maps were first binarised such that any voxel within the sub-cortical ROI with at least 1% of streamlines reaching a given cortical target was regarded as being connected to that target. The number of voxels connected to the cortical target were then calculated and normalised by the sum of the volumes of the corresponding sub-cortical ROI and cortical target, providing a normalised estimate of the volume of the region connected to target. The procedure was repeated for all cortical targets, resulting in a vector describing the connectivity between the striatum and cortex for each subject.

Group-averaged VCPs were generated to allow qualitative analysis of patterns of basal ganglia connectivity. To generate group-averaged VCPs, the individual connectivity probability maps were first warped into standard space using Niftyreg. Specifically, I used a two-step approach, warping the connectivity maps to their corresponding subject T1W image space, before warping the resulting image into Montreal Neurological Institute space. The standard space connectivity maps were then averaged together to create a mean connectivity map for each group. VCPs were generated using the approach described by Draganski et al (Draganski et al., 2008). Finally, the labels of the VCPs were standardised for each structure (i.e. so that the labels for the structure are comparable between groups) by finding the unique patterns of connectivity across all three groups, assigning a new label to each pattern in the set and then remapping the labels of the VCPs to the new scheme.

5.2.9. Statistical Analysis of Cortico-Basal Ganglia Connectivity

Statistical analysis of the cortico-basal ganglia connectivity information was performed on the individual connectivity maps using a mass-univariate approach. This involved permutation testing as outlined in the graph theoretical analysis. Age, gender, study site and education were included as covariates when assessing group differences. CAG length was also included as a covariate in the correlation analyses. An FDR correction was applied for 210 cortico-basal ganglia connections and a Bonferroni correction applied for six clinical tests. The

inputs to both analyses were vectors describing the volume of the basal ganglia ROIs that connected to each of the cortical targets. Specifically, the individual connectivity maps were first binarised such that any voxel within the basal ganglia ROI with at least 1% of streamlines reaching a given cortical target was regarded as being connected to that target. The number of voxels connected to the cortical target were then calculated and normalised by the sum of the volumes of the corresponding basal ganglia ROI and cortical target, providing a normalised estimate of the volume of the region connected to target. The procedure was repeated for all cortical targets, resulting in a vector describing the connectivity between the basal ganglia and cortex for each subject.

5.3. Results

5.3.1. Cohort

The cohort consisted of 38 early HD participants (25 female; mean age 49.5±10.4 years; mean CAG repeat length 43.4±2.4, mean DBS 370.6±10.4) 50 preHD participants (24 female; mean age 42.2±8.9 years; mean CAG repeat length 40.3±2.1, estimated years to onset 11.1±3.9, mean DBS 301.3±7.4) and 47 healthy controls (32 female; mean age 47.6±9.0 years). PreHD participants were significantly younger in age when compared with controls ($p = 0.006$) and HD ($p = 0.0005$) participants. There were no group differences in gender, education or study site (see table 5.1). The analysis was pseudo-longitudinal in that I included two different stages of the same condition with preHD and HD having a temporal spacing of at least 10 years (Langbehn et al., 2004).

Table 5.1. Structural brain network degeneration study: Patient demographics. N – participant number, SD – standard deviation, M – male, F – female, CAG – CAG repeat length, EYO - Estimated years to onset, DBS – disease burden score. PreHD shows significant age differences between controls (p = 0.006) and HD (p = 0.0005) accounting for overall significance in the model.

	HD	PreHD	Control	Statistical test	P-value
N	38	50	47	-	-
Age (SD)	49.5 (10.4)	42.2 (8.9)*	47.6 (9.0)	ANOVA	0.001
Gender (M/F)	13/25	26/24	15/32	Chi-square	0.09
Education (SD)	38 (1.01)	50 (0.84)	47 (1.12)	Chi-square	0.209
Study Site (N) (Leiden/London/Paris)	10/15/13	13/21/16	12/20/15	Chi-square	0.999
EYO (SD)	-	11.1 (3.9)	-	-	-
CAG (SD)	43.2 (2.4)	40.3 (2.1)	-	-	-
DBS	370.6 (10.4)	301.3 (7.4)	-	-	-

5.3.2. Rich club organisation

All groups showed significant rich club organisation (Control; degree 20-63, preHD; degree 19-63, HD; degree 19-63). Rich club regions were in perfect agreement across groups. The regions were as follows (in order of highest degree); Right and left thalamus, precuneus and caudate, right superior parietal, left superior frontal, right superior frontal, left superior parietal, right insula, left insula. These regions are very similar to the hub regions identified in chapter 3, with the exception of the superior parietal replacing the precentral regions.

5.3.3. Regional brain network measures

Significant reductions in degree (number of brain connections) were seen between preHD and controls in the left and right caudate and left anterior cingulate (see figure 5.2(a)). HD vs. preHD showed significant reductions in the left and right caudate, right thalamus, right putamen, right paracentral and left supramarginal regions (see figure 5.2(b)). Numerous regions showed significant decreases in HD vs. controls including cortical and basal ganglia rich club regions, as well as cingulate, motor, temporal and occipital areas (see figure 5.2(c)). Volume normalised results and the three additional graph metrics examined (strength, betweenness centrality (network traffic) and clustering coefficient) are presented in table 5.2.

Table 5.2. Regional graph metrics group differences. A Bonferroni correction of $p < 0.0125$ is applied for 4 graph metrics. NS – not significant

	Graph metric	Degree	Strength	Betweenness centrality	Clustering coefficient
a	Premanifest HD vs.controls	See main text	Left (p=0.008) and right caudate (p=0.008)	NS	Left caudate (p=0.008)
Volume un-normalised	HD vs. Premanifest HD	See main text	NS	NS	NS
	HD vs. controls	See main text	Left (p=0.003) and right caudate (p=0.003), left (p=0.004) and right putamen (p=0.003)	NS	Right caudate (p=0.01) and left (p=0.008) and right putamen (p=0.008)
b	Premanifest HD vs. controls	Left (p=0.001) and right caudate (p=0.008)	NS	NS	NS
Volume normalised	HD vs. Premanifest HD	Left (p=0.008) and right caudate (p=0.013), right putamen (p=0.008), right thalamus (p=0.008) and right paracentral (p=0.008)	**Increase** in left thalamus (p=0.008) and left hippocampus (p=0.008)	NS	NS
	HD vs. controls		**Increase** in left (p=0.008) and right (p=0.011) caudate	Right inferior temporal (p=0.011) and right lingual (p=0.007)	NS

Figure 5.2. Significant group differences in degree for (a) PreHD disease vs. controls (p = 0.01 for all regions), (b) HD vs. preHD (* p= 0.009, ** p= 0.006, *** p= 0.005, **** p= 0.001) and (c) HD vs. controls. For (c) only those regions with p < 0.0003 are displayed to highlight most significant regions. HD, preHD disease and controls are presented in each graph to illustrate consistent step-wise reductions in degree across groups. A brain network is displayed above each bar chart. Spheres represent brain regions with red spheres indicating the brain regions showing significance between groups. Data are represented as a group mean (confidence intervals are not included as not standard for permutation tests).

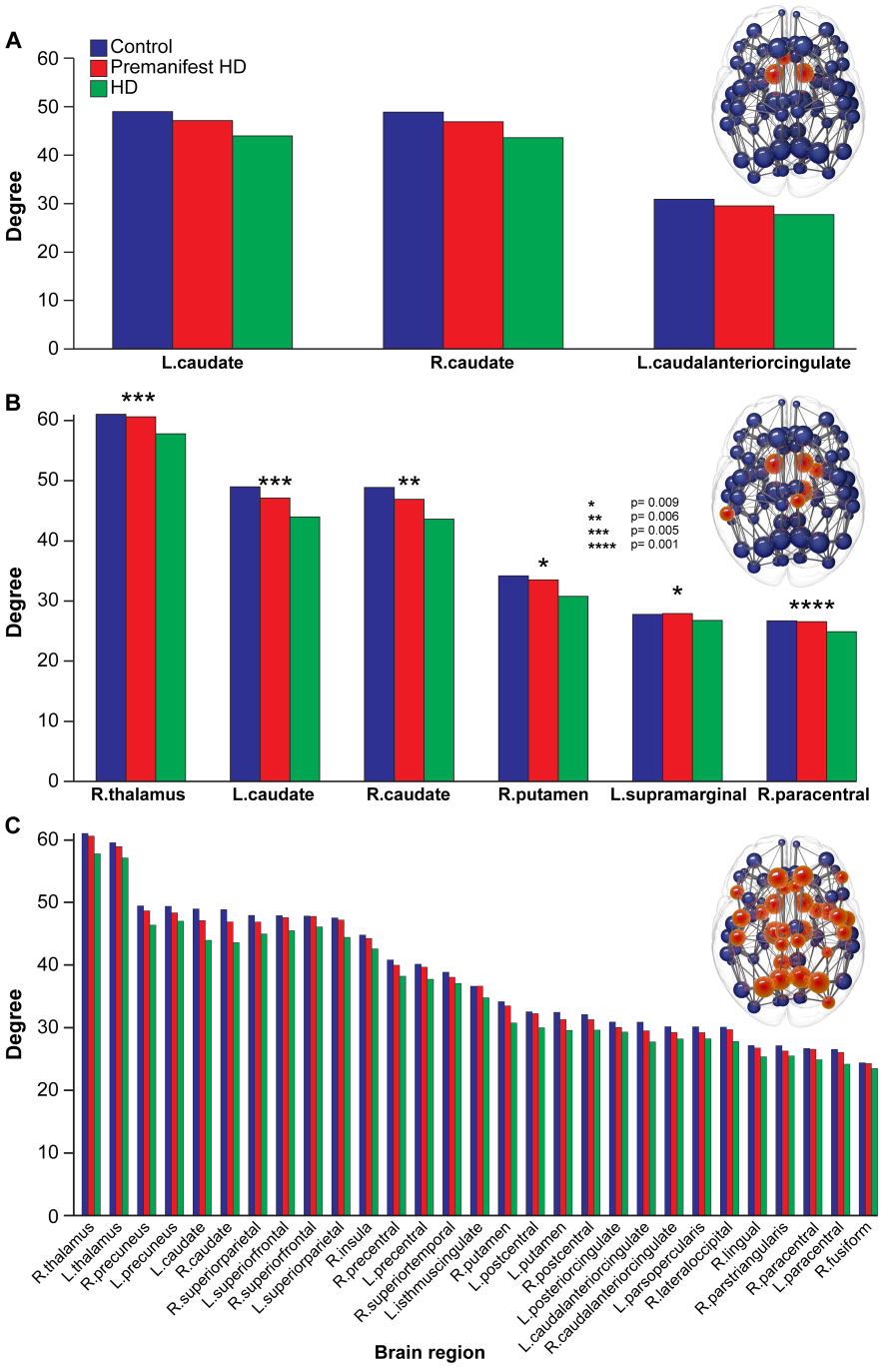

5.3.4. Network integration and segregation

Significant increases were seen in normalised clustering coefficient in HD vs. controls ($p = 0.0001$), HD vs. preHD ($p = 0.0007$) and preHD vs. controls ($p = 0.0082$) (see figure 5.3(a)). Modularity showed significant increases in HD vs. controls ($p = 0.0001$) and in preHD vs. controls ($p = 0.0037$) (see figure 5.3(b)).

Normalised average path length showed significant increases in HD vs. controls ($p = 0.0004$) and HD vs. preHD ($p = 0.0032$) (Figure 5.3(c)). Significant decreases were seen in global efficiency in HD vs. controls ($p = 0.006$) (see figure 5.3(d)). No significant group differences were seen in small worldness.

Table 5.3. Whole brain network group differences across 0%, 25%, 50%, 75%, 100% control group thresholds. A Bonferroni correction for the 5 whole brain network metrics is applied ($p < 0.01$). NS – not significant

	Control group threshold (%)	0	25	50	75	100
Normalised clustering coeffficient	Premanifest HD vs. controls	NS	NS	NS	0.0082	NS
Volume un-normalised	HD vs. Premanifest HD	0.0072	0.0041	0.0019	0.0007	0.0001
a	HD vs. controls	0.0001	0.0001	0.0001	0.0001	0.0001
	Premanifest HD vs. controls	0.0057	0.002	0.002	NS	NS
Volume normalised	HD vs. Premanifest HD	NS	0.0096	0.0057	0.0015	NS
	HD vs. controls	0.0001	0.0001	0.0001	0.0001	0.0001
Modularity	Premanifest HD vs. controls	0.0039	0.0035	0.004	0.0037	0.0084
Volume un-normalised	HD vs. Premanifest HD	NS	NS	NS	NS	NS
b	HD vs. controls	0.0001	0.0001	0.0001	0.0001	0.0001
	Premanifest HD vs. controls	NS	NS	NS	NS	NS
Volume normalised	HD vs. Premanifest HD	0.0048	0.0035	0.0075	NS	NS
	HD vs. controls	0.0001	0.0001	0.0001	0.0001	0.0001
Normalised average pathlength	Premanifest HD vs. controls	NS	NS	NS	NS	NS
Volume un-normalised	HD vs. Premanifest HD	0.0009	0.0023	0.0009	0.0032	0.0005
c	HD vs. controls	0.0001	0.0002	0.0001	0.0004	0.0001
	Premanifest HD vs. controls	NS	NS	NS	NS	NS
Volume normalised	HD vs. Premanifest HD	NS	0.0053	NS	NS	NS
	HD vs. controls	NS	0.0019	NS	NS	NS
Global efficiency	Premanifest HD vs. controls	NS	NS	NS	NS	NS
Volume un-normalised	HD vs. Premanifest HD	NS	NS	NS	NS	NS
d	HD vs. controls	0.0069	0.0049	0.0053	0.006	0.0048
	Premanifest HD vs. controls	NS	NS	NS	NS	NS
Volume normalised	HD vs. Premanifest HD	NS	NS	NS	NS	NS
	HD vs. controls	NS	NS	NS	NS	NS
Smallworldness	Premanifest HD vs. controls	NS	NS	NS	NS	NS
Volume un-normalised	HD vs. Premanifest HD	NS	NS	NS	NS	NS
e	HD vs. controls	NS	NS	NS	NS	NS
	Premanifest HD vs. controls	NS	NS	NS	NS	NS
Volume normalised	HD vs. Premanifest HD	NS	NS	NS	NS	NS
	HD vs. controls	0.0035	NS	0.0008	NS	NS

Figure 5.3. Group differences in network segregation and integration. Segregation: (a) normalised clustering coefficient (b) modularity. Integration: (c) normalised average path length and (d) global efficiency. * = p < 0.01. Data are represented as a group mean (confidence intervals are not included as not standard for permutation tests).

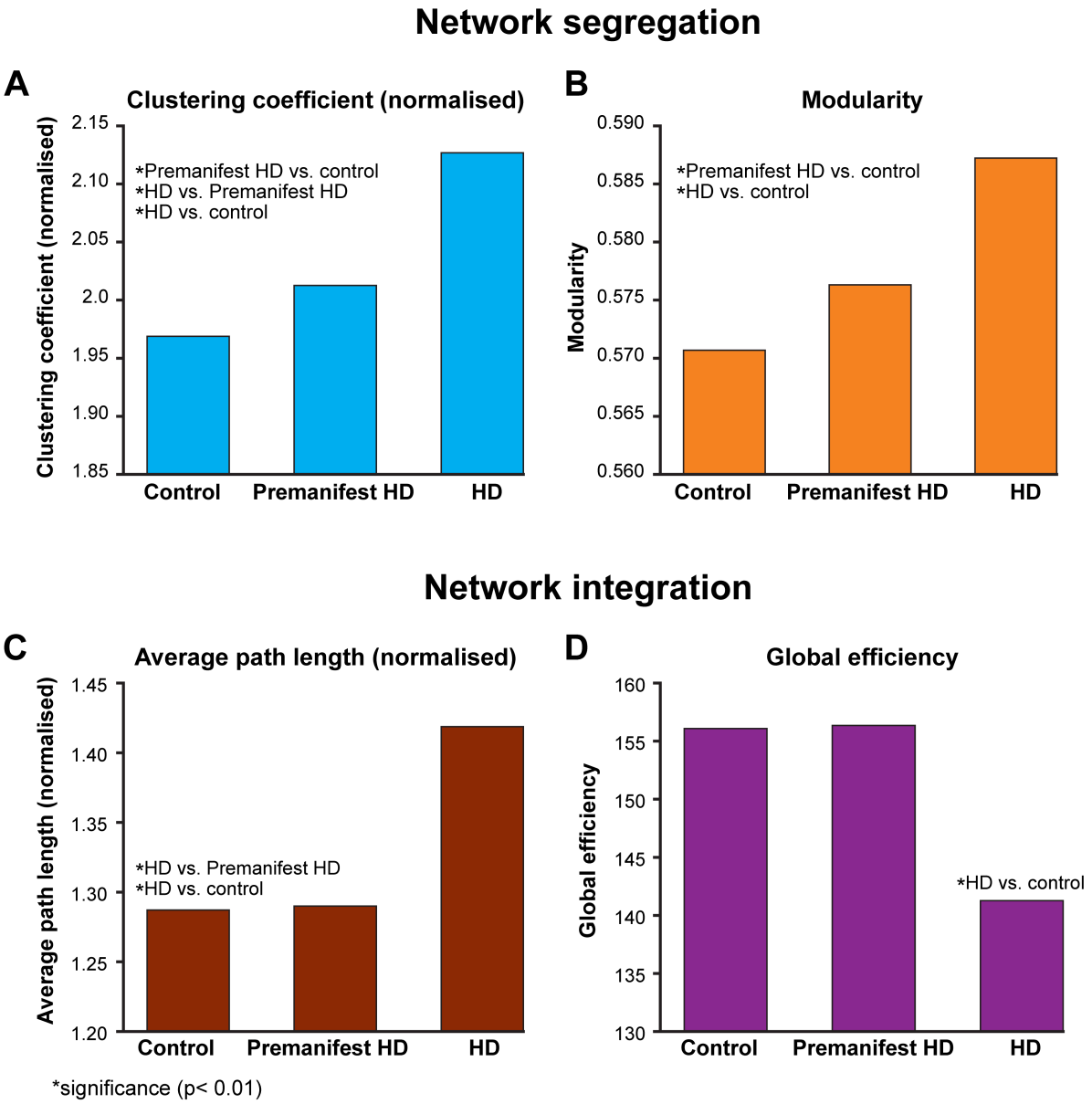

5.3.5. Cortico-Basal ganglia connections

When comparing preHD vs. controls significant reductions were predominantly seen in cortico-caudate connections in the NBS analysis (see figure 5.4). These included a number of basal ganglia connections to cortical rich club and non-rich club regions (see table 5.4).

Figure 5.4. Network-based Statistics analysis showing significantly reduced connectivity between preHD vs. controls in cortico-caudate connections. Red - caudate, blue – cortical rich club regions, yellow – cortico-caudate connections.

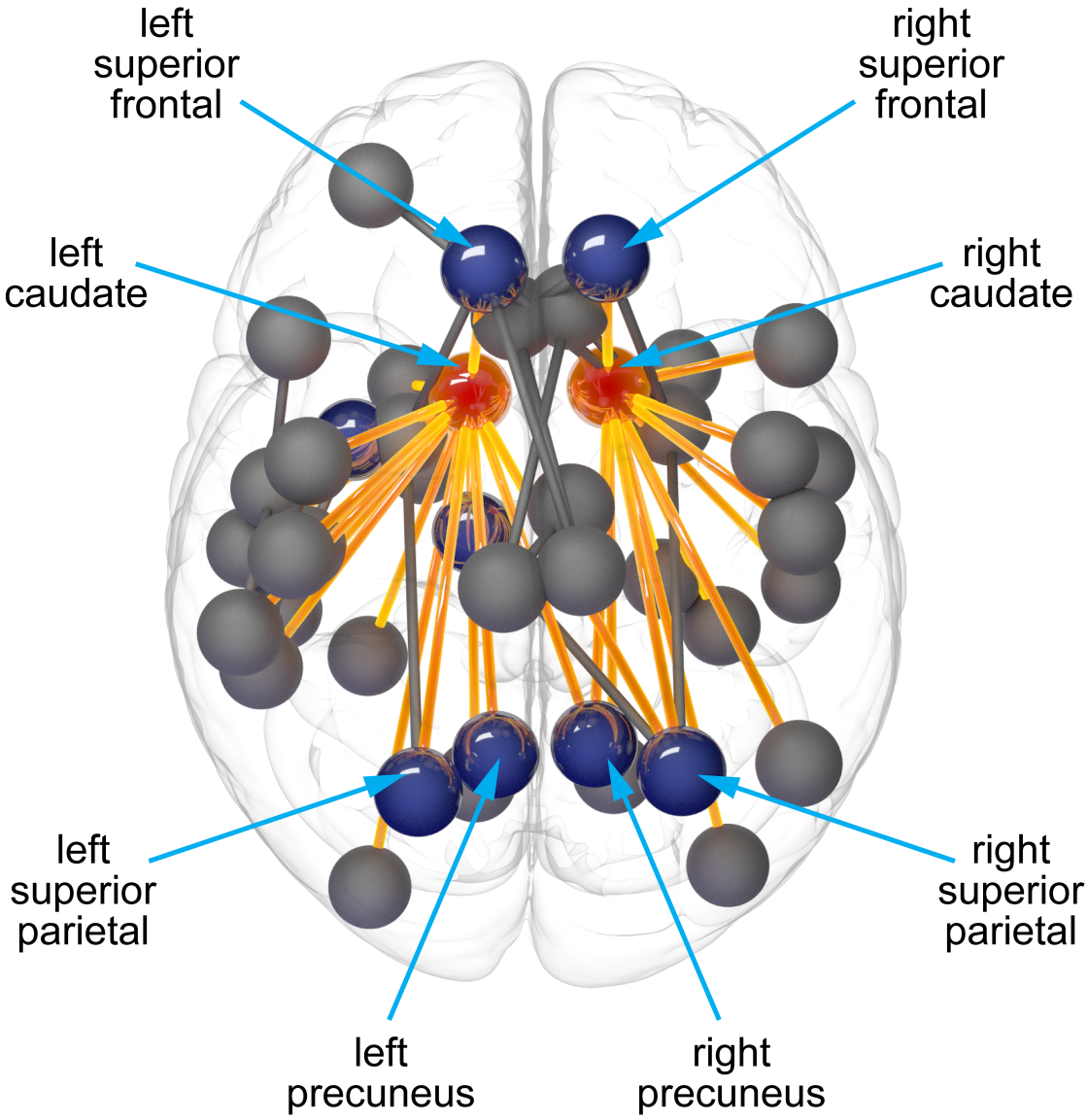

Table 5.4. Network based statistic analysis: PreHD vs. control group differences (volume un-normalised) (cortical rich club connections are highlighted in red).

Connection	Test statistic	Connection	Test statistic
R.caudate-R.inferiortemporal	5.89	L.putamen-L.superiorparietal	3.7
L.caudate-R.superiorparietal	5.36	L.caudate-L.postcentral	3.67
L.caudate-L.superiortemporal	5.24	L.caudate-L.putamen	3.67
R.caudate-R.fusiform	4.75	L.caudate-L.lateralorbitofrontal	3.6
L.caudate-L.transversetemporal	4.7	L.caudate-L.entorhinal	3.59
L.caudate-L.precuneus	4.69	R.putamen-L.superiorfrontal	3.55
L.paracentral-R.posteriorcingulate	4.51	L.superiorfrontal-R.paracentral	3.53
R.caudate-R.temporalpole	4.48	R.caudate-R.inferiorparietal	3.52
R.caudate-R.precuneus	4.45	L.bankssts-L.precentral	3.51
L.putamen-L.superiorfrontal	4.28	R.caudate-R.parahippocampal	3.49
R.caudate-R.superiortemporal	4.2	L.thalamus-R.superiorparietal	3.46
L.caudate-L.lingual	4.17	R..caudate-R.parsopercularis	3.44
R.caudate-R.precentral	4.17	L.caudate-L.middletemporal	3.43
L.caudate-L.superiorfrontal	4.16	L.transverse-temporal-L.insula	3.41
L.caudate-L.fusiform	4.12	L.parsopercularis-L.superiortemporal	3.37
R.caudate-R.lingual	4.09	L.caudate-L.bankssts	3.32
R.caudate-R.postcentral	4.03	L.caudate-L.supramarginal	3.29
L.caudate-L.precentral	3.97	R.putamen-R.superiorfrontal	3.28
L.caudate-L.inferiortemporal	3.91	L.caudate-L.superiorparietal	3.26
R.caudate-R.superiorparietal	3.87	L.caudate-L.temporalpole	3.18
R.caudate-R.superiorfrontal	3.79	R.putamen-L.rostralmiddlefrontal	3.18
L.paracentral-R.caudalanteriorcingulate	3.76	L.caudalanteriorcingulate-R.superiorfrontal	3.17
R.putamen-R.caudalanteriorcingulate	3.74	R.caudate-R.isthmuscingulate	3.14
R.paracentral-L.caudalanteriorcingulate	3.74	L.superiortemporal-L.supramarginal	3.12
R.putamen-R.superiorparietal	3.71	L.caudate-R.precuneus	3.11

The cortico-basal ganglia connectivity univariate analysis ($p < 0.05$), using streamline density, showed that of those connections showing group differences, 57% (13/23) connected to rich club regions for preHD participants vs. controls, 51% (18/35) for manifest HD vs. preHD participants and 68% (75/111) for HD participants vs. controls (Figure 5.5). For manifest HD participants vs. controls increases were seen in streamline density in connections to the anterior and posterior cingulate

Figure 5.5. Cortico-basal ganglia connectivity univariate analysis. Group differences between (a) PreHD vs. controls (* p= 0.008, ** p= 0.006, *** p= 0.004, **** p=0.003) (b) HD vs. preHD and (c) HD vs. controls. Only those connections with (a) p < 0.009, (b) and (c) p < 0.002 are displayed to highlight most significant connections. Data are represented as a group mean (confidence intervals are not included as not standard for permutation tests).

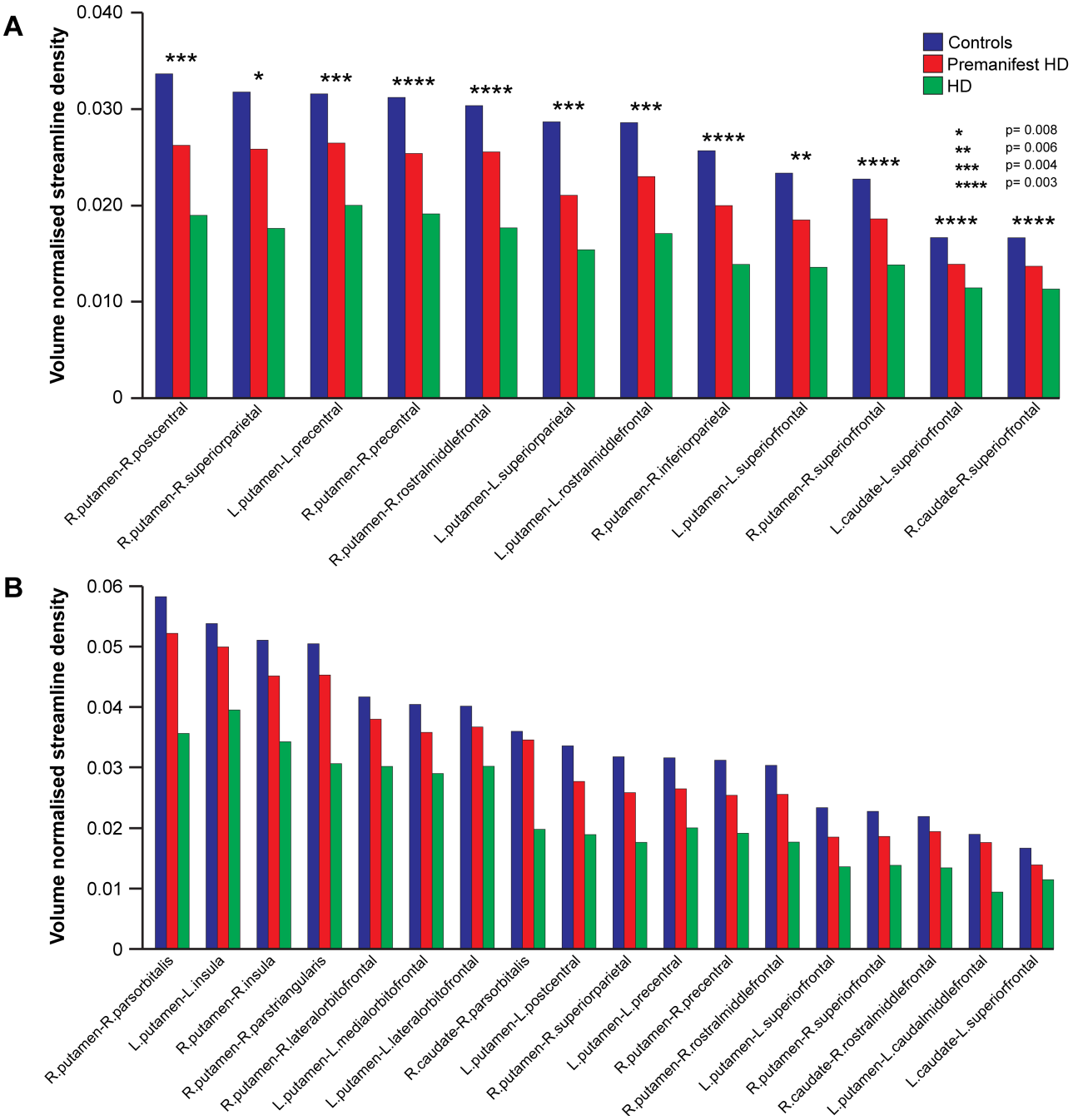

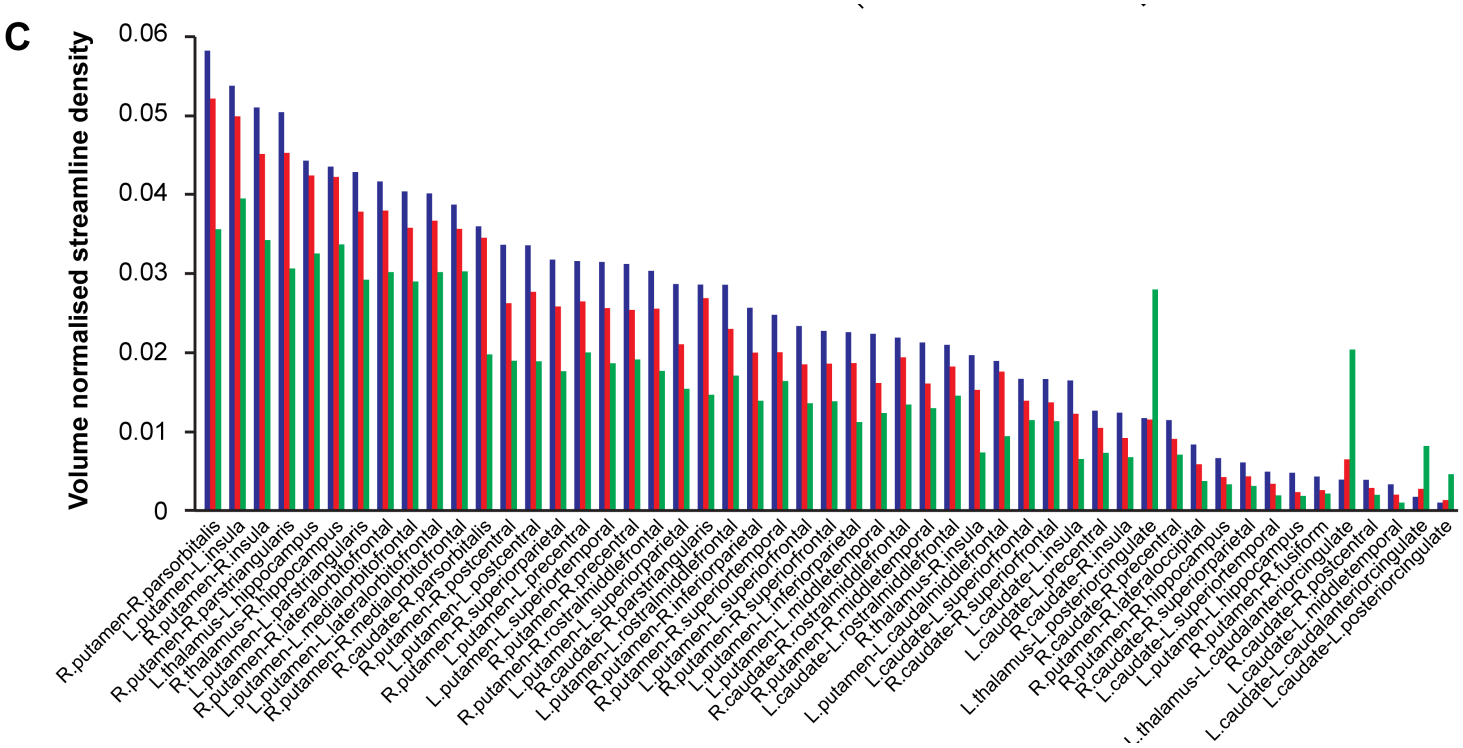

5.3.6. Altered patterns of cortico-basal ganglia connectivity

Group averaged VCPs showed altered patterns of cortical connectivity to the caudate, putamen and thalamus, with all connectivity patterns including one or more cortical rich club regions. In the caudate there was loss of connectivity to the superior frontal and insula rich club regions in manifest HD participants compared with controls and preHD (see light and dark blue voxels in figure 5.6(a)). The putamen shows loss of connectivity to the superior frontal, superior parietal and insula rich club regions both in manifest HD and preHD compared to controls (see purple voxels in figure 5.6(b)), while the thalamus showed loss of connectivity to the superior parietal, precuneus and superior frontal rich club regions in manifest HD compared to preHD and controls (see yellow voxels in figure 5.6(c)).

Figure 5.6. Voxel Connectivity Profiles across groups for (a) Caudate (b) Putamen and (c) Thalamus. Labels are combined as follows: parietal – superior and inferior, orbitofrontal – lateral and medial, temporal – inferior, middle and superior. Each label list corresponds to the colour in the legend to the left of it. Label lists are displayed in black and red font alternately for ease of viewing.

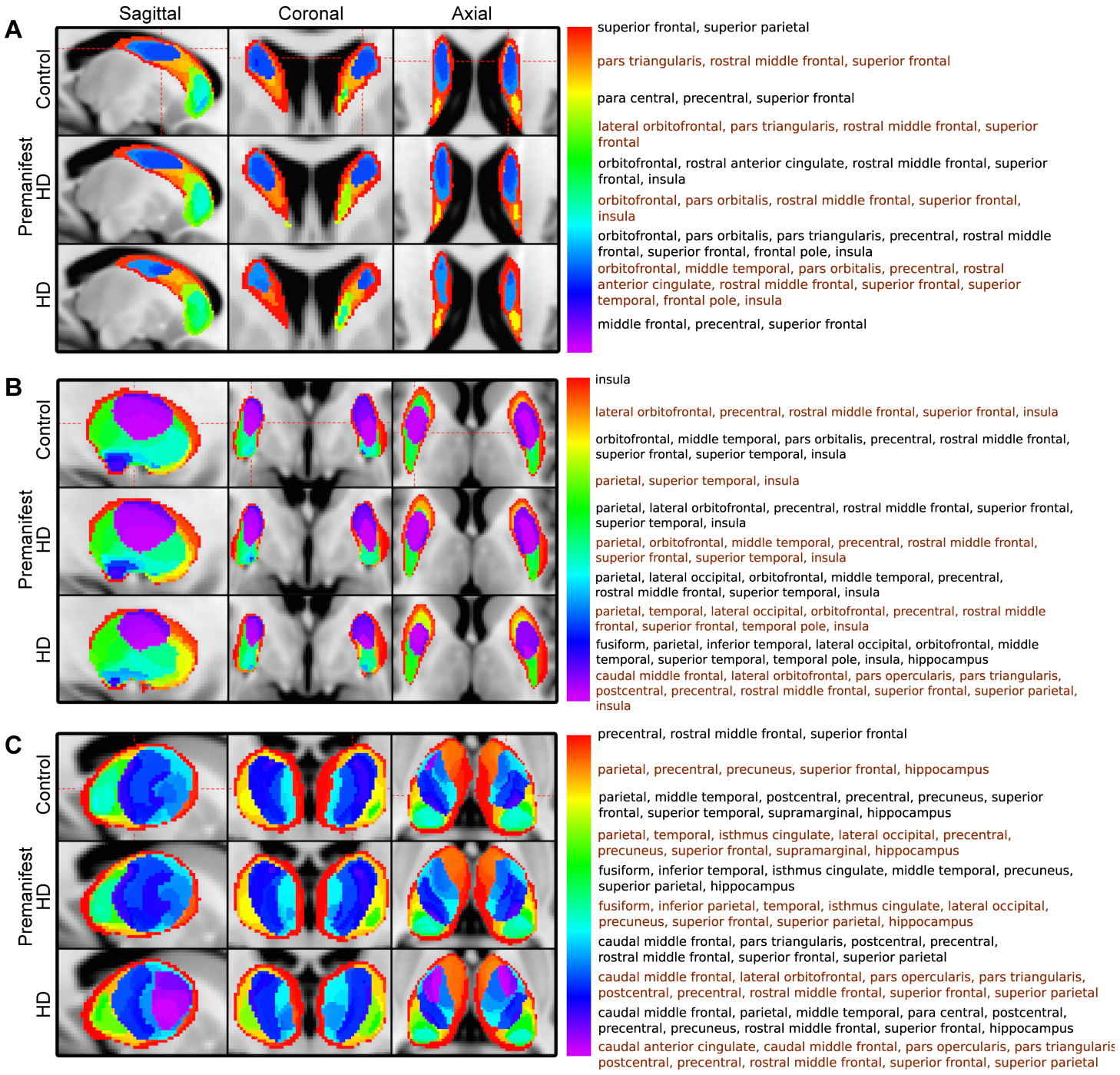

5.3.7. Clinical correlations with graph theory metrics

Clinical measures revealed correlations with the degree (number of brain connections) of rich club and non-rich club brain regions (*df* = 86, for all clinical correlations). For TMS correlations were seen with the left (Rho = -0.48, p = 2.6 $x10^{-4}$) and right inferior parietal (Rho = -0.44, p = 0.001), left caudal middle frontal (Rho = -0.43, p = 0.001), left precentral (Rho = -0.4, p = 0.002), left superior frontal (Rho = -0.41, p = 0.002) and left rostral middle frontal regions (Rho = -0.4, p = 0.002). Indirect circle tracing correlated with the left superior frontal (Rho = 0.45, p = 0.002) and right lingual (Rho = 0.43, p = 0.002), while Negative Emotion Recognition test performance correlated with the right caudate (Rho = 0.49, p = 2.3 $x10^{-4}$), left inferior parietal (Rho = 0.44, p = 0.001) and left precentral (Rho = 0.43, p = 0.001). No significant ($P<0.05$) correlations were seen with any other regional graph metric and SWR, SDMT or Speeded Tapping mean inter-tap interval.

Network segregation: normalised clustering coefficient showed significant correlations with TMS (Rho = 0.42, p = 7.55 $x10^{-5}$) and indirect circle tracing (Rho -0.43, p = 7.62 $x10^{-5}$), while modularity significantly correlated with TMS (Rho = 0.34, p = 1.15 $x10^{-6}$). Network integration: Correlations were seen for normalised average path length and TMS (Rho = 0.51, p = 1.15 $x10^{-6}$) and emotion recognition (Rho = -0.34, p = 0.002).

5.3.8. Clinical correlation with cortico-basal ganglia connectivity

For the cortico-basal ganglia connectivity analysis our univariate results showed significant negative correlations with TMS and streamline density for 27 cortico-basal ganglia connections, 16 (59%) of which were connected to rich club regions.

5.3.9. Higher connection density, greater network traffic and less regional clustering result in greater susceptibility to structural connectivity loss.

Significant ($p < 0.05$ corrected) positive correlations were identified between average control streamline density and group differences in streamline density for HD vs. controls. Group differences in streamline density in preHD vs. controls did not show a correlation (see figure 5.7(a)). Similar results were seen for cortico-basal ganglia connections in both the graph theory and cortico-basal ganglia connectivity analysis. A positive correlation was seen between average control streamline density and group differences in streamline density for preHD vs. controls in the cortico-basal ganglia connectivity analysis (see figure 5.7(b)).

Significant positive correlations were seen with average control brain region network traffic and group differences in (graph theory) strength across all groups (see figure 5.7(c)), however this was not maintained after volume normalisation (see table 5.4). No significant correlations were seen with average control brain region network traffic and group differences in degree. This suggests that regions with high brain network traffic (betweenness centrality) are more show greater structural connectivity loss and are in keeping with the findings in chapter 3.

Significant negative correlations were seen with average control clustering coefficient and group differences in degree across all groups (see figure 5.7(d)). No significant correlations were seen with average control clustering coefficient and group differences in (graph theory) strength. This suggests that regions with strong connections to their neighbours show less connectivity loss and are in keeping with the findings in chapter 3.

There were no significant correlations between path length to the basal ganglia and group differences in streamline density for either the graph theory or cortico-basal ganglia connectivity analysis. Volume normalised results are provided in table 5.5.

Table 5.5. Selective vulnerability: connection density, network traffic (betweenness centrality), regional clustering and distance from the striatum (volume normalised). Bonferroni corrected $p < 0.05/27$. *Cortico-basal ganglia connectivity analysis.

Volume normalised	HD vs. controls	HD vs. Premanifest HD	Premanifest HD vs. controls
Streamline density	Rho = -0.25, p = 1.49 x10^{-40}	Rho = -0.45, p = 2.32 x10^{-142}	Rho = 0.38, p = 1.45 x10^{-98}
Basal ganglia streamline density	NS	NS	NS
Basal ganglia streamline density*	Rho = 0.65, p = 1.05 x10^{-26}	Rho = 0.64, p = 2.24 x10^{-25}	Rho = 0.45, p = 1.05 x10^{-11}
Betweenness centrality (degree)	NS	NS	NS
Betweenness centrality (strength)	NS	NS	NS
Clustering coefficient (degree)	Rho = -0.64, p = 3.35 x10^{-10}	Rho = -0.66, p = 7.14 x10^{-11}	Rho = -0.37, p = 0.001
Clustering coefficient (strength)	NS	NS	NS
Basal ganglia pathlength	NS	NS	NS
Basal ganglia pathlength*	NS	NS	NS

Figure 5.7. Selective vulnerability analysis: (a) Correlation of average control streamline density against group differences in streamline density (based on graph theoretical analysis (volume un-normalised)) - each data point represents a single brain connection. (b) Correlation of average control cortico-basal ganglia streamline density against group differences in streamline density (based on cortico-basal ganglia connectivity analysis (volume normalised)) - each data point represents a single cortico-basal ganglia connection. (c) Correlation of average control brain region network traffic against group differences in (graph theory) strength (based on graph theoretical analysis (volume un-normalised)) - each data point represents a single ROI. (d) Correlation of average control clustering coefficient against group differences in degree (based on graph theoretical analysis (volume un-normalised)) - each data point represents a single ROI.

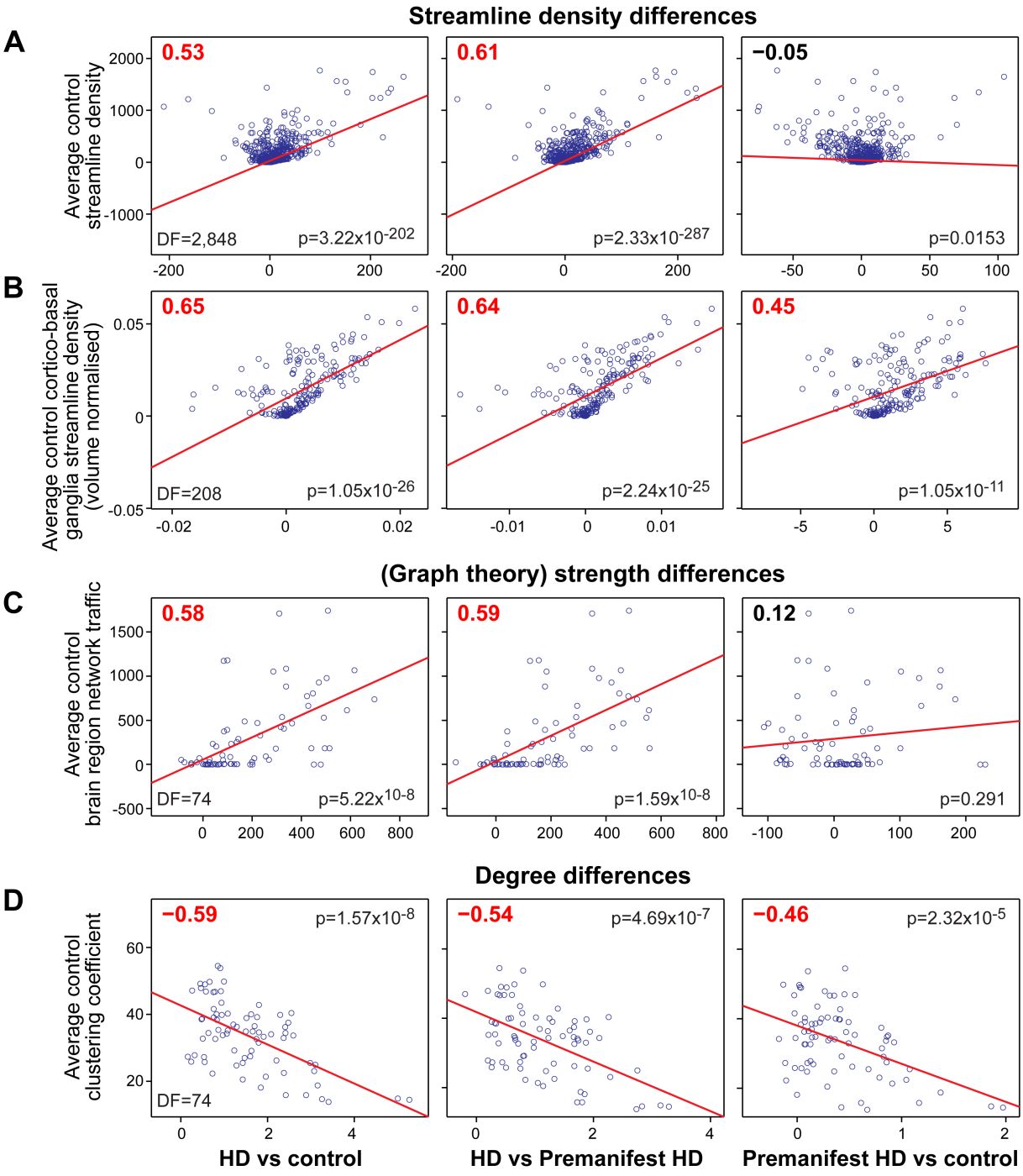

5.4. Discussion

5.4.1. Brain network breakdown and disease manifestation

In this chapter I performed a graph theory analysis, complemented by NBS, cortico-basal ganglia connectivity and VCP analyses to focus on structural connectivity loss of rich club regions in HD. I found altered brain network connectivity specifically affecting rich club regions, predominantly in the basal ganglia (caudate) in preHD, but extending to cortical rich club regions (superior frontal, superior parietal, precuneus and insula) in manifest HD. By using NBS, cortico-basal ganglia connectivity and VCP analyses, I was also able to demonstrate selective loss of connections and altered patterns of connectivity between the basal ganglia and cortical rich club regions. In conjunction with these regional group differences I identified altered whole brain network topology with isolated increase of network segregation in the preHD participants when compared to controls; this extended to increase in segregation and loss of integration when comparing manifest against both preHD and controls. This suggests that increases of whole brain network segregation occur in the earliest stages of the neurodegenerative disease process, before symptom onset, and subsequently progress to loss of network integration in the manifest stages. I postulate that conversion from preHD to manifest HD, in addition to the emergence of chorea through an imbalance in the indirect and direct pathways of the basal ganglia (Andre et al., 2011), may reflect a breakdown of such network integration (see figure 5.8).

Figure 5.8. The schematic summarises our findings: There is selective loss of basal ganglia rich club connectivity due to high higher connection to the basal ganglia, higher network traffic and reduced clustering coefficients of rich club regions. This results in increased network segregation leading to the subtle motor and cognitive symptoms seen in preHD. Further loss of cortical rich club connectivity results in reduced network integration resulting in the overt cognitive and motor symptoms seen in manifest HD.

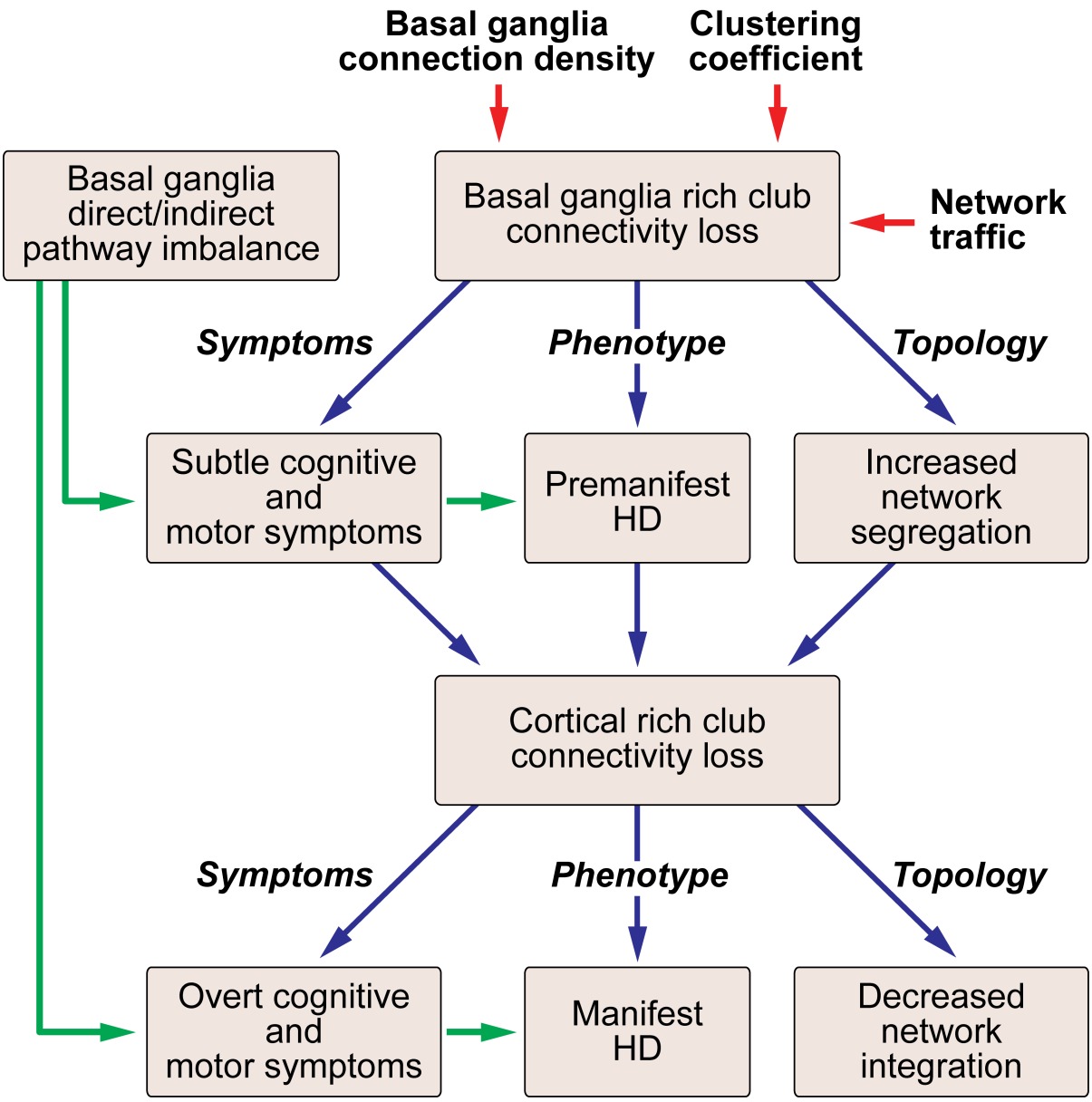

5.4.2. Rich club vulnerability and the global network

While reduction in the degree of rich club brain regions was seen at a regional level, increase in network segregation was seen at a global level in both preHD and manifest HD. Connections among rich club brain regions make up the majority of long-range connections in the human connectome (van den Heuvel et al., 2012). This suggests that the loss of these long-range rich club connections, connecting distant brain regions, results in increased network segregation in preHD, and loss of integration in the manifest HD. In contrast to degree of the rich club regions, relatively few group differences were seen in network traffic (betweenness centrality), (graph theory) strength and clustering coefficient. Network traffic is the most sensitive graph theory measure in traumatic brain injury (Fagerholm et al., 2015). However our data show that HD predominantly results in loss of brain connections (degree) as opposed to alterations of regional brain network topography.

5.4.3. Rich club connectivity loss and clinical deficits

Rich club regions are brain hubs that form the backbone of the brain network (van den Heuvel et al., 2012) allowing integration of specialised cortical regions (Senden et al., 2014). I demonstrate positive correlation with emotion recognition performance and degree of the right caudate and left superior frontal region. It is unsurprising that loss of degree to these rich club regions is associated with impaired emotion recognition. Previous work by our group, using task fMRI in preHD, showed a number of the regions defined as rich club (for example caudate, thalamus, superior frontal, superior parietal, precuneus and insula) are activated when performing an emotion recognition task (Novak et al., 2012). I also report negative correlation between emotion recognition performance and normalised clustering coefficient (a measure of network segregation). This suggests increased segregation of the network leads to impaired communication between specialised brain regions resulting in impaired emotion recognition performance. Similar results are seen when correlating TMS with degree of the left superior frontal, normalised clustering coefficient and normalised average path length (a measure of network integration). Thus loss of rich club connectivity, coupled with increased network segregation and reduced integration is likely contribute to the clinical manifestation of HD. The lack of correlation of SWR, SDMT or Speeded Tapping mean inter-tap interval with rich club graph theory measures suggest that these tasks may be less dependent on optimal communication between diverse brain regions.

The rich club regions reported in this study are similar to those reported in other studies in the literature. The cortical rich club regions in particular, such as superior frontal, superior parietal and insula have been reported in many studies (Collin et al., 2014; van den Heuvel and Sporns, 2011; van den Heuvel et al., 2013). There is slightly more variation in the basal ganglia regions reported. In the seminal rich club paper the hippocampus, putamen and thalamus are reported (van den Heuvel and Sporns, 2011), compared to the caudate and thalamus in this study. While the rich club members were defined as those with the highest degree in both studies, I used a probabilistic tractography algorithm while (van den Heuvel and Sporns, 2011) used a deterministic algorithm. Thus differences in the performance of these algorithms in deep white matter may explain the discrepancy between studies. Other studies have used nodes with the highest betweenness centrality (Fagerholm et al., 2015), strength (Harrington et al., 2015) or a composite of graph theory measures (Betzel et al., 2014) to define rich club or hub regions. Studies using more complex centrality measures tend to report the posterior cingulate cortex (PCC) among the top hub regions (Betzel et al., 2014; Fagerholm et al., 2015; Hagmann et al., 2008). This is an interesting observation in that the PCC is one of the major regions of the DFM (Fox and Raichle, 2007). Furthermore this suggests that using degree to define hubs may be too simplistic. Similar regions are seen with hub regions defined using other modalities such as rs-fMRI (Harrington et al., 2015) and MEG (de Pasquale et al., 2016), suggesting these regions are hubs with respect to both structure and function. Indeed there is significant overlap between the structural connectome and resting state networks in healthy subjects (van den Heuvel and Sporns, 2013).

5.4.3. Mechanisms of selective rich club vulnerability

By testing several mechanistic hypotheses, I shed light on the reasons for the region and connection selective changes I have shown in preHD and manifest HD. I demonstrated a strong positive correlation with streamline density (particularly to the basal ganglia) and group differences in streamline density. I show correlations between group differences in (graph theory) strength and brain region network traffic. Furthermore I show negative correlation between regional clustering coefficient and group differences in degree. These findings are in keeping with observations made in chapter 3, where brain regions with strong connections to distant regions and weak connections to their neighbours, as evidenced by high betweenness centrality and low clustering coefficient, are most susceptible to structural connectivity loss in HD. This findings extend my previous observations by showing that both regional and connection level properties of the healthy white matter brain network can inform on regional and connection vulnerability in both preHD and manifest HD.

In contrast to a previous study in Alzheimer's disease and fronto-temporal dementia (Zhou et al., 2012), I found a very low correlation with group differences in streamline density and path length to the area showing earliest atrophy, which in HD is the striatum (Tabrizi et al., 2011). The reason for this difference is likely methodological. Zhou and colleagues based their calculation of path length on resting state fMRI data of healthy controls and correlated path length with voxel based morphometry atrophy patterns seen in dementia patterns. In contrast, I used diffusion tractography to generate both variables, in order to examine correlation between path length to the striatum and group difference in streamline density, which I suggest may be a more robust approach.

In other neurodegenerative disorders, similar whole brain network disruption is seen. In Alzheimer's disease there is a loss of both network integration and segregation in the structural connectome, which is also seen to a lesser extent in mild cognitive impairment (Bai et al., 2012; Yao et al., 2010). Mild cognitive impairment is a syndrome with increased risk of developing Alzheimer's disease, which can perhaps be thought of as loosely comparable to preHD, in that it is a preclinical form of Alzheimer's disease. However studies of preHD are more specific, in that 100% of preHD gene carriers will develop the disease, whereas only a much smaller proportion of participants with mild cognitive impairment develop Alzheimer's disease. While the authors of a recent review suggest increased network segregation is a direct consequence of loss of integration (Griffa et al., 2013), our results suggest that these network phenomenon are not directly linked but rather develop *sequentially* as the disease progresses.

5.4.4. Implications for disease modifying treatments

The findings of this study have direct relevance for many of the emerging therapeutic strategies in HD. The conceptually most compelling therapeutic strategy is gene silencing using a range of potential agents/compounds (Godinho et al., 2014). However one challenge to the potential effectiveness of such therapies is their ability to distribute widely enough and to reach therapeutically relevant concentrations in the brain e.g. (Wild and Tabrizi, 2014). A recent animal study suggests that when mutant HTT is still present in the striatum but removed from the cerebral cortex there is improvement in motor and behavioural deficits (Wang et al., 2014). This is consistent with our results showing that there is preserved global efficiency when mainly cortico-striatal rich club connections are affected in preHD, when gene carriers have subtle symptoms. It may

therefore be the case that if antisense oligonucleotides are only able to target the cortex this may cause sufficient huntingtin lowering to preserve structural network integrity and prevent conversion to manifest HD.

5.4.4. Technical considerations

Our study is the first to investigate the structural connectome in HD using graph theory. Previously, (Poudel et al., 2014b) used deterministic tractography and NBS to investigate FA, radial diffusivity and streamline density changes in a frontal-parietal-striatal network in preHD and manifest HD and control participants. They show group differences of these metrics in the frontal-parietal-striatal network and correlations of these metrics with cognitive and motor variables. However the use of deterministic tractography with the diffusion tensor formalism is incapable of resolving crossing fibers (Behrens et al., 2007). Furthermore the study is limited to an NBS analysis of the frontal-parietal-striatal network and was therefore unable to address the selective vulnerability of rich club brain regions or global changes in the brain network as I have done in this work.

For the first time in a clinical population, I used both CSD, which deals more effectively with crossing fibres than the diffusion tensor or multi-tensor methods (Tournier et al., 2012) and SIFT, which has higher reproducibility and is more representative of the underlying biology of WM connections than conventional methods (Smith et al., 2015a). CSD has been shown to perform well at the acquisition protocol specifications used in this study (b =1000) (Ramirez-Manzanares et al., 2011; Wilkins et al., 2015). At b=1000 a minimum number of 28 gradient directions is required (Tournier et al., 2013). Therefore the angular coverage achieved using CSD at b=1000 is more than sufficient with 42 directions. While the performance of diffusion tractography methods in patients with atrophy has not been explicitly examined in the literature, previous work by our group has demonstrated low within-subject variability of diffusion metrics in manifest HD participants suggesting atrophy does not cause significant distortion of the diffusion signal (Cole et al., 2014).

I seed streamlines using two complimentary approaches. In the graph theory analysis streamlines are seeded throughout the WM and allowed to connect to any of our 76 ROIs. In contrast for the cortico-basal ganglia analysis, streamlines are seeded in the grey matter of basal ganglia structures at the voxel level and allowed to connect to multiple regions in their corresponding hemisphere. This allows us to probe cortico-basal ganglia structural connectivity change both at the ROI and voxel level therefore taking into account local basal ganglia changes in architecture that one may expect in HD.

Our group employed this latter approach in combination with CVA, a multivariate technique, and VCP analyses in a previous study where group differences between preHD and controls were not detected (Novak et al., 2015). This was likely due to methodological differences, particularly the use of multi-tensor reconstruction as opposed to CSD used in this study. While the previous study suggested a relative increase in structural connectivity to the putamen, volume normalisation was only carried out on basal ganglia structures. In this study I volume normalised for all brain regions. Furthermore, since CVA-based multivariate analysis has limited interpretation in terms of suggesting changes in individual connections' contribution to the overall connectivity pattern, in this study I performed a univariate analysis to uncover direction of change in connectivity. This univariate analyses did not suggest any increase in connectivity per se as was reported in (Novak et al., 2015) based on CVA analysis.

Our results suggest that loss of sub-cortical rich club connectivity in preHD leads to increased network segregation followed by loss of cortical rich club connectivity after clinical disease manifests causing a breakdown of network integration. This was a pseudo-longitudinal analyses allowing a snapshot that encompasses, in one analysis, a timespan of over 25 years with preHD gene carriers up to 15 years before predicted onset (Langbehn et al., 2004) and early stage clinically symptomatic participants (up to 10 years after onset). In the next chapter of this thesis I will perform a longitudinal analysis of the white matter brain network in HD in order to investigate how the brain network changes over time.

With respect to limitations, there were significant differences in age between preHD and controls and preHD and manifest HD in our cohort, an unavoidable consequence of the natural history of HD. I aimed to minimise this effect by including age as a covariate of no interest in all analyses to model and remove this variance. I acknowledge that streamline density is not a direct marker of axonal fibre count. I also acknowledge the limitations of diffusion tractography. However I have taken steps to address the biases that exist in diffusion tractography, namely longer streamlines are more likely to terminate prematurely whereas ROIs closer together have shorter streamlines and are therefore likely to have higher 'connection densities'. To overcome these limitations I used the SIFT method which is more reproducible and biologically accurate than conventional methods (Smith et al., 2015a).

This study focuses on inter-brain region structural connectivity. Therefore abnormalities occurring within specific brain regions, such as the caudate and putamen has not been taken into account. I do however account for brain region atrophy by reporting both volume un-normalised and volume normalised results.
Currently in the literature there is no consensus regarding volume normalisation in connectome studies. There is a suggestion that volume normalisation may overcompensate volume driven effects on streamline count (Zalesky and Fornito, 2009). I have found results suggestive of this in our study. In our graph theoretical analysis volume normalised results show increases in strength in the left thalamus and left hippocampus in Huntington's disease vs. controls. Additionally in the cortico-basal ganglia connectivity analysis increases were seen in connection density in connections to the anterior and posterior cingulate. While there is a suggestion that compensatory mechanisms come into play in HD, these are more likely to occur in the preHD stage (Papoutsi et al., 2014; Scheller et al., 2014). This suggests our results showing increased (graph theory) strength or connection densities in these regions are spurious results of volume normalisation. Similarly in assessing regional betweenness centrality and group differences in (graph theory) strength, the positive correlation I observed in the un-normalised results was not maintained after volume normalisation. While the optimal choice of brain parcellation scheme in connectome studies is unknown some authors suggest that less dense parcellation schemes with larger ROIs allow for more robust reproducible findings than dense parcellation schemes with thousands of ROIs (Smith et al., 2015a).

5.4.5. Conclusions

In this chapter I show highly connected rich club brain regions are most susceptible to structural connectivity loss in HD. This results in clinically relevant brain network changes of increased segregation in preHD and loss of integration in manifest HD. These findings highlight the role of the rich club as a substrate for the structural connectivity loss seen in HD and have broader implications for understanding the connection between molecular and systems level pathology in neurodegenerative disease. In the next chapter of this thesis I will investigate how the white matter brain network in preHD changes over time and how properties of the healthy brain network can predict regional variations in the rate of structural connectivity loss.

5.5. Publications relating to this chapter

The work presented in this chapter was published as:

Selective vulnerability of Rich Club brain regions is an organizational principle of structural connectivity loss in Huntington's disease. **McColgan P**, Seunarine KK, Razi A, Cole JH, Gregory S, Durr A, Roos RA, Stout JC, Landwehrmeyer B, Scahill RI, Clark CA, Rees G, Tabrizi SJ; Track-HD Investigators. **Brain**. 2015 Nov;138(Pt 11):3327-44.

Chapter 6. Topological length of white matter connections predicts their atrophy in premanifest HD

6.1. Introduction

In chapter 5 I demonstrated how the white matter network breaks down showing loss of segregation in preHD with subsequent loss of both segregation and integration in manifest HD. These changes are driven by structural connectivity loss between the striatum and cortical rich club regions, such that the cortical regions with the strongest connections are most vulnerable to cortio-striatal connectivity loss. While the use of graph theory metrics are informative their interpretation can be difficult. For example loss of degree for a given brain region suggests connections are lost but provides no information as to what those connections are. Conversely while network based statistics can provide specific information as to the type of connections lost, this approach test many thousands of connections, also making interpretation difficult.

In this chapter, I examine how the white matter network changes over time in preHD. To simplify interpretation of white matter connections and to allow me to make disease specific inferences, I employ a modularity approach that focuses on connections between the cortex and striatum and connections within the cortex. Using this framework, the cortex is partitioned into brain modules in a data driven manner. White matter connections can then be classified into sub-types based on connections between the cortical modules and the striatum (cortico-striatal); between cortical modules in different hemispheres (inter-hemispheric); between cortical modules within the same hemisphere (intra-hemispheric); and connections within cortical modules (intra-modular).

Individuals with preHD show grey matter loss in the striatum and white matter volume loss around the striatum, within the corpus callosum and in the posterior white matter tracts (Tabrizi et al., 2012). Micro-structural white matter changes have also been demonstrated in these regions in preHD (Di Paola et al., 2012; Dumas et al., 2012; Faria et al., 2016). While these findings provide strong evidence for the earliest white matter changes in preHD it is still unclear the order in which white matter connections degenerate and why some white matter connections are more vulnerable than others. With the antisense oligonucleotide (ASO) huntingtin lowering trial (Wexler et al., 2016) currently underway there is an urgent need to understand the time course of white matter changes and the mechanisms that drive them so that brain areas can be identified that may benefit from the highest concentrations of ASO.

Medium spiny neurons (MSNs) of the striatum are selectively vulnerable to the effects of mutant huntingtin (Graveland et al., 1985). One theory for this selective vulnerability is that the high-energy demands of MSNs (Pickrell et al., 2011) makes them particularly susceptible to mitochondrial dysfunction induced by the presence of mutant huntingtin (Costa and Scorrano, 2012). Given that long range white matter connections are the most metabolically active (Karbowski, 2007) and mutant huntingtin causes metabolic disturbance through mitochondrial dysfunction (Browne et al., 1997) I hypothesized that the length of white matter connections would determine their vulnerability in preHD.

To test this hypothesis I studied white matter connectivity in a longitudinal cohort of preHD participants over 24 months. By classifying white matter connections into cortico-striatal, inter-hemispheric, intra-hemispheric and intra-modular subtypes I was able to examine how these connections differ from controls both cross-sectionally and longitudinally. To test whether the length of white matter connections determined vulnerability I then investigated whether shortest weighted path length, a topological measure of distance between a pair of brain regions, determined cross-sectional and/or longitudinal change.

6.2. Materials and Methods

6.2.1. Cohort

The cohort included preHD gene-carriers and control participants from the Track-On HD study (Kloppel et al., 2015), followed up at 3 time-points over 24 months at four sites (London, Leiden, Paris and Vancouver). The total number of participants at each year was as follows: year 1 (72 preHD, 85 controls), year 2 (82 preHD, 87 controls) and year 3 (80 preHD, 80 controls). Track-On is an extension of the Track-HD (Tabrizi et al., 2009) study, but with only preHD and control participants carried over (early HD participants from Track-HD were excluded). Of the participants included, 31 preHD and 29 controls had participated previously in Track-HD (Tabrizi et al., 2009). The preHD participants required a disease burden score (DBS) > 250 (Penney et al., 1997), on the basis of their medical records at the time of assessment. Controls were selected from the spouses or partners of preHD individuals or were gene-negative siblings, to ensure consistency of environments. For this study I excluded participants who had manifest disease at baseline, were left handed or ambidextrous, or had poor quality diffusion-weighted imaging (DWI) data, as defined by visual quality control. Informed consent was obtained from each participant, and the study protocol was approved by the local ethics committees.

With respect to missing data 56 preHD and 65 controls had data at 3 time points, 28 preHD and 24 controls had data at 2-time points and 10 preHD and 9 controls had data only at one time point. A LMER was used to account for missing data (see statistics section), such that all data were included in the LMER analysis. See table 6.1 for baseline demographic information. For the rate of connection atrophy vs. shortest weighted path length (longitudinal) analysis only preHD participants who had diffusion data from all 3-time points were included (56 preHD, 65 controls). See tables 6.1 and 6.2 for demographic information on the baseline and longitudinal cohorts.

Table 6.1. Baseline demographic information. SD = standard deviation, M = male, F = female, N = number. ISCED = International standard classification of education. CAG = CAG repeat expansion length, DBS = disease burden scale (Penney et al., 1997)

	PreHD	Control	Statistical test	P-value
N	72	85	-	-
Age (SD)	43.3 (9.2)	48.8 (9.8)	T-test	0.0004
Gender (M/F)	38/34	32/53	Chi-square	0.057
Study Site (N) (Leiden/London/Paris/Vancouver)	14/25/18/15	20/26/23/16	Chi-square	0.89
ISCED (2/3/4/5/6)	5/16/23/27/1	8/16/29/30/2	Chi-square	0.94
CAG (SD)	42 (2.3)	-	-	-
DBS (SD)	317 (55)	-	-	-

Table 6.2. Rate of connection atrophy longitudinal cohort. SD = standard deviation, M = male, F = female, N = number. ISCED = International standard classification of education. CAG = CAG repeat expansion length, DBS = disease burden scale (Penney et al., 1997).

	PreHD	Control	Statistical test	P-value
N	56	65	-	-
Age (SD)	43.6 (9.3)	49.2 (9.7)	T-test	0.002
Gender (M/F)	30/26	24/41	Chi-square	0.066
Study Site (N) (Leiden/London/Paris/Vancouver)	8/22/16/10	15/20/20/10	Chi-square	0.57
ISCED (2/3/4/5/6)	5/13/14/23/1	5/16/22/20/2	Chi-square	0.74
CAG (SD)	42.8 (2.4)	-	-	-
DBS (SD)	316.7 (58)	-	-	10

6.2.2. Voxel connectivity profiles

DWI data was processed as described in chapter 2. For the VCPs, 5000 streamlines were seeded for each voxel within the sub-cortical ROIs and terminated when they reached the cortical mask or exited the hemisphere mask. The probability of connectivity between every seed voxel and every target region was established for each subject and the data were stored as individual subject connectivity probability maps. The connectivity maps were first binarised such that any voxel within the sub-cortical ROI with at least 1% of streamlines reaching a given cortical target was regarded as being connected to that target. The number of voxels connected to the cortical target were then calculated and normalised by the sum of the volumes of the corresponding sub-cortical ROI and cortical target, providing a normalised estimate of the volume of the region connected to target. The procedure was repeated for all cortical targets, resulting in a vector describing the connectivity between the striatum and cortex for each subject.

6.2.3. Construction of structural connectivity matrices

For structural connectivity matrices ROIs were defined as connected if a fibre originated in ROI 1 and terminated in ROI 2. Structural connections were weighted by streamline count and a cross-sectional area multiplier as implemented in SIFT2 (Smith et al., 2015b). Connections were then combined into 76x76, undirected and weighted matrices. As there is no consensus in the literature regarding the optimal graph thresholding strategy (Qi et al., 2015) and results can vary widely based on the chosen approach (Garrison et al., 2015) SIFT2 was my preferred method of bias correction. Indeed the creators of SIFT2 argue against the use of graph theory thresholding as it introduces an arbitrary threshold value (Yeh et al., 2016). SIFT2 was chosen in preference to SIFT as it requires much less processing time and retains the full connectome (Smith et al., 2015b).

6.2.4. Modular organization

The cortex was split into distinct modules using the community Louvain algorithm (Blondel et al., 2008) as implemented in the brain connectivity toolbox (Rubinov and Sporns, 2010) (BCT) version 2016-01-16. This was performed on a group connectivity matrix created by averaging connectivity matrices across all participants. As module assignment can vary between runs of the algorithm, the algorithm was run 1000 times and the most common assignment chosen using a consensus approach, also implemented in BCT. I chose the default resolution parameter $\gamma = 1$ as this represents classic modularity. This resulted in a module partition number of 6.

6.2.5. Statistics

All statistical analysis was performed in MATLAB *v*8.3. Linear mixed effects regression (LMER) was used as implemented in the MATLAB statistics and machine learning toolbox with the fitlme() function. An LMER was used as it provides unbiased estimates under the assumption that the missing data is ignorable. LMER accounts for the dependence due to repeated measures, and our application was similar to a previous approach used in a longitudinal HD imaging study (Harrington et al., 2016). Suppose that Y_{ij} is the connection strength for the i^{th} participant ($i = 1, \dots, N$) at the j^{th} time point ($j = 1, \dots, n_i$), with time metric $t_{ij} = visit_{ij} - 1$, so that $t_{i1} = 0$. Furthermore, $group_i$ is a dummy variable taking the value of 0 if a participant is in the control group and the value of 1 if preHD. Then the LMER model was,

$$Y_{ij} = \alpha + \beta t_{ij} + \gamma(group_i) + \delta(group_i)(t_{ij}) + \boldsymbol{\theta X}_i + a_i + b_i t_{ij} + e_{ij}, \qquad (1)$$

where Greek letters denote fixed effects; α is the control group mean at the first visit, β is the control group linear slope, γ is the mean difference among the preHD and control groups at the first visit (difference of intercepts), δ is the slope difference among the groups (rate of change difference), $\boldsymbol{X}_i$ is the matrix of covariates (age, sex, site, education) with associated regression coefficient vector $\boldsymbol{\theta}$; a_i and b_i are random effects (random intercepts and slopes), and e_{ij} is random error. Maximum likelihood methods were used for estimation under the assumption that the random effects have a joint-normal distribution with zero-means and non-singular covariance matrix, and the random error is normally distributed with zero-mean and constant non-zero variance. The objects of inference in Equation 1 were γ and δ, with the former being the initial cross-sectional mean difference among the groups adjusting for the covariates, and the latter being the group difference in the rate of change (slope difference) adjusting for the covariates. The null hypothesis of interest were $H_0: \gamma = 0$ (no initial mean group difference) and $H_0: \delta = 0$ (no group difference in rate of change), which were tested with the χ-

values of $z = \hat{\gamma}/SE(\hat{\gamma})$ and $z = \hat{\delta}/SE(\hat{\delta})$. False discovery rate (FDR) was applied for testing multiple connections in each connection sub-group (Benjamini, 1995).

I used a similar model as Equation 1 was used to explore the association between connection strength and cognition in preHD, where the continuous baseline cognitive variable (c_i) replaced the dummy group variable in the LMER model (i.e., $\gamma c_i + \delta c_i t_{ij}$). A global cognitive composite score (Kloppel et al., 2015) was chosen as the cognitive variable of interest as this encompasses many of the cognitive tests that have been shown to be sensitive in HD (Stout et al., 2012) and thus provides an overall indicator of cognitive function at the start of the study.

6.2.6. Connection sub-types

Connections were classed as cortico-striatal; defined as the sum of connection weights between the striatum (caudate and putamen) and cortical modules, inter-hemispheric; defined as connections between left and right cortical modules, intra-hemispheric; defined as connections between cortical modules in the left and right hemispheres separately and intra-modular: defined as the sum of connection weights with cortical modules.

6.2.7. Shortest weighted path length and connection sub-type in healthy controls

Connection length, defined as shortest weighted path length, was computed for every pair of brain regions in the averaged healthy control brain network using the BCT (Rubinov and Sporns, 2010). An illustration of the

shortest weighted path length from an example network is shown in figure 3(a). First the weighted connectivity matrix was converted to a connection-lengths matrix were higher weights are interpreted as shorter lengths. This connection-lengths matrix is defined as the inverse of the weighted connectivity matrix. Dijkstra's algorithm (Dijkstra, 1959) was then used to calculate the shortest weighted path between each pair of brain regions. The relationship between connection length and connection type was then investigated using a one-way ANOVA. Post hoc analysis was then performed using the Tukey-Kramer test (Kramer, 1956) in order to investigate if the connection length for each connection sub-type was significantly different from the connection length of other connection sub-types.

6.2.8. Shortest weight path length in healthy controls and connection atrophy in preHD

Spearman correlations were performed in order to assess the relationship between shortest weighted path length of a connection in healthy participants and connection atrophy in preHD participants. For each participant age and gender where regressed out from connection strength measures and subsequent analyses were performed using the resulting residuals.

A Z-score was calculated as follows:

$$Z_C(i) = \frac{\mu\big(C_h(i)\big) - C_k(i)}{\sigma(C_h(i))}$$

Where i is the connection, h is healthy controls, k is preHD, C is connection strength, μ is mean and σ is standard deviation. This was then transformed in order to produce atrophy measures between -1 and 1 where positive values denote atrophy. This was done using the hyperbolic function tanh, which fits values between -1 and 1:

$$Z_{C-T}(i) = \tanh\left(Z_C(i)\right)$$

This resulted in a transformed Z-score for each connection for each preHD participant. An average was then calculated across the preHD group resulting in a single transformed Z-score for each connection and these were correlated with shortest weighted path length for each connection, calculated from an average control group.

6.3. Results

6.3.1. White matter connection sub-types

Using a data-driven community Louvain approach (Blondel et al., 2008), cortical regions of interest (ROIs) were assigned to a cortical module, where each module represents a set of cortical ROIs that have maximum connections with each other but minimum connections with all other regions outside the module. This resulted in 6 modules, 3 in the left hemisphere and 3 in the right hemisphere. Module assignment was as follows: Module 1 - left sided frontal regions, left caudal anterior and rostral anterior cingulate regions and left insula; module 2 - right sided frontal regions and right caudal anterior, rostral anterior and posterior cingulate regions; module 3 - left temporal regions; module 4 - right temporal regions and right insula; module 5 - left motor, occipital, parietal and isthmus and posterior cingulate regions; module 6 - right motor, occipital and parietal and left isthmus cingulate regions (see figure 6.1(a) and table 6.3 for details).

Connections were then classified into subtypes: these included 6 cortico-striatal connections (between the striatum (caudate and putamen) and each cortical module), 9 inter-hemispheric connections (between modules in different hemispheres), 6 intra-hemispheric connections (between modules in the same hemisphere) and 6

intra-modular connections (within each module). The strength of each connection is represented by the sum of its connection weights. See figure 6.1(c) and figure 6.1(d) for an illustration of connection sub-types.

Figure 6.1. Module assignment, cohort and connection types: (A) Module assignment derived using the Louvain community detection algorithm on the average control baseline network. This results in 6 putative cortical modules: fronto-cingulate, temporal and motor-occipital-parietal (B) Cortico-striatal connections. For the connectome analysis these are defined as the sum of streamline weights (connection strength) from the caudate and putamen to a cortical module. (C) Connection types in the cortex. Intra-modular: sum of streamline weights (connection strength) within the same module (Red-Red). Intra-hemispheric: sum of streamline weights (connection strength) between modules in the same hemisphere (Blue-Red) and inter-hemispheric (Red-Green): sum of streamline weights (connection strength) between modules in different hemispheres.

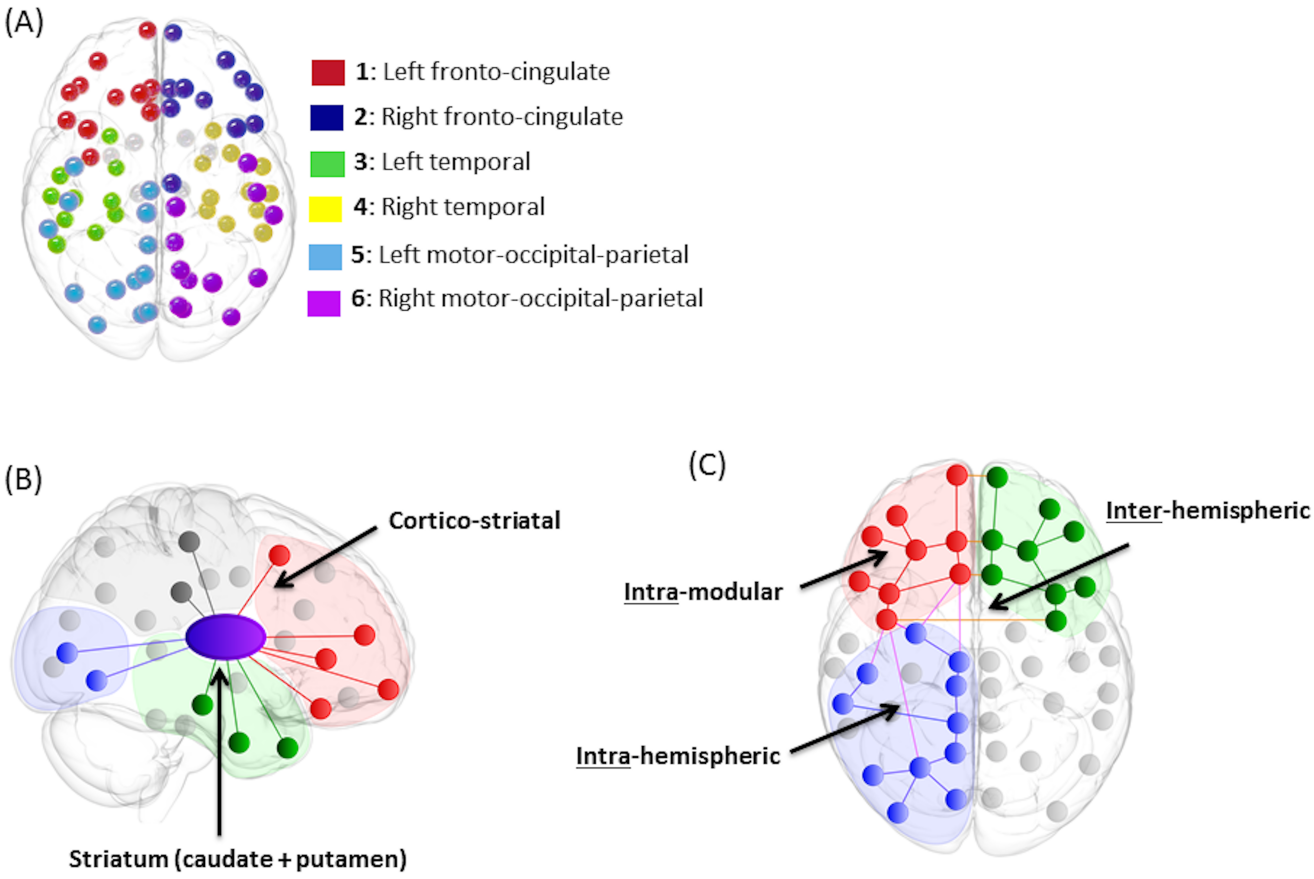

Table 6.3. Cortical module assignments

	Cortical Region		Cortical Region
Module 1	L.caudalanteriorcingulate L.caudalmiddlefrontal L.lateralorbitofrontal L.medialorbitofrontal L.parsopercularis L.parsorbitalis L.parstriangularis L.rostralanteriorcingulate L.rostralmiddlefrontal L.superiorfrontal L.frontalpole L.insula	**Module 2**	R.caudalanteriorcingulate R.caudalmiddlefrontal R.lateralorbitofrontal R.medialorbitofrontal R.parsopercularis R.parsorbitalis R.parstriangularis R.posteriorcingulate R.rostralanteriorcingulate R.rostralmiddlefrontal R.superiorfrontal R.frontalpole
Module 3	L.bankssts L.entorhinal L.fusiform L.inferiortemporal L.middletemporal L.parahippocampal L.superiortemporal L.temporalpole L.transversetemporal L.hippocampus	**Module 4**	R.hippocampus R.bankssts R.entorhinal R.fusiform R.inferiortemporal R.middletemporal R.parahippocampal R.superiortemporal R.temporalpole R.transversetemporal R.insula
Module 5	L.cuneus L.inferiorparietal L.isthmuscingulate L.lateraloccipital L.lingual L.paracentral L.pericalcarine L.postcentral L.posteriorcingulate L.precentral L.precuneus L.superiorparietal L.supramarginal	**Module 6**	R.cuneus R.inferiorparietal R.isthmuscingulate R.lateraloccipital R.lingual R.paracentral R.pericalcarine R.postcentral R.precentral R.precuneus R.superiorparietal R.supramarginal

6.3.2. Hierarchy of white matter connection vulnerability in preHD vs. controls

In order to maximize the robustness of my results, the cortico-striatal connections were analysed using two complimentary tractography approaches: voxel connectivity profiles (VCPs) (Draganski et al., 2008) and a connectome (Fornito and Bullmore, 2015) approach. For the VCPs streamlines are seeded in the striatum (caudate and putamen) and project to multiple regions in the cortex. Cortico-striatal connections are then normalized by the volumes of the ROIs they connect thus taking into account grey matter atrophy both in the cortex and striatum. In the connectome approach streamlines are seeded throughout the white matter and terminate when they reach grey matter regions, such that connections between all pairs of ROIs are investigated and are independent of the origin of specific tracts.

Linear mixed effects regression (LMER) was used to investigate longitudinal group differences in connection strength between preHD and controls (differences in slopes), with baseline (study entry) cross-sectional differences being represented by intercept differences. Baseline covariates included age at study entry, sex, education and study site. The time metric was time on study in years (0 = baseline). Z-ratios of fixed effects estimates were used to test the null hypothesis of no group differences. The false discovery rate (FDR) correction was used for multiple comparisons and unadjusted p-values or FDR-adjusted q-values are reported depending on the effects of interest ($p < 0.05$ and $q < 0.05$).

The first question I asked was how do different connection subtypes differ between groups at baseline? This was addressed by testing for intercept differences between the groups (preHD minus controls). For cortico-striatal connections both VCP and connectome analyses showed statistically significant ($q<0.05$) weaker

connection strength in preHD relative to controls for all 6 cortico-striatal connections (100%). See table 6.4.1 for connectome results and 6.4.2 for VCP results.

For inter-hemispheric connections, preHD showed significantly ($q<0.05$) weaker connection strength compared to controls in 6 connections (67%). These included the connections between the posterior motor-occipital parietal modules and their connections with the anterior fronto-cingulate modules. Connections between left and right temporal modules and left and right fronto-cingulate modules were also affected.

No significant cross-sectional FDR-corrected group differences were seen in intra-hemispheric (0%) or intra-modular connections (0%). PreHD showed weaker connection strength ($p < 0.05$) for one intra-hemispheric connection and one intra-modular connection compared to controls. See figure 6.2 and tables 6.4.1 and 6.4.2 for the cross-sectional results.

In summary, the weakest preHD connection strength at baseline was for cortico-striatal connections, followed by inter-hemispheric connections, intra-hemispheric and intra-modular connections. This suggests a temporal hierarchical pattern of degeneration. To verify whether this was the case, I characterised the group rate of change over time (group slopes) and whether the same connections showed greater change over time.

Table 6.4.1. Cross-sectional mixed linear model results. γ– estimated group intercept difference (preHD minus control; see Equation 1), SE – standard error of the difference, p-value – probability value, q-value – FDR corrected p-value, * = q < 0.05. Cross-sectional group difference at first visit was defined as the intercept main effect of group in the full linear mixed effects model.

Cortico-striatal connection (Connectome)	γ	**SE**	**p-value**	**q-value**
Left striatum fronto-cingulate	-374.1861154	57.17	$1.56x10^{-10}$	$9.36x10^{-10}$*
Right striatum fronto-cingulate	-267.05	47.17	$2.62x10^{-8}$	$7.87x10^{-8}$*
Left striatum temporal	-50.83	14.20	$3.8x10^{-4}$	$3.8x10^{-4}$*
Right striatum temporal	-151.69	28.60	$1.75x10^{-07}$	$3.5x10^{-7}$*
Left striatum motor-occiptial-parietal	-100.50	24.23	$3.98x10^{-5}$	$4.78x10^{-5}$*
Right striatum motor-occiptial-parietal	-98.34	22.57	$1.6x10^{-5}$	$2.44x10^{-5}$*
Inter-hemispheric connection	γ	**SE**	**p-value**	**q-value**
left fronto-cingulate right fronto-cingulate	-4601.145	1696.644	$6.9x10^{-3}$	0.012*
left temporal right temporal	-111.821	36.827	$2.5x10^{-3}$	0.006*
left motor-occipital-parietal right motor-occipital-parietal	-4304.345	1348.059	$1.5x10^{-3}$	0.006*
left fronto-cingulate right motor-occipital-parietal	-769.153	231.876	$9.8x10^{-4}$	0.006*
right fronto-cingulate left motor-occipital-parietal	-964.416	312.773	$2.2x10^{-3}$	0.006*
left fronto-cingulate right temporal	-159.441	59.985	$8.1x10^{-3}$	0.012*
right fronto-cingulate left temporal	-30.767	25.870	0.235	0.294
left temporal right motor-occipital-parietal	-135.003	120.126	0.262	0.294
right temporal left motor-occipital-parietal	-34.450	154.274	0.823	0.823
Intra-hemispheric connection	γ	**SE**	**p-value**	**q-value**
left fronto-cingulate left temporal	-1644.658	821.438	0.046	0.208
left fronto-cingulate left motor-occipital-parietal	2340.769	1402.457	0.096	0.208
left temporal left motor-occipital-parietal	-959.145	1721.465	0.578	0.608
right fronto-cingulate right temporal	-1235.767	758.235	0.104	0.208
right fronto-cingulate right motor-occipital-parietal	1299.804	1312.485	0.323	0.484
right temporal right motor-occipital-parietal	-1017.823	1984.348	0.608	0.608
Intra-modular connection	γ	**SE**	**p-value**	**q-value**
left fronto-cingulate	325.299	4496.184	0.942	0.942
right fronto-cingulate	6126.354	4248.015	0.150	0.300
left temporal	-3548.794	5525.934	0.521	0.625
right temporal	-13643.181	6685.873	0.042	0.251
left motor-occipital-motor	-6054.634	6344.644	0.340	0.511
right motor-occipital-motor	-9391.770	6333.663	0.139	0.300

6.4.2. Cross-sectional mixed linear model results: Cortico-striatal (VCP) and intra-modular connections. γ – estimated group intercept difference (preHD minus control; see Equation 1), SE – standard error of the difference, p-value – probability value, q-value – FDR corrected p-value. Cross-sectional group difference at first visit was defined as the intercept main effect of group in the full linear mixed effects model.

Cortico-striatal connection (VCP)	γ	**SE**	**p-value**	**q-value**
Left striatum fronto-cingulate	-0.159	0.020	$1.2x10^{-14}$	$7.23x10^{-14}$
Right striatum fronto-cingulate	-0.061	0.009	$2.23x10^{-10}$	$6.69x10^{-10}$
Left striatum temporal	-0.046	0.014	$1.1x10^{-3}$	$1.1x10^{-3}$
Right striatum temporal	-0.049	0.009	$2.48x10^{-7}$	$4.95x10^{-7}$
Left striatum motor-occipital-parietal	-0.067	0.020	$6.37x10^{-4}$	$7.64x10^{-4}$
Right striatum motor-occipital-parietal	-0.043	0.010	$2.37x10^{-5}$	$3.55x10^{-5}$
Intra-modular connection	γ	**SE**	**p-value**	**q-value**
left fronto-cingulate	325.299	4496.184	0.942	0.942
right fronto-cingulate	6126.354	4248.015	0.150	0.300
left temporal	-3548.794	5525.934	0.521	0.625
right temporal	-13643.181	6685.873	0.042	0.251
left motor-occipital-motor	-6054.634	6344.644	0.340	0.511
right motor-occipital-motor	-9391.770	6333.663	0.139	0.300

6.3.3. Rate of change in connection strength over time in preHD vs. controls

For cortico-striatal connections both VCPs and connectome analyses showed significant decreases in connection strength over time in preHD relative to controls for the bilateral striatal motor-occipital-parietal connections, although for the left connection in the connectome analysis and the right connection in the VCP analysis this reduction was only seen for $p < 0.05$. See figure 6.2(b) and table 6.5.1 for connectome results. The VCP analysis also showed significant reductions in the striatum fronto-cingulate connections bilaterally, although only for $p < 0.05$ in the left, while the connectome analysis revealed ($p < 0.05$) decrease in connection strength over time in the left striatum-temporal connection in the preHD group compared to controls. See table 6.5.1.

No significant longitudinal changes were seen for inter-hemispheric connections (see table 6.5.2). I did find (only for $p < 0.05$) longitudinal increase in connection strength in the right fronto-cingulate to right temporal intra-hemispheric connection in preHD relative to controls (see table 6.5.1). No significant longitudinal changes were seen for intra-modular connections (see table 6.5.2).

In summary, over 24 months only cortico-striatal connections significantly degenerated in the preHD group relative to controls. I hypothesized that the reason why these connections might be so vulnerable is because of their length. Therefore, in the next stage of our study, I performed an analysis to test the relationship between connection length and connection atrophy.

Figure 6.2. Hierarchy of connection vulnerability: Mixed linear model results for connectome analysis: preHD vs. controls. Cortico-striatal connections are most affected followed inter-hemispheric connections and then intra-hemispheric connections. (A) Far left axial brain figure illustrates cross-sectional cortico-striatal differences where preHD show reduced connection strength between the striatum (caudate and putamen) and cortical modules. Centre left axial brain figure illustrates cross-sectional inter-hemispheric differences where preHD show reduced connection strength between left and right hemisphere cortical modules. Bottom left axial brain figure illustrates cross-sectional intra-hemispheric differences where preHD show reduced connection strength between left cortical modules and right cortical modules separately (F – front-cingulate, T – temporal, M – motor-occipital-parietal, S-striatum. Red – False discovery rate (FDR)-corrected, Blue – uncorrected, Black – not significant). (B) Connection strength at baseline and 24-month follow-up for cortico-striatal and inter-hemispheric connections. Cross-sectional group difference was defined as the intercept main effect of group in the full linear mixed effects model. Longitudinal change was defined as a significantly superior fit for the full Linear mixed effects regression (LMER) compared to the reduced LMER omitting group by time interaction. (see methods for further details), which means that the group by time interaction effect was significant and pre-HD patients show more connectivity loss over time compared to controls. Data presented as dot plots with group means ± 95% confidence intervals at each time point for Control - magenta, preHD – green, * < 0.05, ** <0.01. Y-axis: connection strength, X-axis: follow-up time in years. Y-axis differs between graphs as connection strengths vary in range between different connections (486 data points displayed for each figure).

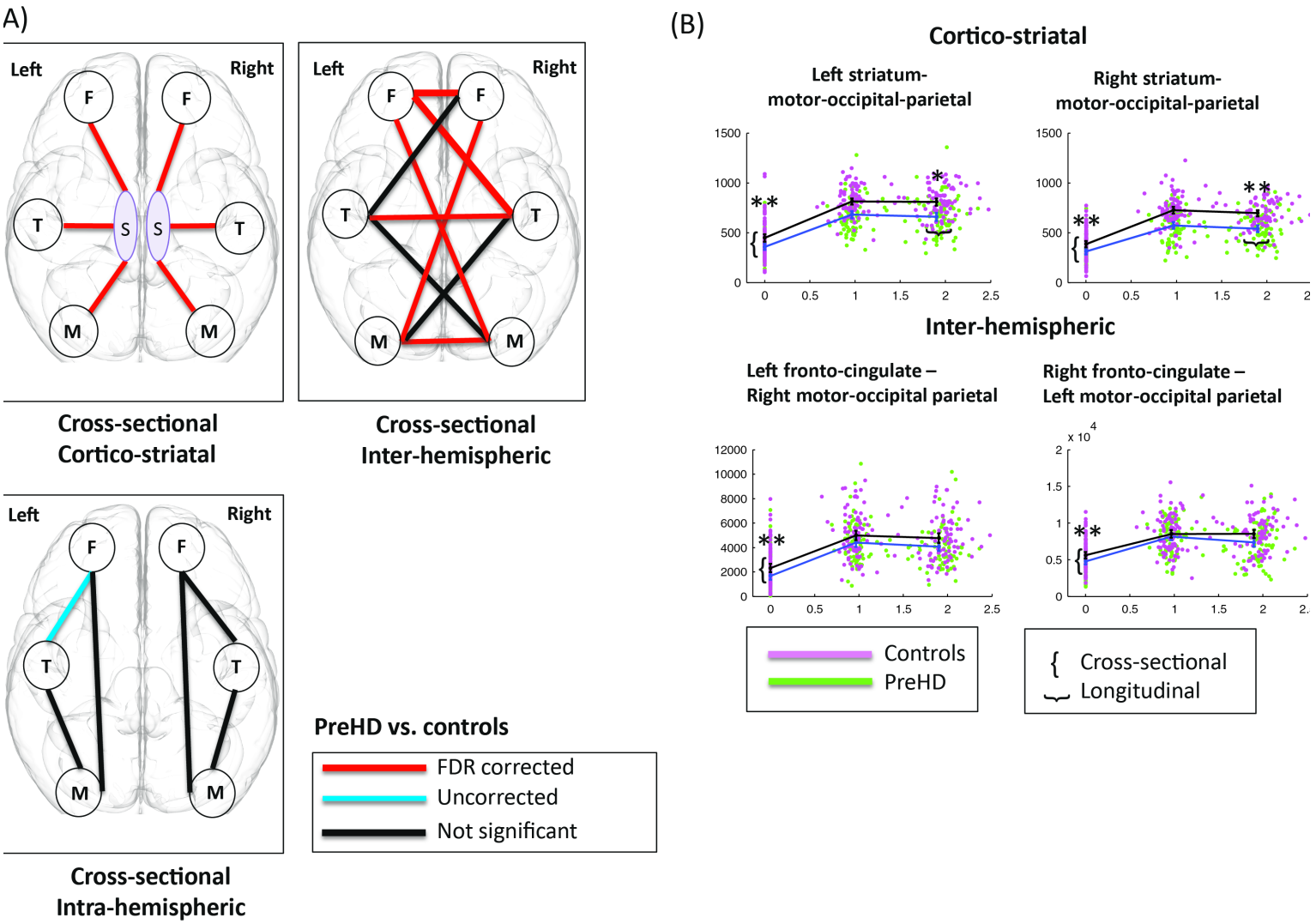

Table 6.5.1. Longitudinal results: Group slope differences in the cortico-striatal and intra-hemispheric connections. δ – estimated group slope difference (preHD minus controls; see Equation 1), SE – standard error, p-value – probability value, q-value – FDR corrected p-value, * = q < 0.05. Longitudinal change was defined as a significantly superior fit for the full LMER compared to the reduced LMER omitting group by time interaction.

Cortico-striatal connection (Connectome)	**δ**	**SE**	**p-value**	**q-value**
Left striatum fronto-cingulate	25.98	37.38	0.490	0.584
Right striatum fronto-cingulate	-4.96	29.21	0.870	0.865
Left striatum temporal	-18.57	8.57	0.030	0.062
Right striatum temporal	28.24	17.39	0.110	0.158
Left striatum motor-occiptial-parietal	-40.59	17.39	0.020	0.060
Right striatum motor-occiptial-parietal	-48.77	16.34	0.003	0.018*
Cortico-striatal connection (VCP)	**δ**	**SE**	**p-value**	**q-value**
Left striatum fronto-cingulate	-0.024	0.012	0.037	0.055
Right striatum fronto-cingulate	-0.020	0.007	0.004	0.010*
Left striatum temporal	-0.011	0.008	0.177	0.212
Right striatum temporal	0.006	0.006	0.32	0.320
Left striatum motor-occiptial-parietal	-0.057	0.015	1.54×10^{-4}	8.74×10^{-4}*
Right striatum motor-occiptial-parietal	-0.015	0.007	0.0331	0.055
Intra-hemispheric connection (Connectome)	**δ**	**SE**	**p-value**	**q-value**
left fronto-cingulate left temporal	941.135	510.914	0.068	0.198
left fronto-cingulate left motor-occipital-parietal	-784.515	907.122	0.389	0.659
left temporal left motor-occipital-parietal	-467.636	1288.415	0.717	0.717
right fronto-cingulate right temporal	1095.422	478.544	0.023	0.135
right fronto-cingulate right motor-occipital-parietal	-590.595	863.816	0.495	0.659
right temporal right motor-occipital-parietal	-865.472	1443.641	0.549	0.659

6.5.2. Longitudinal mixed linear model results: Inter-hemispheric and Intra-modular connections. δ – parameter estimate, SE – standard error, p-value – probability valve, q-value – FDR corrected p-value. Longitudinal change was defined as a significantly superior fit for the full LMER compared to the reduced LMER omitting group * time interaction.

Inter-hemispheric connection	δ	SE	p-value	q-value
left fronto-cingulate right fronto-cingulate	-8.548	1064.484	0.994	0.994
left temporal right temporal	7.415	28.474	0.795	0.946
left motor-occipital-parietal right motor-occipital-parietal	123.274	614.003	0.841	0.946
left fronto-cingulate right motor-occipital-parietal	-112.598	143.000	0.431	0.647
right fronto-cingulate left motor-occipital-parietal	-281.773	184.737	0.128	0.383
left fronto-cingulate right temporal	-52.692	40.285	0.192	0.383
right fronto-cingulate left temporal	-39.018	20.837	0.062	0.383
left temporal right motor-occipital-parietal	-135.995	97.276	0.162	0.383
right temporal left motor-occipital-parietal	-158.435	127.021	0.213	0.383
Intra-modular connection	δ	**SE**	**p-value**	**q-value**
left fronto-cingulate	3977.641	2647.570	0.134	0.401
right fronto-cingulate	2250.200	2861.948	0.432	0.520
left temporal	2698.917	4211.651	0.523	0.522
right temporal	3901.665	4978.346	0.434	0.520
left motor-occipital-motor	6834.844	4460.051	0.126	0.401
right motor-occipital-motor	4121.240	4923.315	0.403	0.520

6.3.4. Relationship between connection length and connection sub-type in healthy controls

Connection length was defined as the shortest weighted path length between two brain regions in the healthy brain network. An example schematic of the shortest weighted path is shown in figure 6.3 (A). For connections in the averaged healthy control brain a one-way ANOVA was performed to assess differences in connection length for different connection sub-types: intra-modular, intra-hemispheric, inter-hemispheric and cortico-striatal. This was highly significant ($F(3, 2691)= 739.23$, $p< 0.000$), see figure 6.3 (B). Following this post-hoc testing using the Tukey-Kramer test revealed clear step-wise differences in connection length across connection sub-types for healthy controls, such that all groups were significantly different from each other ($p< 0.000$). See table 6.6. Cortico-striatal connections were the longest, followed by inter-hemispheric, intra-hemispheric and intra-modular connections.

Table 6.6. Tukey-Kramer post hoc analysis of differences in connection length between different connections types. Intra-M –intra-modular, Intra-H –intra-hemispheric, Inter-H – inter-hemispheric, CS – cortico-striatal. CI – confidence interval.

Group 1	Group 2	95% lower CI	Mean difference	95% CI upper	p-value
Intra-M	Intra-H	-0.000302067	-0.000259613	-0.000217159	3.77E-09
Intra-M	Inter-H	-0.000582694	-0.000542553	-0.000502413	3.77E-09
Intra-M	CS	-0.000897343	-0.000843599	-0.000789855	3.77E-09
Intra-H	Inter-H	-0.000313728	-0.00028294	-0.000252152	3.77E-09
Intra-H	CS	-0.000631157	-0.000583986	-0.000536816	3.77E-09
Inter-H	CS	-0.000346146	-0.000301046	-0.000255947	3.77E-09

6.3.5. Length of white matter connection in healthy controls determines connection atrophy in preHD

Next I investigated the relationship between connection length and its vulnerability to atrophy. For each connection within each sub-type, connection strength for preHD were normalized for preHD relative to controls. These were then transformed to give atrophy measures, where higher scores represent greater connection atrophy. These scores were then averaged across the preHD group and correlated with the connection length for the same connection in the average healthy control group. Positive correlation between connection length and connection atrophy across sub-types collectively was seen (rho = 0.31, $p < 0.000$, $df = 2{,}693$) See figure 6.3(C). The cortico-striatal connections, the longest connections, showed the greatest atrophy, followed by inter-hemispheric connections, intra-hemispheric connections and intra-modular connections, confirming our hypothesis that their vulnerability is related to their length. Given the differences in age and gender between cohorts all analyses were performed on residuals of connection strength after regressing out age and gender covariates for each participant.

Figure 6.3. Connection length varies according to connection type and correlates with connection atrophy in preHD. (A) Illustration of *shortest weighted path length* between A and D in an example network. Numbers represent connection weights. When calculating shortest weighted path length connections are weighted by the inverse of streamline weights as stronger connections represent shorter paths in graph theory **(B)** Comparison of *shortest weighted path length* for different classes of connection. Intra-M –intra-modular (magneta), Intra-H –intra-hemispheric (green), Inter-H – inter-hemispheric (red), CS – cortico-striatal (blue). Lower-line: minimum, upper-line: maximum, middle-box-line: median lower-box-line: 1st quartile, upper-box-line: 3rd quartile. Red crosses indicate outliers. **(C) Connection atrophy vs. shortest weighted path length:** Z-scores, denoting loss of connection strength, were

transformed into positive atrophy measures using the tanh transform. Average transformed connection strength Z-score for preHD participants was plotted against connection weighted path length for average control and Spearman rank correlations performed. Connections are colour coded according to type**.** Each data point represents a brain connection. The black line represents a least squares linear regression line. rho = correlation, p = p-value, DF = degrees of freedom (2695 data points displayed for each figure).

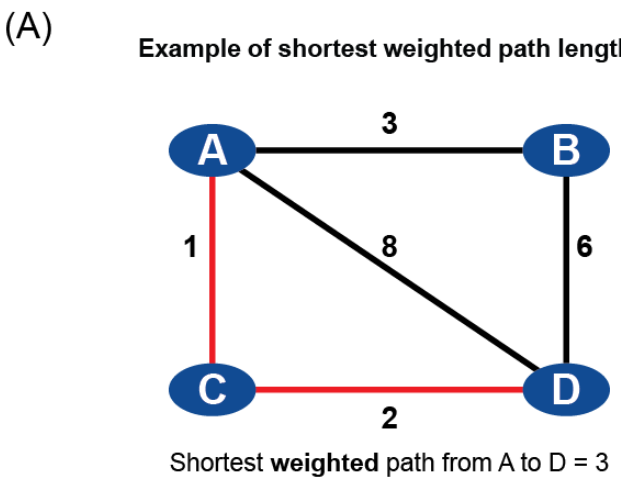

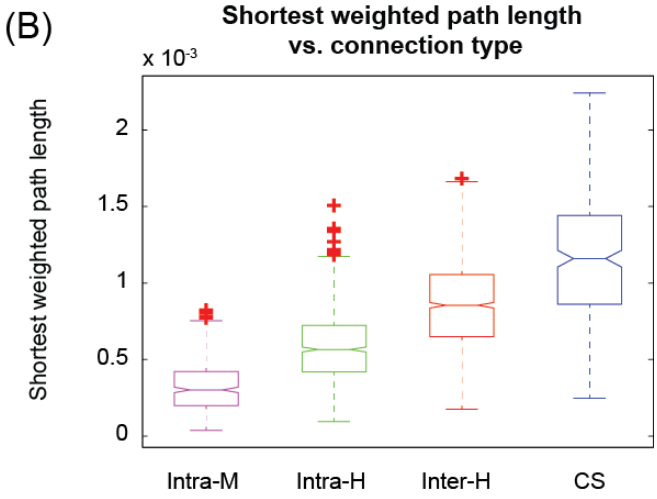

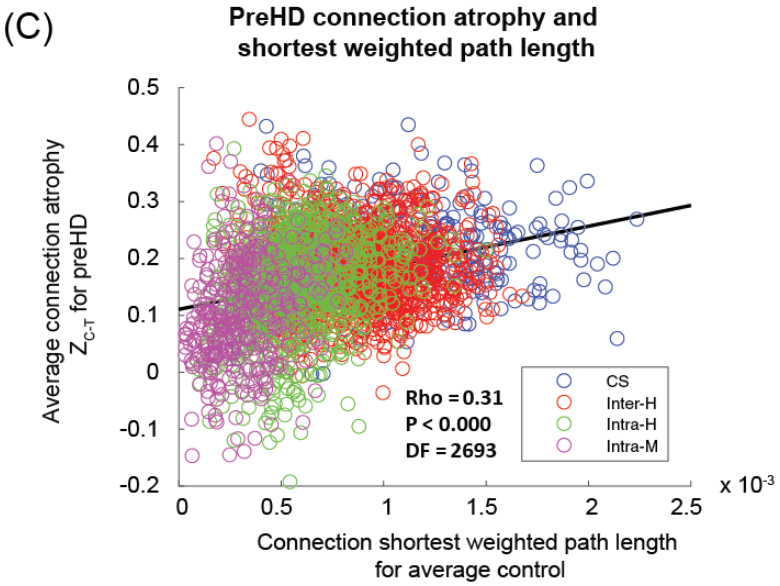

6.3.6. White matter connection sub-types are associated with global cognitive performance

My next aim was to investigate the pathophysiological relevance of white matter connection loss with respect to connection sub-type. I used a global cognitive composite score (Kloppel et al., 2015) as this encompasses many of the cognitive tests that are sensitive in HD (Stout et al., 2012). Association between connection strength and cognition was assessed by the main effect of global cognitive composite score at baseline for a LMER. Age, site, education, CAG and time-by-CAG interaction were included as covariates.

Significant ($q < 0.05$) positive association was seen between connection strength and global cognitive composite score for the inter-hemispheric connection between the left and the right motor-occipital-parietal modules. Intra-modular left fronto-cingulate connection strength also showed significant ($q < 0.05$) positive association with global cognitive composite score. Only $p < 0.05$ positive association was seen for cortico-striatal and intra-hemispheric connections and global cognitive composite score (see table 6.7).

Longitudinally no ($q<0.05$) significant associations were seen between connection strength and global cognitive composite score. Negative association ($p < 0.05$) was seen for the connection strength in the inter-hemispheric connections between the left temporal and right temporal modules and the interaction between global cognitive composite and follow-up, similarly negative association ($p < 0.05$) was seen for intra-modular left fronto-cingulate connection strength and the interaction between global cognitive composite and follow-up (See tables 6.8.1 and 6.8.2). My results therefore provide a link between connectivity loss and global cognitive impairment and suggest that loss of inter-hemispheric and intra-modular connectivity, which seems to occur later in preHD, is the main driver of global cognitive impairment.

Table 6.7. Cross-sectional global cognitive composite effects in preHD. γ – parameter estimate of baseline cognitive composite effect, SE – standard error, p-value – probability valve, q-value, * = q < 0.05 – FDR corrected p-value. Association between connection strength and cognition was assessed by the main effect of global cognitive composite score at baseline for the full LMER.

Cortico-striatal connection (connectome)	γ	SE	p-value	q-value
Left striatum fronto-cingulate	562.333	651.429	0.389	0.467
Right striatum fronto-cingulate	251.436	612.182	0.682	0.682
Left striatum temporal	159.245	169.057	0.347	0.467
Right striatum temporal	243.611	269.113	0.366	0.467
Left striatum motor-occiptial-parietal	376.561	254.410	0.140	0.421

Right striatum motor-occiptial-parietal	525.147	222.911	0.019	0.116
Inter-hemispheric connection	γ	**SE**	**p-value**	**q-value**
left fronto-cingulate right fronto-cingulate	3840.496	2081.724	0.066	0.199
left temporal right temporal	69.685	44.214	0.116	0.260
left motor-occipital-parietal right motor-occipital-parietal	4455.082	1483.113	0.003	0.027*
left fronto-cingulate right motor-occipital-parietal	360.318	274.994	0.191	0.260
right fronto-cingulate left motor-occipital-parietal	490.271	383.611	0.203	0.260
left fronto-cingulate right temporal	52.603	61.856	0.396	0.396
right fronto-cingulate left temporal	30.365	30.368	0.318	0.358
left temporal right motor-occipital-parietal	271.731	138.939	0.052	0.199
right temporal left motor-occipital-parietal	259.001	179.950	0.152	0.260
Intra-hemispheric connection	γ	**SE**	**p-value**	**q-value**
left fronto-cingulate left temporal	2214.495	981.634	0.025	0.063
left fronto-cingulate left motor-occipital-parietal	129.625	1725.264	0.940	0.940
left temporal left motor-occipital-parietal	4641.127	2142.948	0.031	0.063
right fronto-cingulate right temporal	2095.088	964.824	0.031	0.063
right fronto-cingulate right motor-occipital-parietal	1507.943	1667.724	0.367	0.440
right temporal right motor-occipital-parietal	2365.293	2507.079	0.347	0.440
Intra-modular connection	γ	**SE**	**p-value**	**q-value**
left fronto-cingulate	18183.414	5498.320	0.001	0.007
right fronto-cingulate	8072.412	5483.045	0.142	0.241
left temporal	-9647.675	6848.409	0.160	0.241
right temporal	5385.428	7470.754	0.472	0.537
left motor-occipital-motor	5059.337	8175.221	0.537	0.537
right motor-occipital-motor	-11969.077	7782.574	0.126	0.241
Cortico-striatal connection (VCP)	γ	**SE**	**P-value**	**q-value**
Left striatum fronto-cingulate	0.037	0.023	0.114	0.412
Right striatum fronto-cingulate	0.017	0.011	0.137	0.412
Left striatum temporal	0.009	0.014	0.528	0.723
Right striatum temporal	0.005	0.010	0.623	0.723
Left striatum motor-occipital-parietal	0.026	0.021	0.217	0.433
Right striatum motor-occipital-parietal	-0.004	0.012	0.723	0.723

Table 6.8.1. Longitudinal global cognitive composite effects in preHD: Cortical connections. δ – parameter estimate of baseline cognitive composite effect, SE – standard error, p-value – probability valve, q-value – FDR corrected p-value. Longitudinal change was defined as a significantly superior fit for the full LMER compared to the reduced LMER omitting global cognitive composite * time interaction.

Inter-hemispheric connection	δ	**SE**	**p-value**	**q-value**
left fronto-cingulate right fronto-cingulate	290.472	1352.185	0.830	0.914
left temporal right temporal	-76.655	31.395	0.015	0.139

left motor-occipital-parietal right motor-occipital-parietal	582.052	780.157	0.456	0.781
left fronto-cingulate right motor-occipital-parietal	-18.155	168.517	0.914	0.914
right fronto-cingulate left motor-occipital-parietal	221.011	235.550	0.349	0.781
left fronto-cingulate right temporal	27.539	42.800	0.521	0.781
right fronto-cingulate left temporal	-9.478	21.281	0.657	0.844
left temporal right motor-occipital-parietal	-91.957	108.829	0.399	0.781
right temporal left motor-occipital-parietal	-286.764	140.863	0.043	0.193
Intra-hemispheric connection	***δ***	**SE**	**p-value**	**q-value**
left fronto-cingulate left temporal	-1138.861	586.779	0.054	0.225
left fronto-cingulate left motor-occipital-parietal	-343.698	1123.016	0.760	0.760
left temporal left motor-occipital-parietal	-2756.217	1581.689	0.083	0.225
right fronto-cingulate right temporal	-974.896	611.831	0.113	0.225
right fronto-cingulate right motor-occipital-parietal	-686.440	1115.276	0.539	0.647
right temporal right motor-occipital-parietal	-1664.563	1803.591	0.357	0.536
Intra-modular connection	***δ***	**SE**	**p-value**	**q-value**
left fronto-cingulate	-6636.924	3203.536	0.039	0.207
right fronto-cingulate	-3984.763	3729.899	0.286	0.430
left temporal	6582.062	5131.308	0.201	0.402
right temporal	548.183	5749.975	0.924	0.964
left motor-occipital-motor	-253.806	5633.787	0.964	0.964
right motor-occipital-motor	10993.406	6017.274	0.069	0.207

Table 6.8.2. Longitudinal global cognitive composite effects in preHD: Cortico-striatal connections. *δ* – parameter estimate of baseline cognitive composite effect, SE – standard error, p-value – probability valve, q-value – FDR corrected p-value. Longitudinal change was defined as a significantly superior fit for the full LMER compared to the reduced LMER omitting global cognitive composite * time interaction.

Cortico-striatal connection (Connectome)	*δ*	SE	P-value	q-value
Left striatum fronto-cingulate	-431.959	444.913	0.333	0.909
Right striatum fronto-cingulate	-218.826	378.821	0.564	0.909

Left striatum temporal	-103.621	102.919	0.315	0.909
Right striatum temporal	47.646	180.734	0.792	0.909
Left striatum motor-occipital-parietal	18.488	158.160	0.907	0.909
Right striatum motor-occipital-parietal	-16.283	142.786	0.909	0.909
Cortico-striatal connection (VCP)	***δ***	**SE**	**P-value**	**q-value**
Left striatum fronto-cingulate	0.007	0.013	0.573	0.608
Right striatum fronto-cingulate	0.008	0.008	0.280	0.608
Left striatum temporal	-0.004	0.008	0.574	0.608
Right striatum temporal	0.003	0.006	0.608	0.608
Left striatum motor-occipital-parietal	-0.008	0.016	0.594	0.608
Right striatum motor-occipital-parietal	0.012	0.007	0.112	0.608

6.4. Discussion

6.4.1. Hierarchy of vulnerability

In this chapter I reveal a hierarchy of white matter connection vulnerability in preHD relative to controls, where greatest loss in connection strength is seen in cortico-striatal connections, followed by inter-hemispheric, intra-hemispheric and intra-modular connections. The topological length of white matter connections determined this hierarchy with evidence of a positive association between topological white matter connection length and loss of connection strength over 24 months (see figure 6.4 for summary schematic). Furthermore, the pathophysiological relevance of these changes was demonstrated by correlations with global cognition.

Figure 6.4. Schematic showing empirically determined hierarchy of white matter connection vulnerability in preHD. Connections with the largest *shortest weighted path length* have a higher rate of degeneration and show significant ($q < 0.05$) longitudinal change. Both cortico-striatal and inter-hemispheric connections showed significant ($q < 0.05$) cross-sectional change, while neither intra-hemispheric or intra-modular connections showed significant ($q < 0.05$) group differences. Red arrow indicates increasing path length with respect to connection type. Blue wedge indicates rate of degeneration, slow rate – thin wedge, fast rate – thick wedge. Full black arrow – $q < 0.05$ significance, dashed black arrow – $p < 0.05$ significance.

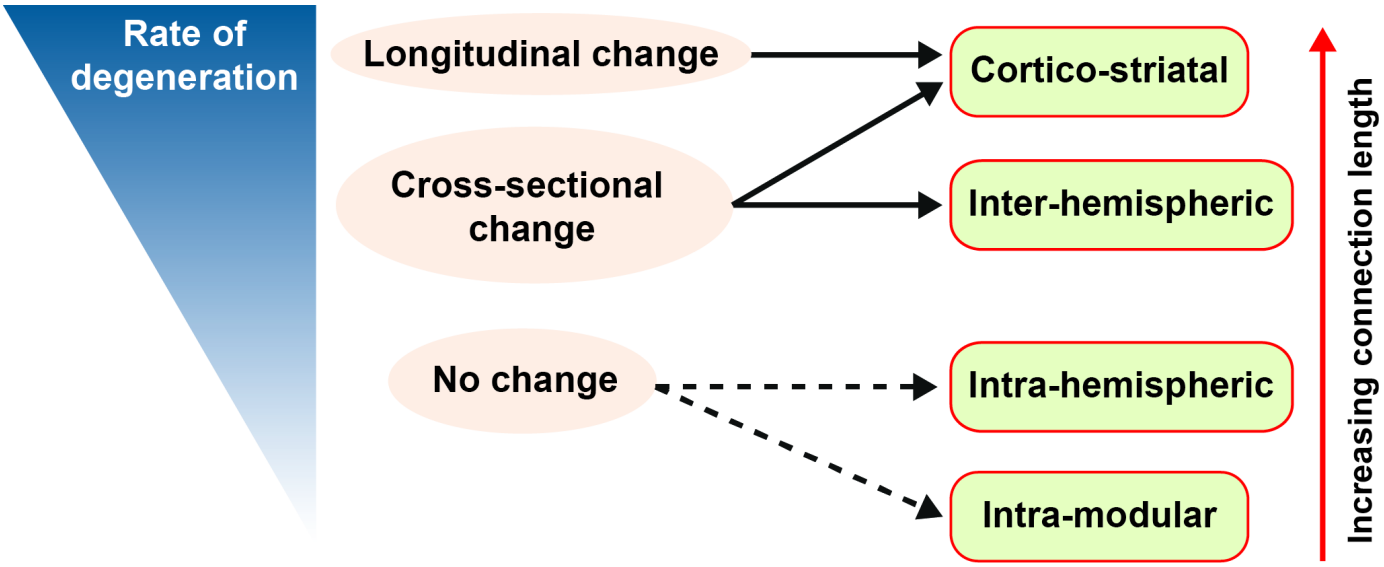

In chapter 4 I demonstrated a strong positive correlation with streamline density (particularly to the basal ganglia) and group differences in streamline density, suggesting that stronger connections are more vulnerable to HD related neurodegeneration. The work presented in this chapter goes beyond this showing that topological

length of white matter connections in the healthy brain can provide a mechanistic explanation for the hierarchy of white matter vulnerability seen in preHD

This is the first study in HD to identify a temporal neuroanatomical pattern of white matter connection vulnerability. In preHD reduced connection strength is seen in cortico-striatal connections both longitudinally and cross-sectionally compared to controls. While longitudinal change is seen in predominantly posterior cortico-striatal connections, cross-sectional differences were seen in all cortico-striatal connections. Inter-hemispheric connections also show significant cross-sectional reductions in preHD compared to controls between the posterior motor-occipital parietal modules and in their connections with the anterior fronto-cingulate modules. These findings are consistent with the cortico-striatal (Kloppel et al., 2008; McColgan et al., 2015; Poudel et al., 2014b), corpus callosum (Crawford et al., 2013; Di Paola et al., 2012; Phillips et al., 2013; Rosas et al., 2010) and posterior (Faria et al., 2016; Tabrizi et al., 2012) white matter changes that have been identified in preHD.

6.4.2. Relationship to striatal pathology

Striatal pathology in HD occurs along a caudo-rostral, medio-lateral, dorso-ventral gradient (Vonsattel, 1985) and thus the posterior vulnerability of cortico-striatal white matter connections is in keeping with striatal pathology. Of the inter-hemispheric connections that did not differ cross-sectionally, all were connected to the temporal modules, again following the medial-lateral gradient of striatal pathology in HD (Vonsattel, 1985) and temporal sparing that has been demonstrated previously (Rosas et al., 2008). Cortical regions that show either vulnerability or resilience in preHD should be taken into account when assessing the distribution of ASOs in the

cortex, such that higher concentrations in posterior cortical regions may be more beneficial than an equal distribution throughout the cortex.

Only one other study has investigated longitudinal change in brain networks in preHD (Odish et al., 2015). However only regional changes in graph theory metrics were investigated. Changes in white matter connections were not examined therefore it is difficult to draw comparative conclusions regarding the longitudinal cortical-striatal connectivity changes I demonstrate here. In the afore mentioned study no group differences were seen at baseline and longitudinal changes were only seen in the left orbitofrontal cortex and left paracentral lobule with no regional changes seen in the striatum. These findings are not consistent with our previous cross-sectional structural connectivity study in HD (McColgan et al., 2015). This may be due to the very small sample size and the fact a streamline filtering algorithm, such as SIFT (Smith et al., 2013) or SIFT2 (Smith et al., 2015b), was not applied following diffusion tractography.

6.4.3. Prion-like spread vs. metabolic dysfunction

'Prion-like' spread is the spread of pathogenic proteins throughout the brain from cell-to-cell and is seen in a number of neurodegenerative diseases (Angot et al., 2010; Yin et al., 2014). Systems level evidence for this has been shown in fronto-temporal dementia (FTD) (Mandelli et al., 2016; Zhou et al., 2012), where the distance from the brain region showing the earliest atrophy to other brain regions in the brain network predicts atrophy. However in chapter 5, I was unable to replicate this finding in an HD cohort (McColgan et al., 2015). While I did find selective vulnerability of highly connected hub or 'rich club' brain regions, this finding is generalisable across a number of brain disorders (Crossley et al., 2014) and may be due to the high metabolic demands (Liang

et al., 2013; Tomasi et al., 2013) of hub brain regions as opposed to a disease-specific mechanism such as prion-like spread. Indeed hub brain regions with long-range connections have genetic transcription profiles enriched for oxidative metabolism and mitochondria (Fulcher and Fornito, 2016; Vertes et al., 2016).

6.4.4. Limitations

In this study, I provide evidence for the underlying cause behind the hierarchical loss of connectivity by showing a direct relationship between topological connection length and connection atrophy. As longer white matter connections are more metabolically active (Karbowski, 2007), the fact that these show the greatest rate of atrophy in preHD suggests the metabolic disturbances in HD (Lopez-Mora et al., 2016; Mazziotta et al., 1987; Powers et al., 2007) may be driving the degenerative process. However I acknowledge that the data I present demonstrates association between topological connection length and connection atrophy and not causality. Furthermore I do not assess the relationship between these white matter changes and either metabolism or mitochondrial function. Additionally while path length is a topological measure of white matter length between two brain regions (Schmidt et al., 2016) the relationship of this measure to biological white matter tract length has not been established.

Cortico-striatal VCP and connectome cross-sectional analyses were in agreement, however the longitudinal results differ slightly. VCPs show significant difference in the fronto-striatal connections whereas the connectome analysis did not. This is likely due to methodological differences between each technique. VCPs calculate the number of voxels in the striatum that connect to a cortical region and are normalized by striatal and cortical volumes. The connectome analysis is based on the strength of connections between the striatum and

cortical regions. Volume normalization was not performed in the connectome analysis as I have shown in chapter 5 that it can lead to spurious results (McColgan et al., 2015).

Despite the fact that cortico-striatal connections show the largest change in connection strength, they did not show a strong association with the global composite score. Inter-hemispheric and intra-modular connections show the strongest relationship with global composite cognitive score showing FDR-corrected significance cross-sectionally and uncorrected significance longitudinal. The absence of a strong relationship between cortical-striatal connection strength and global cognition may be the reason why there is relatively little suggest degeneration of inter-hemispheric and intra-modular connections is slower and occurs after cortico-striatal connection loss. Alternatively by using a modular approach in order to simply the interpretation of large numbers of brain connections summing together connections from multiple regions may result in loss of associations between cognitive variables and specific cortico-striatal connections that would otherwise be detectable. It is notable however that only emotion recognition showed correlation with white matter networks in the cross-sectional analysis in chapter. Emotion recognition data was not available in the Track-On HD cohort, although this may be a more sensitive measure with respect to white matter change and cognition, especially as emotion recognition requires the involvement of a number of diverse brain regions (Novak et al., 2012).

In this study I chose to focus on the caudate and putamen sub-cortical structures. This was based on observations from our cross-sectional structural connectivity study (McColgan et al., 2015) and from the earlier Track-HD studies (Tabrizi et al., 2012; Tabrizi et al., 2011) that show the caudate and putamen are the sub-cortical structures most affected in preHD both in terms of grey matter volume and white matter connections.

While some studies have shown changes in the thalamus, globus pallidus and nucleus accumbens in preHD these tend to occur in preHD participants closer to disease onset (Faria et al., 2016; van den Bogaard et al., 2011). Furthermore automatic segmentation of globus pallidus and nucleus accumbens is not sufficiently reliable (Hibar et al., 2015). Loss of white matter connections within the striatum was not examined, as the cross-sectional analysis in chapter 5 did not show loss of these connections in preHD relative to controls (McColgan et al., 2015).

6.4.5. Conclusion

Topological length of white matter connections predicts their atrophy in preHD, this results in a hierarchy of vulnerability were cortico-striatal connections are most affected, followed by inter-hemispheric, intra-hemispheric and intra-modular connections. This demonstrates a new principle underlying neurodegeneration in Huntington's disease, whereby the brain connections with the greatest topological length are the first to suffer damage that can account for the stereotyped pattern of white matter loss observed in preHD. In chapter 7 I will link these patterns of white matter loss in preHD with regional gene expression from the healthy human brain using the Allen Institute of Brain Science (AIBS) transcriptome atlas. In doing so I can investigate regional gene expression associated with white matter loss and through gene ontology I can define the biological processes that these genes are involved in. This will enable me to potentially link white matter systems level abnormalities with biological processes at the cellular level thus achieving the ultimate aim of this thesis.

6.5. Publications relating to this chapter

The work presented in this chapter was published as:

Topological length of white matter connections predicts their rate of atrophy in premanifest Huntington's disease. **McColgan P**, Seunarine KK, Gregory S, Razi A, Papoutsi M, Long JD, Mills JA, Johnson E, Durr A, A C Roos R, Leavitt BR, Stout JC, Scahill RI, Clark CA, Rees G, Tabrizi SJ and the Track-On HD Investigators. **JCI Insight**. 2017 Apr 20;2(8).

Chapter 7. Brain regions showing white matter loss in HD are enriched for synaptic and metabolic genes

7.1. Introduction

In chapter 6 I revealed how greater topographical length of white matter connections is associated with atrophy of white connections in preHD. I demonstrated a hierarchy of vulnerability were cortico-striatal connections are most affected followed by inter-hemispheric and intra-hemispheric connections. I postulated that this could be due to longer connections having greater metabolic demand coupled with metabolic abnormalities caused by mutant huntingtin. In this chapter I investigate the specific biological processes associated with white matter loss in preHD with the aim of identifying the biological processes associated with white matter connection atrophy.

In order to do this I utilise data from the AIBS transcriptome atlas. This includes gene expression microarray data from 6 post mortem human brains from individuals with no prior neurological or psychiatric diagnoses. This is the most extensive gene expression atlas of the human brain comprising gene expression data from 900 anatomically defined brain regions. The use of gene expression data from the healthy human brain to explain white matter loss in preHD is limited to the extent that transcription in preHD may be different than that seen in healthy brains. However studies from post mortem manifest HD brains show that the transcription in the striatum is most affected with limited abnormalities in the cortex (Hodges et al., 2006). Indeed the transcription of only 25 genes in the cortex is abnormal in both human and animal studies, compared to 515 in the striatum (Langfelder et al., 2016). Therefore, I mitigate for the likely transcription abnormalities in preHD by using only cortical gene expression data from the AIBS transcriptome atlas (Hawrylycz et al., 2012).

Mutant huntingtin protein causes cellular dysfunction and ultimately neuronal cell death through a number of processes (Ross and Tabrizi, 2011; Saudou and Humbert, 2016). These include downstream effects on synaptic signalling (Plotkin and Surmeier, 2015), cellular metabolism (Lee et al., 2007), mitochondrial dysfunction (Tabrizi et al., 2000), immune activation (Andre et al., 2016) and alterations in transcription (Seredenina and

Luthi-Carter, 2012). Furthermore transcription levels of genes involved in these processes are atypical in human HD and animal models (Miller et al., 2016; Seredenina and Luthi-Carter, 2012), with abnormal transcription of specific genes correlating with clinical variables in human studies (Mastrokolias et al., 2015).

Decreased expression of synaptic proteins in cortical pyramidal neurons of HD mouse models is linked to abnormal cortico-striatal connectivity (Zucker et al., 2010), while changes in transcription levels of Brain Derived Neurotrophic Factor (BDNF), another protein involved in synaptic transmission, are associated with changes in cortico-cortical connectivity (Gambazzi et al., 2010). Furthermore, some genes show a direct association with WM integrity. Loss of Peroxisome-proliferator-activated receptor gamma co-activator α (PGC1α), which is involved in the transcription regulation of energy metabolism, results in degeneration of striatal neurons and WM abnormalities of the corpus callosum in HD mouse models (Xiang et al., 2011). More recently, reduced transcription levels of myelin-related genes have been associated with WM abnormalities in HD mouse models (Teo et al., 2016).

Given the relationship between WM connectivity and gene transcription in HD, I sought to investigate how regional gene transcription profiles of the healthy human brain, obtained from the AIBS human transcriptome atlas (Hawrylycz et al., 2015) may be associated with regional variation in WM connectivity loss over time in preHD relative to controls. Based on association between synaptic and metabolic genes and WM loss in HD (Teo et al., 2016; Xiang et al., 2011) I hypothesized that WM connectivity loss in preHD would be associated with regional transcription profiles enriched for synaptic and metabolic genes.

7.2. Methods and Materials

7.2.1. Overview

To test my hypothesis, WM connectivity loss was determined using diffusion weighted imaging (DWI) data from the longitudinal Track-On HD cohort of preHD and control participants who were scanned at 0, 12 and 24 months. This is the same cohort analysed in chapter 6. Brains were parcellated into 70 cortical regions of interest (ROI) and 2 sub-cortical regions (caudate and putamen) based on the Desikan Freesurfer atlas (Desikan et al., 2006). The caudate and putamen were chosen as these sub-cortical regions show the greatest changes in preHD (Tabrizi et al., 2011). Whole brain tractography was then performed using these parcellations to construct WM brain networks.

For each set of connections associated with a cortical ROI, WM connectivity loss was defined as either cortico-striatal (connections between cortex and striatum (caudate and putamen)), inter-hemispheric (cortico-cortical connections between hemispheres) or intra-hemispheric (cortico-cortical connections within the same hemisphere) (see Figure 7.1). WM connectivity and rate of change in WM connectivity over 24 months were normalised for preHD relative to controls for each participant. The connectivity measures were then transformed to give atrophy and rate of atrophy measures. The resulting atrophy score was used in the cross-sectional analysis, while the rate of atrophy score was used in the longitudinal analysis (see below for further details).

Figure 7.1. Schematic illustrating sub-groups of regional white matter connectivity. (a) Cortico-striatal: connections between cortex and striatum (caudate and putamen) for each cortical region of interest (ROI). (b) Inter-hemispheric: connections to the opposite hemisphere for each cortical ROI. Intra-hemispheric: connections within the same hemisphere for each cortical ROI. Light blue – left hemisphere, purple – right hemisphere, dark blue – caudate, yellow – putamen.

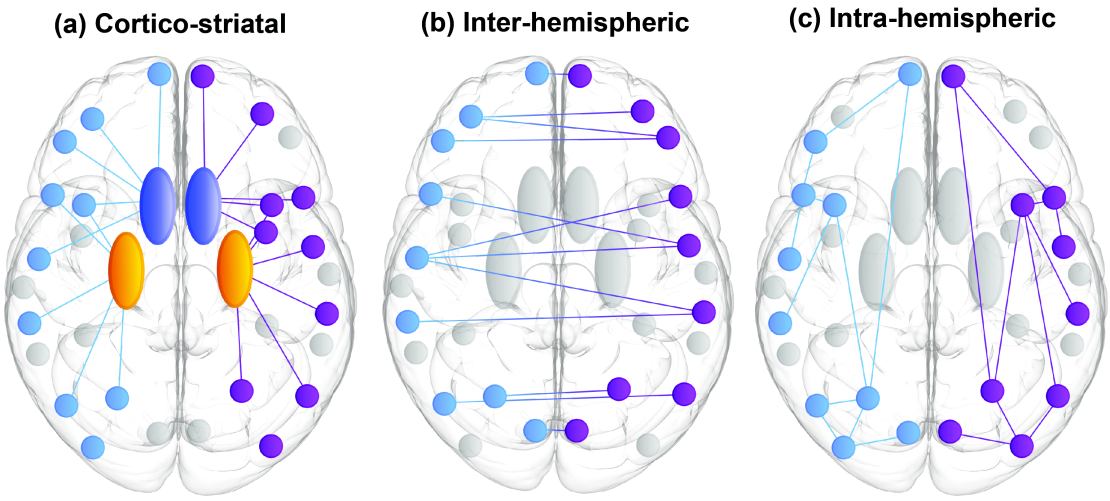

To compare regional WM loss in preHD with regional gene expression in the healthy brain the 70 cortical ROIs from the Desikan atlas (Desikan et al., 2006) were matched to the closest AIBS ROI and gene expression data were averaged across RNA probes corresponding to the same gene. ROIs with gene expression values greater than 2 standard deviations above the mean or range were excluded from the analysis in keeping with other AIBS transcriptome atlas studies in the literature (Rittman et al., 2016; Vertes et al., 2016; Whitaker et al., 2016). This resulted in the inclusion of 20,737 genes across 68 cortical ROIs.

Partial least squares (PLS) regression was used to investigate the relationship between regional gene expression and regional white matter loss. PLS is a multivariate technique that is used when the number of predictor variables (i.e. regional gene expression) is much larger than the number of observations (i.e. regional white matter loss). This approach has been used previously to investigate the relationship between gene expression and MRI-derived regional brain measures in healthy volunteers (Vertes et al., 2016; Whitaker et al., 2016). In the case of my analysis the predictor variable consisted of a gene x ROI matrix 20,737 x 68 and the response variable consisted of a WM loss x ROI matrix; 68 x 4 for the cortico-striatal analysis (68 cortical ROIs x left and

right caudate and putamen WM loss to each ROI region) and 68 x 1 for the inter and intra-hemispheric analyses (68 cortical ROIs x inter/intra hemispheric WM loss for each ROI). PLS identified components or patterns of regional gene expression that have maximum covariance with regional white matter loss, such that the first few PLS components will provide the greatest representation of the covariance. For each component individual genes are assigned weights based on their contribution to the variance explained (Vertes et al., 2016).

The PLS analysis provided a weight for each gene indicating its contribution to the extent of WM connectivity loss for each component or pattern. Using this information, genes were ranked according to their PLS weight. Gene enrichment analysis was then performed to identify the biological functions of genes with the highest weights using gene ontology (GO) terms (Eden et al., 2009). Here, the significance of a GO term was determined based on the rank of genes associated with that GO term. I also removed general GO terms by excluding those with greater than 1000 genes in their classification, in keeping with other studies in the literature (Vertes et al., 2016; Whitaker et al., 2016). This allowed me to focus on specific gene sets as opposed to GO terms encompassing thousands of genes covering a range of processes.

To investigate the spatial patterns of gene expression profiles in the brain, ROI PLS weights from the cortico-striatal, inter-hemispheric and intra-hemispheric analyses were visualised on brain meshes. I also investigated whether genes showing abnormal transcription in HD (identified from (Langfelder et al., 2016)) were over-expressed (greater than chance) in the gene expression profiles from each analysis.

7.2.2. Imaging Cohort

The cohort included preHD gene-carriers and control participants from the Track-On HD study (Kloppel et al., 2015), followed up at three time-points over 24 months at four sites (London, Leiden, Paris and Vancouver). Baseline participants included 72 preHD and 85 controls. For the longitudinal analysis only preHD participants who had diffusion data from all 3-time points were included (56 preHD, 65 controls). This is the same cohort analysed in chapter 6. DWI data was processed as described in chapter 2 and structural connectivity matrices were constructed as described in chapter 6.

7.2.3. Regional white matter atrophy

Regional white matter connectivity was classed as cortico-striatal, inter-hemispheric and intra-hemispheric. For each participant age and gender where regressed out from these measures and subsequent analysis was performed using residuals. Connection strength and rate of change in connection strength over 24 months for preHD were normalized for preHD relative to controls using a Z-score. These were then transformed to give positive atrophy and rate of atrophy measures. The atrophy score was used in the cross-sectional analysis, while the rate of atrophy score was used in the longitudinal analysis.

7.2.3.1. Cross-sectional analysis

For the cross-sectional analysis a Z-score was calculated as follows:

$$Z_C(i) = \frac{\mu\big(C_h(i)\big) - C_k(i)}{\sigma(C_h(i))}.$$

where i is the regional connection strength, k is preHD, h is healthy controls, C is connection strength, μ is mean and σ is standard deviation. This was then transformed in order to produce atrophy measures between -1 and 1, using the following equation:

$$Z_{C-T}(i) = \tanh\left(Z_C(i)\right).$$

This resulted in a transformed Z-score for each cortical region for each preHD participant concerning cortico-striatal, inter-hemispheric and intra-hemispheric connections. An average was then calculated across the preHD group resulting in a single transformed Z-score for each cortical region.

7.2.3.1. Longitudinal analysis

For each preHD participant and for each connection a least squares line was fitted over the regional connection strengths across time points and the rate of connection atrophy defined as the gradient of the least squares line. A Z-score was then calculated using the following equation:

$$Z_R(i) = \frac{\mu\left(R_h(i)\right) - R_k(i)}{\sigma(R_h(i))}.$$

where R is the rate of change of connection strength. This was then transformed in order to produce atrophy measures between -1 and 1, using the following equation:

$$Z_{R-T}(i) = \tanh\left(Z_R(i)\right).$$

this resulted in a transformed Z-score of rate of regional atrophy for cortico-striatal, inter-hemispheric and intra-hemispheric connections for each preHD participant. An average was then calculated across the preHD group resulting in a single transformed Z-score for each cortical region.

7.2.4. Mapping gene expression data to MRI space

Gene expression microarray data were used from the Allen Human brain atlas (Hawrylycz et al., 2015). This atlas is based on data from 6 post-mortem human brains with no known neuropsychiatric or neuropathological history (H0351.2001, H0351.2002, H0351.1009, H0351.1012, H0351.1015, H0351.1016). Five donors were male and one was female with a mean age 42.5yrs. Three were Caucasian, two were African-American and one was Hispanic. This data is freely available to download from AIBS (http://human.brain-map.org/static/download).

Maybrain software (https://github.com/rittman/maybrain) was used to match centroids of MRI regions to the closest AIBS region. The nearest gene expression profile to the ROI coordinates was used as the expression profile for that ROI. Therefore for each ROI only one tissue sample was used from the AIBS atlas. Probes were excluded that did not match to gene symbols in the AIBS data resulting in 20,737 genes included in the analysis. Expression data was then averaged across all samples from all donors. Data were also averaged across both hemispheres as two donors had data for both hemispheres, while four only had data for the left hemisphere. The maximum standard deviation across participants for each gene probe in each brain region ranged from 0.1 to 4.6. To account for this variability the mean and range of expression values for each brain region were calculated and regions excluded if they had values greater than two standard deviations from either the mean or range. This resulted in the exclusion of two brain regions (right pars orbitalis and right rostral middle frontal),

leaving a total of 68 cortical ROIs included in the analysis. Expression data were then normalised by calculating the Z-score across the 68 Freesurfer regions. Similar approaches as those outlined above have been used when matching AIBS data to MRI atlases in other studies (Rittman et al., 2016; Vertes et al., 2016; Whitaker et al., 2016).

7.2.5. Statistical analysis

All statistical analysis was performed in MATLAB *v*8.3. Partial least squares regression was used to investigate the association between gene transcriptome of the healthy brain and WM connectivity loss in preHD both cross-sectionally and longitudinally. Code used to perform this analysis was adapted from Whitaker et al. (Whitaker et al., 2016). The original code is freely available (https://github.com/KirstieJane/NSPN_WhitakerVertes_PNAS2016).

Partial least squares regression is a multivariate technique used to identify associations between response and predictor variables. In my case the predictor variable was a 20,737 gene x 68 ROI matrix, as outlined above. For the cortico-striatal analysis the MRI data response variable was a 4 x 68 matrix of left and right caudate and putamen WM connectivity loss (preHD relative to controls) to 68 cortical ROIs. This was performed for both white matter atrophy (cross-sectional) and rate of white matter atrophy (longitudinal). For the inter-hemispheric analysis the MRI response variable was a vector of 1 x 68, representing WM inter-hemispheric connectivity loss for each cortical ROI. Similarly for the intra-hemispheric analysis the MRI response variable was a vector of 1 x 68, representing WM intra-hemispheric connectivity loss for each cortical ROI. For a cortical region inter-hemispheric connectivity was calculated as the sum of streamline volumes between that region and regions in

the opposite hemisphere. Similarly intra-hemispheric connectivity was defined as the sum of streamline volumes between that region and regions in the same hemisphere. Atrophy scores were then calculated using Z-scores and the tanh transform as described above.

For the majority of analyses the greatest amount of variance was explained by the first PLS component therefore genes were ranked based on their contribution to this component. Second components were also investigated if they explained a large amount of the variance. The error in estimating the weight of each gene was assessed by boot strapping and the ratio of the weight of each gene to its bootstrap standard deviation was used to rank the genes in descending order based on their contribution to the PLS component.

7.2.6. Gene ontology enrichment analysis

I used the gene ontology enrichment analysis and visualisation tool (GOrilla) (http://cbl-gorilla.cs.technion.ac.il) (Eden et al., 2009) to identify GO terms that were significantly enriched in the target gene list, based on the first PLS component. GOrilla GO terms are updated weekly. The target gene list is defined by finding the optimal hypergeometric tail probability over all possible partitions induced by gene ranking (see (Eden et al., 2009) for further details). Significance of a GO term is determined based on the rank of genes associated with that GO term and a false discovery rate (FDR) correction for multiple comparisons. This was performed for the first PLS component for the cortico-striatal, inter-hemispheric and intra-hemispheric analysis both cross-sectionally and longitudinally. The reduce and visualize gene ontology tool REViGO (Supek et al., 2011) (http://revigo.irb.hr) was then used to summarise significant GO terms by removing redundant terms.

7.2.7. Cortical regional enrichment

I used ROI weights from the PLS analysis to assess which cortical regions where enriched for genes in the first PLS component for the cortico-striatal, inter-hemispheric and intra-hemispheric analysis. ROI weights were plotted for each analysis using BrainNet Viewer (Xia et al., 2013).

7.2.8. Enrichment for Huntington's disease related genes

I also investigated whether genes showing abnormal transcription in human and animal models of Huntington's disease were enriched at a level greater than chance in the first PLS components of the cortico-striatal, inter-hemispheric and intra-hemispheric analyses. Gene lists were obtained from Langfelder et al. (Langfelder et al., 2016). These included 515 genes in the striatum and 25 in the cortex.

The Langfelder gene lists for the striatum include the 6-month allelic series striatum from Langfelder et al. (Langfelder et al., 2016) and the human caudate nucleus (CN) data sets by Durrenberger et al. (Durrenberger et al., 2015) and Hodges et al. (Hodges et al., 2006) are reported. Each striatal gene satisfies the following criteria: FDR<0.05 in the allelic series striatum, FDR<0.1 in each of the human data sets, and same sign of fold change across all 3 data sets. For the cortex the gene lists include the allelic series 6-month cortex, Broadmann area (BA) 4 and BA9 data by Hodges et al. (Hodges et al., 2006), and prefrontal cortex (PFC) and visual cortex (VC) data from the Harvard Brain Tissue Resource Centre are reported (Zhang et al., 2013). Each cortical gene satisfies the following criteria: FDR<0.05 in the allelic series cortex, FDR<0.1 in at least 3 of the 4 of the human data sets, and same sign of fold change in the allelic series cortex and at least 3 of the 4 human data sets. Genes

in the Langfelder lists not included in the AIBS gene set were excluded; this resulted in the exclusion of 28 striatum genes.

The mean PLS weight of candidate gene sets were compared against the mean PLS weight of 1000 random permutations of genes. A p-value was calculated based on the number of times in 1000 that the random gene list showed a higher mean rank than the candidate gene list. To further investigate the relationship between changes in gene expression in Huntington's disease relative to controls and cortico-striatal WM loss I performed correlations between the log2 fold change in the Hodges (Hodges et al., 2006), Durrenberger (Durrenberger et al., 2015) and Langfelder studies (Langfelder et al., 2016) for the 515 striatum gene set and the PLS weights from the cross-sectional cortico-striatal analysis.

7.2.9. Enrichment for alternative gene sets

Enrichment of the PLS components of the cortico-striatal, inter-hemispheric and intra-hemispheric analyses were also tested for a range of other gene sets. I included a set of human supragranular genes (n = 19) as these have been implicated in long-range connectivity (Krienen et al., 2016) and in chapter 6 I showed that cortico-striatal connections to have the longest topological length of the white connections subtypes investigated here. Genes specific to oligodendroctyes (n = 94) (Cahoy et al., 2008) were also included to investigate whether white matter loss may be driven by axonal or myelination dysfunction. Finally, genes involved in cell cycle metabolism (n = 252) (http://www.bmrb.wisc.edu/data_library/Genes/Metabolic_Pathways/Cell_cycle.html) were included as mutant huntingtin as been shown to cause cell cycle abnormalities (Molina-Calavita et al., 2014).

7.3. Results

7.3.1. Gene expression profiles of the healthy human brain explain the variance of regional white matter connectivity loss in preHD

For the majority of analyses the first PLS component accounted for a large percentage of the variance in regional WM loss. I therefore focused on the first PLS component. Gene expression data explained 66% of the variance of regional WM connectivity loss in the cortico-striatal cross-sectional analysis and 70% in the longitudinal analysis for the first component of the PLS and 11% and 6% respectively for the second component. For the inter-hemispheric analysis, gene expression explained 67% WM loss cross-sectionally and 17% longitudinally for the first component and 9% and 60% respectively for the second component. For the intra-hemispheric analysis 24% and 65% variance was explained for the cross-sectional and longitudinal analyses respectively and 47% and 11% respectively for the second component. For each analysis the first components of the PLS were explored. The second components for the intra-hemispheric cross-sectional and the inter-hemispheric longitudinal analyses were also explored as these accounted for a large amount of the variance.

7.3.2. Expression profiles associated with cross-sectional variation in white matter connections in preHD relative to controls

Similar significant GO terms were seen for the cortico-striatal and inter-hemispheric analyses these included modulation of chemical synaptic transmission, regulation of cell projection organisation and cell projection organisation, which I refer to as a synaptic profile. For the intra-hemispheric analysis the most significant GO terms included mRNA metabolic process, RNA processing and chromatin organisation (see Table 7.1 and Figures 7.2.1-7.2.3), which I refer to as a metabolic/chromatin profile. For the intra-hemispheric analysis the second component of the PLS was significantly associated with GO terms involved in myelination and lipid metabolism (see Figure 7.2.4).

Table 7.1. Cortico-striatal, inter-hemispheric and intra-hemispheric cross-sectional analyses: Gene ontology (GO) terms for biological processes associated with top ranking genes from the first component of the partial least squares (PLS) analysis. The top 5 most significant GO terms are displayed for each analysis. Redundant GO terms and those associated with greater than 1000 genes have been excluded. B – total number of genes associated with a specific GO term, n – number of genes in the target set, b – is the number of genes in the intersection. Enrichment (E) = (b/n) / (B/total number of genes). See (Eden et al., 2009) for further details.

PLS1 Cortico-striatal Cross-sectional							
GO Term	**Description**	**P-value**	**FDR q-value**	**Enrichment**	**B**	**n**	**b**
GO:0050773	regulation of dendrite development	8.05E-07	3.03E-03	2.18	124	3150	48
GO:0050804	modulation of chemical synaptic transmission	1.06E-06	3.19E-03	1.4	297	6419	151
GO:0031344	regulation of cell projection organization	1.88E-06	4.06E-03	1.29	549	6375	255
GO:0044057	regulation of system process	3.31E-06	4.98E-03	1.33	481	5795	209
GO:0030030	cell projection organization	4.31E-06	5.41E-03	1.24	699	6498	319
PLS1 Inter-hemispheric Cross-sectional							
GO Term	**Description**	**P-value**	**FDR q-value**	**Enrichment**	**B**	**n**	**b**
GO:0050804	modulation of chemical synaptic transmission	1.40E-14	3.51E-11	1.74	297	5246	153
GO:0031344	regulation of cell projection organization	1.99E-13	2.73E-10	1.64	549	3924	199
GO:0043623	cellular protein complex assembly	7.20E-13	8.34E-10	1.65	371	4892	169
GO:0061024	membrane organization	1.51E-11	1.19E-08	1.45	820	4221	283
GO:0030030	cell projection organization	6.38E-11	3.85E-08	1.47	699	4281	248
PLS1 Intra-hemispheric Cross-sectional							
GO Term	**Description**	**P-value**	**FDR q-value**	**Enrichment**	**B**	**n**	**b**
GO:0016071	mRNA metabolic process	2.91E-33	1.12E-30	1.84	593	5085	313
GO:0006396	RNA processing	4.39E-30	1.58E-27	1.65	806	5357	402
GO:0006325	chromatin organization	1.11E-25	3.73E-23	1.79	657	4364	289
GO:0006397	mRNA processing	4.33E-21	1.42E-18	1.78	402	5435	219
GO:0019083	viral transcription	2.79E-20	8.77E-18	3.01	99	4044	68

Figure 7.2.1. Cortico-striatal cross-sectional analysis semantic similarity scatter plot: Significant gene ontology (GO) terms for biological processes associated with the first component of the partial least squares (PLS) analysis are plotted in semantic space, where similar terms are clustered together. The top 5 most significant GO terms are labelled for each analysis. Redundant GO terms and those associated with greater than 1000 genes have been excluded. Markers are scaled based on the log10 q-value for the significance of each GO term. Large blue circles are highly significant, while red circles are less significant (see colour bar).

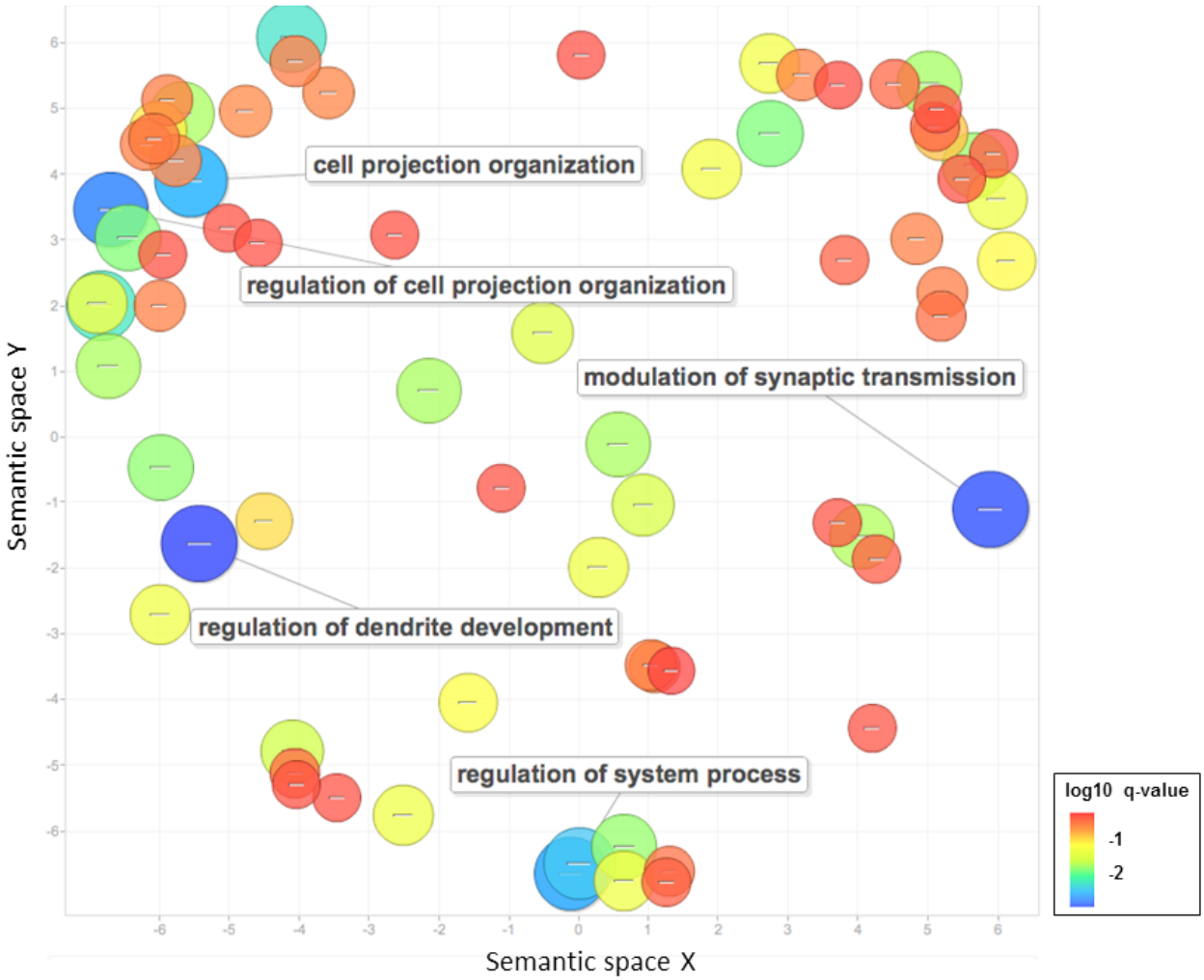

Figure 7.2.2. Inter-hemispheric cross-sectional analysis semantic similarity scatter plot: Significant gene ontology (GO) terms for biological processes associated with the first component of the partial least squares (PLS) analysis are plotted in semantic space, where similar terms are clustered together. The top 5 most significant GO terms are labelled for each analysis. Redundant GO terms and those associated with greater than 1000 genes have been excluded. Markers are scaled based on the log10 q-value for the significance of each GO term. Large blue circles are highly significant, while red circles are less significant (see colour bar)

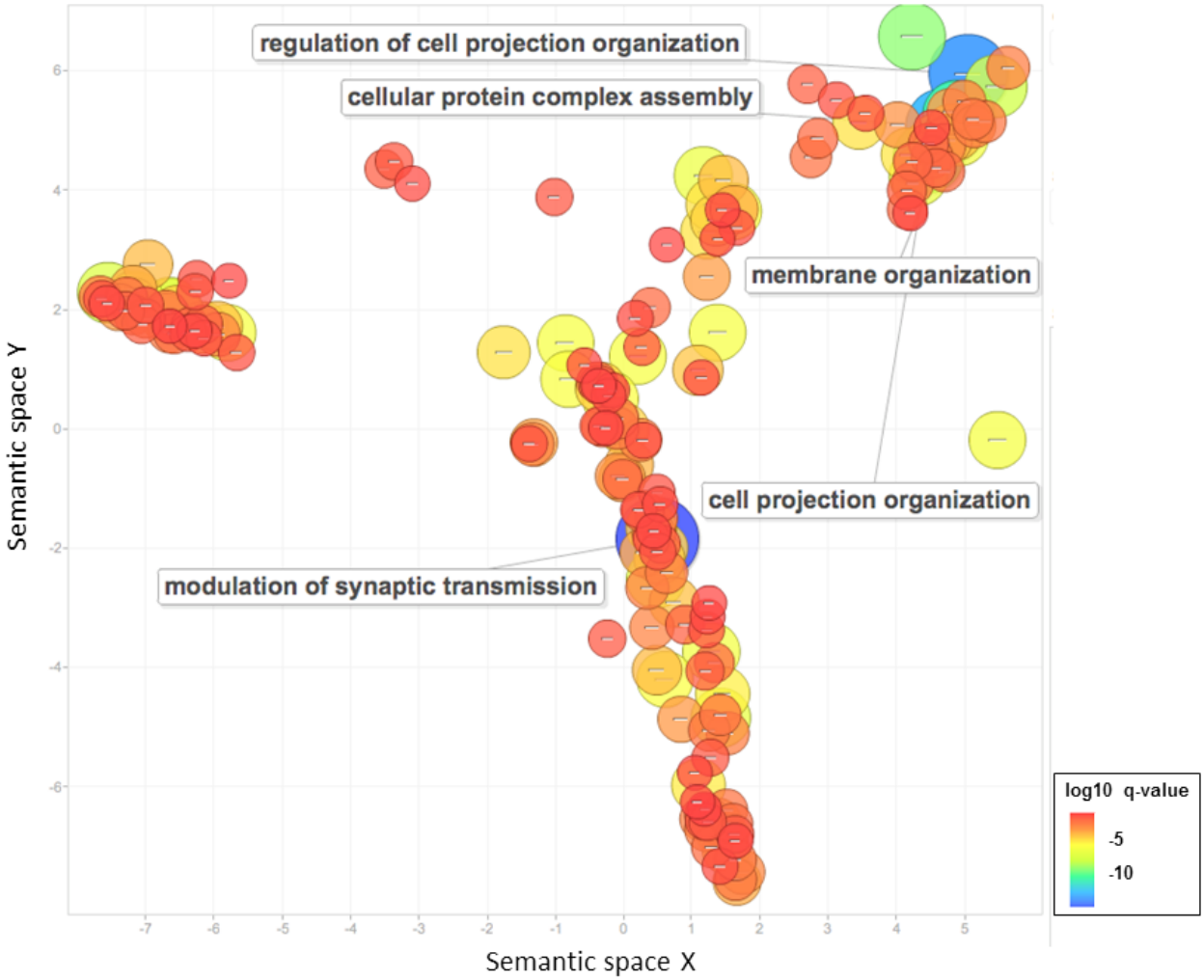

Figure 7.2.3. Intra-hemispheric cross-sectional analysis semantic similarity scatter plot: Significant gene ontology (GO) terms for biological processes associated with the first component of the partial least squares (PLS) analysis are plotted in semantic space, where similar terms are clustered together. The top 5 most significant GO terms are displayed for each analysis. Redundant GO terms and those associated with greater than 1000 genes have been excluded. Markers are scaled based on the log10 q-value for the significance of each GO term. Large blue circles are highly significant, while red circles are less significant (see colour bar).

Figure 7.2.4. Intra-hemispheric cross-sectional analysis semantic similarity scatter plot (second component): Significant gene ontology (GO) terms for biological processes associated with the second component of the partial least squares (PLS) analysis are plotted in semantic space, where similar terms are clustered together. The top 5 most significant GO terms are displayed for each analysis. Redundant GO terms and those associated with greater than 1000 genes have been excluded. Markers are scaled based on the log10 q-value for the significance of each GO term. Large blue circles are highly significant, while red circles are less significant (see colour bar).

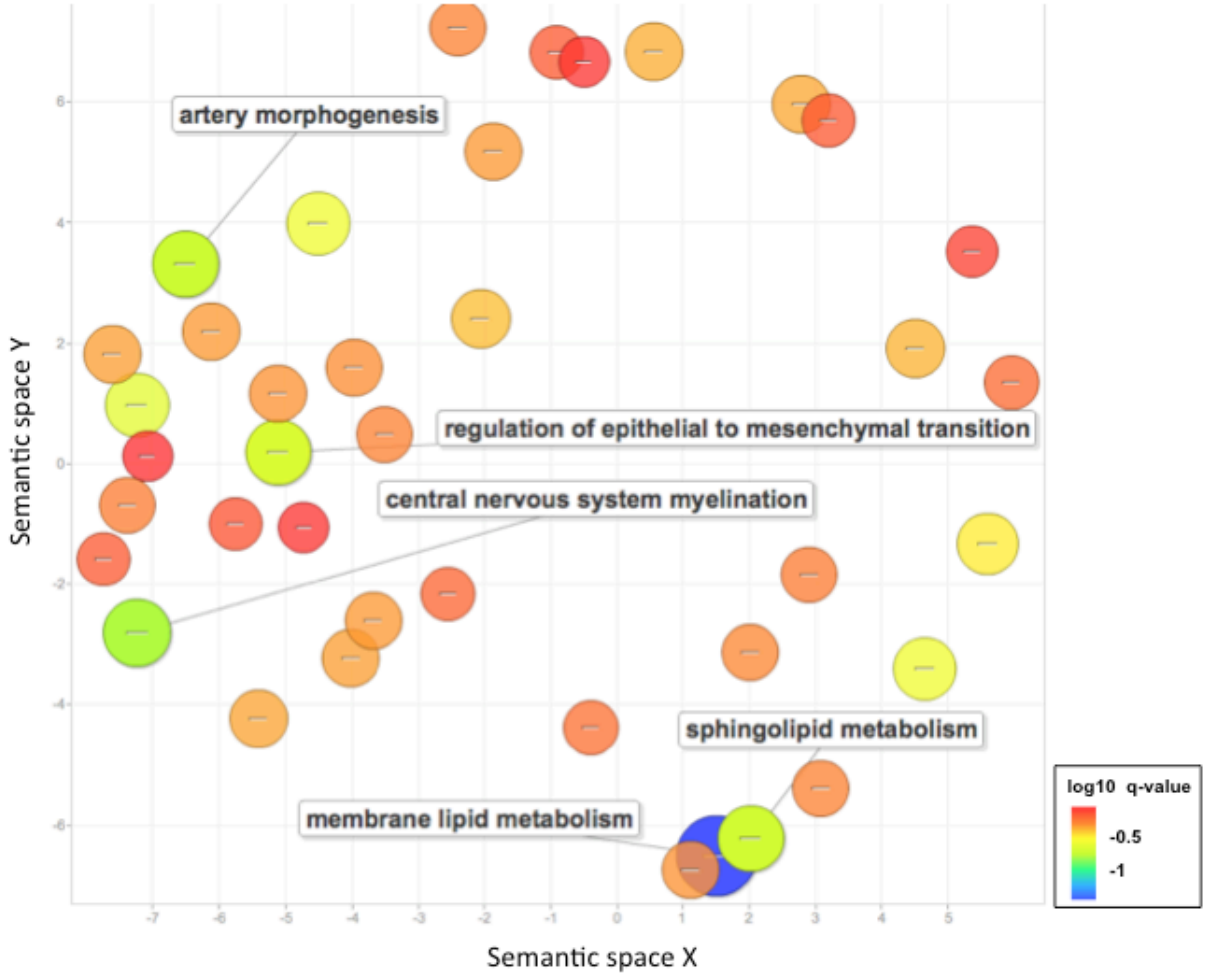

7.3.3. Expression profiles associated with longitudinal change in white matter connections in preHD relative to controls

For both the cortico-striatal and inter-hemispheric analyses longitudinal change in white matter was associated with GO terms involving metabolism or chromatin organisation (see Table 7.2 and Figures 7.3.1 and 7.3.2). For intra-hemispheric analysis longitudinal change was associated with GO terns involved in mitochondrial function, metabolism and synaptic transmission (see Table 7.2 and Figure 7.3.3). The second component of the PLS for the inter-hemispheric analysis was significantly associated with a range of GO terms involved in a diverse range of biological processes, however these were only minimally significant. In summary, these results suggest regional gene expression profiles associated with loss of WM connectivity in preHD are involved in synaptic, metabolic and chromatin related biological processes.

Table 7.2. Cortico-striatal, inter-hemispheric and intra-hemispheric longitudinal analysis: Gene ontology (GO) terms for biological processes associated with top ranking genes from the first component of the partial least squares (PLS) analysis. The top 5 most significant GO terms are displayed for each analysis. Redundant GO terms and those associated with greater than 1000 genes have been excluded. B – total number of genes associated with a specific GO term, n – number of genes in target set, b – is the number of genes in the intersection. Enrichment (E) = (b/n) / (B/total number of genes). See (Eden et al., 2009) for further details.

PLS1 Cortico-striatal Longitudinal							
GO Term	**Description**	**P-value**	**FDR q-value**	**Enrichment**	**B**	**n**	**b**
GO:0016071	**mRNA metabolic process**	**3.51E-33**	**1.35E-30**	**1.81**	**593**	**5324**	**322**
GO:0006396	**RNA processing**	**7.90E-29**	**2.77E-26**	**1.64**	**806**	**5324**	**397**
GO:0019083	**viral transcription**	**3.28E-28**	**1.12E-25**	**2.86**	**99**	**5251**	**84**
GO:0006325	**chromatin organization**	**9.85E-26**	**3.22E-23**	**1.77**	**657**	**4520**	**296**
GO:0000184	**nuclear-transcribed mRNA catabolic process, nonsense-mediated decay**	**2.16E-19**	**6.78E-17**	**2.53**	**102**	**5298**	**77**
PLS1 Inter-hemispheric Longitudinal							
GO Term	**Description**	**P-value**	**FDR q-value**	**Enrichment**	**B**	**n**	**b**
GO:0016071	**mRNA metabolic process**	**3.98E-16**	**1.67E-13**	**1.48**	**593**	**6539**	**323**
GO:0006325	**chromatin organization**	**4.09E-14**	**1.47E-11**	**1.4**	**657**	**6476**	**337**
GO:0006396	**RNA processing**	**7.78E-14**	**2.66E-11**	**1.36**	**806**	**6410**	**397**
GO:0006397	**mRNA processing**	**6.16E-12**	**2.02E-09**	**1.49**	**402**	**6323**	**213**
GO:0016569	**covalent chromatin modification**	**4.62E-09**	**1.36E-06**	**1.38**	**455**	**6476**	**230**
PLS1 Intra-hemispheric Longitudinal							
GO Term	**Description**	**P-value**	**FDR q-value**	**Enrichment**	**B**	**n**	**b**
GO:0022904	**respiratory electron transport chain**	**2.29E-13**	**1.15E-09**	**2.71**	**92**	**3917**	**55**
GO:0050804	**modulation of chemical synaptic transmission**	**2.95E-11**	**6.35E-08**	**1.84**	**297**	**3658**	**113**
GO:0006091	**generation of precursor metabolites and energy**	**1.42E-10**	**2.38E-07**	**1.64**	**263**	**5414**	**132**
GO:0009117	**nucleotide metabolic process**	**4.97E-10**	**7.48E-07**	**1.88**	**418**	**2364**	**105**
GO:0070271	**protein complex biogenesis**	**9.42E-10**	**1.01E-06**	**2.46**	**81**	**4186**	**47**

Figure 7.3.1. Cortico-striatal longitudinal analysis semantic similarity scatter plot: Significant gene ontology (GO) terms for biological processes associated with the first component of the partial least squares (PLS) analysis are plotted in semantic space, where similar terms are clustered together. The top 5 most significant GO terms are labelled for each analysis. Redundant GO terms and those associated with greater than 1000 genes have been excluded. Markers are scaled based on the log10 q-value for the significance of each GO term. Large blue circles are highly significant, while red circles are less significant (see colour bar).

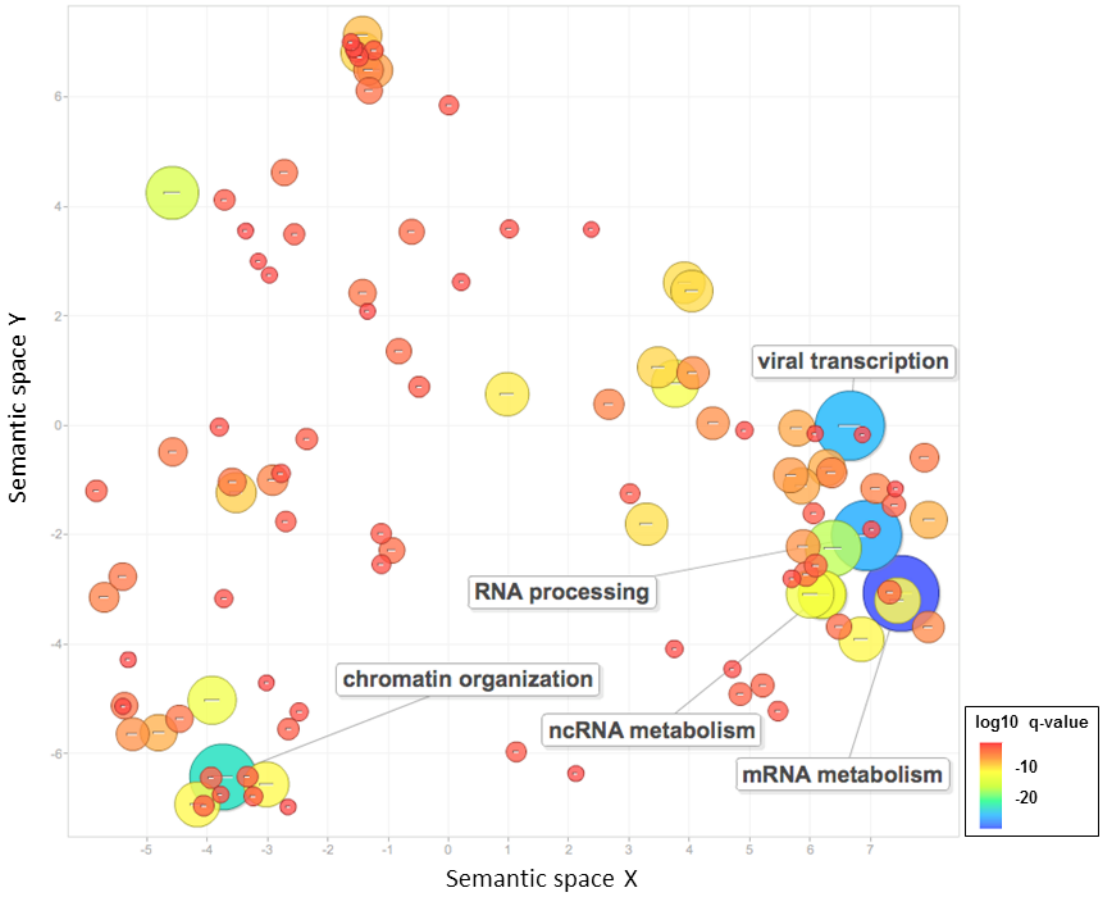

Figure 7.3.2. Inter-hemispheric longitudinal analysis semantic similarity scatter plot: Significant gene ontology (GO) terms for biological processes associated with the first component of the partial least squares (PLS) analysis are plotted in semantic space, where similar terms are clustered together. The top 5 most significant GO terms are labelled for each analysis . Redundant GO terms and those associated with greater than 1000 genes have been excluded. Markers are scaled based on the log10 q-value for the significance of each GO term. Large blue circles are highly significant, while red circles are less significant (see colour bar).

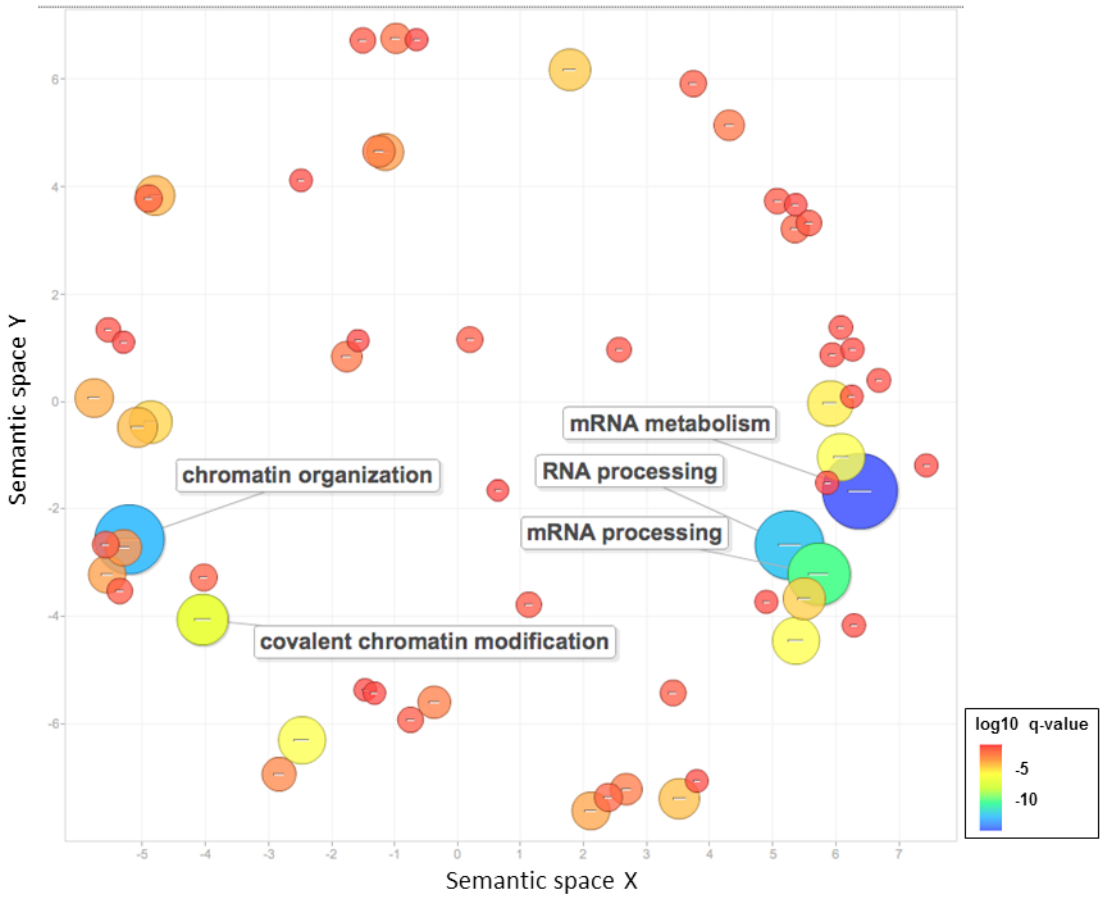

Figure 7.3.3. Intra-hemispheric longitudinal analysis semantic similarity scatter plot: Significant gene ontology (GO) terms for biological processes associated with the first component of the partial least squares (PLS) analysis are plotted in semantic space, where similar terms are clustered together. The top 5 most significant GO terms are labelled for each analysis. Redundant GO terms and those associated with greater than 1000 genes have been excluded. Markers are scaled based on the log10 q-value for the significance of each GO term. Large blue circles are highly significant, while red circles are less significant (see colour bar).

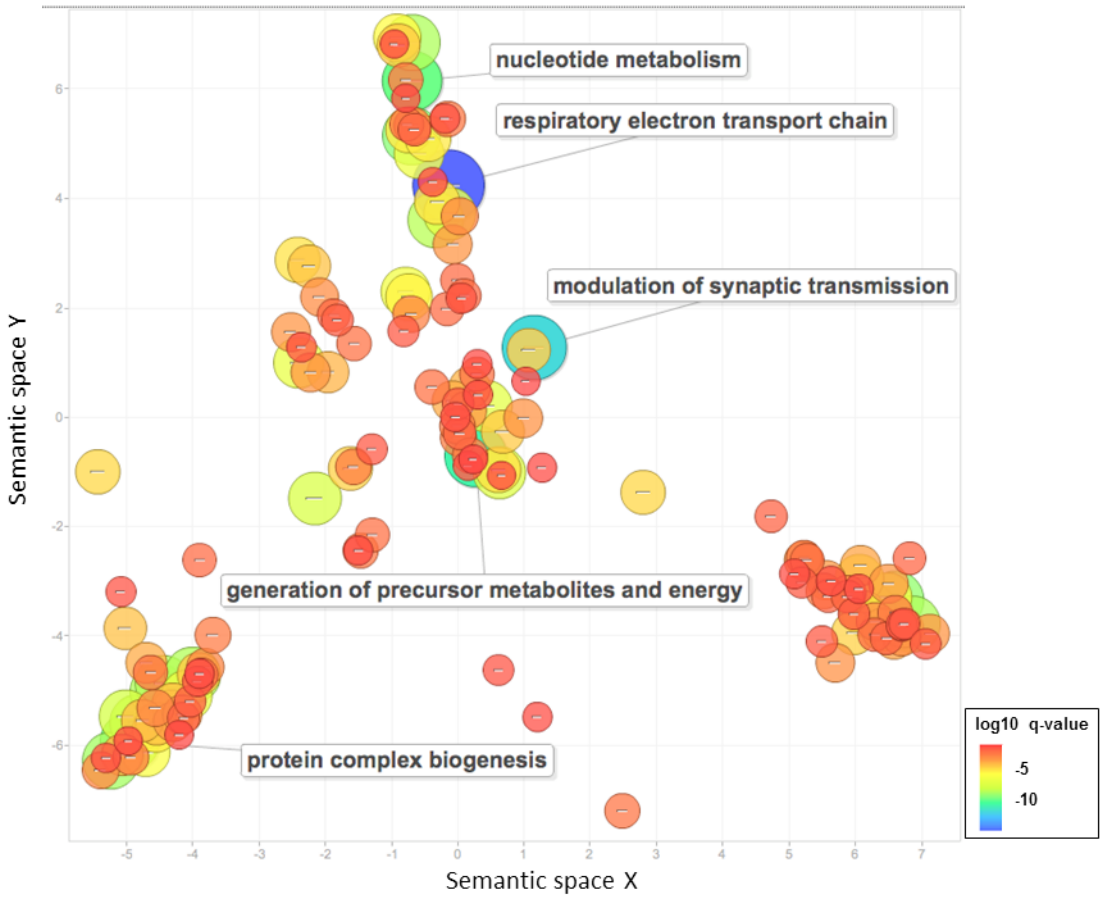

7.3.4. Overlap between synaptic and metabolic gene profiles

Given the change from synaptic to metabolic profiles in cross-sectional vs. longitudinal I hypothesised that there may be common genes ranked highly in both synaptic and metabolic/chromatin profiles. To explore this I investigated the top 7,000 genes (based on target gene lists from top GO terms) from the cross-sectional cortico-striatal analysis (showing a synaptic profile) and the intra-hemispheric analysis (showing a metabolic/chromatin profile). An overlap of 346 genes was found. These were then compared to the striatal genes showing transcriptional abnormalities in HD humans and animal models. This revealed 8 genes in common, encoding proteins involved in cell cycle (CEP135), axon development (NEK1) and G-protein coupling (ADORA2A).

7.3.5. Dissociation of synaptic and metabolic gene enrichment in the cortex

The next step in my analysis was to explore the spatial pattern of each gene expression profile in the brain. To determine what brain regions were enriched with each gene expression profile, I analysed PLS ROI weights from each analysis where higher weights related to greater gene profile enrichment (see Table 7.3). Cortical regions with the highest weights in the cortico-striatal analysis (cross-sectional) were predominantly in the motor, parietal and occipital cortices. Conversely, cortical regions with the highest weights in the inter-hemispheric analysis (cross-sectional) were predominantly in the frontal and temporal and insular cortices. Cortical regions with the highest weights in the intra-hemispheric analysis (cross-sectional) included frontal, temporal and occipital regions (see Figure 7.4). Plotting cortico-striatal ROI weights against both inter-hemispheric and intra-hemispheric ROI weights revealed dissociation in terms of regions involved, where regions enriched in the

cortical-striatal analysis were distinctly different from those enriched in the inter-hemispheric and intra-hemispheric analyses (see Figure 7.5).

Table 7.3. ROI weights from first PLS components. BG – basal ganglia, IH – Inter-hemispheric, IA – Intra-hemispheric, cross – cross-sectional, long – longitudinal**.** Weights ordered for basal ganglia cross-sectional analysis, decreasing strongest to weakest. Only the top 25 weights are presented.

Region	CS cross	IH cross	IA cross	CS long	IH long	IA long
R.inferiorparietal	0.22034	0.028159	-0.077541	-0.11582	-0.068989	0.15782
R.precentral	0.20856	0.047965	-0.088025	-0.12867	-0.059647	0.17176
R.superiorparietal	0.20856	0.047965	-0.088025	-0.12867	-0.059647	0.17176
L.cuneus	0.15725	0.10562	-0.12229	-0.12238	-0.10801	0.13927
L.inferiorparietal	0.15725	0.10562	-0.12229	-0.12238	-0.10801	0.13927
L.isthmuscingulate	0.15725	0.10562	-0.12229	-0.12238	-0.10801	0.13927
L.lateraloccipital	0.15725	0.10562	-0.12229	-0.12238	-0.10801	0.13927
L.paracentral	0.15725	0.10562	-0.12229	-0.12238	-0.10801	0.13927
L.pericalcarine	0.15725	0.10562	-0.12229	-0.12238	-0.10801	0.13927
L.posteriorcingulate	0.15725	0.10562	-0.12229	-0.12238	-0.10801	0.13927
L.precuneus	0.15725	0.10562	-0.12229	-0.12238	-0.10801	0.13927
L.superiorparietal	0.15725	0.10562	-0.12229	-0.12238	-0.10801	0.13927
L.supramarginal	0.15725	0.10562	-0.12229	-0.12238	-0.10801	0.13927
R.isthmuscingulate	0.15725	0.10562	-0.12229	-0.12238	-0.10801	0.13927
R.paracentral	0.15725	0.10562	-0.12229	-0.12238	-0.10801	0.13927
R.posteriorcingulate	0.15725	0.10562	-0.12229	-0.12238	-0.10801	0.13927
R.precuneus	0.15725	0.10562	-0.12229	-0.12238	-0.10801	0.13927
R.supramarginal	0.15725	0.10562	-0.12229	-0.12238	-0.10801	0.13927
R.caudalmiddlefrontal	0.14542	0.10192	-0.093706	-0.090327	-0.16404	0.11031
R.postcentral	0.14542	0.10192	-0.093706	-0.090327	-0.16404	0.11031
R.cuneus	0.12658	0.097045	-0.10093	-0.1211	-0.078746	0.10593
L.postcentral	0.11425	0.099365	-0.10889	-0.12017	-0.094212	0.1137
L.caudalmiddlefrontal	0.054748	0.11976	-0.11586	-0.10097	-0.12061	0.097573
L.transversetemporal	0.030688	0.11459	-0.10071	-0.10298	-0.055668	0.067514
R.caudalanteriorcingulate	0.030688	0.11459	-0.10071	-0.10298	-0.055668	0.067514

Figure 7.4. ROI weights for cross-sectional partial least squares regression analyses. (a) Cortico-striatal (b) Inter-hemispheric (c) Intra-hemispheric. Brain regions displayed on brain mesh. Size and colour of region indicates size of ROI weight (ranked from smallest-largest, 1-6). See colour map.

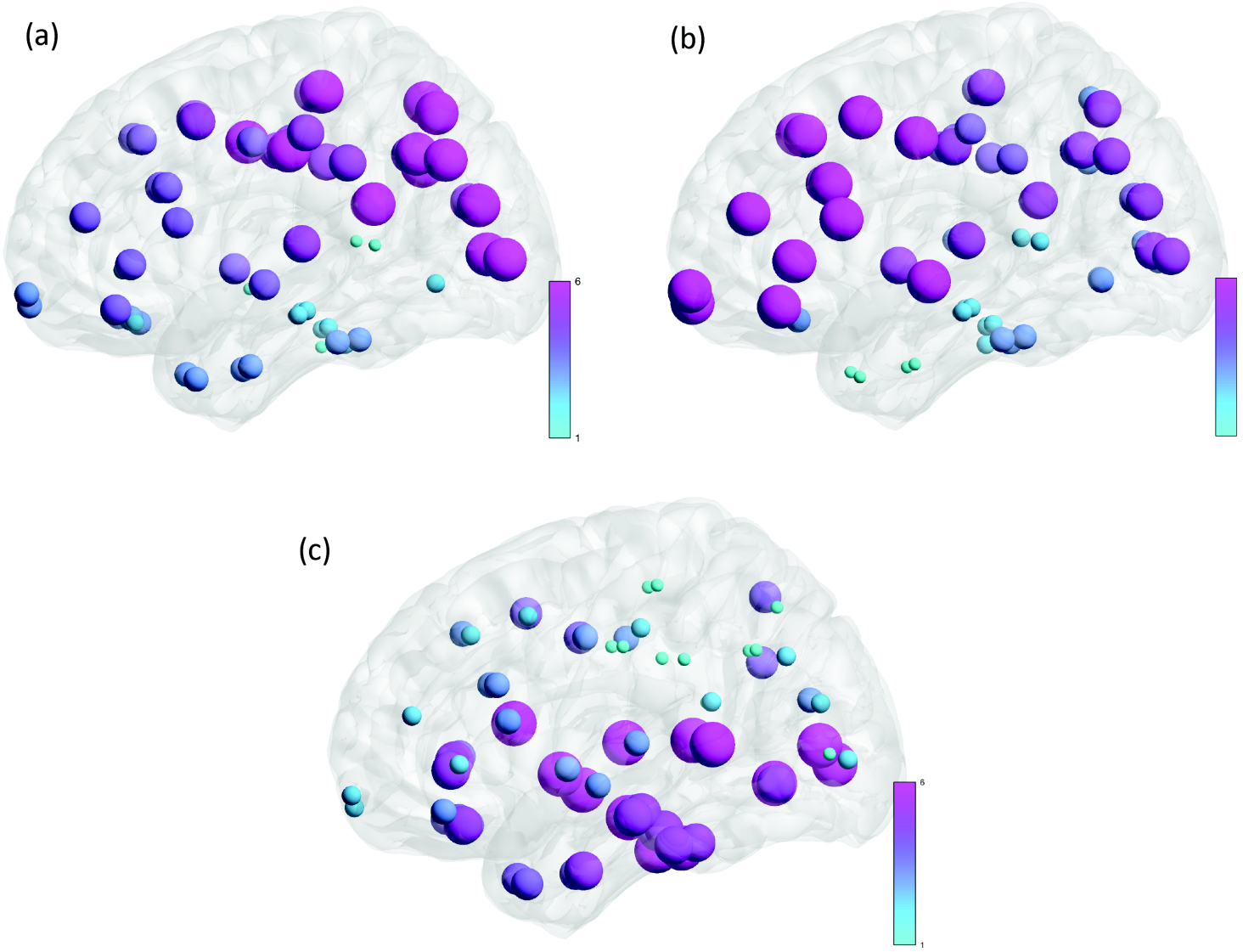

7.5. Dissociation of cortico-striatal and inter/intra-hemispheric gene enrichment in the cortex. (a) ROI weights for the first PLS component of the cross-sectional analysis for inter-hemispheric vs. cortical-striatal. (b) ROI weights for the first PLS component of the longitudinal analysis for inter-hemispheric vs. cortical-striatal. (c) ROI weights for the first PLS component of the cross-sectional analysis for intra-hemispheric vs. cortical-striatal. (d) ROI weights for the first PLS component of the longitudinal analysis for intra-hemispheric vs. cortical-striatal. Each red circle represents a cortical ROI.

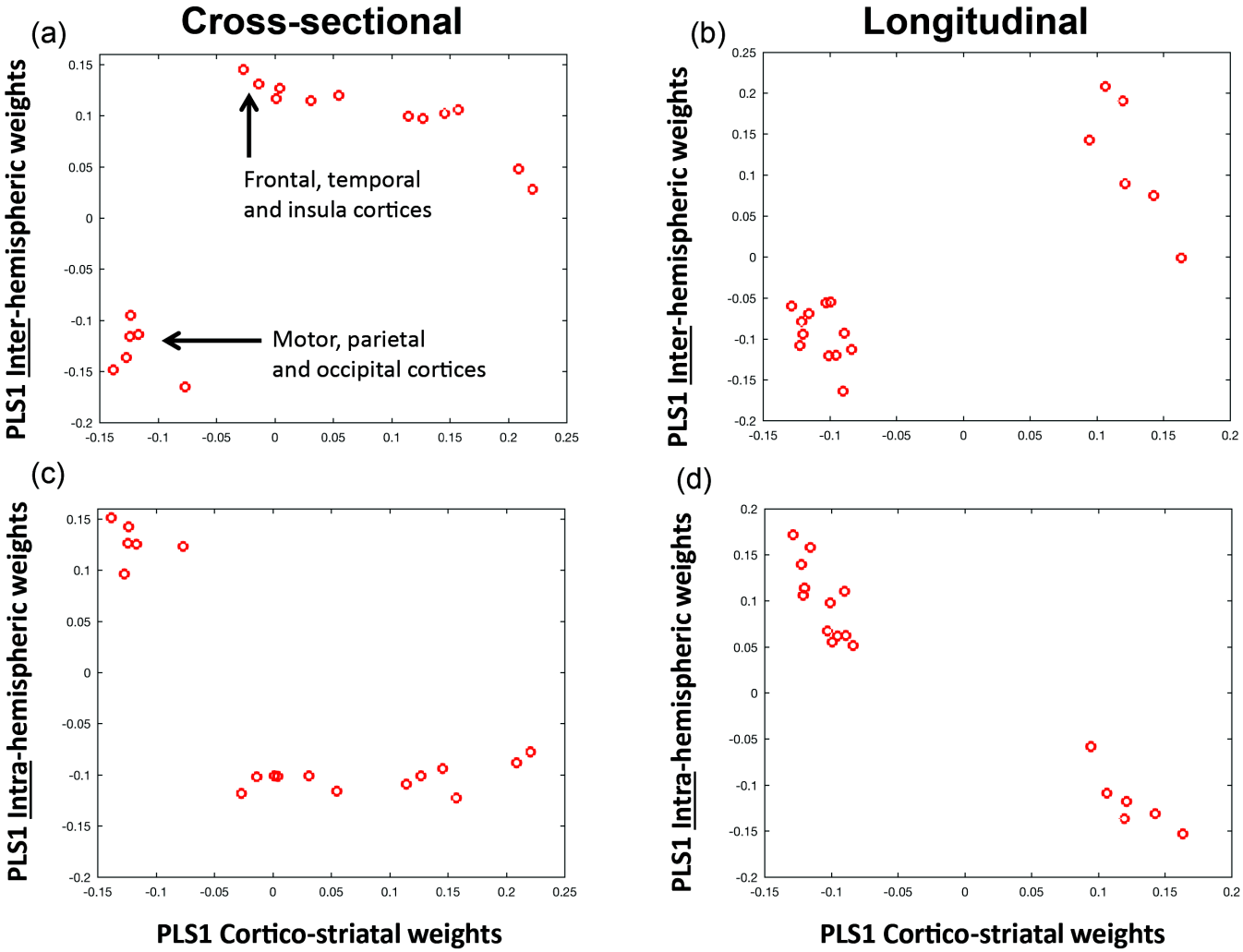

7.3.6. Enrichment of genes showing abnormal transcription in HD is seen in the cortico-striatal and inter-hemispheric gene expression profiles

My next step was to assess whether genes that show abnormal transcription in HD, both in the cortex and striatum, might be driving white matter loss. The cortico-striatal gene list was significantly enriched for abnormal HD genes in the striatum ($p < 0.001$) and in the cortex ($p < 0.001$). The inter-hemispheric gene list with significantly enriched for genes in the striatum ($p < 0.001$) but not the cortex. No significant enrichment was seen for the intra-hemispheric gene list (see Figure 7.6). To ensure the significance difference for the striatum gene list was not related to the size of the gene data set I repeated the analysis using the top 25 most significant genes based on Hodges q-value. Results were consistent with the 515 gene list showing significant enrichment for HD genes in the striatum for the cortico-striatal ($p = 0.019$) and inter-hemispheric ($p = 0.004$) analyses. This suggests that abnormal transcription in HD may drive cortico-striatal and inter-hemispheric WM connectivity loss.

Figure 7.6. Enrichment of genes showing abnormal transcription in Huntington's disease in the first PLS components of cortico-striatal, inter-hemispheric and intra-hemispheric cross-sectional analyses. Red circle illustrates the mean weight (on the x-axis) for the gene list of interest in the first PLS component. The y-axis represents the number of permutations of random genes from the first PLS component. Gene lists over expressed in the first PLS component have a mean great than that of the random permutations (red circle to the right of the permutation distribution).

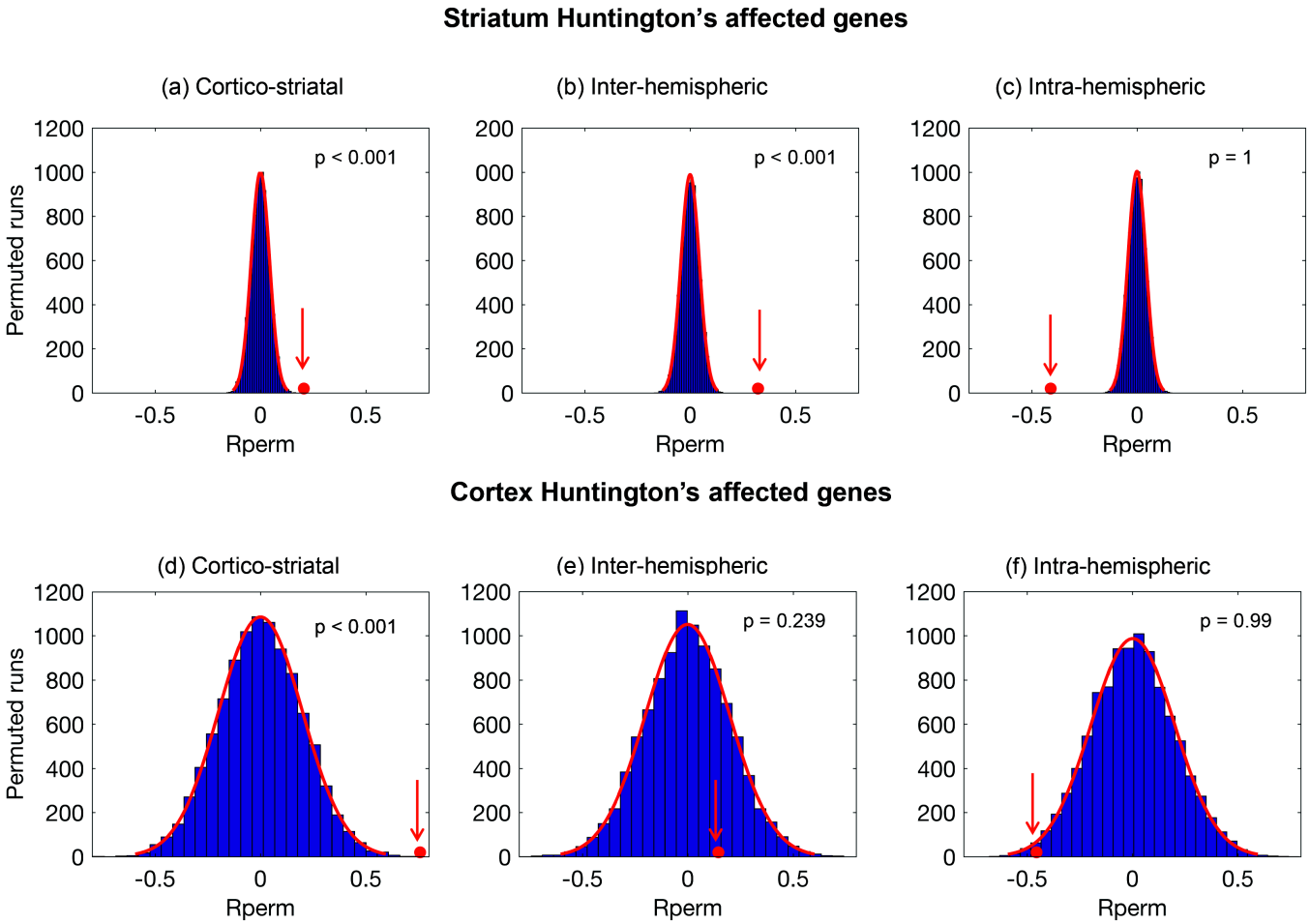

To further investigate the relationship between changes in gene expression in HD relative to controls and cortico-striatal WM loss I performed correlations between the log2 fold change in the Hodges (Hodges et al., 2006), Durrenberger (Durrenberger et al., 2015) and Langfelder studies (Langfelder et al., 2016) for the 515 striatum gene set and the PLS weights from the cross-sectional cortico-striatal analysis. This revealed negative correlations between PLS weights and Log2 fold change (Hodges, rho = -0.23, $p = 1.1x10^{-7}$, Durrenberger, rho = -0.23, $8.4x10^{-8}$, Langfelder, rho = -0.19, $p = 1.6x10^{-5}$). This suggests that genes associated with cortico-striatal white matter loss in preHD are also those that show reduced levels of transcription in human HD and animal models.

7.3.7. Enrichment for other gene lists

I also investigated enrichment for genes associated with human supragranular cortex, oligodendrocytes and cell cycle metabolism. The cortico-striatal (CS) and inter-hemispheric (IH) gene lists were significantly enriched for human supragranular cortex genes (CS, $p = 0.002$, IH, $p = 0.006$) and oligodendrocyte genes (CS, $p < 0.001$, IH, $p < 0.001$) but not cell cycle metabolism genes. Conversely the intra-hemispheric gene list was significantly enriched for cell cycle metabolism genes ($p < 0.001$) but not human supragranular or oligodendrocyte genes. This suggests cortico-striatal white matter loss may be driven by abnormal transcription in oligodendrocytes thereby causing demyelination. Additionally cortical supragranular genes are implicated in long-range connectivity (Krienen et al., 2016) and abnormal transcription of these genes in the cortex may result in connectivity loss to the striatum and between hemispheres. The lack of enrichment of these genes in the intra-hemispheric gene list further supports the observation that white matter loss may also be due to abnormal metabolism, especially given significant enrichment for cell cycle metabolism genes.

7.4. Discussion

7.4.1. White matter loss is associated with synaptic and metabolic genes

In this chapter I show that the regional variance in white matter loss in preHD is differentially associated with the pattern of expression of genes involved in synaptic, metabolic and chromatin related processes in the healthy human brain. Cortico-striatal and intra-hemispheric WM loss is associated with synaptic genes, whereas intra-hemispheric WM loss is associated with metabolic and chromatin-related genes. There is also a distinction between gene enrichment in cortical regions where enrichment associated with cortico-striatal connections is seen in more posterior regions such as motor, occipital and parietal cortices, whereas enrichment associated with inter-hemispheric connections is seen in frontal, temporal and insula cortices. I reveal that genes showing abnormal transcription in HD humans and animal models are over expressed in the ranked gene lists associated with cortico-striatal and inter-hemispheric WM loss but not intra-hemispheric WM connection loss. I focus on synaptic, metabolic and chromatin related genes to simplify interpretation of my results. However specific GO terms such as DNA metabolism may relate to abnormal DNA repair (Moss et al., 2017), while mRNA metabolism may relate to abnormal splicing of mRNA, both processes that are implicated in HD pathogenesis (Sathasivam et al., 2013). I note that further work would be needed to link these specific gene sets directly to white matter loss in HD.

7.4.2. Transcription abnormalities in HD

Widespread gene transcription abnormalities occur in HD and represent some of the earliest pathological changes. Genes showing abnormal transcription are involved in a range of diverse biological processes including transcription and chromatin remodelling, synaptic transmission, metabolism and inflammation (Seredenina and Luthi-Carter, 2012). A number of studies have analysed gene expression profiles both in human HD and animal models. Post mortem brain samples from HD patients have been used to investigate gene expression in the caudate, motor cortex and prefrontal association cortex (Hodges et al., 2006). This showed that gene expression was most affected in the caudate, followed by the motor cortex, while no abnormalities were detected in the prefrontal association cortex. The GO term showing greatest significance for both the caudate and motor cortex was synaptic transmission. Furthermore, significance for the GO terms metabolism and glucose metabolism were seen in the cortex, but not the caudate. These findings are in agreement with the associations between synaptic genes and cortico-striatal WM connection loss and metabolic genes and intra-hemispheric WM connection loss that I demonstrate here.

7.4.3. Common genes between synaptic and metabolic profiles

Changes from synaptic to metabolic profiles in cross-sectional vs. longitudinal were seen for cortico-striatal and inter-hemispheric connections. I investigated this further showing common genes highly ranked in both profiles. These genes showed overlap with striatum genes showing transcriptional abnormalities in HD humans and animal models. Notably these included genes encoding proteins involved in cell cycle (CEP135), axon development (NEK1) and G-protein coupling (ADORA2A). One explanation for the switch between synaptic and metabolic profiles in the cross-sectional and longitudinal analyses may be that atrophy scores cross-

sectionally are higher than longitudinal rate of atrophy scores. Enrichment for specific gene lists were in keeping with these findings. Cortico-striatal and inter-hemispheric gene profiles were enriched for human supragranular cortex genes, implicated in long-range connectivity, and oligodendrocyte genes, whereas the intra-hemispheric gene profile was enriched for genes involved in cell cycle metabolism.

7.4.4. Limitations

I acknowledge the limitations of diffusion tractography. To address these I used both CSD, which deals more effectively with crossing fibres than the diffusion tensor or multi-tensor methods (Tournier et al., 2012) and SIFT2, which has higher reproducibility and is more representative of the underlying biology of WM connections than conventional methods (Smith et al., 2015a). CSD performs well at the acquisition protocol specifications used in this study (b =1000) (Ramirez-Manzanares et al., 2011; Wilkins et al., 2015). At b=1000 a minimum number of 28 gradient directions is required (Tournier et al., 2013). Therefore the angular coverage achieved using CSD at b=1000 is more than sufficient with 42 directions.

I map the anatomical location of ROIs to corresponding regions in AIBS atlas. However the resolution of these atlases are different and thus I acknowledge that the correspondence may not be exact and may be a limitation of my methodology. There are other human brain transcriptome atlas such as Braineac (Ramasamy et al., 2014) and the Human Brain Transcriptome Project (Kang et al., 2011). However, these atlases offer low resolution compared to the AIBS atlas, where only a small number of cortical regions have been sampled therefore the analysis carried out in this study could not be reproduced using Braineac or the Human Brain Transcriptome Project atlas.

The utility of using information from the healthy human brain to inform us about the patterns and mechanisms of neurodegeneration has been demonstrated numerous times in the field of neuroimaging. Functional connectivity and white matter networks from healthy participants can predict atrophy in Alzheimer's disease, corticobasal syndrome, fronto-temporal dementia and Parkinson's disease (Mandelli et al., 2016; Seeley et al., 2009; Zeighami et al., 2015; Zhou et al., 2012). More recently transcriptome data from the healthy brains of the AIBS atlas has been used in schizophrenia to investigate the association between the expression of schizophrenia risk genes and white matter disconnectivity (Romme et al., 2016). The regional expression of the tau gene MAPT from the AIBS atlas has also been linked to the selective vulnerability of highly connected brain regions in Parkinson's disease and progressive supranuclear palsy (Rittman et al., 2016).

7.4.5. Conclusions

In this chapter, I show that cortico-striatal and inter-hemispheric WM connection loss is associated with the expression of synaptic genes in preHD, while intra-hemispheric WM loss is associated with metabolic genes. Genes showing abnormal transcription in HD are associated with the synaptic but not metabolic gene profiles, suggesting that cortico-striatal and inter-hemispheric WM loss in preHD may be driven by abnormal transcription. These findings have important implications for linking the earliest WM changes in preHD to the underlying pathological processes that may drive them. In the next and final chapter of my thesis I will review the findings from my experimental chapters and discuss the new hypothesis these results have generated and how to test them in future work.

7.5. Publications relating to this chapter

The work presented in this chapter was published as:

Brain regions showing white matter loss in Huntington's disease are enriched for synaptic and metabolic genes. **McColgan P**, Gregory S, Seunarine K.K, Razi A, Papoutsi M, Johnson E, Durr A, Roos R.A, Leavitt B.R, Holmans P, Scahill R.I, Clark C.A, Rees G, Tabrizi S.J and the Track-On HD Investigators. **Biological Psychiatry**. 2017; S0006-3223(17):32129-7

Chapter 8. General discussion

8.1. Introduction

In this thesis I began by investigating the relationship between structural and functional connectivity in preHD (chapter 3) and show how these relate to psychiatric features of HD, that occur years before the manifestation of motor symptoms (chapter 4). I then revealed how the white matter brain network breaks down from preHD to manifest HD linking this brain network degeneration to deficits in cognitive and motor function (chapter 5). In the subsequent longitudinal analyses I demonstrated a hierarchy of white matter vulnerability where cortico-striatal connections are the most affected followed by inter-hemispheric and intra-hemispheric connections (chapter 6). I then linked these white matter changes to synaptic and metabolic gene profiles in keeping with the cellular pathobiology of HD (chapter 7). In this chapter, I will review the findings of the experimental chapters and discuss ongoing and future work aimed at addressing some of the new questions and new hypotheses that the experiments in this thesis have generated.

8.2. Linking brain structure and function in HD

In the first experimental chapter I demonstrated how the organisational properties of healthy white matter can predict decreases in structural connectivity and increases in functional connectivity in preHD relative to controls. Specifically, brain regions with strong connections to distant regions show decreases in structural connectivity, while those with strong connections to their neighours show increases in functional connectivity in preHD relative to healthy controls. I also revealed a striking A-P dissociation where anterior regions in the brain showed functional up-regulation of connectivity while posterior regions in the brain showed down-regulation. While it is

unclear whether these increases in functional connectivity are compensatory or pathological, the fact these increases are seen in regions with low white matter connectivity loss suggest they may either represent the earliest signs of the disease process prior to structural connectivity loss or may indeed represent regions with intact structural connectivity up-regulating as a compensatory mechanism.

Increased brain activity, measured during task or resting state fMRI, is often deemed compensatory in the context if neurodegenerative disease. However a complete definition of compensation would incorporate not only brain activation but also disease load and task performance. Therefore testing whether the functional up-regulation I observe in preHD represents compensation would require a model incorporating these additional factors (Gregory et al., 2017b). This has been performed previously on the baseline preHD cohort of the Track-On HD study. Increased performance related activity, during a working memory task, was seen as atrophy increased in the right parietal cortex. Additionally increased functional coupling, in resting state fMRI, between the right dorsolateral prefrontal cortex and a left hemisphere network was predictive cognitive performance (Kloppel et al., 2015). These findings suggest functional compensation occurs in preHD. This model used in this study has been further developed for longitudinal data using a linear mixed model (see figure 8.1) (Gregory et al., 2017a) and work is currently underway using this approach to investigate functional compensation over time in preHD. This model can potentially be applied to data from this thesis in order to test if regions showing functional up-regulation in chapter 3 are the same regions that show functional compensation, therefore addressing whether these changes are compensatory or pathological.

Figure 8.1. Visualization of simulated longitudinal sample data (n = 200, three time points) with three key variables (activation, volume, performance). The spaghetti plots connect the three repeated measures for each individual with a line; each variable is depicted in a different panel (same participants in each), and all the variables are standardized to have the same mean for the first age. Reproduced from (Gregory et al., 2015a).

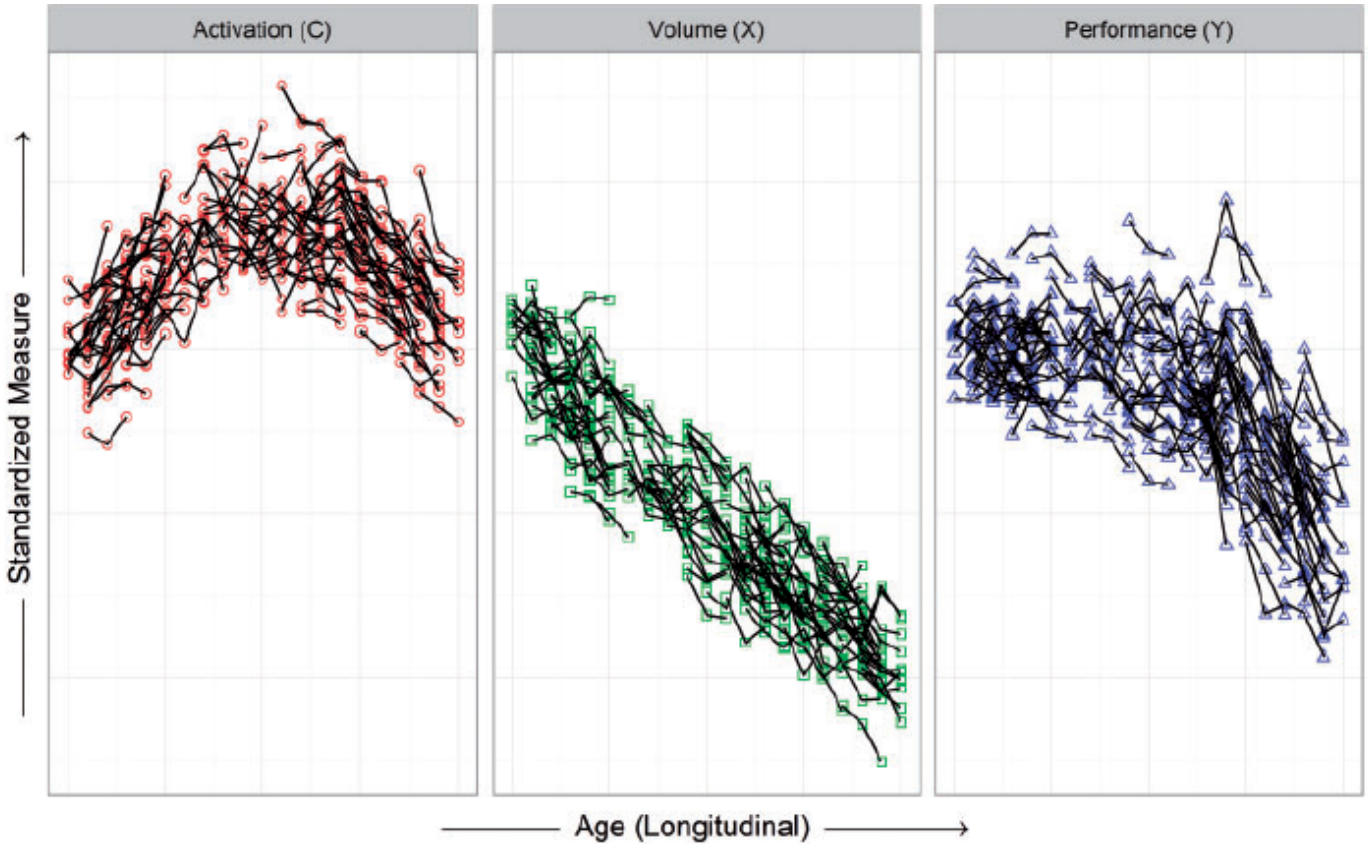

8.3. Psychiatric symptoms and brain networks in HD

In chapter 4 I investigated the relationship between structural and functional brain network connections and symptoms of depression and apathy in preHD. Positive correlations between depressive symptoms and apathy scores were seen with functional connections, predominantly between the default mode regions, while negative correlations in structural connections were seen between the cortex and basal ganglia (for depressive symptoms but not apathy). These findings suggest that the increases in functional connectivity demonstrated in chapter 3 represent early pathological change that manifests clinically as neuropsychiatric disturbance. This may be due to attempted compensation resulting in aberrant increases in functional connectivity. This was a cross-sectional study, therefore it is important to know how these brain networks abnormalities change over time. These brain network changes may allow the prediction of those at risk of psychiatric symptoms in the future.

While the work presented here focused on depression, apathy and anxiety symptoms the use of data decomposition methods, such as principle components analysis (PCA), would allow the incorporation of all psychiatric data from Track-On HD into one score based on principal component weights. This approach has been used recently in HD to generate a progression score that was used as a quantitative phenotype in a genome wide association study (Moss et al., 2017). Functional connectivity profiles and PCA data could then be used to generate a predictive model, where functional connectivity could predict psychiatric phenotypes. Recently connectome based predictive modeling (Shen et al., 2017) (see figure 8.2) has been proposed for this purpose. In this approach individual connections are correlated with behavioural measures. Connections showing significant correlation ($p < 0.05$) are summed together and a linear model for brain connection – behavior relationship is fitted. This model can then be validated in a separate cohort. Work is currently ongoing in our group using this approach.

Figure 8.2. Schematic of connectome based predictive modeling (CPM). For each subject, inputs to CPM are a connectivity matrix and behavioral measures. Connectivity matrices can be from several different modalities, and behavioral measures should have a sufficient dynamic range or spread across subjects to support prediction in novel data. The input data need to be divided into a training set and a testing set (Steps 1 and 2). Next, across all subjects in the training set, each edge in the connectivity matrices is related to the behavioral measures using a form of linear regression, including Pearson's correlation, Spearman's correlation, or robust regression (Step 3). Next, after linear regression, the most important edges are selected for further analysis. Typically, important edges are selected using significance testing, although other strategies exist—e.g., selecting edges whose correlation value is above a predefined threshold (Step 4). Next, for each subject, the most important edges are then summarized into a single subject value. Usually, the edge strengths are simply summed (Step 5). Next, a predictive model is built that assumes a linear relationship between the single-subject summary value of connectivity data (independent variable) and the behavioral variable (the dependent variable) (Step 6). Next, summary values are calculated for each subject in the testing set. This value is then input into the predictive model. The resulting value is the predicted behavioral measure for the current test subject (Step 7). Reproduced from (Shen et al., 2017).

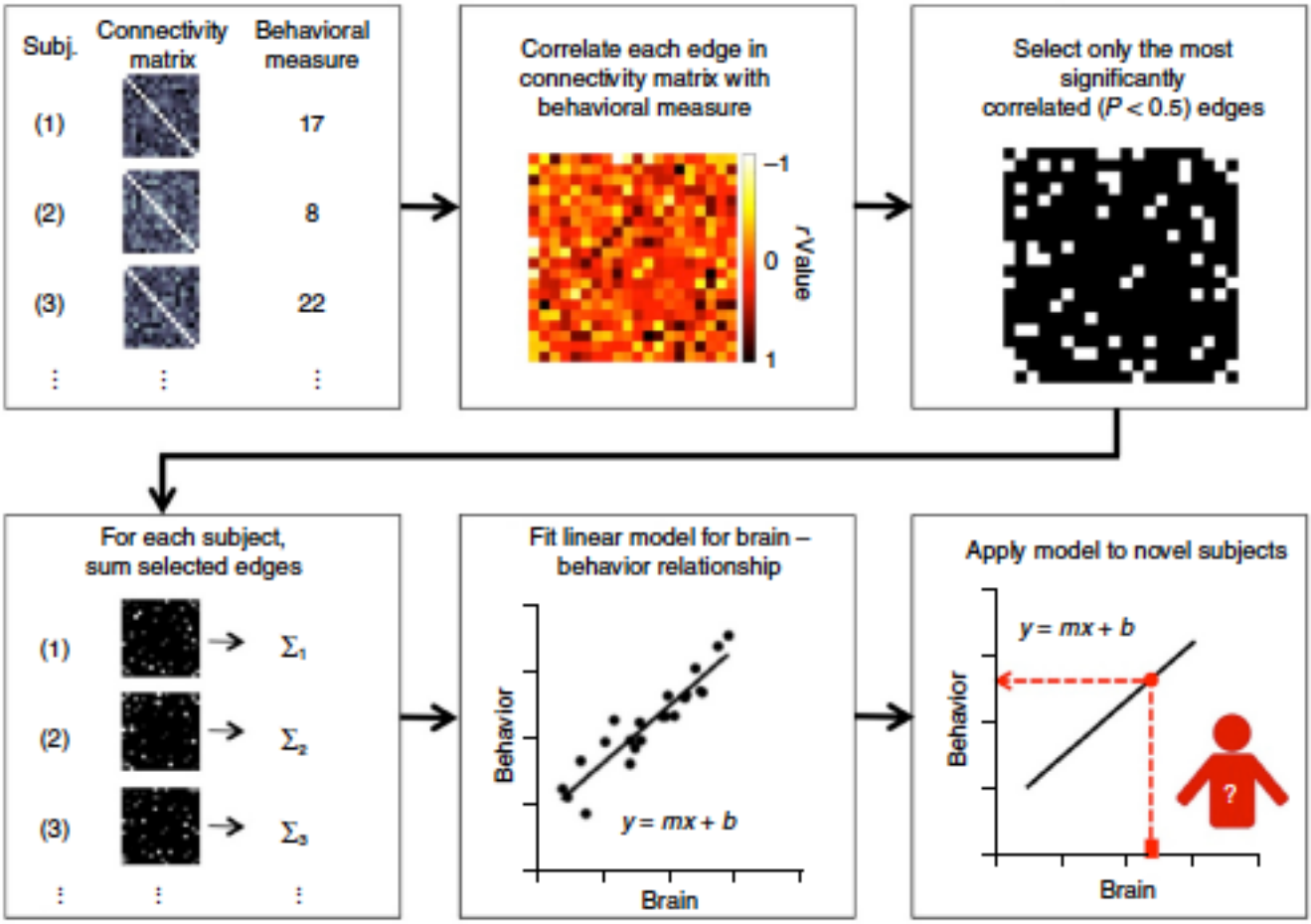

8.4. Selective vulnerability of white matter brain networks in HD

In the cross-sectional analysis in chapter 5 I demonstrated selective vulnerability of cortico-striatal white matter connections, particularly those between the caudate and the highly connected rich club brain regions in the cortex. At the global level I revealed isolated increase of network segregation in the preHD participants when compared to controls, extending to increase in segregation and loss of integration when comparing manifest against both preHD and controls. These global changes correlated with motor and cognitive deficits suggesting they have pathophysiological relevance. In the longitudinal analysis in chapter 6 I focused specifically on white matter connections with the aim of identifying which white matter connections were most vulnerable in preHD. This revealed a hierarchy of vulnerability in that cortico-striatal connections were most affected followed by inter-hemispheric and intra-hemispheric connections. Cortico-striatal connections were the only connection sub-type to show change over time. In order to account for this vulnerability I hypothesised that longer connections would have a higher metabolic demand and therefore be more vulnerable to the metabolic disturbance caused by mutant huntingtin. The topological length of connection sub-types was in keeping with this, with cortico-striatal connections being the longest followed by inter-hemispheric and intra-hemispheric connections. Furthermore I demonstrated a direct relationship between connection atrophy and topological length.

These findings establish the selective vulnerability of cortico-striatal white matter connections in HD. However it is unclear whether there is a gradient of cortico-striatal white matter connection vulnerability in keeping with the caudo-rostral, medio-lateral, dorso-ventral gradients of striatal atrophy demonstrated in post-mortem HD brains (Vonsattel, 1985). This is an important question, as identification of the earliest brain changes in HD will

enable us to target future therapies effectively in the earliest stages of disease prior to potentially irreversible structural damage.

The HD young adult study aims to address this (http://hdresearch.ucl.ac.uk/current-studies/hd-young-adult-study-hd-yas). In future work sub-segmentation of the striatum using the Parkes tripartite striatum atlas (Parkes et al., 2017) (see figure 8.3) combined with whole brain tractography will allow investigation of cortico-striatal white matter connection vulnerability gradients in preHD. The Parkes atlas segments the striatum into ventral, dorsal and caudal regions based on structural connectivity profiles based on 100 healthy participants (Parkes et al., 2017). Given the posterior vulnerability of white matter demonstrated in chapter 6 coupled with the dorso-ventral gradient of striatum atrophy in HD (Vonsattel, 1985) I hypothesise that dorsal striatum connectivity would be most affected in young adults carrying the HD gene compared to connectivity of other regions in the striatum. Furthermore cortico-striatal connectivity loss of the dorsal striatum may be linked to the earliest motor, cognitive and psychiatric symptoms that can be detected in young adult gene carriers.

Figure 8.3. Parcellation of the human striatum based on whole-brain structural connectivity. Subregions of the tripartite striatum show distinct cortical connectivity profiles that are consistent with their functional roles. (a) Using k-means clustering, with k =3, to parcellate the striatum based on connectivity with 86 cortical and subcortical targets covering the whole brain, yields a 'caudal' cluster (blue), a 'dorsal' cluster (green) and a 'ventral' cluster (red). (b–d) At higher levels of k, striatal clusters subdivide along mediolateral and rostrocaudal gradients. (e–g) Connectivity data for all participants were z-scored and averaged across voxels within each cluster for each target in each hemisphere separately. Single sample t-tests were performed to determine significant cluster to target connectivity for each hemisphere. Significant absolute t-values (P <0.05 FDR-corrected) were averaged across the left and right hemispheres and plotted on the surface of the brain to visualize the specific patterns of connectivity characteristic of each striatal cluster. (e) The caudal striatum shows strong connectivity with sensorimotor areas of the cortex. (f) The dorsal striatum shows connectivity to frontal regions. (g) The ventral striatum shows strong connectivity to limbic areas. Reproduced from (Parkes et al., 2017).

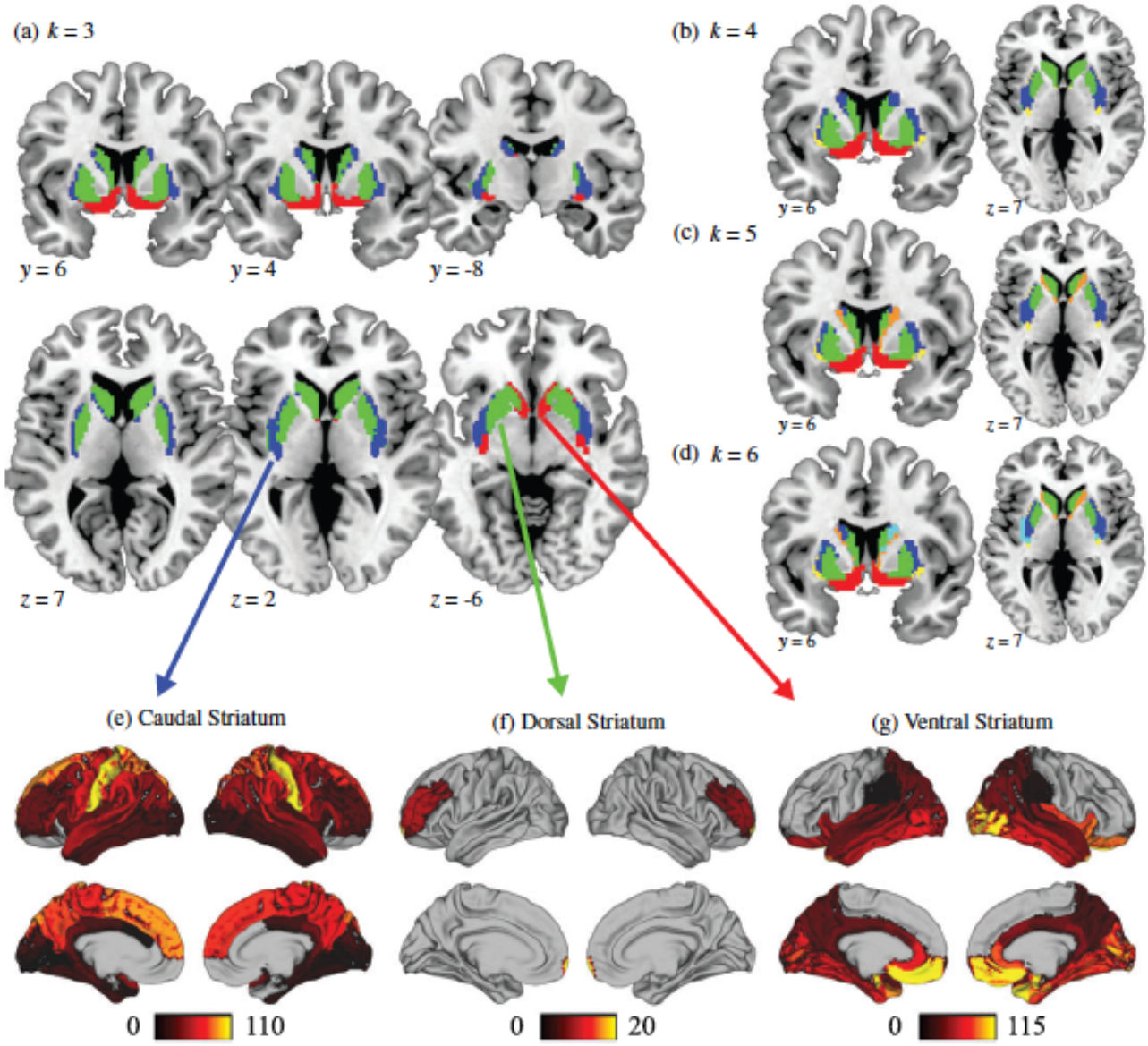

8.5. Linking systems level white matter loss to HD pathobiology

In chapter 7 I investigated the association between regional gene expression and regional white matter loss of different connection subtypes in preHD. I showed that the regional variance in white matter loss in preHD is differentially associated with a pattern of gene expression involved in synaptic, metabolic and chromatin related processes in the healthy human brain. Cortico-striatal and intra-hemispheric WM loss is associated with synaptic genes, whereas intra-hemispheric WM loss is associated with metabolic and chromatin-related genes. I reveal that genes showing abnormal transcription in HD humans and animal models and oligodendrocyte related genes are over expressed in the ranked gene lists associated with cortico-striatal and inter-hemispheric WM, whereas genes related to cell cycle metabolism are over expressed in the ranked gene list associated with intra-hemispheric WM.

The use of gene expression data from the healthy human brain to explain white matter loss in preHD is limited to the extent that transcription in preHD may be different than that seen in healthy brains. In future work the results presented here could be validated in HD animal models. To date, three HD animals show white matter pathology, the R6/2 (Xiang et al., 2011), YAC128 (Teo et al., 2016) (see figure 8.4) and HdhQ250 (Jin et al., 2015). Gene expression RNA-seq analysis of the corpus callosum has been performed in the HD Q175 mouse model. This revealed abnormal transcription of several genes (Langfelder et al., 2016). However RNA-seq analysis has not been performed in a model with documented white matter loss. Combining diffusion imaging with gene expression analyses in white matter around the striatum and in the corpus callosum in animal models would make it possible to directly link white matter changes seen in diffusion imaging with regional gene expression in white matter.

Figure 8.4. Longitudinal magnetic resonance DTI reveals abnormal white matter microstructure in YAC128HD mice. (A) Voxel-wise comparison of FA values between YAC128 and WT at each time point (each row) at different slice positions (columns). Yellow-red indicates WT > YAC128, blue-light blue indicates YAC128 > WT. ac, anterior commissure; cc, corpus callosum; cg, cingulum; cp, cerebral peduncle; ec, external capsule; ic, internal capsule. (B) Region of interest analysis of FA. Examples of ROIs drawn on the FA time-point template. Magenta, anterior corpus callosum; red, posterior corpus callosum; light blue, anterior commissure; dark blue, cingulum; green, external capsule. (C) Comparisons of mean FA in each ROI at the indicated time points between YAC128 and WT mice. n . 8 (4 males) for WT mice; 8 (4 males) for YAC128 mice; * P < 0.05; ** P < 0.01. Reproduced from (Teo et al., 2016)

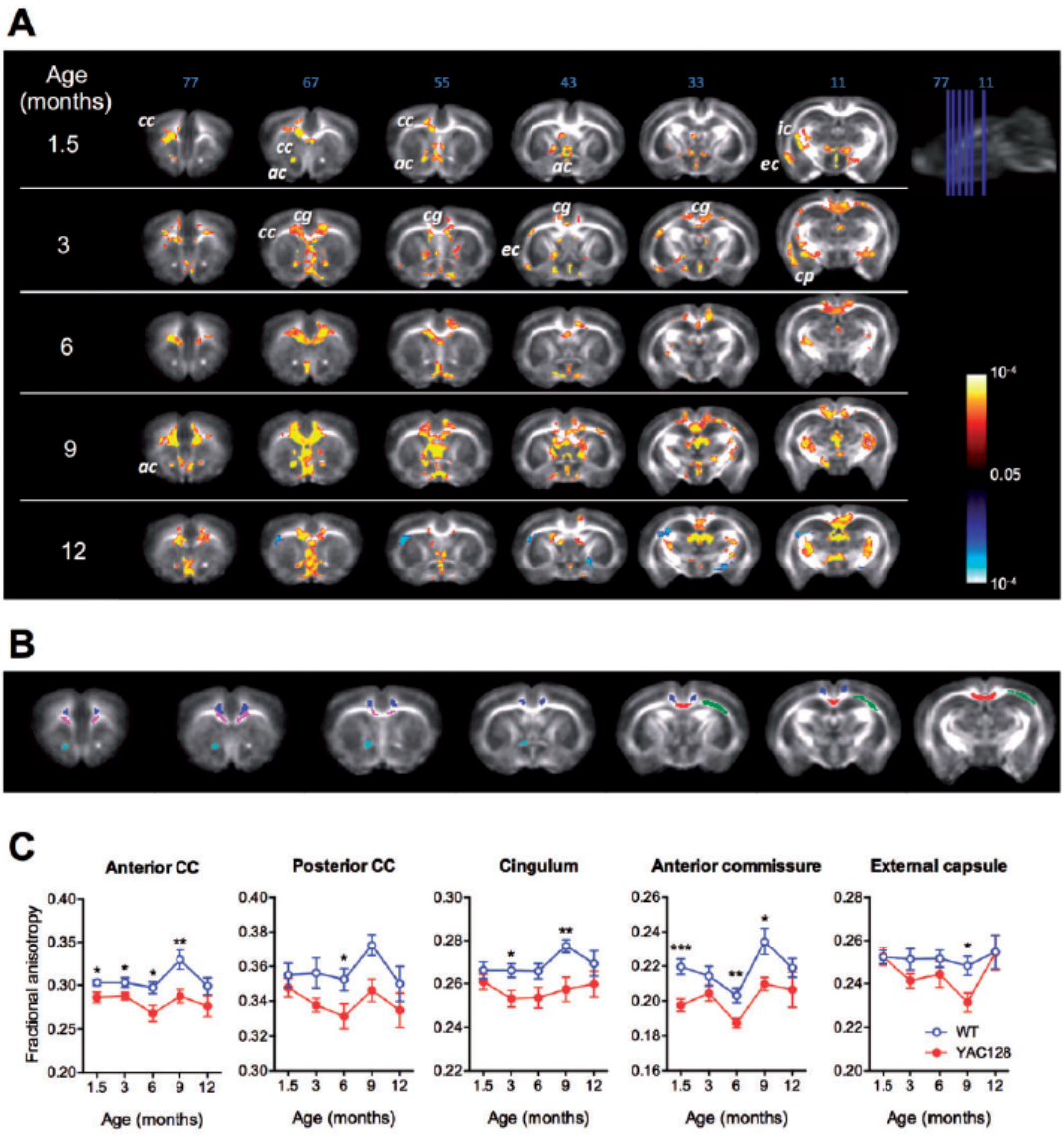

Mutant huntingtin affects the cell cycle in oligodendrocytes compromising their ability to regenerate (Jin et al., 2015). Indeed this is in keeping with the enrichment for cell cycle metabolism genes I demonstrated in intra-hemispheric white matter gene expression profile in chapter 7. Mutant huntingtin also reduces myelin gene expression through its effects on myelin regulatory factor (MYRF), a transcription regulator of myelin genes (Huang et al., 2015). However it still remains an open question as to whether loss of white matter in HD is due to neuronal death or myelin abnormalities. Given the large amount of white matter volume loss seen in HD (Tabrizi et al., 2011) a greater understanding of pathophysiology of white matter loss will help us identify drug targets that could modify or prevent white matter loss. The use of electron microscopy to characterise the histology of white matter around the striatum and in the corpus callosum of HD animal models would also allow one to assess if the changes seen in diffusion imaging are related loss of myelination, dysmyelination or the dying back of axons following the death of neurons. This approach has been used in a Tau mouse model to demonstrate the dying back of axons (Lin et al., 2005).

8.6. Conclusions

The work in this thesis is the first to show how structural connectivity can predict variation in functional connectivity in preHD relative to controls, in doing so I provide a framework for identifying which brain regions show functional up-regulation and down-regulation. This framework can be applied to other preclinical neurodegenerative conditions such as mild cognitive impairment or asymptomatic gene carriers of the genetic forms of front-temporal dementia and Alzheimer's disease. By identifying which brain regions show up-regulation and down-regulation this may indicate which brain regions have the capacity to modulate their functional connectivity. This may allow the identification of potential targets for therapies aimed at enhancing compensatory mechanisms, such as repetitive trans-cranial stimulation (rTMS) (Fregni and Pascual-Leone, 2007) and neurofeedback (Subramanian et al., 2011).

In relating increases in functional connectivity to symptoms of depression and apathy I raise the question of whether increases in functional connectivity are pathological or compensatory. This represents a step change in the HD literature. As until now increases in functional connectivity in preHD cohorts were generally regarded as beneficial and often interpreted as a compensatory mechanism (Gray et al., 2013; Harrington et al., 2015; Sarappa et al., 2016). This has implications for the interpretation functional connectivity increases in other neurodegenerative diseases and will hopefully prompt a move toward modeling of compensation in the context if connectivity, disease load and performance, as in the case of recent approaches in preHD (Gregory et al., 2017a; Kloppel et al., 2015).

I show how the break down of the white matter brain network results in the manifestation of HD and relates to both cognitive and motor symptoms. HD has been classically thought of as a disease of the striatum. More recently there has been a focus on cortico-striatal connectivity loss. However the work presented here is the first to link global changes in the white matter brain network to the manifestation of symptoms. In demonstrating that cortico-striatal white matter connectivity loss is greatest in highly connected rich club regions and is associated with the topographical length of white matter connections I not only identify which white matter connections are most vulnerable but also provide mechanistic explanations for this at the systems level. This represents a move beyond simply identifying group differences in connectivity measures between HD gene carriers and healthy controls to identifying mechanistic drivers of this selective white matter vulnerability.

By investigating the relationship between regional gene expression in the healthy brain and regional white matter loss this is the first work to link systems level white matter loss in preHD to mutant huntingtin induced cellular pathology. The association of white matter loss with synaptic, metabolic and chromatin related genes is in keeping with post mortem human HD (Hodges et al., 2006) and animal models (Seredenina and Luthi-Carter, 2012), however the study here represents the first time such an analysis has been performed invivo with preHD participants. While partial least squares approach has been used in developmental studies (Whitaker et al., 2016) and healthy participants (Vertes et al., 2016), I am the first to adopt this for investigating a brain disease. This can be applied to other neurological and psychiatric diseases in order to link systems level abnormalities to cellular pathology.

8.7. Future work

The over arching aim of this thesis was to link structural and functional brain network abnormalities with regional changes at the cellular level. In doing so my findings have generated a number of important new questions and future directions. I suumarise these by posing the following questions:

1. Is up-regulation of functional connectivity in preHD pathological or compensatory?
2. Can functional connectivity predict the development of future psychiatric symptoms?
3. Is dorsal striatal white matter connectivity loss one of the earliest brain changes in HD gene carriers?
4. Is white matter loss in HD due to dying back of axons, dysmyelination or demyelination?

The answers to these questions have important implications for current and future therapies aimed at modifying disease course and potentially curing HD.

References

1993. A novel gene containing a trinucleotide repeat that is expanded and unstable on Huntington's disease chromosomes. The Huntington's Disease Collaborative Research Group. Cell 72, 971-983.
Abdelnour, F., Voss, H.U., Raj, A., 2014. Network diffusion accurately models the relationship between structural and functional brain connectivity networks. Neuroimage 90, 335-347.
Achard, S., Bullmore, E., 2007. Efficiency and cost of economical brain functional networks. PLoS Comput Biol 3, e17.
Andellini, M., Cannata, V., Gazzellini, S., Bernardi, B., Napolitano, A., 2015. Test-Retest reliability of graph metrics of resting state MRI functional brain networks: a review. J Neurosci Methods.
Andersson, J.L., Sotiropoulos, S.N., 2016. An integrated approach to correction for off-resonance effects and subject movement in diffusion MR imaging. Neuroimage 125, 1063-1078.
Andre, R., Carty, L., Tabrizi, S.J., 2016. Disruption of immune cell function by mutant huntingtin in Huntington's disease pathogenesis. Curr Opin Pharmacol 26, 33-38.
Andre, V.M., Cepeda, C., Levine, M.S., 2010. Dopamine and glutamate in Huntington's disease: A balancing act. CNS Neurosci Ther 16, 163-178.
Andre, V.M., Fisher, Y.E., Levine, M.S., 2011. Altered Balance of Activity in the Striatal Direct and Indirect Pathways in Mouse Models of Huntington's Disease. Front Syst Neurosci 5, 46.
Angot, E., Steiner, J.A., Hansen, C., Li, J.Y., Brundin, P., 2010. Are synucleinopathies prion-like disorders? Lancet Neurol 9, 1128-1138.
Arslan, S., Ktena, S.I., Makropoulos, A., Robinson, E.C., Rueckert, D., Parisot, S., 2017. Human brain mapping: A systematic comparison of parcellation methods for the human cerebral cortex. Neuroimage.
Aurich, N.K., Alves Filho, J.O., Marques da Silva, A.M., Franco, A.R., 2015. Evaluating the reliability of different preprocessing steps to estimate graph theoretical measures in resting state fMRI data. Front Neurosci 9, 48.
Baggio, H.C., Segura, B., Junque, C., de Reus, M.A., Sala-Llonch, R., Van den Heuvel, M.P., 2015. Rich Club Organization and Cognitive Performance in Healthy Older Participants. J Cogn Neurosci, 1-10.
Bai, F., Shu, N., Yuan, Y., Shi, Y., Yu, H., Wu, D., Wang, J., Xia, M., He, Y., Zhang, Z., 2012. Topologically convergent and divergent structural connectivity patterns between patients with remitted geriatric depression and amnestic mild cognitive impairment. J Neurosci 32, 4307-4318.

Barrat, A., Barthelemy, M., Pastor-Satorras, R., Vespignani, A., 2004. The architecture of complex weighted networks. Proc Natl Acad Sci U S A 101, 3747-3752.

Basser, P.J., Mattiello, J., LeBihan, D., 1994. MR diffusion tensor spectroscopy and imaging. Biophys J 66, 259-267.

Bassett, D.S., Bullmore, E., Verchinski, B.A., Mattay, V.S., Weinberger, D.R., Meyer-Lindenberg, A., 2008. Hierarchical organization of human cortical networks in health and schizophrenia. J Neurosci 28, 9239-9248.

Bassett, D.S., Bullmore, E.T., 2016. Small-World Brain Networks Revisited. Neuroscientist.

Bates, G.P., Dorsey, R., Gusella, J.F., Hayden, M.R., Kay, C., Leavitt, B.R., Nance, M., Ross, C.A., Scahill, R.I., Wetzel, R., Wild, E.J., Tabrizi, S.J., 2015a. Huntington disease. Nat Rev Dis Primers 1, 15005.

Bates, G.P., Dorsey, R., Gusella, J.F., Hayden, M.R., Kay, C., Leavitt, B.R., Nance, M., Ross, C.A., Scahill, R.I., Wetzel, R., Wild, E.J., Tabrizi, S.J., 2015b. Huntington disease. Nature Reviews Disease Primers 1, 1-21.

Beglinger, L.J., O'Rourke, J.J., Wang, C., Langbehn, D.R., Duff, K., Paulsen, J.S., Huntington Study Group, I., 2010. Earliest functional declines in Huntington disease. Psychiatry Res 178, 414-418.

Behrens, T.E., Berg, H.J., Jbabdi, S., Rushworth, M.F., Woolrich, M.W., 2007. Probabilistic diffusion tractography with multiple fibre orientations: What can we gain? Neuroimage 34, 144-155.

Benjamini, Y.H., Y. , 1995. Controlling the false discovery rate: a practical and powerful approach to multiple testing. Journal of the Royal Statistical Society, Series B 57, 289-300.

Benoit, M., Koulibaly, P.M., Migneco, O., Darcourt, J., Pringuey, D.J., Robert, P.H., 2002. Brain perfusion in Alzheimer's disease with and without apathy: a SPECT study with statistical parametric mapping analysis. Psychiatry Res 114, 103-111.

Betzel, R.F., Byrge, L., He, Y., Goni, J., Zuo, X.N., Sporns, O., 2014. Changes in structural and functional connectivity among resting-state networks across the human lifespan. Neuroimage 102 Pt 2, 345-357.

Biswal, B., Yetkin, F.Z., Haughton, V.M., Hyde, J.S., 1995. Functional connectivity in the motor cortex of resting human brain using echo-planar MRI. Magn Reson Med 34, 537-541.

Blondel, V.D., Guillaume, J.L., Lambiotte, R., E., L., 2008. Fast unfolding of communities in large networks. J. Stat. Mech. Theor. 10, P10008.

Bohanna, I., Georgiou-Karistianis, N., Egan, G.F., 2011a. Connectivity-based segmentation of the striatum in Huntington's disease: vulnerability of motor pathways. Neurobiol Dis 42, 475-481.

Bohanna, I., Georgiou-Karistianis, N., Hannan, A.J., Egan, G.F., 2008. Magnetic resonance imaging as an approach towards identifying neuropathological biomarkers for Huntington's disease. Brain Res Rev 58, 209-225.
Bohanna, I., Georgiou-Karistianis, N., Sritharan, A., Asadi, H., Johnston, L., Churchyard, A., Egan, G., 2011b. Diffusion tensor imaging in Huntington's disease reveals distinct patterns of white matter degeneration associated with motor and cognitive deficits. Brain Imaging Behav 5, 171-180.
Brett, M., Johnsrude, I.S., Owen, A.M., 2002. The problem of functional localization in the human brain. Nat Rev Neurosci 3, 243-249.
Brodmann, K., 1909. Vergleichende lokalisationslehre der grosshirnrinde in ihren

prinzipien dargestellt auf grund des zellenbaues. Johann Ambrosius Barth, Leipzig.
Browne, S.E., Bowling, A.C., MacGarvey, U., Baik, M.J., Berger, S.C., Muqit, M.M., Bird, E.D., Beal, M.F., 1997. Oxidative damage and metabolic dysfunction in Huntington's disease: selective vulnerability of the basal ganglia. Ann Neurol 41, 646-653.
Buckner, R.L., Andrews-Hanna, J.R., Schacter, D.L., 2008. The brain's default network: anatomy, function, and relevance to disease. Ann N Y Acad Sci 1124, 1-38.
Buckner, R.L., Krienen, F.M., Yeo, B.T., 2013. Opportunities and limitations of intrinsic functional connectivity MRI. Nat Neurosci 16, 832-837.
Bullmore, E., Sporns, O., 2009. Complex brain networks: graph theoretical analysis of structural and functional systems. Nat Rev Neurosci 10, 186-198.
Cahoy, J.D., Emery, B., Kaushal, A., Foo, L.C., Zamanian, J.L., Christopherson, K.S., Xing, Y., Lubischer, J.L., Krieg, P.A., Krupenko, S.A., Thompson, W.J., Barres, B.A., 2008. A transcriptome database for astrocytes, neurons, and oligodendrocytes: a new resource for understanding brain development and function. J Neurosci 28, 264-278.
Cammoun, L., Gigandet, X., Meskaldji, D., Thiran, J.P., Sporns, O., Do, K.Q., Maeder, P., Meuli, R., Hagmann, P., 2012. Mapping the human connectome at multiple scales with diffusion spectrum MRI. J Neurosci Methods 203, 386-397.
Charvin, D., Roze, E., Perrin, V., Deyts, C., Betuing, S., Pages, C., Regulier, E., Luthi-Carter, R., Brouillet, E., Deglon, N., Caboche, J., 2008. Haloperidol protects striatal neurons from dysfunction induced by mutated huntingtin in vivo. Neurobiol Dis 29, 22-29.

Charvin, D., Vanhoutte, P., Pages, C., Borrelli, E., Caboche, J., 2005. Unraveling a role for dopamine in Huntington's disease: the dual role of reactive oxygen species and D2 receptor stimulation. Proc Natl Acad Sci U S A 102, 12218-12223.
Chatterjee, A., Anderson, K.E., Moskowitz, C.B., Hauser, W.A., Marder, K.S., 2005. A comparison of self-report and caregiver assessment of depression, apathy, and irritability in Huntington's disease. J Neuropsychiatry Clin Neurosci 17, 378-383.
Clark, V.P., Lai, S., Deckel, A.W., 2002. Altered functional MRI responses in Huntington's disease. Neuroreport 13, 703-706.
Cole, J.H., Farmer, R.E., Rees, E.M., Johnson, H.J., Frost, C., Scahill, R.I., Hobbs, N.Z., 2014. Test-Retest Reliability of Diffusion Tensor Imaging in Huntington's Disease. PLoS Curr 6.
Costa, V., Scorrano, L., 2012. Shaping the role of mitochondria in the pathogenesis of Huntington's disease. EMBO J 31, 1853-1864.
Craufurd, D., Thompson, J.C., Snowden, J.S., 2001. Behavioral changes in Huntington Disease. Neuropsychiatry Neuropsychol Behav Neurol 14, 219-226.
Crawford, H.E., Hobbs, N.Z., Keogh, R., Langbehn, D.R., Frost, C., Johnson, H., Landwehrmeyer, B., Reilmann, R., Craufurd, D., Stout, J.C., Durr, A., Leavitt, B.R., Roos, R.A., Tabrizi, S.J., Scahill, R.I., Investigators, T.-H., 2013. Corpus callosal atrophy in premanifest and early Huntington's disease. J Huntingtons Dis 2, 517-526.
Crossley, N.A., Mechelli, A., Scott, J., Carletti, F., Fox, P.T., McGuire, P., Bullmore, E.T., 2014. The hubs of the human connectome are generally implicated in the anatomy of brain disorders. Brain 137, 2382-2395.
Currie, S., Hoggard, N., Craven, I.J., Hadjivassiliou, M., Wilkinson, I.D., 2013. Understanding MRI: basic MR physics for physicians. Postgrad Med J 89, 209-223.
Daianu, M., Jahanshad, N., Nir, T.M., Jack, C.R., Jr., Weiner, M.W., Bernstein, M.A., Thompson, P.M., Alzheimer's Disease Neuroimaging, I., 2015. Rich club analysis in the Alzheimer's disease connectome reveals a relatively undisturbed structural core network. Hum Brain Mapp 36, 3087-3103.
Dale, M., van Duijn, E., 2015. Anxiety in Huntington's Disease. J Neuropsychiatry Clin Neurosci 27, 262-271.
Damoiseaux, J.S., Beckmann, C.F., Arigita, E.J., Barkhof, F., Scheltens, P., Stam, C.J., Smith, S.M., Rombouts, S.A., 2008. Reduced resting-state brain activity in the "default network" in normal aging. Cereb Cortex 18, 1856-1864.

Davis, S.W., Dennis, N.A., Daselaar, S.M., Fleck, M.S., Cabeza, R., 2008. Que PASA? The posterior-anterior shift in aging. Cereb Cortex 18, 1201-1209.
Della Nave, R., Ginestroni, A., Tessa, C., Giannelli, M., Piacentini, S., Filippi, M., Mascalchi, M., 2010. Regional distribution and clinical correlates of white matter structural damage in Huntington disease: a tract-based spatial statistics study. AJNR Am J Neuroradiol 31, 1675-1681.
Delmaire, C., Dumas, E.M., Sharman, M.A., van den Bogaard, S.J., Valabregue, R., Jauffret, C., Justo, D., Reilmann, R., Stout, J.C., Craufurd, D., Tabrizi, S.J., Roos, R.A., Durr, A., Lehericy, S., 2012. The structural correlates of functional deficits in early huntington's disease. Hum Brain Mapp.
Descoteaux, M., Deriche, R., Knosche, T.R., Anwander, A., 2009. Deterministic and probabilistic tractography based on complex fibre orientation distributions. IEEE Trans Med Imaging 28, 269-286.
Desikan, R.S., Segonne, F., Fischl, B., Quinn, B.T., Dickerson, B.C., Blacker, D., Buckner, R.L., Dale, A.M., Maguire, R.P., Hyman, B.T., Albert, M.S., Killiany, R.J., 2006. An automated labeling system for subdividing the human cerebral cortex on MRI scans into gyral based regions of interest. Neuroimage 31, 968-980.
Deyts, C., Galan-Rodriguez, B., Martin, E., Bouveyron, N., Roze, E., Charvin, D., Caboche, J., Betuing, S., 2009. Dopamine D2 receptor stimulation potentiates PolyQ-Huntingtin-induced mouse striatal neuron dysfunctions via Rho/ROCK-II activation. PLoS One 4, e8287.
Di Paola, M., Luders, E., Cherubini, A., Sanchez-Castaneda, C., Thompson, P.M., Toga, A.W., Caltagirone, C., Orobello, S., Elifani, F., Squitieri, F., Sabatini, U., 2012. Multimodal MRI analysis of the corpus callosum reveals white matter differences in presymptomatic and early Huntington's disease. Cereb Cortex 22, 2858-2866.
Dierks, T., Linden, D.E., Hertel, A., Gunther, T., Lanfermann, H., Niesen, A., Frolich, L., Zanella, F.E., Hor, G., Goebel, R., Maurer, K., 1999. Multimodal imaging of residual function and compensatory resource allocation in cortical atrophy: a case study of parietal lobe function in a patient with Huntington's disease. Psychiatry Res 90, 67-75.
Dijkstra, E.W., 1959. A note on two problems in connexion with graphs. Numerische Mathematik 1, 269-271.
Dorsey, E.R., Beck, C.A., Darwin, K., Nichols, P., Brocht, A.F., Biglan, K.M., Shoulson, I., Huntington Study Group, C.I., 2013. Natural history of Huntington disease. JAMA Neurol 70, 1520-1530.

Douaud, G., Filippini, N., Knight, S., Talbot, K., Turner, M.R., 2011. Integration of structural and functional magnetic resonance imaging in amyotrophic lateral sclerosis. Brain 134, 3470-3479.
Draganski, B., Kherif, F., Kloppel, S., Cook, P.A., Alexander, D.C., Parker, G.J., Deichmann, R., Ashburner, J., Frackowiak, R.S., 2008. Evidence for segregated and integrative connectivity patterns in the human Basal Ganglia. J Neurosci 28, 7143-7152.
Drakesmith, M., Caeyenberghs, K., Dutt, A., Lewis, G., David, A.S., Jones, D.K., 2015. Overcoming the effects of false positives and threshold bias in graph theoretical analyses of neuroimaging data. Neuroimage 118, 313-333.
Dumas, E.M., van den Bogaard, S.J., Hart, E.P., Soeter, R.P., van Buchem, M.A., van der Grond, J., Rombouts, S.A., Roos, R.A., group, T.-H.i., 2013. Reduced functional brain connectivity prior to and after disease onset in Huntington's disease. Neuroimage Clin 2, 377-384.
Dumas, E.M., van den Bogaard, S.J., Ruber, M.E., Reilman, R.R., Stout, J.C., Craufurd, D., Hicks, S.L., Kennard, C., Tabrizi, S.J., van Buchem, M.A., van der Grond, J., Roos, R.A., 2012. Early changes in white matter pathways of the sensorimotor cortex in premanifest Huntington's disease. Hum Brain Mapp 33, 203-212.
Durrenberger, P.F., Fernando, F.S., Kashefi, S.N., Bonnert, T.P., Seilhean, D., Nait-Oumesmar, B., Schmitt, A., Gebicke-Haerter, P.J., Falkai, P., Grunblatt, E., Palkovits, M., Arzberger, T., Kretzschmar, H., Dexter, D.T., Reynolds, R., 2015. Common mechanisms in neurodegeneration and neuroinflammation: a BrainNet Europe gene expression microarray study. J Neural Transm (Vienna) 122, 1055-1068.
Eden, E., Navon, R., Steinfeld, I., Lipson, D., Yakhini, Z., 2009. GOrilla: a tool for discovery and visualization of enriched GO terms in ranked gene lists. BMC Bioinformatics 10, 48.
Ekman, P., Friesen, V.W., 1976. Pictures of Facial Affect. Consulting Psychologists Press, Palo Alto.
Enzi, B., Edel, M.A., Lissek, S., Peters, S., Hoffmann, R., Nicolas, V., Tegenthoff, M., Juckel, G., Saft, C., 2012. Altered ventral striatal activation during reward and punishment processing in premanifest Huntington's disease: a functional magnetic resonance study. Exp Neurol 235, 256-264.
Epping, E.A., Kim, J.I., Craufurd, D., Brashers-Krug, T.M., Anderson, K.E., McCusker, E., Luther, J., Long, J.D., Paulsen, J.S., Investigators, P.-H., Coordinators of the Huntington Study, G., 2015. Longitudinal Psychiatric Symptoms in Prodromal Huntington's Disease: A Decade of Data. Am J Psychiatry, appiajp201514121551.

Epping, E.A., Mills, J.A., Beglinger, L.J., Fiedorowicz, J.G., Craufurd, D., Smith, M.M., Groves, M., Bijanki, K.R., Downing, N., Williams, J.K., Long, J.D., Paulsen, J.S., Investigators, P.-H., Coordinators of the Huntington Study, G., 2013. Characterization of depression in prodromal Huntington disease in the neurobiological predictors of HD (PREDICT-HD) study. J Psychiatr Res 47, 1423-1431.
Erhardt, E.B., Rachakonda, S., Bedrick, E.J., Allen, E.A., Adali, T., Calhoun, V.D., 2011. Comparison of multi-subject ICA methods for analysis of fMRI data. Hum Brain Mapp 32, 2075-2095.
Fagerholm, E.D., Hellyer, P.J., Scott, G., Leech, R., Sharp, D.J., 2015. Disconnection of network hubs and cognitive impairment after traumatic brain injury. Brain.
Fan, L., Li, H., Zhuo, J., Zhang, Y., Wang, J., Chen, L., Yang, Z., Chu, C., Xie, S., Laird, A.R., Fox, P.T., Eickhoff, S.B., Yu, C., Jiang, T., 2016. The Human Brainnetome Atlas: A New Brain Atlas Based on Connectional Architecture. Cereb Cortex 26, 3508-3526.
Faria, A.V., Ratnanather, J.T., Tward, D.J., Lee, D.S., van den Noort, F., Wu, D., Brown, T., Johnson, H., Paulsen, J.S., Ross, C.A., Younes, L., Miller, M.I., Investigators, P.-H., Coordinators of the Huntington Study, G., 2016. Linking white matter and deep gray matter alterations in premanifest Huntington disease. Neuroimage Clin 11, 450-460.
Fischl, B., Salat, D.H., Busa, E., Albert, M., Dieterich, M., Haselgrove, C., van der Kouwe, A., Killiany, R., Kennedy, D., Klaveness, S., Montillo, A., Makris, N., Rosen, B., Dale, A.M., 2002. Whole brain segmentation: automated labeling of neuroanatomical structures in the human brain. Neuron 33, 341-355.
Fischl, B., Sereno, M.I., Dale, A.M., 1999. Cortical surface-based analysis. II: Inflation, flattening, and a surface-based coordinate system. Neuroimage 9, 195-207.
Fischl, B., van der Kouwe, A., Destrieux, C., Halgren, E., Segonne, F., Salat, D.H., Busa, E., Seidman, L.J., Goldstein, J., Kennedy, D., Caviness, V., Makris, N., Rosen, B., Dale, A.M., 2004. Automatically parcellating the human cerebral cortex. Cereb Cortex 14, 11-22.
Fornito, A., Bullmore, E.T., 2015. Connectomics: a new paradigm for understanding brain disease. Eur Neuropsychopharmacol 25, 733-748.
Fornito, A., Zalesky, A., Breakspear, M., 2015. The connectomics of brain disorders. Nat Rev Neurosci 16, 159-172.
Fox, M.D., Snyder, A.Z., Vincent, J.L., Corbetta, M., Van Essen, D.C., Raichle, M.E., 2005. The human brain is intrinsically organized into dynamic, anticorrelated functional networks. Proc Natl Acad Sci U S A 102, 9673-9678.

Fregni, F., Pascual-Leone, A., 2007. Technology insight: noninvasive brain stimulation in neurology-perspectives on the therapeutic potential of rTMS and tDCS. Nat Clin Pract Neurol 3, 383-393.
Fulcher, B.D., Fornito, A., 2016. A transcriptional signature of hub connectivity in the mouse connectome. Proc Natl Acad Sci U S A 113, 1435-1440.
Gambazzi, L., Gokce, O., Seredenina, T., Katsyuba, E., Runne, H., Markram, H., Giugliano, M., Luthi-Carter, R., 2010. Diminished activity-dependent brain-derived neurotrophic factor expression underlies cortical neuron microcircuit hypoconnectivity resulting from exposure to mutant huntingtin fragments. J Pharmacol Exp Ther 335, 13-22.
Gargouri, F., Messe, A., Perlbarg, V., Valabregue, R., McColgan, P., Yahia-Cherif, L., Fernandez-Vidal, S., Ben Hamida, A., Benali, H., Tabrizi, S., Durr, A., Lehericy, S., 2016. Longitudinal changes in functional connectivity of cortico-basal ganglia networks in manifests and premanifest huntington's disease. Hum Brain Mapp 37, 4112-4128.
Garrison, K.A., Scheinost, D., Finn, E.S., Shen, X., Constable, R.T., 2015. The (in)stability of functional brain network measures across thresholds. Neuroimage.
Georgiou-Karistianis, N., Gray, M.A., Dominguez, D.J., Dymowski, A.R., Bohanna, I., Johnston, L.A., Churchyard, A., Chua, P., Stout, J.C., Egan, G.F., 2013. Automated differentiation of pre-diagnosis Huntington's disease from healthy control individuals based on quadratic discriminant analysis of the basal ganglia: the IMAGE-HD study. Neurobiol Dis 51, 82-92.
Georgiou-Karistianis, N., Sritharan, A., Farrow, M., Cunnington, R., Stout, J., Bradshaw, J., Churchyard, A., Brawn, T.L., Chua, P., Chiu, E., Thiruvady, D., Egan, G., 2007. Increased cortical recruitment in Huntington's disease using a Simon task. Neuropsychologia 45, 1791-1800.
Gispert, J.D., Reig, S., Pascau, J., Vaquero, J.J., Garcia-Barreno, P., Desco, M., 2004. Method for bias field correction of brain T1-weighted magnetic resonance images minimizing segmentation error. Hum Brain Mapp 22, 133-144.
Glasser, M.F., Coalson, T.S., Robinson, E.C., Hacker, C.D., Harwell, J., Yacoub, E., Ugurbil, K., Andersson, J., Beckmann, C.F., Jenkinson, M., Smith, S.M., Van Essen, D.C., 2016. A multi-modal parcellation of human cerebral cortex. Nature.
Godinho, B.M., Malhotra, M., O'Driscoll, C.M., Cryan, J.F., 2014. Delivering a disease-modifying treatment for Huntington's disease. Drug Discov Today.

Gong, Q., He, Y., 2015. Depression, neuroimaging and connectomics: a selective overview. Biol Psychiatry 77, 223-235.
Goni, J., van den Heuvel, M.P., Avena-Koenigsberger, A., Velez de Mendizabal, N., Betzel, R.F., Griffa, A., Hagmann, P., Corominas-Murtra, B., Thiran, J.P., Sporns, O., 2014. Resting-brain functional connectivity predicted by analytic measures of network communication. Proc Natl Acad Sci U S A 111, 833-838.
Graham, M.S., Drobnjak, I., Zhang, H., 2016. Realistic simulation of artefacts in diffusion MRI for validating post-processing correction techniques. Neuroimage 125, 1079-1094.
Graveland, G.A., Williams, R.S., DiFiglia, M., 1985. Evidence for degenerative and regenerative changes in neostriatal spiny neurons in Huntington's disease. Science 227, 770-773.
Gray, M.A., Egan, G.F., Ando, A., Churchyard, A., Chua, P., Stout, J.C., Georgiou-Karistianis, N., 2013. Prefrontal activity in Huntington's disease reflects cognitive and neuropsychiatric disturbances: the IMAGE-HD study. Exp Neurol 239, 218-228.
Gregory, S., Cole, J.H., Farmer, R.E., Rees, E.M., Roos, R.A., Sprengelmeyer, R., Durr, A., Landwehrmeyer, B., Zhang, H., Scahill, R.I., Tabrizi, S.J., Frost, C., Hobbs, N.Z., 2015a. Longitudinal Diffusion Tensor Imaging Shows Progressive Changes in White Matter in Huntington's Disease. J Huntingtons Dis 4, 333-346.
Gregory, S., Long, J.D., Kloppel, S., Razi, A., Scheller, E., Minkova, L., Papoutsi, M., Mills, J.A., Durr, A., Leavitt, B.R., Roos, R.A.C., Stout, J.C., Scahill, R.I., Langbehn, D.R., Tabrizi, S.J., Rees, G., 2017a. Operationalizing compensation over time in neurodegenerative disease. Brain 140, 1158-1165.
Gregory, S., Long, J.D., Tabrizi, S.J., Rees, G., 2017b. Measuring compensation in neurodegeneration using MRI. Curr Opin Neurol 30, 380-387.
Gregory, S., Scahill, R.I., Seunarine, K.K., Stopford, C., Zhang, H., Zhang, J., Orth, M., Durr, A., Roos, R.A., Langbehn, D.R., Long, J.D., Johnson, H., Rees, G., Tabrizi, S.J., Craufurd, D., 2015b. Neuropsychiatry and White Matter Microstructure in Huntington's Disease. J Huntingtons Dis.
Greicius, M.D., Flores, B.H., Menon, V., Glover, G.H., Solvason, H.B., Kenna, H., Reiss, A.L., Schatzberg, A.F., 2007. Resting-state functional connectivity in major depression: abnormally increased contributions from subgenual cingulate cortex and thalamus. Biol Psychiatry 62, 429-437.
Griffa, A., Baumann, P.S., Thiran, J.P., Hagmann, P., 2013. Structural connectomics in brain diseases. Neuroimage 80, 515-526.

Guo, J.L., Lee, V.M., 2014. Cell-to-cell transmission of pathogenic proteins in neurodegenerative diseases. Nat Med 20, 130-138.
Hagmann, P., Cammoun, L., Gigandet, X., Meuli, R., Honey, C.J., Wedeen, V.J., Sporns, O., 2008. Mapping the structural core of human cerebral cortex. PLoS Biol 6, e159.
Hagmann, P., Jonasson, L., Maeder, P., Thiran, J.P., Wedeen, V.J., Meuli, R., 2006. Understanding diffusion MR imaging techniques: from scalar diffusion-weighted imaging to diffusion tensor imaging and beyond. Radiographics 26 Suppl 1, S205-223.
Hagmann, P., Sporns, O., Madan, N., Cammoun, L., Pienaar, R., Wedeen, V.J., Meuli, R., Thiran, J.P., Grant, P.E., 2010. White matter maturation reshapes structural connectivity in the late developing human brain. Proc Natl Acad Sci U S A 107, 19067-19072.
Hahn, E., 1950. Spin echoes. Phys Rev 80, 580-594.
Harrington, D.L., Long, J.D., Durgerian, S., Mourany, L., Koenig, K., Bonner-Jackson, A., Paulsen, J.S., Group, P.-H.I.o.t.H.S., Rao, S.M., 2016. Cross-sectional and longitudinal multimodal structural imaging in prodromal Huntington's disease. Mov Disord.
Harrington, D.L., Rubinov, M., Durgerian, S., Mourany, L., Reece, C., Koenig, K., Bullmore, E., Long, J.D., Paulsen, J.S., Group, P.-H.i.o.t.H.S., Rao, S.M., 2015. Network topology and functional connectivity disturbances precede the onset of Huntington's disease. Brain.
Hawrylycz, M., Miller, J.A., Menon, V., Feng, D., Dolbeare, T., Guillozet-Bongaarts, A.L., Jegga, A.G., Aronow, B.J., Lee, C.K., Bernard, A., Glasser, M.F., Dierker, D.L., Menche, J., Szafer, A., Collman, F., Grange, P., Berman, K.A., Mihalas, S., Yao, Z., Stewart, L., Barabasi, A.L., Schulkin, J., Phillips, J., Ng, L., Dang, C., Haynor, D.R., Jones, A., Van Essen, D.C., Koch, C., Lein, E., 2015. Canonical genetic signatures of the adult human brain. Nat Neurosci 18, 1832-1844.
Hawrylycz, M.J., Lein, E.S., Guillozet-Bongaarts, A.L., Shen, E.H., Ng, L., Miller, J.A., van de Lagemaat, L.N., Smith, K.A., Ebbert, A., Riley, Z.L., Abajian, C., Beckmann, C.F., Bernard, A., Bertagnolli, D., Boe, A.F., Cartagena, P.M., Chakravarty, M.M., Chapin, M., Chong, J., Dalley, R.A., Daly, B.D., Dang, C., Datta, S., Dee, N., Dolbeare, T.A., Faber, V., Feng, D., Fowler, D.R., Goldy, J., Gregor, B.W., Haradon, Z., Haynor, D.R., Hohmann, J.G., Horvath, S., Howard, R.E., Jeromin, A., Jochim, J.M., Kinnunen, M., Lau, C., Lazarz, E.T., Lee, C., Lemon, T.A., Li, L., Li, Y., Morris, J.A., Overly, C.C., Parker, P.D., Parry, S.E., Reding, M., Royall, J.J., Schulkin, J., Sequeira, P.A., Slaughterbeck, C.R., Smith, S.C., Sodt, A.J., Sunkin, S.M., Swanson, B.E., Vawter, M.P., Williams, D., Wohnoutka, P., Zielke, H.R., Geschwind, D.H., Hof,

P.R., Smith, S.M., Koch, C., Grant, S.G., Jones, A.R., 2012. An anatomically comprehensive atlas of the adult human brain transcriptome. Nature 489, 391-399.
Heeger, D.J., Ress, D., 2002. What does fMRI tell us about neuronal activity? Nat Rev Neurosci 3, 142-151.
Heiland, S., 2008. From A as in Aliasing to Z as in Zipper: Artifacts in MRI. Clin Neuroradiol 18, 25-36.
Henley, S.M., Novak, M.J., Frost, C., King, J., Tabrizi, S.J., Warren, J.D., 2012. Emotion recognition in Huntington's disease: a systematic review. Neurosci Biobehav Rev 36, 237-253.
Hibar, D.P., Stein, J.L., Renteria, M.E., Arias-Vasquez, A., Desrivieres, S., Jahanshad, N., Toro, R., Wittfeld, K., Abramovic, L., Andersson, M., Aribisala, B.S., Armstrong, N.J., Bernard, M., Bohlken, M.M., Boks, M.P., Bralten, J., Brown, A.A., Chakravarty, M.M., Chen, Q., Ching, C.R., Cuellar-Partida, G., den Braber, A., Giddaluru, S., Goldman, A.L., Grimm, O., Guadalupe, T., Hass, J., Woldehawariat, G., Holmes, A.J., Hoogman, M., Janowitz, D., Jia, T., Kim, S., Klein, M., Kraemer, B., Lee, P.H., Olde Loohuis, L.M., Luciano, M., Macare, C., Mather, K.A., Mattheisen, M., Milaneschi, Y., Nho, K., Papmeyer, M., Ramasamy, A., Risacher, S.L., Roiz-Santianez, R., Rose, E.J., Salami, A., Samann, P.G., Schmaal, L., Schork, A.J., Shin, J., Strike, L.T., Teumer, A., van Donkelaar, M.M., van Eijk, K.R., Walters, R.K., Westlye, L.T., Whelan, C.D., Winkler, A.M., Zwiers, M.P., Alhusaini, S., Athanasiu, L., Ehrlich, S., Hakobjan, M.M., Hartberg, C.B., Haukvik, U.K., Heister, A.J., Hoehn, D., Kasperaviciute, D., Liewald, D.C., Lopez, L.M., Makkinje, R.R., Matarin, M., Naber, M.A., McKay, D.R., Needham, M., Nugent, A.C., Putz, B., Royle, N.A., Shen, L., Sprooten, E., Trabzuni, D., van der Marel, S.S., van Hulzen, K.J., Walton, E., Wolf, C., Almasy, L., Ames, D., Arepalli, S., Assareh, A.A., Bastin, M.E., Brodaty, H., Bulayeva, K.B., Carless, M.A., Cichon, S., Corvin, A., Curran, J.E., Czisch, M., de Zubicaray, G.I., Dillman, A., Duggirala, R., Dyer, T.D., Erk, S., Fedko, I.O., Ferrucci, L., Foroud, T.M., Fox, P.T., Fukunaga, M., Gibbs, J.R., Goring, H.H., Green, R.C., Guelfi, S., Hansell, N.K., Hartman, C.A., Hegenscheid, K., Heinz, A., Hernandez, D.G., Heslenfeld, D.J., Hoekstra, P.J., Holsboer, F., Homuth, G., Hottenga, J.J., Ikeda, M., Jack, C.R., Jr., Jenkinson, M., Johnson, R., Kanai, R., Keil, M., Kent, J.W., Jr., Kochunov, P., Kwok, J.B., Lawrie, S.M., Liu, X., Longo, D.L., McMahon, K.L., Meisenzahl, E., Melle, I., Mohnke, S., Montgomery, G.W., Mostert, J.C., Muhleisen, T.W., Nalls, M.A., Nichols, T.E., Nilsson, L.G., Nothen, M.M., Ohi, K., Olvera, R.L., Perez-Iglesias, R., Pike, G.B., Potkin, S.G., Reinvang, I., Reppermund, S., Rietschel, M., Romanczuk-Seiferth, N., Rosen, G.D., Rujescu, D., Schnell, K., Schofield, P.R., Smith, C., Steen, V.M., Sussmann, J.E., Thalamuthu, A., Toga, A.W., Traynor, B.J., Troncoso, J., Turner, J.A., Valdes Hernandez, M.C., van 't Ent, D., van der Brug, M., van der Wee, N.J., van Tol, M.J., Veltman, D.J., Wassink, T.H.,

Westman, E., Zielke, R.H., Zonderman, A.B., Ashbrook, D.G., Hager, R., Lu, L., McMahon, F.J., Morris, D.W., Williams, R.W., Brunner, H.G., Buckner, R.L., Buitelaar, J.K., Cahn, W., Calhoun, V.D., Cavalleri, G.L., Crespo-Facorro, B., Dale, A.M., Davies, G.E., Delanty, N., Depondt, C., Djurovic, S., Drevets, W.C., Espeseth, T., Gollub, R.L., Ho, B.C., Hoffmann, W., Hosten, N., Kahn, R.S., Le Hellard, S., Meyer-Lindenberg, A., Muller-Myhsok, B., Nauck, M., Nyberg, L., Pandolfo, M., Penninx, B.W., Roffman, J.L., Sisodiya, S.M., Smoller, J.W., van Bokhoven, H., van Haren, N.E., Volzke, H., Walter, H., Weiner, M.W., Wen, W., White, T., Agartz, I., Andreassen, O.A., Blangero, J., Boomsma, D.I., Brouwer, R.M., Cannon, D.M., Cookson, M.R., de Geus, E.J., Deary, I.J., Donohoe, G., Fernandez, G., Fisher, S.E., Francks, C., Glahn, D.C., Grabe, H.J., Gruber, O., Hardy, J., Hashimoto, R., Hulshoff Pol, H.E., Jonsson, E.G., Kloszewska, I., Lovestone, S., Mattay, V.S., Mecocci, P., McDonald, C., McIntosh, A.M., Ophoff, R.A., Paus, T., Pausova, Z., Ryten, M., Sachdev, P.S., Saykin, A.J., Simmons, A., Singleton, A., Soininen, H., Wardlaw, J.M., Weale, M.E., Weinberger, D.R., Adams, H.H., Launer, L.J., Seiler, S., Schmidt, R., Chauhan, G., Satizabal, C.L., Becker, J.T., Yanek, L., van der Lee, S.J., Ebling, M., Fischl, B., Longstreth, W.T., Jr., Greve, D., Schmidt, H., Nyquist, P., Vinke, L.N., van Duijn, C.M., Xue, L., Mazoyer, B., Bis, J.C., Gudnason, V., Seshadri, S., Ikram, M.A., Alzheimer's Disease Neuroimaging, I., Consortium, C., Epigen, Imagen, Sys, Martin, N.G., Wright, M.J., Schumann, G., Franke, B., Thompson, P.M., Medland, S.E., 2015. Common genetic variants influence human subcortical brain structures. Nature 520, 224-229.

Hillary, F.G., Grafman, J.H., 2017. Injured Brains and Adaptive Networks: The Benefits and Costs of Hyperconnectivity. Trends Cogn Sci 21, 385-401.

Hillman, E.M., 2014. Coupling mechanism and significance of the BOLD signal: a status report. Annu Rev Neurosci 37, 161-181.

Ho, A.K., Gilbert, A.S., Mason, S.L., Goodman, A.O., Barker, R.A., 2009. Health-related quality of life in Huntington's disease: Which factors matter most? Mov Disord 24, 574-578.

Hobbs NZ, C.J., Farmer RE, Rees EM, Crawford HE, Malone IB et al. , 2013. Evaluation of multimodal, multi-site neuroimaging measures in Huntington's disease: Baseline results from the PADDINGTON study. Neuroimage: Clinical in press.

Hobbs, N.Z., Pedrick, A.V., Say, M.J., Frost, C., Dar Santos, R., Coleman, A., Sturrock, A., Craufurd, D., Stout, J.C., Leavitt, B.R., Barnes, J., Tabrizi, S.J., Scahill, R.I., 2011. The structural involvement of the cingulate cortex in premanifest and early Huntington's disease. Mov Disord 26, 1684-1690.

Hodges, A., Strand, A.D., Aragaki, A.K., Kuhn, A., Sengstag, T., Hughes, G., Elliston, L.A., Hartog, C., Goldstein, D.R., Thu, D., Hollingsworth, Z.R., Collin, F., Synek, B., Holmans, P.A., Young, A.B., Wexler, N.S., Delorenzi, M., Kooperberg, C., Augood, S.J., Faull, R.L., Olson, J.M., Jones, L., Luthi-Carter, R., 2006. Regional and cellular gene expression changes in human Huntington's disease brain. Hum Mol Genet 15, 965-977.

Hogarth, P., Kayson, E., Kieburtz, K., Marder, K., Oakes, D., Rosas, D., Shoulson, I., Wexler, N.S., Young, A.B., Zhao, H., 2005. Interrater agreement in the assessment of motor manifestations of Huntington's disease. Mov Disord 20, 293-297.

Honey, C.J., Sporns, O., Cammoun, L., Gigandet, X., Thiran, J.P., Meuli, R., Hagmann, P., 2009. Predicting human resting-state functional connectivity from structural connectivity. Proc Natl Acad Sci U S A 106, 2035-2040.

Huang, B., Wei, W., Wang, G., Gaertig, M.A., Feng, Y., Wang, W., Li, X.J., Li, S., 2015. Mutant huntingtin downregulates myelin regulatory factor-mediated myelin gene expression and affects mature oligodendrocytes. Neuron 85, 1212-1226.

Huntington Study Group, C.I., 1996. Unified Huntington's Disease Rating Scale: reliability and consistency. Mov Disord 11, 136-142.

Iturria-Medina, Y., Carbonell, F.M., Sotero, R.C., Chouinard-Decorte, F., Evans, A.C., Alzheimer's Disease Neuroimaging, I., 2017. Multifactorial causal model of brain (dis)organization and therapeutic intervention: Application to Alzheimer's disease. Neuroimage 152, 60-77.

Iturria-Medina, Y., Evans, A.C., 2015. On the central role of brain connectivity in neurodegenerative disease progression. Front Aging Neurosci 7, 90.

Iturria-Medina, Y., Sotero, R.C., Toussaint, P.J., Evans, A.C., Alzheimer's Disease Neuroimaging, I., 2014. Epidemic spreading model to characterize misfolded proteins propagation in aging and associated neurodegenerative disorders. PLoS Comput Biol 10, e1003956.

Iturria-Medina, Y., Sotero, R.C., Toussaint, P.J., Mateos-Perez, J.M., Evans, A.C., Alzheimer's Disease Neuroimaging, I., 2016. Early role of vascular dysregulation on late-onset Alzheimer's disease based on multifactorial data-driven analysis. Nat Commun 7, 11934.

Jbabdi, S., Behrens, T.E., 2013. Long-range connectomics. Ann N Y Acad Sci 1305, 83-93.

Jeurissen, B., Leemans, A., Tournier, J.D., Jones, D.K., Sijbers, J., 2012. Investigating the prevalence of complex fiber configurations in white matter tissue with diffusion magnetic resonance imaging. Hum Brain Mapp.

Jeurissen, B., Leemans, A., Tournier, J.D., Jones, D.K., Sijbers, J., 2013. Investigating the prevalence of complex fiber configurations in white matter tissue with diffusion magnetic resonance imaging. Hum Brain Mapp 34, 2747-2766.

Jin, J., Peng, Q., Hou, Z., Jiang, M., Wang, X., Langseth, A.J., Tao, M., Barker, P.B., Mori, S., Bergles, D.E., Ross, C.A., Detloff, P.J., Zhang, J., Duan, W., 2015. Early white matter abnormalities, progressive brain pathology and motor deficits in a novel knock-in mouse model of Huntington's disease. Hum Mol Genet 24, 2508-2527.

Jones, D.K., Knosche, T.R., Turner, R., 2013. White matter integrity, fiber count, and other fallacies: the do's and don'ts of diffusion MRI. Neuroimage 73, 239-254.

Julien, C.L., Thompson, J.C., Wild, S., Yardumian, P., Snowden, J.S., Turner, G., Craufurd, D., 2007. Psychiatric disorders in preclinical Huntington's disease. J Neurol Neurosurg Psychiatry 78, 939-943.

Kang, H.J., Kawasawa, Y.I., Cheng, F., Zhu, Y., Xu, X., Li, M., Sousa, A.M., Pletikos, M., Meyer, K.A., Sedmak, G., Guennel, T., Shin, Y., Johnson, M.B., Krsnik, Z., Mayer, S., Fertuzinhos, S., Umlauf, S., Lisgo, S.N., Vortmeyer, A., Weinberger, D.R., Mane, S., Hyde, T.M., Huttner, A., Reimers, M., Kleinman, J.E., Sestan, N., 2011. Spatio-temporal transcriptome of the human brain. Nature 478, 483-489.

Karbowski, J., 2007. Global and regional brain metabolic scaling and its functional consequences. BMC Biol 5, 18.

Kim, J.S., Reading, S.A., Brashers-Krug, T., Calhoun, V.D., Ross, C.A., Pearlson, G.D., 2004. Functional MRI study of a serial reaction time task in Huntington's disease. Psychiatry Res 131, 23-30.

Kloppel, S., Draganski, B., Golding, C.V., Chu, C., Nagy, Z., Cook, P.A., Hicks, S.L., Kennard, C., Alexander, D.C., Parker, G.J., Tabrizi, S.J., Frackowiak, R.S., 2008. White matter connections reflect changes in voluntary-guided saccades in pre-symptomatic Huntington's disease. Brain 131, 196-204.

Kloppel, S., Draganski, B., Siebner, H.R., Tabrizi, S.J., Weiller, C., Frackowiak, R.S., 2009. Functional compensation of motor function in pre-symptomatic Huntington's disease. Brain 132, 1624-1632.

Kloppel, S., Gregory, S., Scheller, E., Minkova, L., Razi, A., Durr, A., Roos, R.A., Leavitt, B.R., Papoutsi, M., Landwehrmeyer, G.B., Reilmann, R., Borowsky, B., Johnson, H., Mills, J.A., Owen, G., Stout, J.,

Scahill, R.I., Long, J.D., Rees, G., Tabrizi, S.J., Track-On, i., 2015. Compensation in Preclinical Huntington's Disease: Evidence From the Track-On HD Study. EBioMedicine 2, 1420-1429.
Kloppel, S., Stonnington, C.M., Petrovic, P., Mobbs, D., Tuscher, O., Craufurd, D., Tabrizi, S.J., Frackowiak, R.S., 2010. Irritability in pre-clinical Huntington's disease. Neuropsychologia 48, 549-557.
Korgaonkar, M.S., Fornito, A., Williams, L.M., Grieve, S.M., 2014. Abnormal structural networks characterize major depressive disorder: a connectome analysis. Biol Psychiatry 76, 567-574.
Kramer, C.Y., 1956. Extension of multiple range tests to group means with unequal numbers of replications. Biometrics 12, 309-310.
Krienen, F.M., Yeo, B.T., Ge, T., Buckner, R.L., Sherwood, C.C., 2016. Transcriptional profiles of supragranular-enriched genes associate with corticocortical network architecture in the human brain. Proc Natl Acad Sci U S A 113, E469-478.
Langbehn, D.R., Brinkman, R.R., Falush, D., Paulsen, J.S., Hayden, M.R., 2004. A new model for prediction of the age of onset and penetrance for Huntington's disease based on CAG length. Clin Genet 65, 267-277.
Langfelder, P., Cantle, J.P., Chatzopoulou, D., Wang, N., Gao, F., Al-Ramahi, I., Lu, X.H., Ramos, E.M., El-Zein, K., Zhao, Y., Deverasetty, S., Tebbe, A., Schaab, C., Lavery, D.J., Howland, D., Kwak, S., Botas, J., Aaronson, J.S., Rosinski, J., Coppola, G., Horvath, S., Yang, X.W., 2016. Integrated genomics and proteomics define huntingtin CAG length-dependent networks in mice. Nat Neurosci 19, 623-633.
Le Bihan, D., Johansen-Berg, H., 2012. Diffusion MRI at 25: exploring brain tissue structure and function. Neuroimage 61, 324-341.
Le Bihan, D., Mangin, J.F., Poupon, C., Clark, C.A., Pappata, S., Molko, N., Chabriat, H., 2001. Diffusion tensor imaging: concepts and applications. J Magn Reson Imaging 13, 534-546.
Le Bihan, D., Poupon, C., Amadon, A., Lethimonnier, F., 2006. Artifacts and pitfalls in diffusion MRI. J Magn Reson Imaging 24, 478-488.
Lee, J.M., Ivanova, E.V., Seong, I.S., Cashorali, T., Kohane, I., Gusella, J.F., MacDonald, M.E., 2007. Unbiased gene expression analysis implicates the huntingtin polyglutamine tract in extra-mitochondrial energy metabolism. PLoS Genet 3, e135.
Leonardi, N., Richiardi, J., Gschwind, M., Simioni, S., Annoni, J.M., Schluep, M., Vuilleumier, P., Van De Ville, D., 2013. Principal components of functional connectivity: a new approach to study dynamic brain connectivity during rest. Neuroimage 83, 937-950.

Levy, M.L., Cummings, J.L., Fairbanks, L.A., Masterman, D., Miller, B.L., Craig, A.H., Paulsen, J.S., Litvan, I., 1998. Apathy is not depression. J Neuropsychiatry Clin Neurosci 10, 314-319.
Li, B., Liu, L., Friston, K.J., Shen, H., Wang, L., Zeng, L.L., Hu, D., 2013. A treatment-resistant default mode subnetwork in major depression. Biol Psychiatry 74, 48-54.
Li, K., Liu, L., Yin, Q., Dun, W., Xu, X., Liu, J., Zhang, M., 2016. Abnormal rich club organization and impaired correlation between structural and functional connectivity in migraine sufferers. Brain Imaging Behav.
Liang, X., Wang, J., Yan, C., Shu, N., Xu, K., Gong, G., He, Y., 2012. Effects of different correlation metrics and preprocessing factors on small-world brain functional networks: a resting-state functional MRI study. PLoS One 7, e32766.
Liang, X., Zou, Q., He, Y., Yang, Y., 2013. Coupling of functional connectivity and regional cerebral blood flow reveals a physiological basis for network hubs of the human brain. Proc Natl Acad Sci U S A 110, 1929-1934.
Lidow, M.S., Goldman-Rakic, P.S., Rakic, P., Innis, R.B., 1989. Dopamine D2 receptors in the cerebral cortex: distribution and pharmacological characterization with [3H]raclopride. Proc Natl Acad Sci U S A 86, 6412-6416.
Lin, W.L., Zehr, C., Lewis, J., Hutton, M., Yen, S.H., Dickson, D.W., 2005. Progressive white matter pathology in the spinal cord of transgenic mice expressing mutant (P301L) human tau. J Neurocytol 34, 397-410.
Lindauer, U., Leithner, C., Kaasch, H., Rohrer, B., Foddis, M., Fuchtemeier, M., Offenhauser, N., Steinbrink, J., Royl, G., Kohl-Bareis, M., Dirnagl, U., 2010. Neurovascular coupling in rat brain operates independent of hemoglobin deoxygenation. J Cereb Blood Flow Metab 30, 757-768.
Liu, W., Yang, J., Burgunder, J., Cheng, B., Shang, H., 2016. Diffusion imaging studies of Huntington's disease: A meta-analysis. Parkinsonism Relat Disord 32, 94-101.
Logothetis, N.K., Pauls, J., Augath, M., Trinath, T., Oeltermann, A., 2001. Neurophysiological investigation of the basis of the fMRI signal. Nature 412, 150-157.
Lopez-Mora, D.A., Camacho, V., Perez-Perez, J., Martinez-Horta, S., Fernandez, A., Sampedro, F., Montes, A., Lozano-Martinez, G.A., Gomez-Anson, B., Kulisevsky, J., Carrio, I., 2016. Striatal hypometabolism in premanifest and manifest Huntington's disease patients. Eur J Nucl Med Mol Imaging.

Maier-Hein, K.H., Neher, P.F., Houde, J.C., Cote, M.A., Garyfallidis, E., Zhong, J., Chamberland, M., Yeh, F.C., Lin, Y.C., Ji, Q., Reddick, W.E., Glass, J.O., Chen, D.Q., Feng, Y., Gao, C., Wu, Y., Ma, J., Renjie, H., Li, Q., Westin, C.F., Deslauriers-Gauthier, S., Gonzalez, J.O.O., Paquette, M., St-Jean, S., Girard, G., Rheault, F., Sidhu, J., Tax, C.M.W., Guo, F., Mesri, H.Y., David, S., Froeling, M., Heemskerk, A.M., Leemans, A., Bore, A., Pinsard, B., Bedetti, C., Desrosiers, M., Brambati, S., Doyon, J., Sarica, A., Vasta, R., Cerasa, A., Quattrone, A., Yeatman, J., Khan, A.R., Hodges, W., Alexander, S., Romascano, D., Barakovic, M., Auria, A., Esteban, O., Lemkaddem, A., Thiran, J.P., Cetingul, H.E., Odry, B.L., Mailhe, B., Nadar, M.S., Pizzagalli, F., Prasad, G., Villalon-Reina, J.E., Galvis, J., Thompson, P.M., Requejo, F.S., Laguna, P.L., Lacerda, L.M., Barrett, R., Dell'Acqua, F., Catani, M., Petit, L., Caruyer, E., Daducci, A., Dyrby, T.B., Holland-Letz, T., Hilgetag, C.C., Stieltjes, B., Descoteaux, M., 2017. The challenge of mapping the human connectome based on diffusion tractography. Nat Commun 8, 1349.

Mandelli, M.L., Vilaplana, E., Brown, J.A., Hubbard, H.I., Binney, R.J., Attygalle, S., Santos-Santos, M.A., Miller, Z.A., Pakvasa, M., Henry, M.L., Rosen, H.J., Henry, R.G., Rabinovici, G.D., Miller, B.L., Seeley, W.W., Gorno-Tempini, M.L., 2016. Healthy brain connectivity predicts atrophy progression in non-fluent variant of primary progressive aphasia. Brain.

Marrakchi-Kacem, L., Delmaire, C., Guevara, P., Poupon, F., Lecomte, S., Tucholka, A., Roca, P., Yelnik, J., Durr, A., Mangin, J.F., Lehericy, S., Poupon, C., 2013. Mapping Cortico-Striatal Connectivity onto the Cortical Surface: A New Tractography-Based Approach to Study Huntington Disease. PLoS One 8, e53135.

Marrie, R.A., Zhang, L., Lix, L.M., Graff, L.A., Walker, J.R., Fisk, J.D., Patten, S.B., Hitchon, C.A., Bolton, J.M., Sareen, J., El-Gabalawy, R., Marriott, J.J., Bernstein, C.N., 2017. The validity and reliability of screening measures for depression and anxiety disorders in multiple sclerosis. Mult Scler Relat Disord 20, 9-15.

Martinez-Horta, S., Perez-Perez, J., van Duijn, E., Fernandez-Bobadilla, R., Carceller, M., Pagonabarraga, J., Pascual-Sedano, B., Campolongo, A., Ruiz-Idiago, J., Sampedro, F., Landwehrmeyer, G.B., Spanish, R.i.o.t.E.H.s.D.N., Kulisevsky, J., 2016. Neuropsychiatric symptoms are very common in premanifest and early stage Huntington's Disease. Parkinsonism Relat Disord 25, 58-64.

Mason, S., Barker, R.A., 2015. Rating Apathy in Huntington's Disease: Patients and Companions Agree. J Huntingtons Dis 4, 49-59.

Mastrokolias, A., Ariyurek, Y., Goeman, J.J., van Duijn, E., Roos, R.A., van der Mast, R.C., van Ommen, G.B., den Dunnen, J.T., t Hoen, P.A., van Roon-Mom, W.M., 2015. Huntington's disease biomarker

progression profile identified by transcriptome sequencing in peripheral blood. Eur J Hum Genet 23, 1349-1356.
Matsui, J.T., Vaidya, J.G., Johnson, H.J., Magnotta, V.A., Long, J.D., Mills, J.A., Lowe, M.J., Sakaie, K.E., Rao, S.M., Smith, M.M., Paulsen, J.S., 2013. Diffusion weighted imaging of prefrontal cortex in prodromal huntington's disease. Hum Brain Mapp.
Mazziotta, J.C., Phelps, M.E., Pahl, J.J., Huang, S.C., Baxter, L.R., Riege, W.H., Hoffman, J.M., Kuhl, D.E., Lanto, A.B., Wapenski, J.A., et al., 1987. Reduced cerebral glucose metabolism in asymptomatic subjects at risk for Huntington's disease. N Engl J Med 316, 357-362.
McColgan, P., Seunarine, K.K., Razi, A., Cole, J.H., Gregory, S., Durr, A., Roos, R.A., Stout, J.C., Landwehrmeyer, B., Scahill, R.I., Clark, C.A., Rees, G., Tabrizi, S.J., Track, H.D.I., 2015. Selective vulnerability of Rich Club brain regions is an organizational principle of structural connectivity loss in Huntington's disease. Brain.
Messe, A., Rudrauf, D., Benali, H., Marrelec, G., 2014. Relating structure and function in the human brain: relative contributions of anatomy, stationary dynamics, and non-stationarities. PLoS Comput Biol 10, e1003530.
Miller, J.A., Horvath, S., Geschwind, D.H., 2010. Divergence of human and mouse brain transcriptome highlights Alzheimer disease pathways. Proc Natl Acad Sci U S A 107, 12698-12703.
Miller, J.R., Lo, K.K., Andre, R., Hensman Moss, D.J., Trager, U., Stone, T.C., Jones, L., Holmans, P., Plagnol, V., Tabrizi, S.J., 2016. RNA-Seq of Huntington's disease patient myeloid cells reveals innate transcriptional dysregulation associated with proinflammatory pathway activation. Hum Mol Genet 25, 2893-2904.
Misic, B., Betzel, R.F., de Reus, M.A., van den Heuvel, M.P., Berman, M.G., McIntosh, A.R., Sporns, O., 2016. Network-Level Structure-Function Relationships in Human Neocortex. Cereb Cortex 26, 3285-3296.
Modat, M., Ridgway, G.R., Taylor, Z.A., Lehmann, M., Barnes, J., Hawkes, D.J., Fox, N.C., Ourselin, S., 2010. Fast free-form deformation using graphics processing units. Comput Methods Programs Biomed 98, 278-284.
Molina-Calavita, M., Barnat, M., Elias, S., Aparicio, E., Piel, M., Humbert, S., 2014. Mutant huntingtin affects cortical progenitor cell division and development of the mouse neocortex. J Neurosci 34, 10034-10040.

Moss, D.J.H., Pardinas, A.F., Langbehn, D., Lo, K., Leavitt, B.R., Roos, R., Durr, A., Mead, S., investigators, T.-H., investigators, R., Holmans, P., Jones, L., Tabrizi, S.J., 2017. Identification of genetic variants associated with Huntington's disease progression: a genome-wide association study. Lancet Neurol.
Mueller, S.G., Ng, P., Neylan, T., Mackin, S., Wolkowitz, O., Mellon, S., Yan, X., Flory, J., Yehuda, R., Marmar, C.R., Weiner, M.W., 2015. Evidence for disrupted gray matter structural connectivity in posttraumatic stress disorder. Psychiatry Res 234, 194-201.
Muller, H.P., Gorges, M., Gron, G., Kassubek, J., Landwehrmeyer, G.B., Sussmuth, S.D., Wolf, R.C., Orth, M., 2016. Motor network structure and function are associated with motor performance in Huntington's disease. J Neurol 263, 539-549.
Mykletun, A., Stordal, E., Dahl, A.A., 2001. Hospital Anxiety and Depression (HAD) scale: factor structure, item analyses and internal consistency in a large population. Br J Psychiatry 179, 540-544.
Naarding, P., Janzing, J.G., Eling, P., van der Werf, S., Kremer, B., 2009. Apathy is not depression in Huntington's disease. J Neuropsychiatry Clin Neurosci 21, 266-270.
Novak, M.J., Seunarine, K.K., Gibbard, C.R., McColgan, P., Draganski, B., Friston, K., Clark, C.A., Tabrizi, S.J., 2015. Basal ganglia-cortical structural connectivity in Huntington's disease. Hum Brain Mapp.
Novak, M.J., Warren, J.D., Henley, S.M., Draganski, B., Frackowiak, R.S., Tabrizi, S.J., 2012. Altered brain mechanisms of emotion processing in pre-manifest Huntington's disease. Brain 135, 1165-1179.
Odish, O.F., Caeyenberghs, K., Hosseini, H., van den Bogaard, S.J., Roos, R.A., Leemans, A., 2015. Dynamics of the connectome in Huntington's disease: A longitudinal diffusion MRI study. Neuroimage Clin 9, 32-43.
Odish, O.F., van den Berg-Huysmans, A.A., van den Bogaard, S.J., Dumas, E.M., Hart, E.P., Rombouts, S.A., van der Grond, J., Roos, R.A., on behalf of the, T.-H.D.I.G., 2014. Longitudinal resting state fMRI analysis in healthy controls and premanifest Huntington's disease gene carriers: A three-year follow-up study. Hum Brain Mapp.
Ogawa, S., Lee, T.M., Kay, A.R., Tank, D.W., 1990. Brain magnetic resonance imaging with contrast dependent on blood oxygenation. Proc Natl Acad Sci U S A 87, 9868-9872.
Owen, J.P., Ziv, E., Bukshpun, P., Pojman, N., Wakahiro, M., Berman, J.I., Roberts, T.P., Friedman, E.J., Sherr, E.H., Mukherjee, P., 2013. Test-retest reliability of computational network measurements derived from the structural connectome of the human brain. Brain Connect 3, 160-176.

Papoutsi, M., Labuschagne, I., Tabrizi, S.J., Stout, J.C., 2014. The cognitive burden in Huntington's disease: pathology, phenotype, and mechanisms of compensation. Mov Disord 29, 673-683.
Parkes, L., Fulcher, B.D., Yucel, M., Fornito, A., 2017. Transcriptional signatures of connectomic subregions of the human striatum. Genes Brain Behav.
Paulsen, J.S., Long, J.D., Ross, C.A., Harrington, D.L., Erwin, C.J., Williams, J.K., Westervelt, H.J., Johnson, H.J., Aylward, E.H., Zhang, Y., Bockholt, H.J., Barker, R.A., Investigators, P.-H., Coordinators of the Huntington Study, G., 2014. Prediction of manifest Huntington's disease with clinical and imaging measures: a prospective observational study. Lancet Neurol 13, 1193-1201.
Paulsen, J.S., Ready, R.E., Hamilton, J.M., Mega, M.S., Cummings, J.L., 2001. Neuropsychiatric aspects of Huntington's disease. J Neurol Neurosurg Psychiatry 71, 310-314.
Paulsen, J.S., Smith, M.M., Long, J.D., investigators, P.H., Coordinators of the Huntington Study, G., 2013. Cognitive decline in prodromal Huntington Disease: implications for clinical trials. J Neurol Neurosurg Psychiatry 84, 1233-1239.
Paulsen, J.S., Zimbelman, J.L., Hinton, S.C., Langbehn, D.R., Leveroni, C.L., Benjamin, M.L., Reynolds, N.C., Rao, S.M., 2004. fMRI biomarker of early neuronal dysfunction in presymptomatic Huntington's Disease. AJNR Am J Neuroradiol 25, 1715-1721.
Penney, J.B., Jr., Vonsattel, J.P., MacDonald, M.E., Gusella, J.F., Myers, R.H., 1997. CAG repeat number governs the development rate of pathology in Huntington's disease. Ann Neurol 41, 689-692.
Phillips, O., Sanchez-Castaneda, C., Elifani, F., Maglione, V., Di Pardo, A., Caltagirone, C., Squitieri, F., Sabatini, U., Di Paola, M., 2013. Tractography of the corpus callosum in Huntington's disease. PLoS One 8, e73280.
Pickrell, A.M., Fukui, H., Wang, X., Pinto, M., Moraes, C.T., 2011. The striatum is highly susceptible to mitochondrial oxidative phosphorylation dysfunctions. J Neurosci 31, 9895-9904.
Plotkin, J.L., Surmeier, D.J., 2015. Corticostriatal synaptic adaptations in Huntington's disease. Curr Opin Neurobiol 33C, 53-62.
Poudel, G.R., Egan, G.F., Churchyard, A., Chua, P., Stout, J.C., Georgiou-Karistianis, N., 2014a. Abnormal synchrony of resting state networks in premanifest and symptomatic Huntington disease: the IMAGE-HD study. J Psychiatry Neurosci 39, 87-96.

Poudel, G.R., Stout, J.C., Dominguez, D.J., Salmon, L., Churchyard, A., Chua, P., Georgiou-Karistianis, N., Egan, G.F., 2014b. White matter connectivity reflects clinical and cognitive status in Huntington's disease. Neurobiol Dis 65, 180-187.
Poustchi-Amin, M., Mirowitz, S.A., Brown, J.J., McKinstry, R.C., Li, T., 2001. Principles and applications of echo-planar imaging: a review for the general radiologist. Radiographics 21, 767-779.
Power, J.D., Mitra, A., Laumann, T.O., Snyder, A.Z., Schlaggar, B.L., Petersen, S.E., 2014. Methods to detect, characterize, and remove motion artifact in resting state fMRI. Neuroimage 84, 320-341.
Powers, W.J., Videen, T.O., Markham, J., McGee-Minnich, L., Antenor-Dorsey, J.V., Hershey, T., Perlmutter, J.S., 2007. Selective defect of in vivo glycolysis in early Huntington's disease striatum. Proc Natl Acad Sci U S A 104, 2945-2949.
Qi, S., Meesters, S., Nicolay, K., Romeny, B.M., Ossenblok, P., 2015. The influence of construction methodology on structural brain network measures: A review. J Neurosci Methods 253, 170-182.
Quarantelli, M., Salvatore, E., Giorgio, S.M., Filla, A., Cervo, A., Russo, C.V., Cocozza, S., Massarelli, M., Brunetti, A., De Michele, G., 2013. Default-mode network changes in Huntington's disease: an integrated MRI study of functional connectivity and morphometry. PLoS One 8, e72159.
Raichle, M.E., MacLeod, A.M., Snyder, A.Z., Powers, W.J., Gusnard, D.A., Shulman, G.L., 2001. A default mode of brain function. Proc Natl Acad Sci U S A 98, 676-682.
Raj, A., Kuceyeski, A., Weiner, M., 2012. A network diffusion model of disease progression in dementia. Neuron 73, 1204-1215.
Raj, A., LoCastro, E., Kuceyeski, A., Tosun, D., Relkin, N., Weiner, M., for the Alzheimer's Disease Neuroimaging, I., 2015. Network Diffusion Model of Progression Predicts Longitudinal Patterns of Atrophy and Metabolism in Alzheimer's Disease. Cell Rep.
Ramasamy, A., Trabzuni, D., Guelfi, S., Varghese, V., Smith, C., Walker, R., De, T., Consortium, U.K.B.E., North American Brain Expression, C., Coin, L., de Silva, R., Cookson, M.R., Singleton, A.B., Hardy, J., Ryten, M., Weale, M.E., 2014. Genetic variability in the regulation of gene expression in ten regions of the human brain. Nat Neurosci 17, 1418-1428.
Ramirez-Manzanares, A., Cook, P.A., Hall, M., Ashtari, M., Gee, J.C., 2011. Resolving axon fiber crossings at clinical b-values: an evaluation study. Med Phys 38, 5239-5253.

Reading, S.A., Dziorny, A.C., Peroutka, L.A., Schreiber, M., Gourley, L.M., Yallapragada, V., Rosenblatt, A., Margolis, R.L., Pekar, J.J., Pearlson, G.D., Aylward, E., Brandt, J., Bassett, S.S., Ross, C.A., 2004. Functional brain changes in presymptomatic Huntington's disease. Ann Neurol 55, 879-883.
Reijmer, Y.D., Schultz, A.P., Leemans, A., O'Sullivan, M.J., Gurol, M.E., Sperling, R., Greenberg, S.M., Viswanathan, A., Hedden, T., 2015. Decoupling of structural and functional brain connectivity in older adults with white matter hyperintensities. Neuroimage 117, 222-229.
Reilmann, R.K., F. Bohlen, S. Saemann, P. Merl, T. Auer, D., 2005. Multimodal objective assessment of motor deficits in Huntington‘s

disease using isometric force analysis. J Neurol Neurosurg Psychiatry 76, A33.
Reuter, M., Fischl, B., 2011. Avoiding asymmetry-induced bias in longitudinal image processing. Neuroimage 57, 19-21.
Reuter, M., Schmansky, N.J., Rosas, H.D., Fischl, B., 2012. Within-subject template estimation for unbiased longitudinal image analysis. Neuroimage 61, 1402-1418.
Richiardi, J., Altmann, A., Milazzo, A.C., Chang, C., Chakravarty, M.M., Banaschewski, T., Barker, G.J., Bokde, A.L., Bromberg, U., Buchel, C., Conrod, P., Fauth-Buhler, M., Flor, H., Frouin, V., Gallinat, J., Garavan, H., Gowland, P., Heinz, A., Lemaitre, H., Mann, K.F., Martinot, J.L., Nees, F., Paus, T., Pausova, Z., Rietschel, M., Robbins, T.W., Smolka, M.N., Spanagel, R., Strohle, A., Schumann, G., Hawrylycz, M., Poline, J.B., Greicius, M.D., consortium, I., 2015. BRAIN NETWORKS. Correlated gene expression supports synchronous activity in brain networks. Science 348, 1241-1244.
Rittman, T., Rubinov, M., Vertes, P.E., Patel, A.X., Ginestet, C.E., Ghosh, B.C., Barker, R.A., Spillantini, M.G., Bullmore, E.T., Rowe, J.B., 2016. Regional expression of the MAPT gene is associated with loss of hubs in brain networks and cognitive impairment in Parkinson disease and progressive supranuclear palsy. Neurobiol Aging 48, 153-160.
Romme, I.A., de Reus, M.A., Ophoff, R.A., Kahn, R.S., van den Heuvel, M.P., 2016. Connectome Disconnectivity and Cortical Gene Expression in Patients With Schizophrenia. Biol Psychiatry.
Rosas, H.D., Lee, S.Y., Bender, A.C., Zaleta, A.K., Vangel, M., Yu, P., Fischl, B., Pappu, V., Onorato, C., Cha, J.H., Salat, D.H., Hersch, S.M., 2010. Altered white matter microstructure in the corpus callosum in Huntington's disease: implications for cortical "disconnection". Neuroimage 49, 2995-3004.

Rosas, H.D., Liu, A.K., Hersch, S., Glessner, M., Ferrante, R.J., Salat, D.H., van der Kouwe, A., Jenkins, B.G., Dale, A.M., Fischl, B., 2002. Regional and progressive thinning of the cortical ribbon in Huntington's disease. Neurology 58, 695-701.

Rosas, H.D., Salat, D.H., Lee, S.Y., Zaleta, A.K., Pappu, V., Fischl, B., Greve, D., Hevelone, N., Hersch, S.M., 2008. Cerebral cortex and the clinical expression of Huntington's disease: complexity and heterogeneity. Brain 131, 1057-1068.

Rosas, H.D., Tuch, D.S., Hevelone, N.D., Zaleta, A.K., Vangel, M., Hersch, S.M., Salat, D.H., 2006. Diffusion tensor imaging in presymptomatic and early Huntington's disease: Selective white matter pathology and its relationship to clinical measures. Mov Disord 21, 1317-1325.

Rosenblatt, A., Liang, K.Y., Zhou, H., Abbott, M.H., Gourley, L.M., Margolis, R.L., Brandt, J., Ross, C.A., 2006. The association of CAG repeat length with clinical progression in Huntington disease. Neurology 66, 1016-1020.

Ross, C.A., Aylward, E.H., Wild, E.J., Langbehn, D.R., Long, J.D., Warner, J.H., Scahill, R.I., Leavitt, B.R., Stout, J.C., Paulsen, J.S., Reilmann, R., Unschuld, P.G., Wexler, A., Margolis, R.L., Tabrizi, S.J., 2014. Huntington disease: natural history, biomarkers and prospects for therapeutics. Nat Rev Neurol 10, 204-216.

Ross, C.A., Tabrizi, S.J., 2011. Huntington's disease: from molecular pathogenesis to clinical treatment. Lancet Neurol 10, 83-98.

Rowe, K.C., Paulsen, J.S., Langbehn, D.R., Duff, K., Beglinger, L.J., Wang, C., O'Rourke, J.J., Stout, J.C., Moser, D.J., 2010. Self-paced timing detects and tracks change in prodromal Huntington disease. Neuropsychology 24, 435-442.

Rubinov, M., Sporns, O., 2010. Complex network measures of brain connectivity: uses and interpretations. Neuroimage 52, 1059-1069.

Saft, C., Schuttke, A., Beste, C., Andrich, J., Heindel, W., Pfleiderer, B., 2008. fMRI reveals altered auditory processing in manifest and premanifest Huntington's disease. Neuropsychologia 46, 1279-1289.

Sampaio, C., Borowsky, B., Reilmann, R., 2014. Clinical trials in Huntington's disease: Interventions in early clinical development and newer methodological approaches. Mov Disord 29, 1419-1428.

Sanchez-Castaneda, C., Cherubini, A., Elifani, F., Peran, P., Orobello, S., Capelli, G., Sabatini, U., Squitieri, F., 2012. Seeking huntington disease biomarkers by multimodal, cross-sectional basal ganglia imaging. Hum Brain Mapp.

Sarappa, C., Salvatore, E., Filla, A., Cocozza, S., Russo, C.V., Sacca, F., Brunetti, A., De Michele, G., Quarantelli, M., 2016. Functional MRI signal fluctuations highlight altered resting brain activity in Huntington's disease. Brain Imaging Behav.

Sathasivam, K., Neueder, A., Gipson, T.A., Landles, C., Benjamin, A.C., Bondulich, M.K., Smith, D.L., Faull, R.L., Roos, R.A., Howland, D., Detloff, P.J., Housman, D.E., Bates, G.P., 2013. Aberrant splicing of HTT generates the pathogenic exon 1 protein in Huntington disease. Proc Natl Acad Sci U S A 110, 2366-2370.

Saudou, F., Humbert, S., 2016. The Biology of Huntingtin. Neuron 89, 910-926.

Say, M.J., Jones, R., Scahill, R.I., Dumas, E.M., Coleman, A., Santos, R.C., Justo, D., Campbell, J.C., Queller, S., Shores, E.A., Tabrizi, S.J., Stout, J.C., Investigators, T.-H., 2011. Visuomotor integration deficits precede clinical onset in Huntington's disease. Neuropsychologia 49, 264-270.

Scheller, E., Minkova, L., Leitner, M., Kloppel, S., 2014. Attempted and successful compensation in preclinical and early manifest neurodegeneration - a review of task FMRI studies. Front Psychiatry 5, 132.

Schmidt, R., de Reus, M.A., Scholtens, L.H., van den Berg, L.H., van den Heuvel, M.P., 2016. Simulating disease propagation across white matter connectome reveals anatomical substrate for neuropathology staging in amyotrophic lateral sclerosis. Neuroimage 124, 762-769.

Schmidt, R., Verstraete, E., de Reus, M.A., Veldink, J.H., van den Berg, L.H., van den Heuvel, M.P., 2014. Correlation between structural and functional connectivity impairment in amyotrophic lateral sclerosis. Hum Brain Mapp 35, 4386-4395.

Seeley, W.W., Crawford, R.K., Zhou, J., Miller, B.L., Greicius, M.D., 2009. Neurodegenerative diseases target large-scale human brain networks. Neuron 62, 42-52.

Seibert, T.M., Brewer, J.B., 2011. Default network correlations analyzed on native surfaces. J Neurosci Methods 198, 301-311.

Seibert, T.M., Majid, D.S., Aron, A.R., Corey-Bloom, J., Brewer, J.B., 2012. Stability of resting fMRI interregional correlations analyzed in subject-native space: a one-year longitudinal study in healthy adults and premanifest Huntington's disease. Neuroimage 59, 2452-2463.

Senden, M., Deco, G., de Reus, M.A., Goebel, R., van den Heuvel, M.P., 2014. Rich club organization supports a diverse set of functional network configurations. Neuroimage 96, 174-182.

Seredenina, T., Luthi-Carter, R., 2012. What have we learned from gene expression profiles in Huntington's disease? Neurobiol Dis 45, 83-98.

Seunarine, K.K., Alexander, D.C., 2013. Multiple Fibers. Beyond the Diffusion Tensor. Diffusion MRI : from quantitative measurement to in vivo neuroanatomy. Academic Press, London, UK, pp. 105-123.
Shaffer, J.J., Ghayoor, A., Long, J.D., Kim, R.E., Lourens, S., O'Donnell, L.J., Westin, C.F., Rathi, Y., Magnotta, V., Paulsen, J.S., Johnson, H.J., 2017. Longitudinal diffusion changes in prodromal and early HD: Evidence of white-matter tract deterioration. Hum Brain Mapp 38, 1460-1477.
Shen, X., Finn, E.S., Scheinost, D., Rosenberg, M.D., Chun, M.M., Papademetris, X., Constable, R.T., 2017. Using connectome-based predictive modeling to predict individual behavior from brain connectivity. Nat Protoc 12, 506-518.
Shoulson, I., Fahn, S., 1979. Huntington disease: clinical care and evaluation. Neurology 29, 1-3.
Simpson, S.L., Bowman, F.D., Laurienti, P.J., 2013. Analyzing complex functional brain networks: Fusing statistics and network science to understand the brain*dagger. Stat Surv 7, 1-36.
Sinha, N., Manohar, S., Husain, M., 2013. Impulsivity and apathy in Parkinson's disease. J Neuropsychol 7, 255-283.
Sled, J.G., Zijdenbos, A.P., Evans, A.C., 1998. A nonparametric method for automatic correction of intensity nonuniformity in MRI data. IEEE Trans Med Imaging 17, 87-97.
Smith, A., 1968. The Symbol Digit Modalities Test: a neuropsychologic test for economic screening of learning and other cerebral disorders. Learning Disorders 3, 83-91.
Smith, R.E., Tournier, J.D., Calamante, F., Connelly, A., 2012. Anatomically-constrained tractography: improved diffusion MRI streamlines tractography through effective use of anatomical information. Neuroimage 62, 1924-1938.
Smith, R.E., Tournier, J.D., Calamante, F., Connelly, A., 2013. SIFT: Spherical-deconvolution informed filtering of tractograms. Neuroimage 67, 298-312.
Smith, R.E., Tournier, J.D., Calamante, F., Connelly, A., 2014. The effects of SIFT on the reproducibility and biological accuracy of the structural connectome. Neuroimage.
Smith, R.E., Tournier, J.D., Calamante, F., Connelly, A., 2015a. The effects of SIFT on the reproducibility and biological accuracy of the structural connectome. Neuroimage 104, 253-265.
Smith, R.E., Tournier, J.D., Calamante, F., Connelly, A., 2015b. SIFT2: Enabling dense quantitative assessment of brain white matter connectivity using streamlines tractography. Neuroimage 119, 338-351.
Smith, S.M., 2002. Fast robust automated brain extraction. Hum Brain Mapp 17, 143-155.

Smith, S.M., Jenkinson, M., Woolrich, M.W., Beckmann, C.F., Behrens, T.E., Johansen-Berg, H., Bannister, P.R., De Luca, M., Drobnjak, I., Flitney, D.E., Niazy, R.K., Saunders, J., Vickers, J., Zhang, Y., De Stefano, N., Brady, J.M., Matthews, P.M., 2004. Advances in functional and structural MR image analysis and implementation as FSL. Neuroimage 23 Suppl 1, S208-219.

Sporns, O., Betzel, R.F., 2015. Modular Brain Networks. Annu Rev Psychol.

Sprengelmeyer, R., Orth, M., Muller, H.P., Wolf, R.C., Gron, G., Depping, M.S., Kassubek, J., Justo, D., Rees, E.M., Haider, S., Cole, J.H., Hobbs, N.Z., Roos, R.A., Durr, A., Tabrizi, S.J., Sussmuth, S.D., Landwehrmeyer, G.B., 2014. The neuroanatomy of subthreshold depressive symptoms in Huntington's disease: a combined diffusion tensor imaging (DTI) and voxel-based morphometry (VBM) study. Psychol Med 44, 1867-1878.

Sritharan, A., Egan, G.F., Johnston, L., Horne, M., Bradshaw, J.L., Bohanna, I., Asadi, H., Cunnington, R., Churchyard, A.J., Chua, P., Farrow, M., Georgiou-Karistianis, N., 2010. A longitudinal diffusion tensor imaging study in symptomatic Huntington's disease. J Neurol Neurosurg Psychiatry 81, 257-262.

Stejskal, E., Tanner, J., 1965. Spin diffusion measurements: spin echoes in the presence of a time dependent field gradient. J Chem Phys 42, 288.

Stoffers, D., Sheldon, S., Kuperman, J.M., Goldstein, J., Corey-Bloom, J., Aron, A.R., 2010. Contrasting gray and white matter changes in preclinical Huntington disease: an MRI study. Neurology 74, 1208-1216.

Stout, J.C., Jones, R., Labuschagne, I., O'Regan, A.M., Say, M.J., Dumas, E.M., Queller, S., Justo, D., Santos, R.D., Coleman, A., Hart, E.P., Durr, A., Leavitt, B.R., Roos, R.A., Langbehn, D.R., Tabrizi, S.J., Frost, C., 2012. Evaluation of longitudinal 12 and 24 month cognitive outcomes in premanifest and early Huntington's disease. J Neurol Neurosurg Psychiatry 83, 687-694.

Stout, J.C., Paulsen, J.S., Queller, S., Solomon, A.C., Whitlock, K.B., Campbell, J.C., Carlozzi, N., Duff, K., Beglinger, L.J., Langbehn, D.R., Johnson, S.A., Biglan, K.M., Aylward, E.H., 2011. Neurocognitive signs in prodromal Huntington disease. Neuropsychology 25, 1-14.

Stroop, J., 1935. Studies of interference in serial verbal reactions. J Exp Psychol 18, 643-662.

Subramanian, L., Hindle, J.V., Johnston, S., Roberts, M.V., Husain, M., Goebel, R., Linden, D., 2011. Real-time functional magnetic resonance imaging neurofeedback for treatment of Parkinson's disease. J Neurosci 31, 16309-16317.

Supek, F., Bosnjak, M., Skunca, N., Smuc, T., 2011. REVIGO summarizes and visualizes long lists of gene ontology terms. PLoS One 6, e21800.

Tabrizi, S.J., Langbehn, D.R., Leavitt, B.R., Roos, R.A., Durr, A., Craufurd, D., Kennard, C., Hicks, S.L., Fox, N.C., Scahill, R.I., Borowsky, B., Tobin, A.J., Rosas, H.D., Johnson, H., Reilmann, R., Landwehrmeyer, B., Stout, J.C., 2009. Biological and clinical manifestations of Huntington's disease in the longitudinal TRACK-HD study: cross-sectional analysis of baseline data. Lancet Neurol 8, 791-801.
Tabrizi, S.J., Reilmann, R., Roos, R.A., Durr, A., Leavitt, B., Owen, G., Jones, R., Johnson, H., Craufurd, D., Hicks, S.L., Kennard, C., Landwehrmeyer, B., Stout, J.C., Borowsky, B., Scahill, R.I., Frost, C., Langbehn, D.R., 2012. Potential endpoints for clinical trials in premanifest and early Huntington's disease in the TRACK-HD study: analysis of 24 month observational data. Lancet Neurol 11, 42-53.
Tabrizi, S.J., Scahill, R.I., Durr, A., Roos, R.A., Leavitt, B.R., Jones, R., Landwehrmeyer, G.B., Fox, N.C., Johnson, H., Hicks, S.L., Kennard, C., Craufurd, D., Frost, C., Langbehn, D.R., Reilmann, R., Stout, J.C., 2011. Biological and clinical changes in premanifest and early stage Huntington's disease in the TRACK-HD study: the 12-month longitudinal analysis. Lancet Neurol 10, 31-42.
Tabrizi, S.J., Scahill, R.I., Owen, G., Durr, A., Leavitt, B.R., Roos, R.A., Borowsky, B., Landwehrmeyer, B., Frost, C., Johnson, H., Craufurd, D., Reilmann, R., Stout, J.C., Langbehn, D.R., 2013. Predictors of phenotypic progression and disease onset in premanifest and early-stage Huntington's disease in the TRACK-HD study: analysis of 36-month observational data. Lancet Neurol.
Tabrizi, S.J., Workman, J., Hart, P.E., Mangiarini, L., Mahal, A., Bates, G., Cooper, J.M., Schapira, A.H., 2000. Mitochondrial dysfunction and free radical damage in the Huntington R6/2 transgenic mouse. Ann Neurol 47, 80-86.
Talairach, J., Tournoux, P., 1988. Co-planar stereotaxic atlas of the human brain. Thieme, New York.
Teo, R.T., Hong, X., Yu-Taeger, L., Huang, Y., Tan, L.J., Xie, Y., To, X.V., Guo, L., Rajendran, R., Novati, A., Calaminus, C., Riess, O., Hayden, M.R., Nguyen, H.P., Chuang, K.H., Pouladi, M.A., 2016. Structural and molecular myelination deficits occur prior to neuronal loss in the YAC128 and BACHD models of Huntington disease. Hum Mol Genet 25, 2621-2632.
Thobois, S., Ardouin, C., Lhommee, E., Klinger, H., Lagrange, C., Xie, J., Fraix, V., Coelho Braga, M.C., Hassani, R., Kistner, A., Juphard, A., Seigneuret, E., Chabardes, S., Mertens, P., Polo, G., Reilhac, A., Costes, N., LeBars, D., Savasta, M., Tremblay, L., Quesada, J.L., Bosson, J.L., Benabid, A.L., Broussolle, E., Pollak, P., Krack, P., 2010. Non-motor dopamine withdrawal syndrome after surgery for Parkinson's disease: predictors and underlying mesolimbic denervation. Brain 133, 1111-1127.

Thompson, J.C., Harris, J., Sollom, A.C., Stopford, C.L., Howard, E., Snowden, J.S., Craufurd, D., 2012. Longitudinal evaluation of neuropsychiatric symptoms in Huntington's disease. J Neuropsychiatry Clin Neurosci 24, 53-60.
Tomasi, D., Wang, G.J., Volkow, N.D., 2013. Energetic cost of brain functional connectivity. Proc Natl Acad Sci U S A 110, 13642-13647.
Tournier, J., Calamante, F., Connelly, A., 2010. Improved probabilistic streamlines tractography by 2nd order integration over fibre orientation distributions. Proc. Intl. Soc. Mag. Reson. Med.
Tournier, J.D., Calamante, F., Connelly, A., 2007. Robust determination of the fibre orientation distribution in diffusion MRI: non-negativity constrained super-resolved spherical deconvolution. Neuroimage 35, 1459-1472.
Tournier, J.D., Calamante, F., Connelly, A., 2012. MRtrix: Diffusion tractography in crossing fiber regions. Imaging Systems and Technology 22, 53-56.
Tournier, J.D., Calamante, F., Connelly, A., 2013. Determination of the appropriate b value and number of gradient directions for high-angular-resolution diffusion-weighted imaging. NMR Biomed 26, 1775-1786.
Tournier, J.D., Mori, S., Leemans, A., 2011. Diffusion tensor imaging and beyond. Magn Reson Med 65, 1532-1556.
Tziortzi, A.C., Haber, S.N., Searle, G.E., Tsoumpas, C., Long, C.J., Shotbolt, P., Douaud, G., Jbabdi, S., Behrens, T.E., Rabiner, E.A., Jenkinson, M., Gunn, R.N., 2014. Connectivity-based functional analysis of dopamine release in the striatum using diffusion-weighted MRI and positron emission tomography. Cereb Cortex 24, 1165-1177.
Unschuld, P.G., Joel, S.E., Pekar, J.J., Reading, S.A., Oishi, K., McEntee, J., Shanahan, M., Bakker, A., Margolis, R.L., Bassett, S.S., Rosenblatt, A., Mori, S., van Zijl, P.C., Ross, C.A., Redgrave, G.W., 2012. Depressive symptoms in prodromal Huntington's Disease correlate with Stroop-interference related functional connectivity in the ventromedial prefrontal cortex. Psychiatry Res 203, 166-174.
van den Bogaard, S.J., Dumas, E.M., Acharya, T.P., Johnson, H., Langbehn, D.R., Scahill, R.I., Tabrizi, S.J., van Buchem, M.A., van der Grond, J., Roos, R.A., Group, T.-H.I., 2011. Early atrophy of pallidum and accumbens nucleus in Huntington's disease. J Neurol 258, 412-420.
van den Heuvel, M.P., Bullmore, E.T., Sporns, O., 2016. Comparative Connectomics. Trends Cogn Sci 20, 345-361.

van den Heuvel, M.P., Hulshoff Pol, H.E., 2010. Exploring the brain network: a review on resting-state fMRI functional connectivity. Eur Neuropsychopharmacol 20, 519-534.
van den Heuvel, M.P., Kahn, R.S., Goni, J., Sporns, O., 2012. High-cost, high-capacity backbone for global brain communication. Proc Natl Acad Sci U S A 109, 11372-11377.
van den Heuvel, M.P., Sporns, O., 2011. Rich-club organization of the human connectome. J Neurosci 31, 15775-15786.
van den Heuvel, M.P., Sporns, O., 2013. An anatomical substrate for integration among functional networks in human cortex. J Neurosci 33, 14489-14500.
van den Heuvel, M.P., Sporns, O., Collin, G., Scheewe, T., Mandl, R.C., Cahn, W., Goni, J., Hulshoff Pol, H.E., Kahn, R.S., 2013. Abnormal Rich Club Organization and Functional Brain Dynamics in Schizophrenia. JAMA Psychiatry, 1-10.
van Duijn, E., Craufurd, D., Hubers, A.A., Giltay, E.J., Bonelli, R., Rickards, H., Anderson, K.E., van Walsem, M.R., van der Mast, R.C., Orth, M., Landwehrmeyer, G.B., European Huntington's Disease Network Behavioural Phenotype Working, G., 2014. Neuropsychiatric symptoms in a European Huntington's disease cohort (REGISTRY). J Neurol Neurosurg Psychiatry 85, 1411-1418.
Vandenberghe, W., Demaerel, P., Dom, R., Maes, F., 2009. Diffusion-weighted versus volumetric imaging of the striatum in early symptomatic Huntington disease. J Neurol 256, 109-114.
Veraart, J., Sijbers, J., Sunaert, S., Leemans, A., Jeurissen, B., 2013. Weighted linear least squares estimation of diffusion MRI parameters: strengths, limitations, and pitfalls. Neuroimage 81, 335-346.
Vertes, P.E., Rittman, T., Whitaker, K.J., Romero-Garcia, R., Vasa, F., Kitzbichler, M.G., Wagstyl, K., Fonagy, P., Dolan, R.J., Jones, P.B., Goodyer, I.M., Consortium, N., Bullmore, E.T., 2016. Gene transcription profiles associated with inter-modular hubs and connection distance in human functional magnetic resonance imaging networks. Philos Trans R Soc Lond B Biol Sci 371.
Viviani, R., Lehmann, M.L., Stingl, J.C., 2014. Use of magnetic resonance imaging in pharmacogenomics. Br J Clin Pharmacol 77, 684-694.
Voermans, N.C., Petersson, K.M., Daudey, L., Weber, B., Van Spaendonck, K.P., Kremer, H.P., Fernandez, G., 2004. Interaction between the human hippocampus and the caudate nucleus during route recognition. Neuron 43, 427-435.
Vonsattel, J.P., DiFiglia, M., 1998. Huntington disease. J Neuropathol Exp Neurol 57, 369-384.

Vonsattel, J.P.M.R.H.S., T. J.; Ferrante R. J.; Bird, E. D.; Richardson, E. P. , 1985. Neuropathological Classification of Huntington's Disease. J Neuropathol Exp Neurol 44, 559-577.
Wang, N., Gray, M., Lu, X.H., Cantle, J.P., Holley, S.M., Greiner, E., Gu, X., Shirasaki, D., Cepeda, C., Li, Y., Dong, H., Levine, M.S., Yang, X.W., 2014. Neuronal targets for reducing mutant huntingtin expression to ameliorate disease in a mouse model of Huntington's disease. Nat Med 20, 536-541.
Wang, Y.P., Gorenstein, C., 2013. Psychometric properties of the Beck Depression Inventory-II: a comprehensive review. Rev Bras Psiquiatr 35, 416-431.
Watts, D.J., Strogatz, S.H., 1998. Collective dynamics of 'small-world' networks. Nature 393, 440-442.
Weaver, K.E., Richards, T.L., Liang, O., Laurino, M.Y., Samii, A., Aylward, E.H., 2009. Longitudinal diffusion tensor imaging in Huntington's Disease. Exp Neurol 216, 525-529.
Werner, C.J., Dogan, I., Sass, C., Mirzazade, S., Schiefer, J., Shah, N.J., Schulz, J.B., Reetz, K., 2014. Altered resting-state connectivity in Huntington's disease. Hum Brain Mapp 35, 2582-2593.
Wexler, A., Wild, E.J., Tabrizi, S.J., 2016. George Huntington: a legacy of inquiry, empathy and hope. Brain 139, 2326-2333.
Whitaker, K.J., Vertes, P.E., Romero-Garcia, R., Vasa, F., Moutoussis, M., Prabhu, G., Weiskopf, N., Callaghan, M.F., Wagstyl, K., Rittman, T., Tait, R., Ooi, C., Suckling, J., Inkster, B., Fonagy, P., Dolan, R.J., Jones, P.B., Goodyer, I.M., Consortium, N., Bullmore, E.T., 2016. Adolescence is associated with genomically patterned consolidation of the hubs of the human brain connectome. Proc Natl Acad Sci U S A 113, 9105-9110.
Whitfield-Gabrieli, S., Nieto-Castanon, A., 2012. Conn: a functional connectivity toolbox for correlated and anticorrelated brain networks. Brain Connect 2, 125-141.
Wild, E.J., 2016. Huntington's Disease: The Most Curable Incurable Brain Disorder? EBioMedicine 8, 3-4.
Wild, E.J., Tabrizi, S.J., 2014. Targets for future clinical trials in Huntington's disease: What's in the pipeline? Mov Disord 29, 1434-1445.
Wilkins, B., Lee, N., Gajawelli, N., Law, M., Lepore, N., 2015. Fiber estimation and tractography in diffusion MRI: development of simulated brain images and comparison of multi-fiber analysis methods at clinical b-values. Neuroimage 109, 341-356.
Wolf, R.C., Sambataro, F., Vasic, N., Wolf, N.D., Thomann, P.A., Saft, C., Landwehrmeyer, G.B., Orth, M., 2012. Default-mode network changes in preclinical Huntington's disease. Exp Neurol 237, 191-198.

Wolf, R.C., Vasic, N., Schonfeldt-Lecuona, C., Landwehrmeyer, G.B., Ecker, D., 2007. Dorsolateral prefrontal cortex dysfunction in presymptomatic Huntington's disease: evidence from event-related fMRI. Brain 130, 2845-2857.
Wolf, T., Lindauer, U., Villringer, A., Dirnagl, U., 1997. Excessive oxygen or glucose supply does not alter the blood flow response to somatosensory stimulation or spreading depression in rats. Brain Res 761, 290-299.
Xia, M., Wang, J., He, Y., 2013. BrainNet Viewer: a network visualization tool for human brain connectomics. PLoS One 8, e68910.
Xiang, Z., Valenza, M., Cui, L., Leoni, V., Jeong, H.K., Brilli, E., Zhang, J., Peng, Q., Duan, W., Reeves, S.A., Cattaneo, E., Krainc, D., 2011. Peroxisome-proliferator-activated receptor gamma coactivator 1 alpha contributes to dysmyelination in experimental models of Huntington's disease. J Neurosci 31, 9544-9553.
Yao, Z., Zhang, Y., Lin, L., Zhou, Y., Xu, C., Jiang, T., 2010. Abnormal cortical networks in mild cognitive impairment and Alzheimer's disease. PLoS Comput Biol 6, e1001006.
Yeh, C.H., Smith, R.E., Liang, X., Calamante, F., Connelly, A., 2016. Correction for diffusion MRI fibre tracking biases: The consequences for structural connectomic metrics. Neuroimage.
Yeo, B.T., Krienen, F.M., Sepulcre, J., Sabuncu, M.R., Lashkari, D., Hollinshead, M., Roffman, J.L., Smoller, J.W., Zollei, L., Polimeni, J.R., Fischl, B., Liu, H., Buckner, R.L., 2011. The organization of the human cerebral cortex estimated by intrinsic functional connectivity. J Neurophysiol 106, 1125-1165.
Yin, R.H., Tan, L., Jiang, T., Yu, J.T., 2014. Prion-like Mechanisms in Alzheimer's Disease. Curr Alzheimer Res 11, 755-764.
Zalesky, A., Fornito, A., 2009. A DTI-derived measure of cortico-cortical connectivity. IEEE Trans Med Imaging 28, 1023-1036.
Zalesky, A., Fornito, A., Bullmore, E.T., 2010. Network-based statistic: identifying differences in brain networks. Neuroimage 53, 1197-1207.
Zalesky, A., Fornito, A., Cocchi, L., Gollo, L.L., van den Heuvel, M.P., Breakspear, M., 2016. Connectome sensitivity or specificity: which is more important? Neuroimage.
Zeighami, Y., Ulla, M., Iturria-Medina, Y., Dadar, M., Zhang, Y., Larcher, K.M., Fonov, V., Evans, A.C., Collins, D.L., Dagher, A., 2015. Network structure of brain atrophy in de novo Parkinson's disease. Elife 4.
Zhang, B., Gaiteri, C., Bodea, L.G., Wang, Z., McElwee, J., Podtelezhnikov, A.A., Zhang, C., Xie, T., Tran, L., Dobrin, R., Fluder, E., Clurman, B., Melquist, S., Narayanan, M., Suver, C., Shah, H., Mahajan, M.,

Gillis, T., Mysore, J., MacDonald, M.E., Lamb, J.R., Bennett, D.A., Molony, C., Stone, D.J., Gudnason, V., Myers, A.J., Schadt, E.E., Neumann, H., Zhu, J., Emilsson, V., 2013. Integrated systems approach identifies genetic nodes and networks in late-onset Alzheimer's disease. Cell 153, 707-720.
Zhang, Z., Liao, W., Chen, H., Mantini, D., Ding, J.R., Xu, Q., Wang, Z., Yuan, C., Chen, G., Jiao, Q., Lu, G., 2011. Altered functional-structural coupling of large-scale brain networks in idiopathic generalized epilepsy. Brain 134, 2912-2928.
Zhou, J., Gennatas, E.D., Kramer, J.H., Miller, B.L., Seeley, W.W., 2012. Predicting regional neurodegeneration from the healthy brain functional connectome. Neuron 73, 1216-1227.
Zimbelman, J.L., Paulsen, J.S., Mikos, A., Reynolds, N.C., Hoffmann, R.G., Rao, S.M., 2007. fMRI detection of early neural dysfunction in preclinical Huntington's disease. J Int Neuropsychol Soc 13, 758-769.
Zuccato, C., Marullo, M., Conforti, P., MacDonald, M.E., Tartari, M., Cattaneo, E., 2008. Systematic assessment of BDNF and its receptor levels in human cortices affected by Huntington's disease. Brain Pathol 18, 225-238.
Zucker, B., Kama, J.A., Kuhn, A., Thu, D., Orlando, L.R., Dunah, A.W., Gokce, O., Taylor, D.M., Lambeck, J., Friedrich, B., Lindenberg, K.S., Faull, R.L., Weiller, C., Young, A.B., Luthi-Carter, R., 2010. Decreased Lin7b expression in layer 5 pyramidal neurons may contribute to impaired corticostriatal connectivity in huntington disease. J Neuropathol Exp Neurol 69, 880-895.